# USING MEASUREMENTS OF CCN ACTIVITY TO CHARACTERIZE THE MIXING STATE, CHEMICAL COMPOSITION, AND DROPLET GROWTH KINETICS OF ATMOSPHERIC AEROSOLS TO CONSTRAIN THE AEROSOL INDIRECT EFFECT

A Dissertation
Presented to
The Academic Faculty

by

Richard H. Moore

In Partial Fulfillment
of the Requirements for the Degree
Doctor of Philosophy in the
School of Chemical & Biomolecular Engineering

Georgia Institute of Technology
December 2011

# USING MEASUREMENTS OF CCN ACTIVITY TO CHARACTERIZE THE MIXING STATE, CHEMICAL COMPOSITION, AND DROPLET GROWTH KINETICS OF ATMOSPHERIC AEROSOLS TO CONSTRAIN THE AEROSOL INDIRECT EFFECT

Approved by:

Professor Athanasios Nenes, Advisor
School of Chemical & Biomolecular Engineering and School of Earth & Atmospheric Sciences
*Georgia Institute of Technology*

Professor Amyn Teja
School of Chemical & Biomolecular Engineering
*Georgia Institute of Technology*

Professor Martha Grover
School of Chemical & Biomolecular Engineering
*Georgia Institute of Technology*

Professor Greg Huey
School of Earth & Atmospheric Sciences
*Georgia Institute of Technology*

Professor Rodney Weber
School of Earth & Atmospheric Sciences
*Georgia Institute of Technology*

Date Approved: 3 November 2011

*To my parents for first introducing me to science...*

# ACKNOWLEDGEMENTS

This dissertation has been made possible by a large number of colleagues, collaborators, and friends. First and foremost, thank you to Prof. Thanos Nenes for being a mentor and professional role model and for giving me numerous opportunities to work on interesting and useful scientific problems, to travel extensively for research and professional development, and for his advice and support in charting a future career path. More than anything, he has taught me to think about how I can take the science to a higher level. Thank you to Prof. Tim Raymond for first introducing me to aerosol science and for teaching me to design and execute careful and well-thought-out experiments and measurements. Thank you to my dissertation reading committee members for pushing me to think broadly about this research and for valuable feedback that has improved this dissertation. Thank you to Prof. Rodney Weber, Prof. Greg Huey and Dave Tanner for their willingness to share their equipment, supplies, and their extensive knowledge with me regarding everything from instrument circuits to putting instruments on aircraft. Thank you to the researchers at the NOAA Earth Systems Research Laboratory, especially Dr. Chuck Brock and Dr. Roya Bahreini whose measurements and ideas are reflected throughout this work. Thank you to Prof. Ellery Ingall, Prof. Armin Sorooshian, Prof. Akua Asa-Awuku, Dr. Luz Padró, Dr. Sara Lance, Dr. Vlassis Karydis, Dr. Tomi Raatikainen, Dr. Gabi Engelhart, Shannon Capps, Kate Cerully, Terry Lathem, Jack Lin, Ricardo Morales, and the many others with whom I've had the opportunity to collaborate these past years for their important contributions toward this dissertation and many interesting discussions.

This Ph.D. could never have been possible without the unconditional love and support of my family and friends. Thank you to my wonderful wife, Emily, who has shared the ups and downs of the last several years with me and who fills my life with so much joy and fun.

This work is a testament to her endless patience with me spending late nights in the lab or weeks away in the field. I'm so lucky to be with you. Thank you also to my mother and father who first taught me to love science and who showed me how to always keep learning and strive for excellence. Thank you both for many weeknights and weekends spent doing science fair projects! Thank you to my brother, Dave, for being a role model and friend all these years. Finally, thank you to all of my friends in Middletown, Lewisburg, and Atlanta for enriching my life in to many ways. Thank you.

# TABLE OF CONTENTS

# LIST OF TABLES

# LIST OF FIGURES

# SUMMARY

Atmospheric aerosols are known to exert a significant influence on the Earth's climate system; however, the magnitude of this influence is highly uncertain because of the complex interaction between aerosols and water vapor to form clouds. Toward reducing this uncertainty, this dissertation outlines a series of laboratory and *in-situ* field measurements, instrument technique development, and model simulations designed to characterize the ability of aerosols to act as cloud condensation nuclei (CCN) and form cloud droplets. Specifically, we empirically quantify the mixing state and thermodynamic properties of organic aerosols (e.g., hygroscopicity and droplet condensational uptake coefficient) measured *in situ* in polluted and non-polluted environments including Alaska, California, and Georgia. It is shown that organic aerosols comprise a substantial portion of the aerosol mass and are often water soluble. CCN measurements are compared to predictions from theory in order to determine the error associated with simplified composition and mixing state assumptions employed by current large-scale models, and these errors are used to constrain the uncertainty of global and regional cloud droplet number and albedo using a recently-developed cloud droplet parameterization adjoint model coupled with the NASA GMI chemical transport model. Quantifying the sensitivities of these cloud parameters to aerosol number is important because cloud droplet number and albedo are the main determinants of climate forcing.

We also present two novel techniques for fast measurements of CCN concentrations with high size, supersaturation, and temporal resolution that substantially improve the state of the art by several orders of magnitude. The first, called Scanning Flow CCN Analysis (SFCA) allows measurement of CCN supersaturation spectra (i.e., CCN concentrations over a range of supersaturations) in as little as 10-15 seconds (versus 30-60 minutes

for the conventional technique). SFCA has been successfully deployed in a ground-based study in Atlanta during 2009 and in an airborne study in California during 2010, both with good success. In addition, we present Scanning Mobility CCN Analysis (SMCA) as a new technique for measuring size-resolved CCN concentrations and droplet growth kinetics by coupling a TSI Scanning Mobility Particle Sizer (SMPS) to a Droplet Measurement Technologies CCN counter. By applying the same inversion algorithm to the CCN data as used for the SMPS, size-resolved CCN distributions can be obtained concurrently with particle size distributions over the timescale of a typical SMPS scan (typically 60-120 seconds). Fast measurement techniques such as SFCA and SMCA are particularly important for airborne studies, where the aircraft may sample particles and pollution plumes over several kilometers in only a few tens of seconds.

The techniques developed in this dissertation provide the means to comprehensively characterize the aerosol-water interactions relevant for constraining the indirect effects of aerosols on climate; however, the current global dataset of CCN observations remains limited mostly to continental regions in the Northern Hemisphere, where we show that cloud properties are relatively insensitive to changes in the CCN-active aerosol number. In directing future field studies focusing on CCN, the results of this dissertation suggest that these efforts should be directed toward the pristine regions in the Alaska-Canadian Arctic and southern oceans, where cloud properties (i.e., droplet number and albedo) are most sensitive to small perturbations in aerosol number. Ultimately, this work represents a step toward better understanding how atmospheric aerosols influence cloud properties and Earth's climate.

# CHAPTER I

# INTRODUCTION

It is widely-recognized that humans are changing Earth's climate in ways that are unsustainable, and which will likely lead to significant changes in the global and regional distribution of food, water, and clean air (*Solomon et al.*, 2007). Meanwhile efforts to mitigate or adapt to these climatic impacts will impose additional constraints on existing energy, health, and regulatory infrastructures. In order to inform future policy efforts toward solving these problems, it is essential to develop regional and global models that can be used to capture current and future climate trends. The key to improving these models is to develop a better understanding of the different physical mechanisms that contribute to Earth's climate.

Much work in past decades has contributed to elucidating how atmospheric gases and particles affect climate; however, the link between aerosols and clouds remains highly uncertain even today (*Solomon et al.*, 2007). This is due, in part, to the non-linearity of cloud processes and also because they span multiple scales from nanometer-sized particles and micrometer-sized droplets to large stratiform cloud decks on the order of hundreds of kilometers. Many of these scales are much smaller than the typical resolution of a global climate model ($\sim$ 100 km by 100 km grid cells), which means that these models must necessarily rely on simplified assumptions and parameterizations of these sub-grid processes. This motivates research into both characterizing aerosol-cloud interactions using these simple parameterizations as well as quantifying the uncertainties associated with these assumptions. In this study, we focus on measuring the properties of atmospheric aerosols and their ability to form cloud droplets, and on how measurements of these interactions can be used to assess and improve their representation in large scale models.

## *1.1 Climatic Effects of Aerosols*

Aerosols can affect climate directly through the absorption and scattering of shortwave and longwave radiation or indirectly by acting as cloud condensation nuclei (CCN) to form droplets that are usually more effective at absorbing and scattering light. These indirect effects manifest themselves in a number of ways shown in Figure 1.1. The first indirect effect (*Twomey*, 1974, 1977a) posits that an increased number of aerosols in a polluted atmosphere leads to a concomitant increase in the number of cloud droplets because there are more particles on which water vapor can condense. The plentiful, "polluted" droplets would be smaller than their "non-polluted" counterparts, assuming a constant amount of liquid water. This would lead to a denser, brighter cloud that would reflect more incoming solar radiation back into space than the less-dense, less-bright "non-polluted" clouds. Since these low-level, liquid clouds are at nearly the same temperature as the surface and assuming them to be black bodies, which is a good assumption for typical droplet concentrations above $\sim$10 cm$^{-3}$ (*Mauritsen et al.*, 2011), the net effect on outgoing infrared radiation is negligible since infrared emission scales with temperature to the fourth power. Thus, the first indirect effect is expected to lead to greater planetary cooling.

The second indirect effects follow logically from the first effect, in that the smaller droplets would be less likely to grow large enough to form drizzle and be removed to the surface as precipitation (*Albrecht*, 1989). Meanwhile, the suppressed precipitation invigorates the cloud updraft, entraining outside air and leading to taller clouds (*Pincus and Baker*, 1994). The increase in cloud lifetime from these phenomena increases the total amount of solar radiation reflected to space, even as the first indirect effect enhances the clouds' reflectivity.

It is currently thought that the cumulative impact of aerosols on climate (both direct and indirect) leads to a net cooling influence, which is comparable to the warming influence of carbon dioxide (*Solomon et al.*, 2007). This is shown in Figure 1.2 in terms of a globally-averaged, anthropogenic radiative forcing that reflects the impact that humans have had

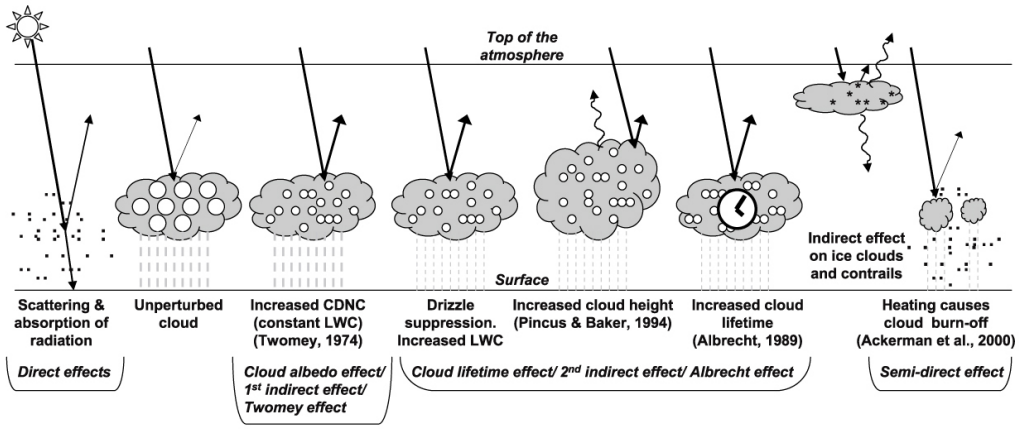


**Figure 1.1:** Schematic diagram showing the various radiative mechanisms associated with cloud effects that have been identified as significant in relation to aerosols (modified from *Haywood and Boucher* (2000)). The small black dots represent aerosol particles; the larger open circles cloud droplets. Straight lines represent the incident and reflected solar radiation, and wavy lines represent terrestrial radiation. The filled white circles indicate cloud droplet number concentration (CDNC). The unperturbed cloud contains larger cloud drops as only natural aerosols are available as cloud condensation nuclei, while the perturbed cloud contains a greater number of smaller cloud drops as both natural and anthropogenic aerosols are available as cloud condensation nuclei (CCN). The vertical grey dashes represent rainfall, and LWC refers to the liquid water content. Figure and caption reproduced with permission from Figure 2.10 of *Solomon et al.* (2007).

on influencing Earth's climate since pre-industrial times. The magnitudes of these forcings ($\pm$1-2 W m$^{-2}$) are tiny compared to the Earth's overall incoming and outgoing energy fluxes ($\sim$341 W m$^{-2}$; *Trenberth et al.*, 2009), but they still have a large impact on climate. For example, the globally-averaged temperature has risen by 0.76$\pm$0.19°C from the latter half of the 19th century to present day, and is currently increasing at a rate of 0.13$\pm$0.03°C per decade (*Solomon et al.*, 2007). This global average reflects a large degree of regional temperature variation with smaller changes near the equator and larger changes near the poles. Predicting future climatic changes requires an accurate assessment of both greenhouse gas-induced warming and aerosol-induced cooling. While the warming effects are fairly well-understood (Figure 1.2), the magnitude of this cooling is highly uncertain, primarily because of the large uncertainty associated with the aerosol indirect effects. Until

we can constrain this quantity with some degree of certainty, it will be impossible for society to assess its impact on the Earth system. The key to understanding the link between aerosols and clouds is their hygroscopic properties (i.e., aerosol-water interactions).

## *1.2 Aerosol Hygroscopicity*

Aerosol hygroscopic properties are chiefly dependent on particle size and chemical composition, and cloud droplet formation depends on this hygroscopicity and on the availability of water vapor (*Seinfeld and Pandis*, 2006; *Dusek et al.*, 2006). The typical size range of atmospheric aerosols spans several orders of magnitude (a few nanometers to tens of micrometers) and particles may contain any of the hundreds of different organic species, the eight or so inorganic species ($Na^+$, $K^+$, $NH_4^+$, $Ca^{2+}$, $Mg^{2+}$, $SO_4^{2-}$, $Cl^-$, $NO_3^-$), and water. Particle size and chemistry vary widely throughout the atmosphere depending on, e.g., local meteorology and proximity to emissions sources. Meanwhile, gas- and aerosol-phase chemical reactions in the atmosphere change both the amount of material in the aerosol phase and also the hygroscopic properties of these aerosols over time. Thus, it is important to investigate the properties of atmospheric aerosols either *in situ* or through realistic laboratory experiments (e.g, ambient filter extracts or the oxidation of gas-phase precursors in a smog chamber).

Köhler theory is the thermodynamic equilibrium model that describes the conditions under which atmospheric particles uptake water and either exist as stable haze droplets or experience rapid and uncontrolled condensational growth as cloud condensation nuclei to form larger cloud droplets (*Köhler*, 1936). The theory is expressed as the competition between the Kelvin effect and the Raoult effect:

$$s = \ln \frac{P_w}{P_w^\circ} = \frac{4 M_w \sigma}{RT \rho_w D_{p,wet}} - \frac{M_w \rho_s \phi_s \nu_s D_{p,dry}}{\rho_w M_s D_{p,wet}^3} \tag{1.1}$$

where $s$ is equilibrium water vapor supersaturation, $P_w$ is the ambient vapor pressure of water, $P_w^\circ$ is the temperature-dependent, saturated vapor pressure of water, $M_w$ is the molar

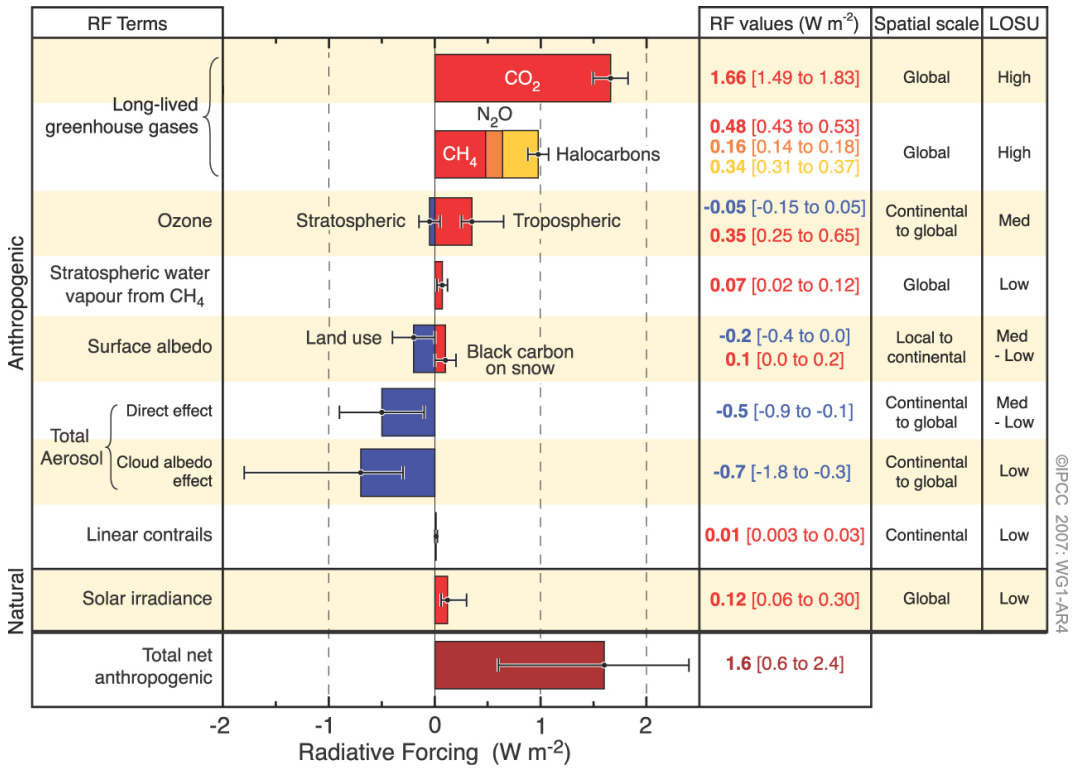


**Figure 1.2:** Global mean radiative forcing (RF) estimates and ranges in 2005 for anthropogenic carbon dioxide ($CO_2$), methane ($CH_4$), nitrous oxide ($N_2O$) and other important agents and mechanisms, together with the typical geographical extent (spatial scale) of the forcing and the assessed level of scientific understanding (LOSU). The net anthropogenic radiative forcing and its range are also shown. These require summing asymmetric uncertainty estimates from the component terms, and cannot be obtained by simple addition. Additional forcing factors not included here are considered to have a very low LOSU. Volcanic aerosols contribute an additional natural forcing but are not included in this figure due to their episodic nature. The range for linear contrails does not include other possible effects of aviation on cloudiness. Figure and caption reproduced with permission from Figure SPM.2 of *Solomon et al.* (2007).

mass of water, $\rho_w$ is the density of water, $\sigma$ is the solution surface tension, $R$ is the universal gas constant, $D_{p,wet}$ is the droplet diameter, $D_{p,dry}$ is the dry particle diameter, and $M_s$, $\rho_s$, $\phi_s$, and $\nu_s$ are the molar mass, density, osmotic coefficient, and stoichiometric van't Hoff factor, respectively. The first term on the right hand side of Equation 1.1 represents the effect of surface tension and droplet curvature to increase the equilibrium vapor pressure over the droplet relative to that over a flat surface (i.e., the Kelvin effect). The second term is the Raoult (or solute) term, which represents the effect of dissolved solute in lowering the equilibrium water vapor pressure over the solution droplet relative to pure water. Example "Köhler curves" for ammonium sulfate, a common aerosol constituent, are shown in Figure 1.3. The maximum of each Köhler curve represents a transition point, commonly referred to as the critical supersaturation, $s_c$, and critical droplet diameter, $D_{c,wet}$. At ambient supersaturations lower than $s_c$ (and $D_{p,wet} < D_{c,wet}$), the droplet exists in a stable equilibrium; small perturbations in droplet size caused by a few molecules of condensing or evaporating water are canceled out by the change in equilibrium supersaturation, and the droplet returns to the unperturbed size. When the ambient supersaturation exceeds $s_c$ (and $D_{p,wet} \geq D_{c,wet}$), however, a small increase in droplet size leads to further uninhibited condensational droplet growth. Such growth is referred to as *activation* and particles capable of activating to form cloud droplets are referred to as *cloud condensation nuclei* (CCN). When the ambient supersaturation exceeds the $s_c$ of the aerosol, even if only for a short time, the particle activates into a cloud droplet and continues to grow unless the ambient supersaturation decreases below roughly 0% supersaturation (see Figure 1.3).

Köhler theory has been shown to adequately capture the CCN activity of single- and multi-component aerosol by a large number of laboratory studies (e.g., *Cruz and Pandis*, 1997; *Raymond and Pandis*, 2002, 2003; *Giebl et al.*, 2002; *Padró et al.*, 2007). However, atmospheric aerosols are much more complex than those in the laboratory, so a number of modifications have been proposed in recent years to account for the presence of soluble trace gases (*Laaksonen et al.*, 1998), slightly-soluble but surface-active solutes (*Shulman*

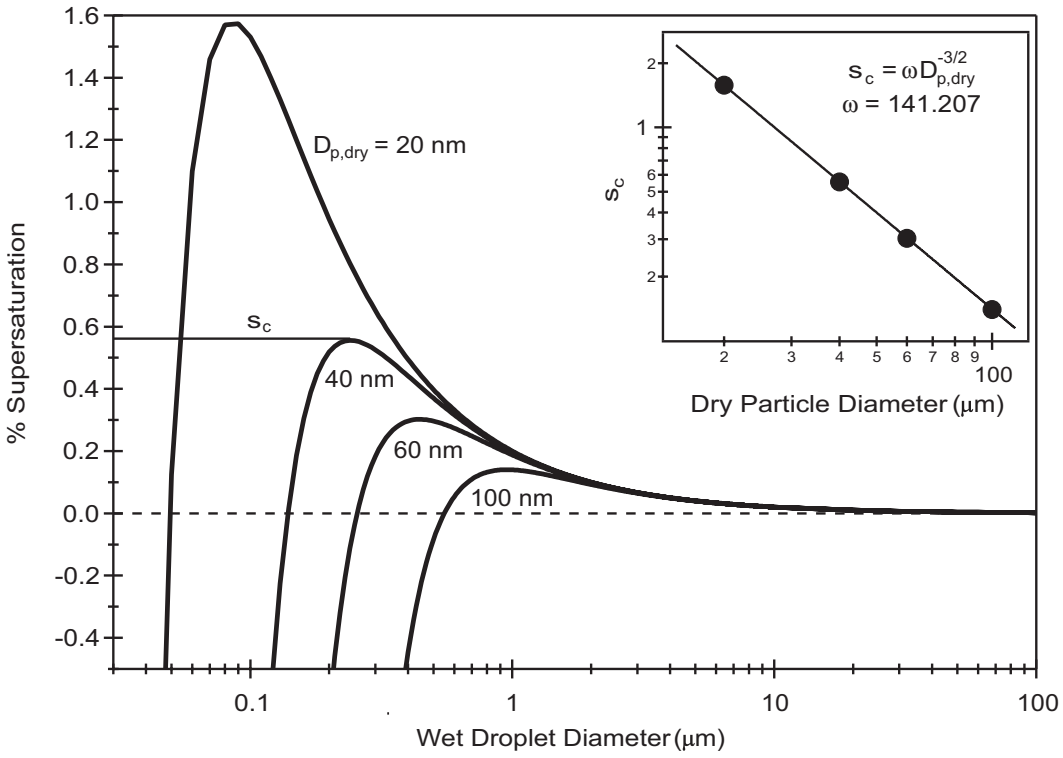


**Figure 1.3:** Köhler curves showing the equilibrium water vapor supersaturation versus wet droplet diameter for 20, 40, 60, and 100 nm dry diameter ammonium sulfate particles. Inset shows the critical supersaturation versus dry particle diameter corresponding to the maxima of the Köhler curves for each dry particle diameter.

*et al.*, 1996), water adsorption on insoluble but hydrophilic particles (*Sorjamaa and Laaksonen*, 2007), curvature enhanced solubility (*Padró and Nenes*, 2007), and slow dissolution kinetics (*Asa-Awuku and Nenes*, 2007). While these approaches are rigorous representations of how aerosols can act as CCN, they require detailed thermodynamic properties (e.g., molar mass, density, surface tension depression, ionic dissociation constants, and activity coefficients) for the dry particle inorganic and organic components. However, the properties and speciation of the organic aerosol components are typically unknown for measurements of atmospheric aerosol.

Consequently, there have been a number of Köhler theory-based parameterizations developed that attempt to simplify much of this complexity into a single, or a few, lumped parameters that capture the "effective" aerosol solubility or hygroscopicity (e.g., *Junge*

*and McLaren*, 1971; *Fitzgerald*, 1973; *Rissler et al.*, 2006; *Petters and Kreidenweis*, 2007; *Lance*, 2007). Of these, the single-parameter parameterization of *Petters and Kreidenweis* (2007) has become the most widely used in recent years, and the hygroscopicity parameter, $\kappa$, has become an effective way of communicating the overall compositional dependence of CCN activity without explicitly differentiating between dissolved solute (Raoult) and surface tension (Kelvin) effects. Insoluble but hydrophilic particles have a $\kappa$ of zero, while soluble salts such as sodium chloride have a $\kappa$ value of around unity (*Petters and Kreidenweis*, 2007). Thus, a simple way of interpreting the $\kappa$ parameterization would be to say that a particle with $\kappa$=0.1 (as is commonly observed for some soluble secondary organic aerosol species) has the same hygroscopicity as a particle composed of 10% NaCl and 90% insoluble material.

As with any empirical parameter, ambient measurements are necessary to constrain the range of realistic values for the atmosphere, and a global picture of aerosol hygroscopicity is beginning to emerge with typical continental $\kappa \sim$ 0.1-0.4 and higher marine $\kappa \sim$ 0.4-1.0 (*Andreae and Rosenfeld*, 2008; *Pringle et al.*, 2010). However, observations of CCN hygroscopicity have been limited to only a few locations worldwide, and continued field measurements are necessary to better understand how $\kappa$ varies in space and time, as well as with aerosol composition and mixing state. Understanding these variations is likely to become even more important as future global modeling efforts begin to focus on smaller, more-regional scales where assuming the aerosol to be well mixed may no longer represent reality.

## *1.3 Cloud Droplet Formation and Growth*

In addition to composition impacts on CCN hygroscopicity, it has also been suggested that the presence of slightly-soluble organics can significantly hinder the rate at which particles activate and grow into droplets (*Nenes et al.*, 2001a; *Shantz et al.*, 2003; *Ruehl et al.*, 2009). This may occur through gradual solute dissolution (*Asa-Awuku and Nenes*, 2007) or

the formation of organic surface films that hinder condensational water uptake (e.g., *Feingold and Chuang*, 2002, and references therein). In terms of climate impacts, slow droplet growth has the same effect as increased aerosol concentration, resulting in more numerous, but smaller droplets (*Nenes et al.*, 2002). This is because the ambient water vapor supersaturation in an ascending cloud parcel is not depleted as quickly as it would otherwise be, and may actually increase (as in the case of a strong convective cloud). Thus, it is essential that we understand the impact of aerosol properties on influencing droplet growth rates.

The growth rate of an activated cloud droplet is governed by the Maxwellian diffusional growth equation (*Seinfeld and Pandis*, 2006)

$$D_p \frac{dD_p}{dt} = \frac{s_\infty - s}{\frac{\rho_w R T_\infty}{4 P_w^\circ(T_\infty) D_v M_w} + \frac{\Delta H_v \rho_w}{4 k_a T_\infty}\left(\frac{\Delta H_v M_w}{T_\infty R} - 1\right)} \tag{1.2}$$

where $s_\infty$ is the water vapor supersaturation far from the droplet, $T_\infty$ is the temperature far from the droplet, $D_v$ is the diffusivity of water vapor in air corrected for noncontinuum effects, $\Delta H_v$ is the enthalpy of vaporization of water, and $k_a$ is the effective thermal conductivity of air corrected for noncontinuum effects. The modified diffusivity and thermal conductivity both include accommodation coefficients to account for the probability that a water vapor molecule that collides with the water droplet is assimilated into the droplet and for the dissipation of heat into the surrounding air. The values of these coefficients can range from 0 to 1 and are highly uncertain; reported values for pure water range from 0.03 to 1, and some suggest that values are closer to unity for pure water (*Mozurkewich*, 1986; *Davis*, 2006). *Li et al.* (2001) found values between 0.17 and 0.32 for the mass accommodation coefficient and unity for the thermal coefficient. *Shaw and Lamb* (1999) suggest 0.06 for the mass accommodation coefficient and 0.7 for the thermal accommodation coefficient. The presence of surface-active organic species in the droplets likely limits water uptake by forming hydrophobic surface films that would decrease the mass accommodation coefficient (*Chuang et al.*, 1997), even as these same surface-active organics may facilitate CCN activation by lowering the droplet surface tension and decreasing

the Kelvin effect (*Facchini et al.*, 1999; *Shulman et al.*, 1996; *Nenes et al.*, 2002). In-situ measurements of atmospheric aerosol provide the means to better assess the influence of aerosol composition on droplet activation and growth in order to better understand under what conditions aerosol composition alters droplet growth rates and under what conditions it does not. As discussed in Chapters 2-4, this dissertation contributes new techniques for fast measurements of droplet growth rates and CCN activation, which are applied to look for slow growth kinetics during a unique case study of organic-rich aerosol near the 2010 Gulf of Mexico oil spill (Chapter 7).

## *1.4 Dissertation Outline*

The goal of this dissertation is to expand the global data set of CCN observations in order to develop robust relationships between aerosol hygroscopicity and aerosol composition and mixing state inferred using a variety of new techniques for fast measurements of CCN suitable for either airborne or ground-based deployment. Chapters 2 and 3 discuss the development and characterization of two new techniques for operating a commercially-available CCN counter, which enable size-resolved and supersaturation-resolved CCN concentration measurements that improve measurement time resolution (and in the case of aircraft measurements, spatial resolution) by several orders of magnitude over the current state of the art. Chapter 4 presents a laboratory study of concentrated marine organic matter using the previously-developed Köhler Theory Analysis (KTA, *Padró et al.*, 2007; *Asa-Awuku et al.*, 2008) technique to simultaneously determine the molar mass and surface tension depression relevant for these organic aerosol.

In Chapters 5 through 8, the hygroscopic properties of ambient CCN sampled in Alaska, California, Atlanta, GA, and near the 2010 Deepwater Horizon oil spill are characterized in terms of aerosol size, chemical composition, and mixing state to constrain the mean values of $\kappa$ and its variability for each region. In addition, size and chemical composition measurements are used to assess "CCN closure", which reflects the discrepancy between measured

CCN concentrations and predictions from Köhler theory using simplifying assumptions typically used in large-scale models. The closure uncertainties are combined with those from approximately thirty other published studies in Chapter 9 to assess the global sensitivity of cloud droplet concentrations and cloud albedo, and hence aerosol indirect forcing, to these CCN uncertainties. This is accomplished using the NASA Global Modeling Initiative chemical transport model and the recently-developed adjoint of the *Kumar et al.* (2009) cloud droplet parameterization. Finally, Chapter 10 discusses the impact of this dissertation in advancing the state of the art in measuring and characterizing aerosol-cloud interactions and possible future directions for measurements of ambient CCN.

# CHAPTER II

# SCANNING FLOW CCN ANALYSIS (SFCA)

The Continuous-Flow Streamwise Thermal-Gradient Cloud Condensation Nuclei Counter is a commercially-available instrument that is widely used for laboratory and field measurements of cloud condensation nuclei (CCN). Typically, the instrument is operated at a constant flow rate, and supersaturation is adjusted by changing the column streamwise temperature difference, which is slow and may introduce particle volatilization biases. This chapter presents a new mode of operation, termed "Scanning Flow CCN Analysis" (SFCA), in which the flow rate in the growth chamber is changed over time, while maintaining a constant temperature gradient. This causes supersaturation to continuously change, allowing the rapid and continuous measurement of supersaturation spectra over timescales relevant for airborne measurements ($\sim$10-60 seconds and potentially even less) without being affected from shifts in activation kinetics and aerosol composition. SFCA has been evaluated with both calibration and ambient aerosol with excellent results.

## *2.1 Introduction*

Atmospheric aerosols, through their ability to act as cloud condensation nuclei (CCN), exert a significant influence on the Earth's climate and hydrological cycle (e.g., *Lohmann and Leck*, 2005; *Ramanathan et al.*, 2001). The ability of aerosol to behave as CCN depends on the ambient water vapor supersaturation as well as aerosol size and chemical composition. While thermodynamic theory (*Köhler*, 1936) has been shown to accurately predict these dependencies (e.g., *Kanakidou et al.*, 2005; *McFiggans et al.*, 2006), ambient aerosols are

This chapter published as: Moore, R., and A. Nenes (2009), Scanning flow CCN analysis – a method for fast measurements of CCN spectra, Aerosol Science and Technology, 43, 1192-1207, doi:10.1080/02786820903289780. 

chemically complex and highly variable. Given this, and the important role of aerosol-cloud interactions on anthropogenic climate change (e.g., *Twomey*, 1977a; *Albrecht*, 1989; *Solomon et al.*, 2007; *Levin and Cotton*, 2009), extensive and long-term measurements of CCN are required to constrain regional and global climate models.

A number of instruments have been developed in recent decades to measure the concentration of CCN as a function of water vapor supersaturation. All are based on the principle of exposing the aerosol to a specified supersaturation and counting the number of particles that "activate" to form cloud droplets. Instruments are classified as either "CCN counters" or "CCN spectrometers", with the former typically operating at a single (or a few) discrete supersaturation(s) and the latter concurrently measuring CCN concentrations over the range of atmospherically-relevant supersaturations (i.e., a CCN spectrum). Since the original parallel-plate static diffusion CCN counter was introduced by *Twomey* (1963), CCN counter designs have evolved by developing new methods for droplet detection (*Lala and Jiusto*, 1977), continuous-flow sampling (*Sinnarwalla and Alofs*, 1973), and cylindrical geometry designs (*Roberts and Nenes*, 2005; *Chuang et al.*, 2000a; *Leaitch and Megaw*, 1982; *Hoppel et al.*, 1979). Another class of counters includes the CCN Remover (*Ji et al.*, 1998) and the Differential Activation Separator (DAS) (*Osborn et al.*, 2008), which use gravitational settling of activated droplets to differentiate CCN from interstitial aerosol. *Fukuta and Saxena* (1979) developed a spectrometer based on the continuous-flow, parallel-plate diffusion concept, but with a temperature difference (and supersaturation) that varies for each streamline. By sampling aerosol across streamlines, a CCN supersaturation spectrum (0.1-0.9%) could be obtained in 10-15 seconds (*Zhang et al.*, 2008; *Fukuta and Saxena*, 1979). Spectra obtained with this instrument are inherently limited to supersaturations above 0.1%, mostly because of the time required for droplets to grow to detectable sizes (*Nenes et al.*, 2001b). To address this, *VanReken et al.* (2004) proposed a trapezoidal geometry to increase the aerosol residence time at the lower-supersaturation streamlines; although promising, the design has not been realized to date. *Hudson* (1989) (and later

*Chuang et al.* (2000a)) designed a continuous-flow CCN spectrometer where the sample aerosol encounters a continuously increasing supersaturation as it moves through the flow chamber. The CCN spectrum is then inferred from the outlet droplet size distribution using critical supersaturation - droplet size relationships obtained from activation of calibration aerosol. Accurate inversion requires that the water uptake coefficient and Köhler curves are identical for ambient and calibration aerosol with the same critical supersaturation – a criterion that may not always be fully satisfied if organic species are present in the CCN (e.g., *Shantz et al.*, 2003; *Asa-Awuku et al.*, 2008; *Ruehl et al.*, 2008).

The continuous flow streamwise thermal gradient CCN counter (CFSTGC) of *Roberts and Nenes* (2005), which has been commercialized by Droplet Measurement Technologies (*Lance et al.*, 2006; *Rose et al.*, 2008), has proven to be reliable, robust, and relatively simple to operate for ground-based and airborne measurements (e.g., *Lance et al.*, 2009; *Cubison et al.*, 2008; *Moore et al.*, 2008; *Sorooshian et al.*, 2008; *Wang et al.*, 2008; *Asa-Awuku et al.*, 2008, 2010; *Medina et al.*, 2007; *Padró et al.*, 2007, and others). The supersaturation profile in the CFSTGC depends on pressure, flow rate, the streamwise temperature gradient, and to a lesser extent, the inlet temperature (*Roberts and Nenes*, 2005). Typically, the streamwise temperature difference is varied in a stepping manner, while maintaining constant flow rate and pressure, to effect a supersaturation change (e.g., *Cubison et al.*, 2008; *Rose et al.*, 2008; *Sorooshian et al.*, 2008; *Wang et al.*, 2008; *Medina et al.*, 2007, and others). While this is a well-established and robust mode of operation, some limitations exist. First, instrument temperature stabilization is slow (on the order of 20-40 seconds for the column temperatures and sometimes as much as 3 minutes for the OPC temperature to stabilize); data collected during these transient periods are often discarded, which may be problematic for airborne measurements in highly heterogeneous environments. Consequently, the CFSTGC is generally limited to only a single (or a few) supersaturations during measurements. In addition, recent work by *Asa-Awuku et al.* (2008) has shown that organic-rich aerosol may partially volatilize in the instrument, which affects the observed

CCN activity. For this reason, CCN activity measurements should be carried out as close to ambient temperatures as possible, which is not always feasible using the "conventional" method of temperature stepping.

To date, there is no technique that combines the simplicity and robustness of a CCN counter (such as the CFSTGC) with the dynamical range and temporal resolution of a CCN spectrometer. This study presents a new methodology for operating the CFSTGC, termed Scanning Flow CCN Analysis (SFCA), which largely addresses this need. SFCA entails scanning the instrument flow rate over a short period of time, while maintaining a constant temperature difference. This allows the measurement of CCN spectra during a flow cycle, using the well-established and robust hardware of the CFSTGC. An added advantage of SFCA is that CCN measurements are carried out at a constant column temperature difference (which can be only a few degrees above ambient), therefore minimizing biases from partial volatilization of aerosol in the instrument. In subsequent sections, we present the theory of SFCA and experimentally demonstrate the power of the method for laboratory-generated calibration aerosol and ambient aerosol sampled in Atlanta, GA.

## *2.2 Instrument Description*

The CCN counter used to develop and demonstrate SFCA was a Droplet Measurement Technologies CFSTGC (CCN-100, DMT). The CFSTGC consists of a cylindrical metal tube (0.5 m in length with a 23 mm inner diameter and 10 mm wall thickness) with a wetted inner wall on which a linear temperature gradient is applied in the streamwise direction. The temperature gradient is controlled using three thermoelectric coolers (TECs) located on the outer wall of the flow chamber (Figure 2.1), and water flows continuously through a 2.5-mm-thick, porous, ceramic bisque that lines the inside of the cylinder. Heat and water vapor diffuse toward the centerline of the flow chamber. Since moist air is largely composed of $N_2$ and $O_2$, which are heavier molecules than $H_2O$, the latter has a higher molecular velocity, hence diffuses more quickly than heat (which is transferred primary via collisions

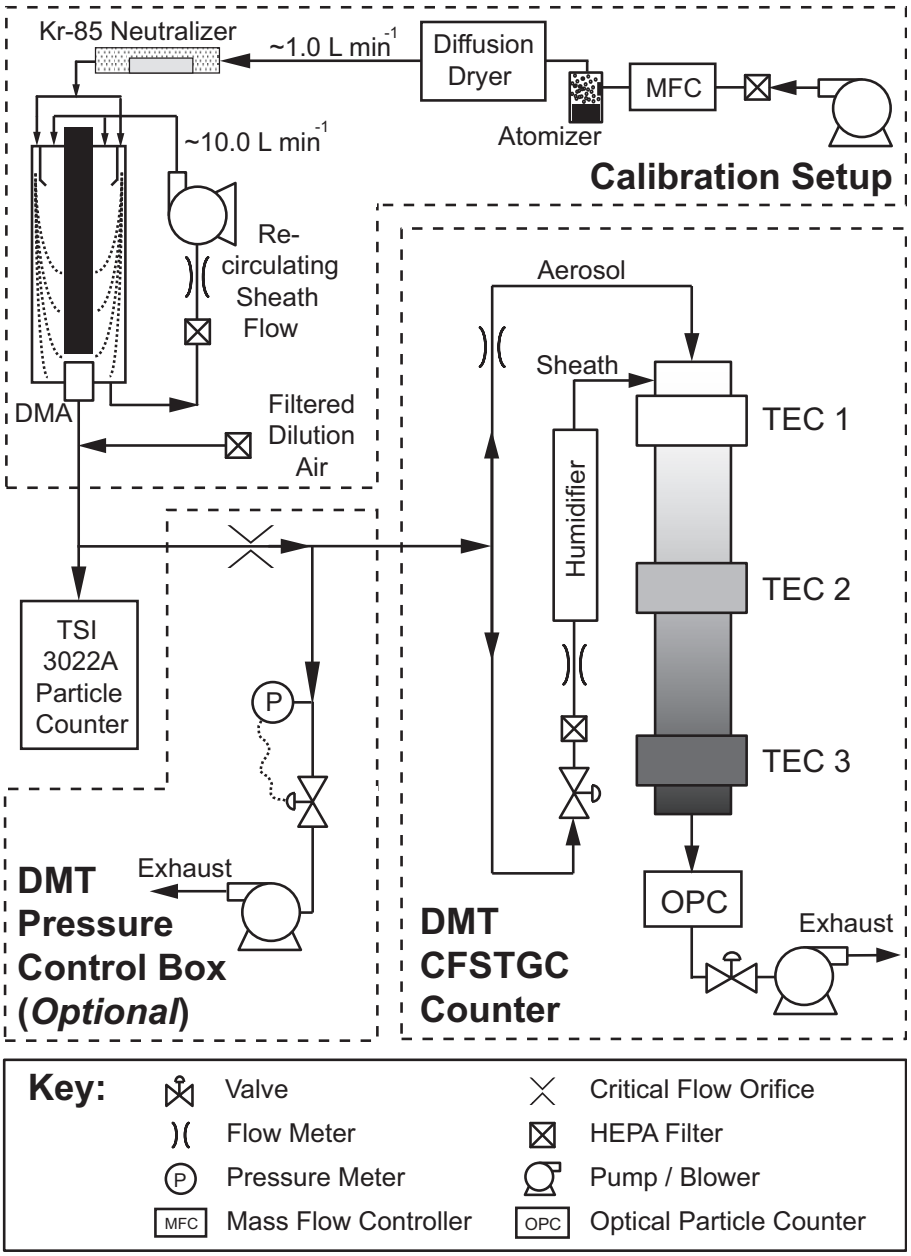


**Figure 2.1:** Schematic of the setup used for the Scanning Flow CCN Analysis (SFCA).

between slower $N_2$, $O_2$). Under developed flow conditions, a quasi-parabolic water vapor supersaturation is generated across the cross-section of the tube, which is maximum at the centerline (*Roberts and Nenes*, 2005). The aerosol sample enters the top of the column at the centerline and is surrounded by a blanket of humidified, aerosol-free sheath air. If the supersaturation in the instrument exceeds the critical supersaturation ($s_c$) of the aerosol,

the particles activate and form droplets, which are counted and sized by an optical particle counter (OPC) using a 50 mW, 658-nm-wavelength laser diode light source. The droplet size distribution information obtained in the OPC also allows using the CFSTGC to study CCN activation kinetics.

## *2.3 Description of SFCA*

### 2.3.1 Method

SFCA entails varying the flow rate through the column in a controlled manner, while maintaining a constant streamwise temperature difference, $\Delta T$, and pressure, $P$. In this work, the flow rate in the chamber is increased linearly between a minimum flow rate ($Q_{min}$) and a maximum flow rate ($Q_{max}$) over a specified "ramp time" ($t_{up}$). The flow is maintained at $Q_{max}$ for a time period, $t_{peak}$, and is then linearly decreased to $Q_{min}$ over another ramp time, $t_{down}$. Finally, the flow rate is held constant at $Q_{min}$ for a period, $t_{base}$, and the scan cycle is repeated. Droplet concentrations and size distributions at the OPC are continuously measured during this scan cycle with 1-second resolution.

A critical step for the success of SFCA is relating instantaneous CCN concentrations measured in the OPC to a specific level of supersaturation, so that a spectrum can be obtained over a scan cycle. This requires an understanding of the dynamics of CCN activation in the instrument. For this, two characteristic timescales are introduced: $i$) $\tau_Q$, the characteristic timescale of flow change ($t_{up}$ or $t_{down}$) and $ii$) $\tau_r$, the diffusivity timescale in the radial direction ($\frac{R^2}{\Gamma}$, where $R$ is the flow tube inner radius and $\Gamma$ is a characteristic diffusivity for momentum, heat, and water vapor). Since the dimensionless Schmidt Number ($Sc$) is less than the Prandtl Number ($Pr$), which are both less than unity, diffusion of momentum is the slowest of all transport processes in the radial direction. Hence, $\Gamma = \frac{\mu}{\rho}$, where $\mu$ and $\rho$ are the air viscosity and density, respectively, and $\tau_r \sim 10$ s at 298 K, and 1013 mbar. If $\tau_Q \gg \tau_r$, then the instantaneous velocity, water vapor, and temperature distributions will approach their steady-state profiles, and particles exiting the flow column at each point in

time will be exposed to this quasi-steady-state supersaturation, $s_{steady}$, and activate. Since $s_{steady}$ depends linearly on flow rate (*Roberts and Nenes*, 2005), supersaturation will vary linearly with time. Under these conditions, SFCA will provide CCN spectra with minimal data processing as concentrations will correspond to the instantaneous supersaturation in the instrument (assuming that the OPC integration time, $\tau_{OPC}$, is much less than $\tau_Q$). When $\tau_Q \leq \tau_r$, the flow rate varies too quickly with respect to the radial transport timescale, and the velocity, temperature and water concentrations deviate substantially from steady-state values. Supersaturation still develops, but it is a nonlinear function of time (flow rate) and the control parameters (scan time, temperature). Quantifying the departure from steady-state behavior, as well as other instrument response characteristics (e.g., the size to which activated droplets grow, which is key for determining droplet growth detection limitations) requires the application of a comprehensive computational fluid dynamics model of SFCA.

In subsequent sections, the numerical model and simulation characteristics are briefly presented, together with an analysis of simulations using the geometric characteristics and operation limitations of the CFSTGC. The objectives of the analysis are to $i$) determine the combination of control parameters for which steady-state approximation of supersaturation applies, $ii$) ensure that sufficient size separation exists between activated droplets and interstitial aerosol, and $iii$) verify that activated droplets are in the detectable size range of the OPC.

### 2.3.2 Instrument and Droplet Growth Models

The CFSTGC instrument and droplet growth models (*Roberts and Nenes*, 2005; *Lance et al.*, 2006) were used to simulate the response of the instrument as a function of the scanning flow cycle parameters. The instrument model numerically solves the Navier-Stokes equations and the conservation equations for heat and water vapor to produce the transient velocity, pressure, water vapor supersaturation, and temperature fields in the instrument. The model has been shown to successfully simulate instrument behavior over a wide range

of operating conditions (*Lance et al.*, 2006; *Rose et al.*, 2008).

Extension of the instrument model to simulate SFCA is fairly straightforward. Operational parameters used in the model are the total flow rate ($Q$), scanning characteristics ($t_{up}$, $t_{peak}$, $t_{down}$, $t_{base}$), inlet pressure ($P$) and temperature ($T_{inlet}$), and the inner wall temperature difference between the entrance and exit of the flow chamber ($\Delta T_{inner}$). Non-steady state forms of the conservation equations are used, where the axial velocity boundary condition at the inlet of the flow chamber is assumed to be uniform in the radial direction and to vary with time in a manner proportional to $Q$; all other boundary conditions are the same as those used in steady-state operation of the model (*Lance et al.*, 2006). Heat and mass balances in the wetted walls, as well as slight nonlinearities in the temperature profile (from thermal resistances) are not accounted for in the analysis.

### 2.3.3 Supersaturation Profiles

Figure 2.2 shows the simulated maximum centerline supersaturation, $s_{max}$, in the instrument as a function of Q, $\Delta T_{inner}$, and flow ramp time ($t_{up} = t_{down}$). The simulated supersaturation curves for different $\Delta T_{inner}$ collapse neatly on top of each other, indicating that, while $\Delta T_{inner}$ determines the magnitude of the maximum supersaturation, it does not affect the shape of the response curve. For slow scans (i.e., $\tau_Q \gg \tau_r \sim 10$ s), supersaturation approaches its steady-state linear dependence on flow rate, while at shorter scan times (i.e., $\tau_Q \leq \tau_r \sim 10$ s) a transient hysteresis develops between the upscan and downscan curves. From Figure 2.2, the linear profile regions appear to be complementary (i.e., the upscan provides good supersaturation resolution at higher $Q$ and vice versa for low $Q$ during the downscan).

The quasi-steady-state behavior is not reflected only in the value of $s_{max}$ but also in the overall profile of $s$ in the flow chamber. This is shown in Figure 2.3, which presents selected instantaneous centerline supersaturation profiles over the course of a 60-second flow scan for $\Delta T_{inner} = 10$ K. Upscan profiles are represented by solid traces, and downscan

profiles are given by dashed traces. The vertical lines in Figure 2.3 denote the steady-state supersaturation entrance length $x_s$ (*Lance et al.*, 2006),

$$x_s = 0.05 Re_D D + \frac{D^2}{4\alpha_T} U \tag{2.1}$$

where $Re_D = \frac{\rho U D}{\mu}$ is the Reynolds number based on the chamber inner diameter, $D$, and the instantaneous average air velocity, $U$, and $\alpha_T$ is the thermal diffusivity of air. The good agreement between $x_s$ and the entry lengths for the transient profiles suggests that the maximum supersaturation and droplet growth kinetics are closely related to the instantaneous flow rate.

The instrument supersaturation also depends on pressure (*Roberts and Nenes*, 2005), and simulations were conducted to evaluate this dependence. Figure 2.4 shows the simulated maximum centerline supersaturation during a flow cycle for a range of ramp times and pressures. Changing the pressure affects both the magnitude and the dynamic behavior of the supersaturation profile, because $\tau_r$, through changes in $\Gamma$, scales inversely with pressure (e.g., $\tau_r \sim 4$, 6, 8 s at 400, 600, 800 mb, respectively). The decrease in $\tau_r$ at lower pressures allows the supersaturation profile to develop more quickly so that the steady-state behavior is even a better approximation than at higher pressures. Hence, SFCA can be operated over a climatically-relevant range of supersaturations and pressures, which ensures that it can be successfully used in aircraft observations of CCN. In fact, the simulation indicates that the decrease in $\tau_r$ at low pressures allows a quasi-steady $s$ profile to develop even at 5 s ramp times (Figure 2.4).

### 2.3.4 Droplet Activation and Size

An important issue with any CCN measurement is whether particles are allowed enough time to activate into cloud droplets and grow to detectable sizes. Simulations were carried out to assess whether SFCA satisfies this requirement. Figure 2.5 presents a characteristic example and shows how the droplet diameter at the exit of the instrument changes during a

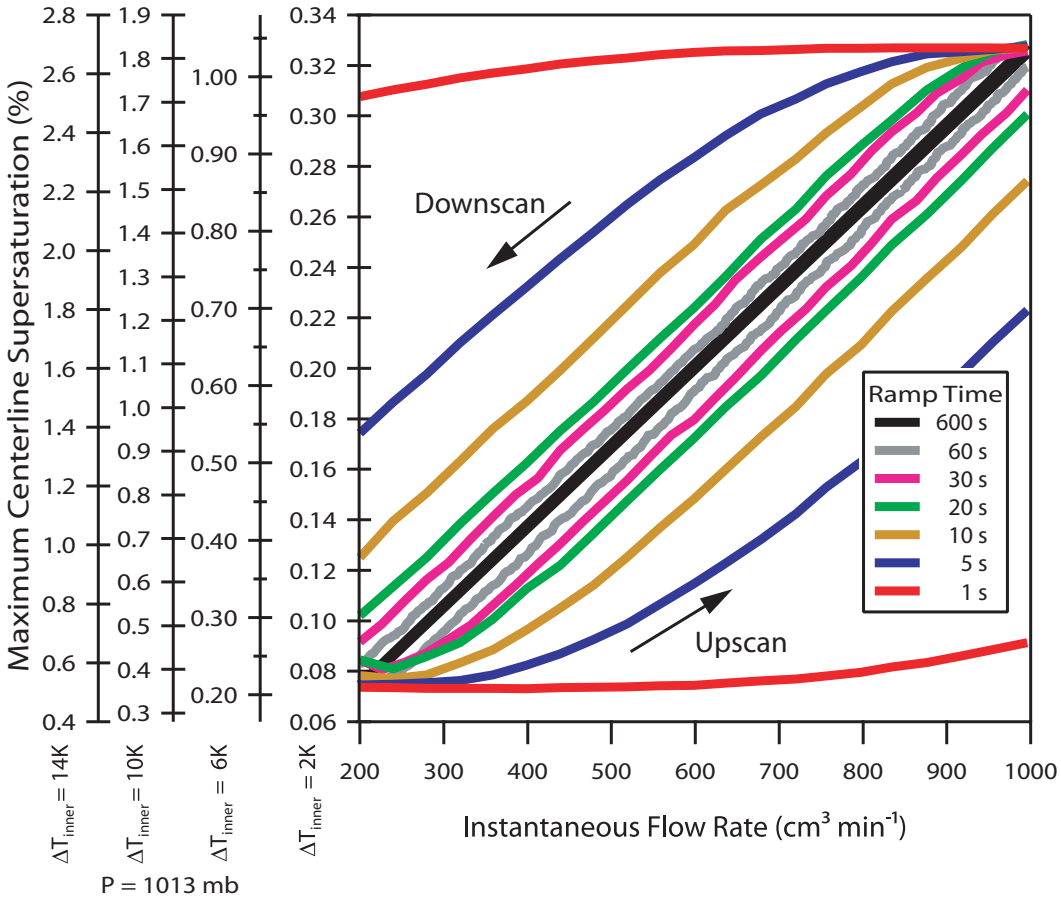


**Figure 2.2:** Simulated instrument maximum centerline supersaturation as a function of flow rate for multiple values of inner wall temperature difference ($\Delta T_{inner}$) and ramp times ($t_{up} = t_{down} = 1$ s, 5 s, 10 s, 20 s, 30 s, 60 s, 600 s). Pressure was maintaned constant at 1013 mb, and, $t_{base} = t_{peak} = 10$ s.

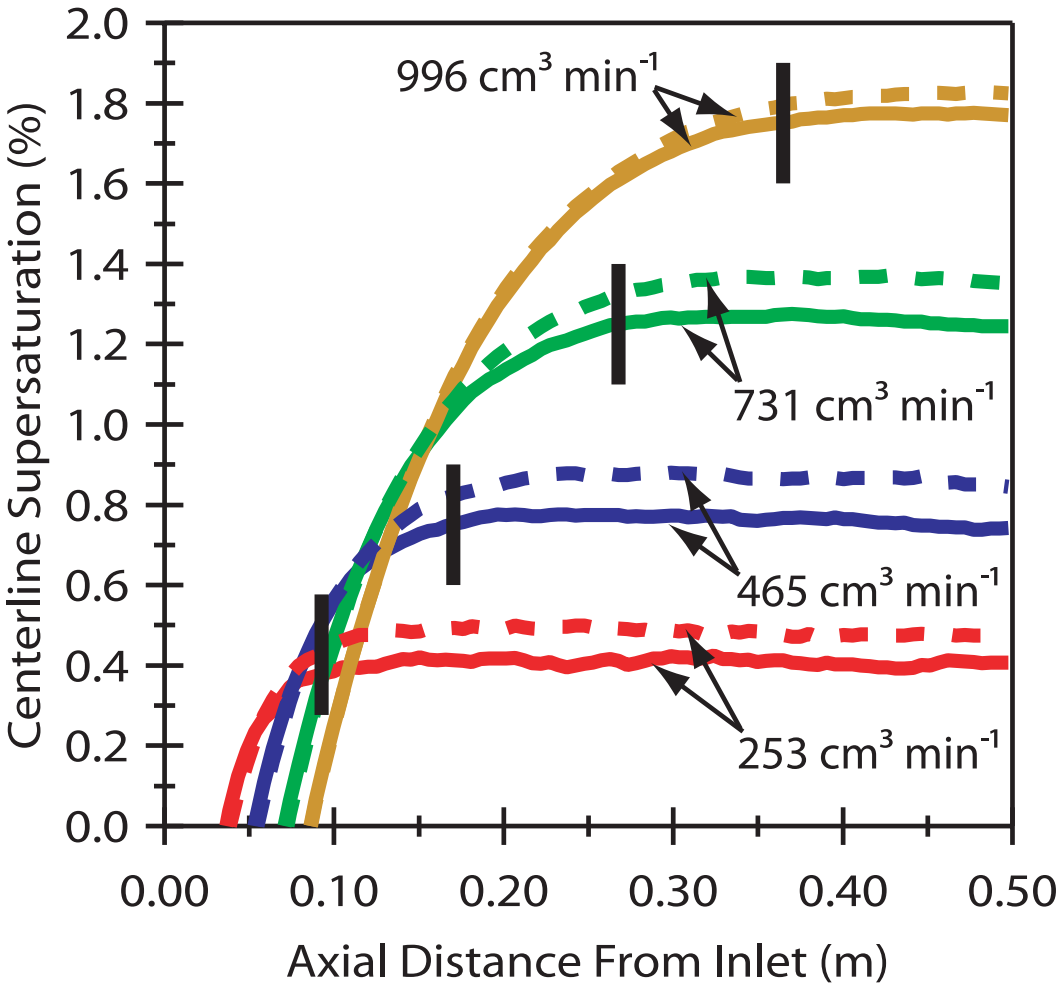


**Figure 2.3:** Simulated instantaneous centerline supersaturation profiles in the flow chamber as a function of axial distance from the inlet for $\Delta T_{inner} = 10$ K, $t_{up} = t_{down} = 60$ s, and $t_{base} = t_{peak} = 10$ s. Solid traces are flow upscan, while dashed traces are flow downscan. The vertical black lines denote the steady-state supersaturation entry length at each instantaneous flow rate (Equation 2.1).

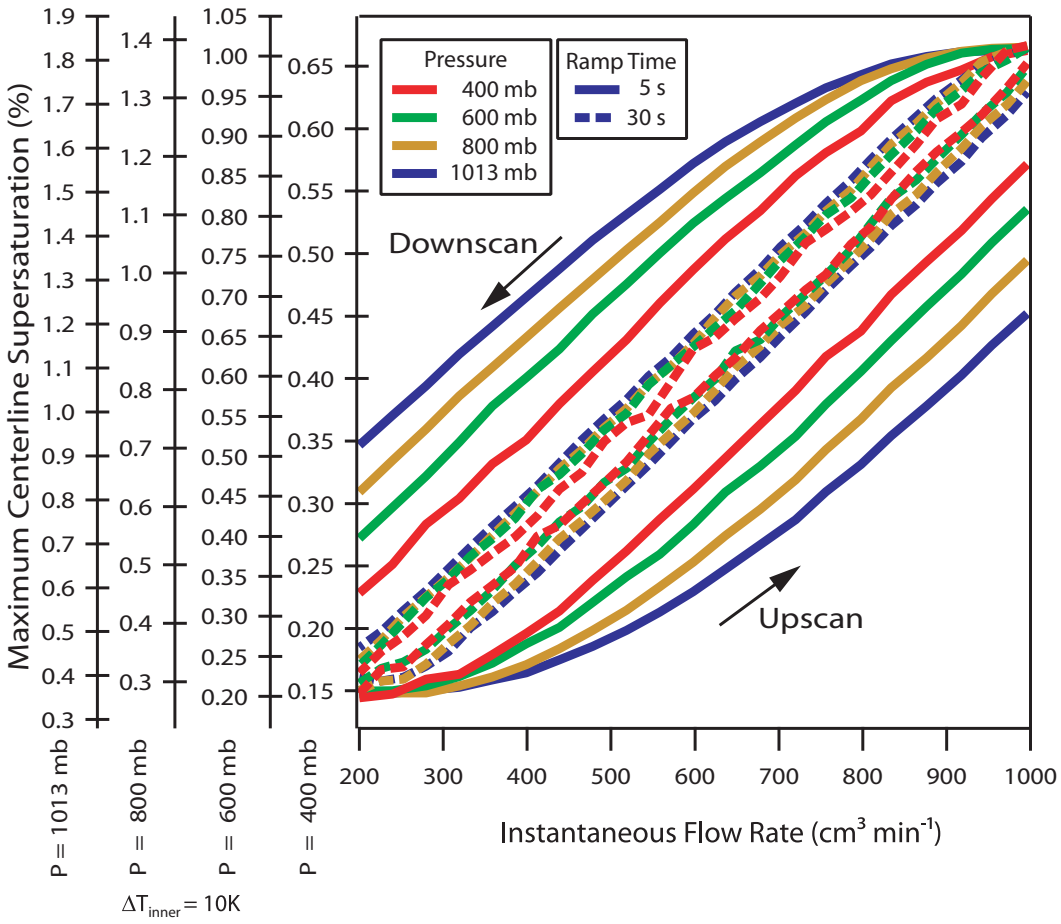


**Figure 2.4:** Simulated instrument maximum centerline supersaturation as a function of flow rate for multiple pressures and ramp times ($t_{up} = t_{down} = 5$ s, 30 s). The inner wall temperature difference ($\Delta T_{inner}$) was maintained at 10 K, and, $t_{base} = t_{peak} = 10$ s.

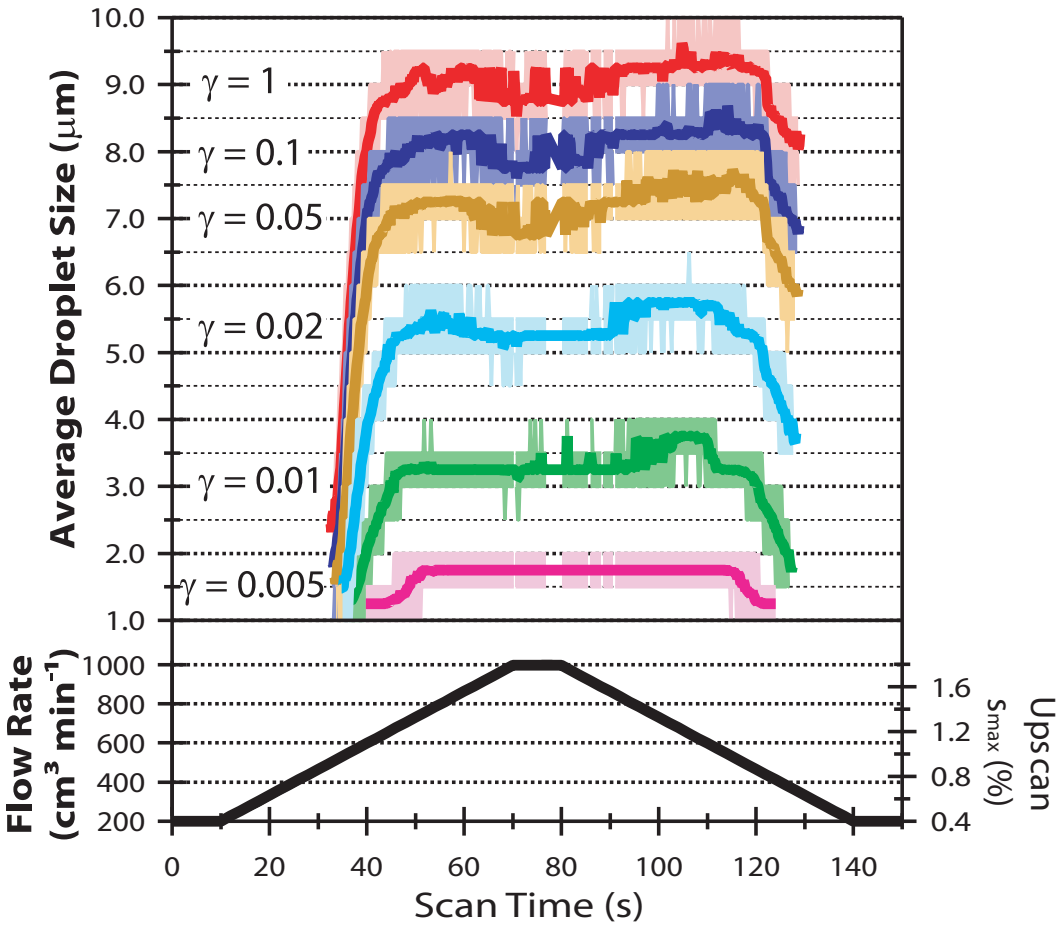


**Figure 2.5:** Simulated droplet growth for 50 nm ammonium sulfate aerosol at $\Delta T_{inner} =$ 10 K and $t_{up} = t_{down} = 60$ s and $t_{base} = t_{peak} = 10$ s. The darker, colored traces denote average droplet size as measured by the OPC, and the shaded areas denote the width of the simulated droplet size distribution.

flow scan cycle. The simulations shown are for 50-nm ammonium sulfate aerosol, a ramp time of 60 s, and a wide range of values for the effective water uptake coefficient ($\gamma$). The effective water uptake coefficient accounts for the transfer of gaseous water vapor across the interfacial surface to the droplet bulk, which affects the mass transfer rate of water vapor onto growing droplets. Reported values of $\gamma$ for water range from 0.01 to 1 (e.g., *Asa-Awuku et al.*, 2008; *Fountoukis et al.*, 2007; *Davis*, 2006; *Li et al.*, 2001). Lower values of $\gamma$ may be associated with the presence of hydrophobic, film-forming organics that hinder water uptake (e.g., *Bigg et al.*, 1969; *Bigg*, 1986; *Rubel and Gentry*, 1984; *Asa-Awuku et al.*, 2008).

The common feature of all of the predicted growth curves of Figure 2.5 is a dramatic shift in droplet size in the OPC when the instantaneous flow rate exceeds the critical flow rate corresponding to the particles' critical supersaturation ($Q > Q_c$). This point reflects the process of CCN activation in the CFSTGC. Overall, activated droplet sizes are relatively constant, despite the supersaturation variations experienced during the flow scan. Some variations, however, are seen in droplet size between $Q_c$ and $Q_{max}$ (at 50-70 s). When the downscan commences ($\sim$80 s), the droplet size exhibits similar variability to the upscan (in reverse), but with droplet size peaking at relatively larger values. This is because supersaturation, for the same instantaneous $Q$, tends to be higher during the downscan than in the upscan (Figures 2.2-2.4) and drives growth to larger sizes. Nevertheless, these variations are relatively small, all to within 0.5 $\mu$m of the average activated diameter size during the upscan (or downscan) phase. Simulations show that $\gamma$ strongly affects the outlet droplet size (particularly for $\gamma < 0.1$), but that the droplet sizes are still above the lower detection limit (1 $\mu$m) of the OPC (Figure 2.5; *Lance et al.* (2006)). This ensures that the hardware currently available in the Droplet Measurement Technologies CCN counter (which is a commercially-available CFSTGC) can be readily used for application of SFCA to measurements of ambient aerosol.

A simple analysis of CCN growth can be used to rationalize CCN activation droplet

growth kinetics in SFCA. As particles move through the flow chamber, condensation and evaporation of water affect their size and is described by Maxwellian diffusional growth (e.g., *Seinfeld and Pandis*, 2006; *Nenes and Seinfeld*, 2003):

$$D_p \frac{dD_p}{dt} = G\left(s - s_{eq}\right) \tag{2.2}$$

where $D_p$ is the wet size of the droplet, $G$ is a growth parameter that depends weakly on particle size and the water vapor mass transfer coefficient (*Nenes and Seinfeld*, 2003; *Seinfeld and Pandis*, 2006), $s$ is the local water vapor supersaturation, and, $s_{eq}$ is the equilibrium water vapor supersaturation of the particle. Integration of Equation 2.2 provides the droplet size at the exit of the flow chamber, but requires knowledge of the supersaturation trajectory during the droplet's transit in the instrument; this is presented below.

As a particle traverses the instrument during a flow upscan (which, by neglecting diffusional and inertial effects, can be assumed to move along the centerline with twice the average air velocity), its displacement from the chamber inlet, $x$, is determined by its instantaneous velocity:

$$\frac{dx}{dt} = \frac{2}{\pi R^2}\left(Q_{min} + \beta t\right) \tag{2.3}$$

where $\beta$=$\left(Q_{max} - Q_{min}\right)/t_{ramp}$. Assuming that $x$=0 at $t$=0, Equation 2.3 can be integrated to relate $x$ and $t$,

$$t = \frac{-Q_{min} + \sqrt{Q_{min}^2 + \beta \pi R^2 x}}{\beta} \tag{2.4}$$

Substituting Equation 2.4 into Equation 2.3 for $t$ yields

$$\frac{dx}{dt} = \frac{2}{\pi R^2}\sqrt{Q_{min}^2 + \beta \pi R^2 x} \tag{2.5}$$

which is the instantaneous velocity as a function of location for particles introduced into the instrument at the beginning of a flow cycle. Equation 2.5 can be combined with Equation

2.2, using the chain rule, to represent the droplet growth rate as a function of axial distance from the inlet

$$D_p \frac{dD_p}{dx} = \left( D_p \frac{dD_p}{dt} \right) \left( \frac{dt}{dx} \right) = \frac{\pi R^2 G \left( s - s_{eq} \right)}{2\sqrt{Q_{min}^2 + \beta \pi R^2 x}} \tag{2.6}$$

Assuming that $G$ is constant over the size range of interest and that $s_{eq}$=0 after droplet activation (*Nenes and Seinfeld*, 2003), Equation 2.6 can be integrated from the point of CCN activation, $x_a$, to the end of the flow tube ($x$=$L$),

$$D_p^2(L) - D_p^2(x_a) = \pi R^2 G \int_{x_a}^{L} \frac{s dx}{\sqrt{Q_{min}^2 + \beta \pi R^2 x}} \tag{2.7}$$

Since $s$ scales linearly with flow rate for quasi-steady-state conditions (i.e., $\tau_Q \gg \tau_r$),

$$\frac{ds}{dt} = \alpha \frac{dQ}{dt} \tag{2.8}$$

where $\alpha$ is the proportionality constant that relates instantaneous instrument $s$ and $Q$ (*Roberts and Nenes*, 2005). Since $s$=0 at $Q$=0, one obtains for the supersaturation at any instant during the upscan:

$$s = \alpha \left( Q_{min} + \beta t \right) \tag{2.9}$$

Substitution of $t$ in Equation 2.9 with Equation 2.4 provides the supersaturation as a function of location (temporarily neglecting the effects of the supersaturation entry length, $x_s$, which are accounted for later on),

$$s = \alpha \sqrt{Q_{min}^2 + \beta \pi R^2 x} \tag{2.10}$$

$s$ in Equation 2.7 can be substituted with Equation 2.10 and integrated to provide the droplet size at the exit of the growth chamber,

$$D_p^2(L) = D_p^2(x_a) + \pi R^2 G \alpha \left( L - x_a \right) \tag{2.11}$$

For most CCN, growth to the critical wet diameter, $D_c$, occurs rapidly when exposed to the critical supersaturation $s_c$ (i.e., $D_p(x_a) \sim D_c$) (*Nenes et al.*, 2001a). Consequently, Equation 2.11 becomes

$$D_p(L) = \sqrt{D_c^2 + \pi R^2 G \alpha \left(L - x_a\right)} \tag{2.12}$$

From Köhler theory, $D_c = \frac{2A}{3s_c}$, where $A = \frac{4\sigma_w(T)M_w}{\rho_w \bar{R}T}$, $\sigma_w\left(T\right)$ is the temperature-dependent surface tension of water, $M_w$ and $\rho_w$ are the molar mass and density of water, $\bar{R}$ is the universal gas constant, and $T$ is absolute temperature.

Equation 2.12 is able to explain the observed growth kinetic behavior shown in Figure 2.5. The first term under the square root represents the initial droplet size at activation, while the second term represents the subsequent condensational growth after activation. Initially, the instrument supersaturation is less than $s_c$ and particles do not activate until $Q = Q_c$ (i.e., $s = s_c$). Then, particles close to the exit of the flow chamber activate, but do not grow to their largest possible size because the particle is already downstream of the point at which $s$ becomes fully-developed (i.e., the supersaturation entry length, $x_s$), and $x_a > x_s$. As time passes, particles initially residing farthest away from the exit reach the OPC; the size of the droplets at the exit thus increases until $x_a \sim x_s$, where the second term of Equation 2.12 reaches a maximum. As the flow rate further increases, $x_a$ and $x_s$ remain equal, approach $L$, and the exit droplet size decreases. During the downscan, the decrease in flow rate increases the droplet residence time in the flow tube after activation, and the exit droplet size increases (as described by the second term of Equation 2.12) until $Q \leq Q_c$ where droplets cease to activate.

Equation 2.12 is valid only if the CCN, once exposed to a supersaturation exceeding $s_c$, remain in the developed flow region (i.e., $x_s$ does not exceed $x_a$ after the particle has activated). Otherwise, the particle will be outside the fully-developed region and the particle may experience deactivation if supersaturation falls below $s_c$. This undesirable situation could be avoided if the particle velocity is larger than the migration rate of $x_s$, i.e., if

$\frac{dx_s}{dt} < \frac{dx}{dt} \sim 2U$, which after substitution yields:

$$\frac{\beta}{2Q}\left(\frac{0.05\rho D^2}{\mu} + \frac{D^2}{4\alpha_T}\right) < 1 \tag{2.13}$$

Since the left hand side of Equation 2.13 scales with $\tau_r/\tau_Q$ and $\tau_Q \gg \tau_r$, Equation 2.13 is always satisfied for a slowly varying field (e.g., $\tau_Q > 18$ s at $T$=298.15 K and $P$=1013 mb). Hence, pseudo-steady state operation of SFCA ensures that the CCN, once exposed to $s > s_c$, will continue to grow as they flow through the instrument. Since the flow field is decelerating during the downscan ($\beta < 0$), Equation 2.13 is satisfied regardless of ramp speed. As $\tau_Q$ approaches $\tau_r$, Equation 2.13 is not satisfied for a fraction of the upscan (e.g., $Q < 365$ cm$^3$ min$^{-1}$ for $t_{up} = t_{down}$=10 s and $Q < 245$ cm$^3$ min$^{-1}$ for $t_{up} = t_{down}$=15 s), which is seen in the numerical simulations (Figure 2.2) and confirmed by the experimental 10-second SFCA data (Section 4).

## *2.4 Evaluation of SFCA*

### 2.4.1 Laboratory Aerosol

Figure 2.1 shows the experimental setup for evaluating SFCA. Calibration aerosol is generated from an aqueous salt solution using an atomizer. The aerosol are subsequently dried in a silica gel diffusion dryer (residence time $\sim$ 5 s, RH $< 20\%$) and charge-neutralized by a Kr-85 ionizer (3077A, TSI) before entering the differential mobility analyzer (DMA 3080, TSI). The sheath-to-aerosol ratio in the DMA is maintained at 10:1 with an aerosol flow of 1 lpm, controlled with a mass flow controller (FC260, Tylan). The classified aerosol stream is combined with filtered dilution air before being introduced into the condensation particle counter (CPC 3022A, TSI) and the CFSTGC. As the flow rate in the CFSTGC increases during a flow scan, additional filtered dilution air is added to the monodisperse stream, proportionately decreasing the total aerosol concentration; conversely, as the flow rate is decreased, the total aerosol concentration increases (this can be observed in the CCN and condensation nuclei (CN) number concentrations in Figure 2.6). This "dilution effect" was

used to synchronize the CCN and CN timeseries during the inversion.

The pressure in the flow chamber was also varied using a Droplet Measurement Technologies' pressure-control box (PCB), developed to maintain constant instrument pressure during aircraft operation. In this study, a 300 $\mu$m orifice, operated sub-critically, was placed upstream of the CFSTGC inlet and the flow was split between the instrument and the PCB (as shown in Figure 2.1). By maintaining a constant flow rate through the orifice, a stable pressure in the flow chamber is achieved.

Examples of CCN and CN concentration timeseries obtained for classified ammonium sulfate aerosol are shown in Figure 2.6 ($t_{up} = t_{down} = 10$ s). CCN activation is characterized by the CCN to CN ratio (activated ratio), $R_a$, which is a function of instantaneous flow rate (or time). $R_a$ data were fit to the sigmoidal equation:

$$R_a \equiv \frac{CCN}{CN} = a_0 + \frac{a_1 - a_0}{1 + (Q/Q_{50})^{-a_2}} \tag{2.14}$$

where $a_0$, $a_1$, $a_2$, and $Q_{50}$ are constants which describe the minimum, maximum, slope, and inflection point of the sigmoid, respectively, and $Q$ is the instantaneous volumetric flow rate. This procedure was applied to $R_a$ data for classified ammonium sulfate and sodium chloride calibration aerosol to determine $Q_{50}$ as a function of dry particle mobility diameter over a range of $t_{up}$, $t_{down}$, and nominal temperature difference ($\Delta T_{nom}$). The contribution of doubly-charged particles and the DMA transfer function width were neglected, as this introduces negligible uncertainty in the determination of $Q_{50}$ for the size range and the sheath-to-aerosol ratios examined.

Exemplary sigmoidal activation curves are shown in Figure 2.7. Ideally, $a_0$ is 0 and $a_1$ is expected to be unity; however, values for $a_1$ obtained from inorganic calibration aerosol are typically in the range of 0.9-1.0 and as low as 0.6 for the smallest $\Delta T_{nom}$, which are in agreement with instrument behavior at steady-state conditions. Consequently, $R_a$ values were scaled by $1/a_1$, similar to the procedure of *Rose et al.* (2008).

A parameter, termed the "critical flow rate", $Q_{50}$, is introduced and corresponds to

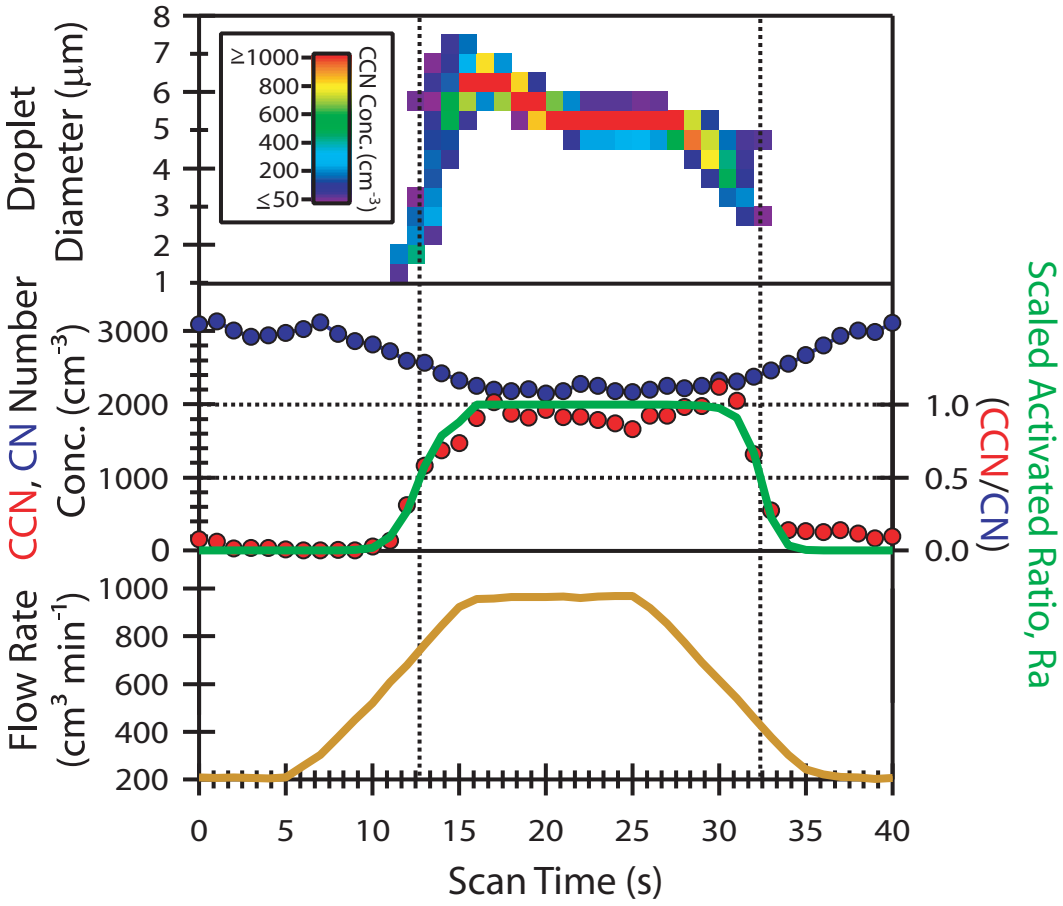


**Figure 2.6:** Exemplary 10-second flow scan for laboratory-generated, 30-nm ammonium sulfate aerosol at $P \sim 990$ mb and $\triangle T_{nom} = 14$ K.

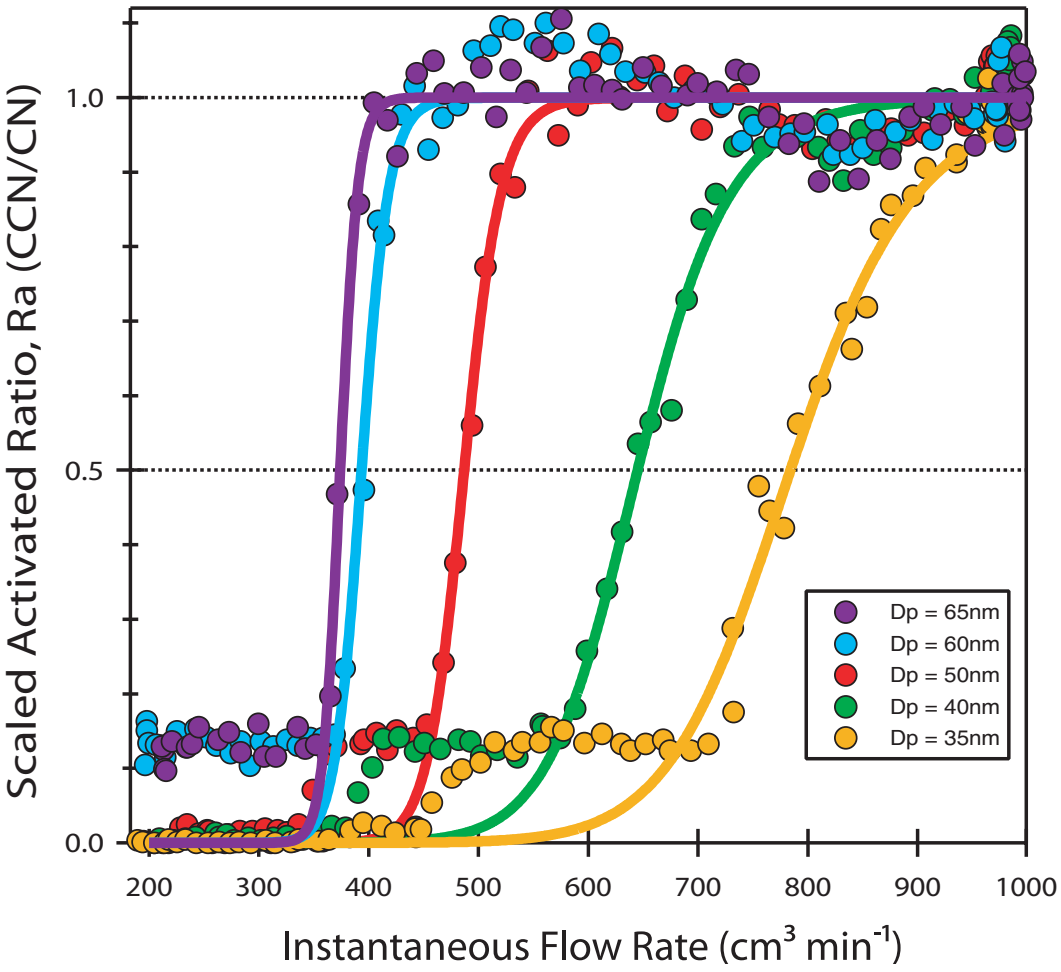


**Figure 2.7:** Sigmoidal activation curves for laboratory-generated ammonium sulfate aerosol at $t_{up} = t_{down} = 60$ s, $t_{base} = t_{peak} = 20$ s, $P \sim 990$ mb and $\triangle T_{nom} = 10$ K.

the instantaneous flow rate that produces a level of supersaturation required to activate the monodisperse calibration aerosol. In other words, $Q_{50}$ corresponds to the critical supersaturation, $s_c$, of the particle. Köhler Theory can then be applied to compute $s_c$ from knowledge of the particle dry diameter, $d_s$, and chemical composition:

$$s_c = \left( \frac{4A^3}{27B} \right)^{1/2} \tag{2.15}$$

where $B = \frac{\phi_s \nu_s M_w \rho_s d_s^3}{\rho_w M_s}$ and $M_s$, $\phi_s$, $\nu_s$, and $\rho_s$ are the molar mass, osmotic coefficient, stoichiometric van't Hoff factor, and density of the solute, respectively. The osmotic coefficient accounts for incomplete solute dissociation and was calculated for $(NH_4)_2SO_4$ and NaCl using the ion-interaction approach of *Pitzer and Mayorga* (1973) with parameters taken from *Clegg and Brimblecombe* (1988). Finally, a dynamic shape factor of 1.08 was applied to account for the non-sphericity of NaCl (*Kämer et al.*, 2000). The simplifying assumptions in applying this form of the Köhler equation to determine $s_c$ of size-resolved calibration aerosol have been critically assessed by *Rose et al.* (2008); based on this analysis, we estimate the cumulative relative uncertainty in $s_c$ to be less than 2%.

Determination of $Q_{50}$ and $s_c$ over a wide range of conditions allows a comprehensive characterization of the relationship between instantaneous flow rate and instrument supersaturation. Calibration curves are shown in Figure 2.8 for a 60-second scan at $\Delta T_{nom} =$ 10 K, and, in Figure 2.9 for 10-second scans at multiple values of $\Delta T_{nom}$. The longer, 60-second scan calibration shown in Figure 2.8 agrees well with the trend predicted from the instrument model (although the hysteresis is more pronounced than the model predictions, which is likely due to thermal wall effects not considered in the simulations). Data obtained from 10-second scans are also in good qualitative agreement with simulations (Figures 2.2 and 2.9), in that the upscan and downscan supersaturation curves appear to follow the same trend with flow rate; however, when the upscan curves are aligned by adjusting the ordinate scaling, the downscan curves do not collapse on top of each other (Figure 2.9). This may result from wall thermal effects, but more likely can be attributed to droplet inertial

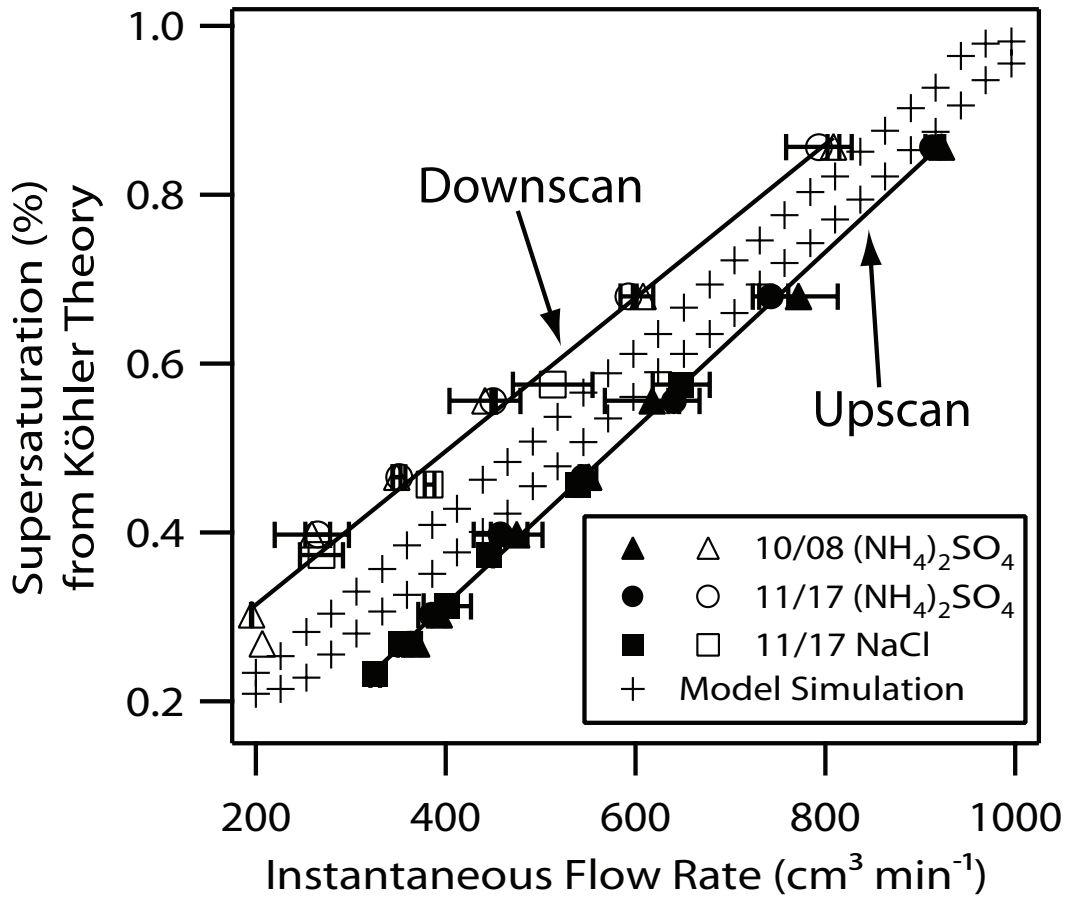


**Figure 2.8:** Calibration curves of instrument supersaturation calculated from Köhler Theory versus flow rate for laboratory-generated ammonium sulfate and sodium chloride aerosol at $t_{up} = t_{down} = 60$ s, $t_{base} = t_{peak} = 20$ s, $P \sim 990$ mb and $\triangle T_{nom} = 10$ K. The model simulation was conducted assuming a thermal efficiency of 0.57 (*Lance et al.*, 2006).

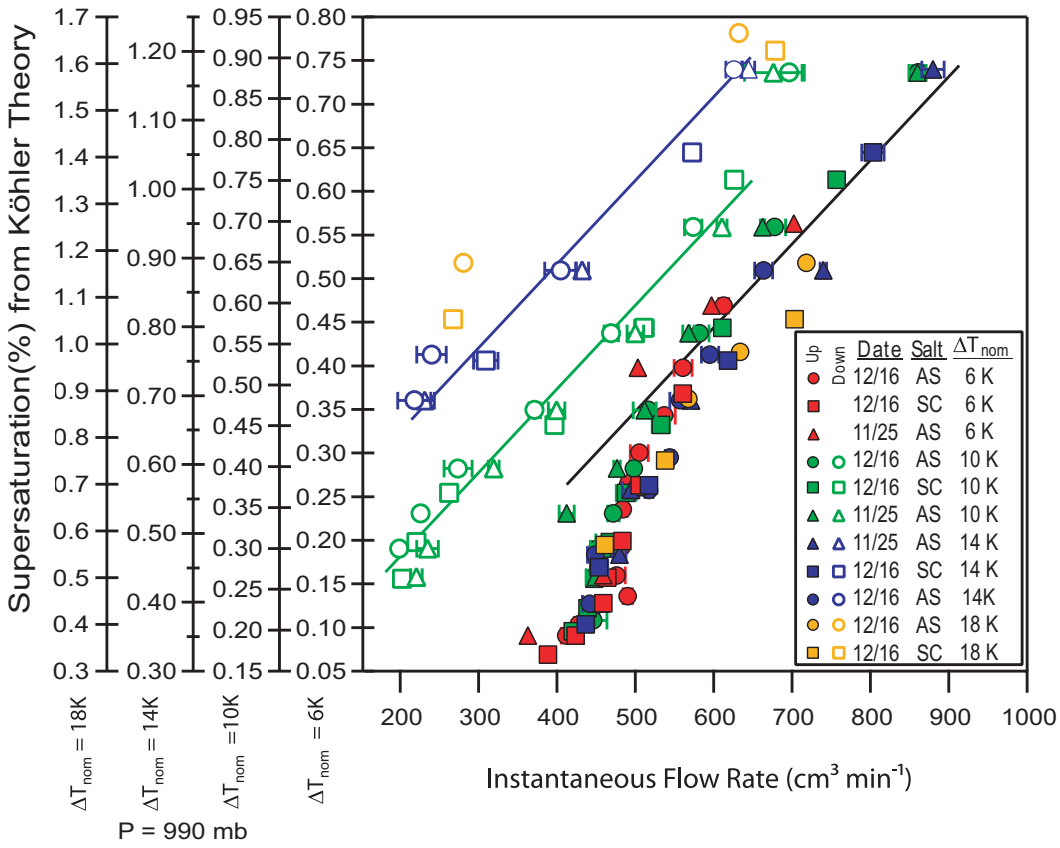


**Figure 2.9:** Calibration curves of instrument supersaturation calculated from Köhler Theory versus flow rate for laboratory-generated ammonium sulfate and sodium chloride aerosol at several values of $\triangle T_{nom}$ where $t_{up} = t_{down} = 10$ s, $t_{base} = t_{peak} = 10$ s, and $P \sim 990$ mb.

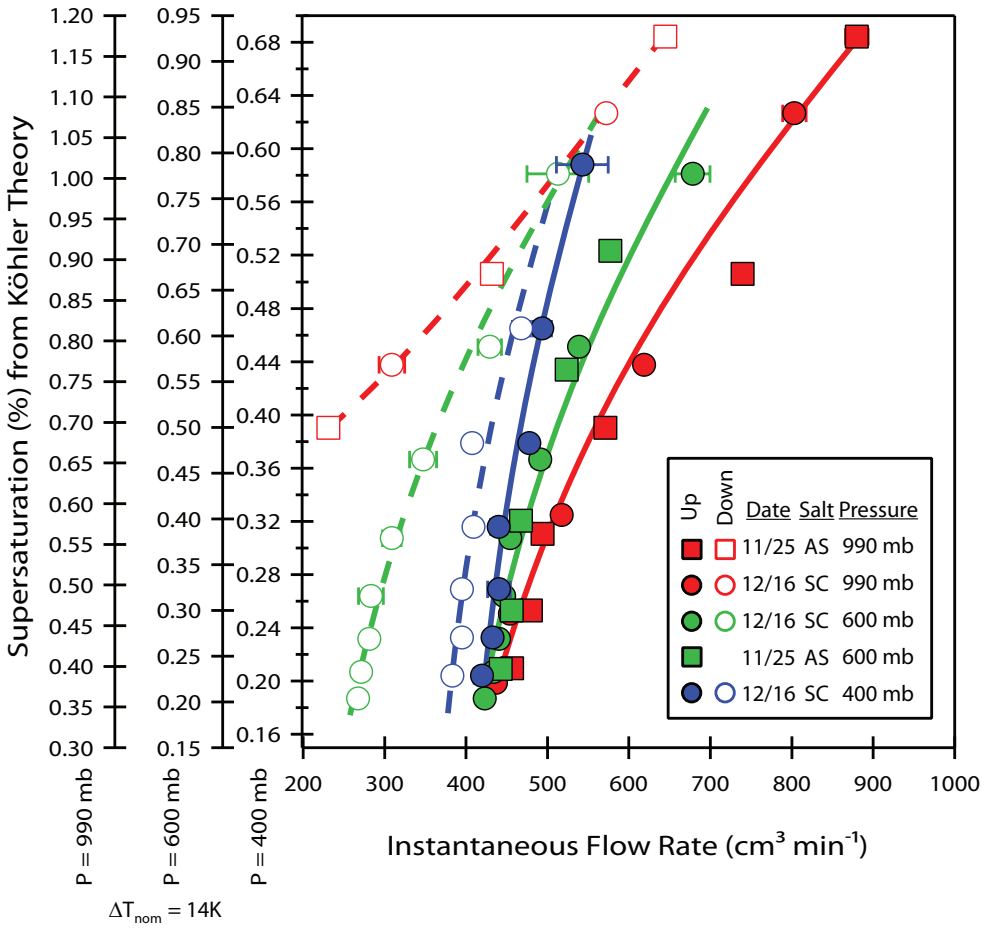


**Figure 2.10:** Calibration curves of instrument supersaturation calculated from Köhler Theory versus flow rate for laboratory-generated ammonium sulfate and sodium chloride aerosol at several pressures, where $t_{up} = t_{down} = 10$ s, $t_{base} = t_{peak} = 10$ s, and $\triangle T_{nom} =$ 14 K. Solid and dashed traces for upscan and downscan data, respectively, are included to guide the eye.

effects causing the droplets to lag slightly behind the rapidly accelerating and decelerating flow. Indeed, this effect is more pronounced at higher $\Delta T$ (Figure 2.9), where the droplets are larger. Activation curves for the 60 s scans (Figure 2.8) are notably steeper and shifted compared to the 10 s scans (Figure 2.9). The difference can be attributed to the aforementioned droplet inertial effects (which accounts for the observed shift) and the OPC integration time, which, as $\tau_Q$ becomes comparable to $\tau_{OPC}$, integrates droplets from multiple supersaturations simultaneously, causing a broadening in the activation ratio. The current OPC acquisition software uses a 1 Hz integration time, so a large supersaturation dynamic range is sampled every second during 10 s scans. Either a data inversion and/or shorter OPC integration time could rectify both effects and will be the subject of a future study.

Calibration curves at reduced pressures, typical of those used during aircraft studies, are shown in Figure 2.10 for a 10-second ramp time and a constant $\Delta T_{nom} = 10$ K. As the operating pressure is reduced, the supersaturation also decreases consistent with steady-state operation. Furthermore, the shape of the response curve during the flow upscan and downscan also changes; the calibration curves move closer together and upscan-downscan segments tend to be parallel, which is consistent with the instrument model simulations.

An example of the stability of SFCA is presented in Figure 2.11 which shows the activation of 50-nm ammonium sulfate aerosol measured continuously over a 12-hour period using both 20-second and 60-second ramp times. The experiment was conducted in a laboratory maintained at nearly constant pressure (P$\sim$990 mb) and temperature varied between 23°C and 27°C. Figure 2.11 suggests that the activation spectrum remains fairly constant with time and no systematic drift is apparent. Some outlying scans are present, particularly for the shorter scan time, and these are related to occasional shifts in column temperature caused by changes in the inlet air temperature (which could be accounted for in an advanced inversion). Activation curves obtained from $(NH_4)_2SO_4$ and NaCl aerosol remained constant over several weeks (Figures 2.8-2.10), which ensures that SFCA is a stable mode of

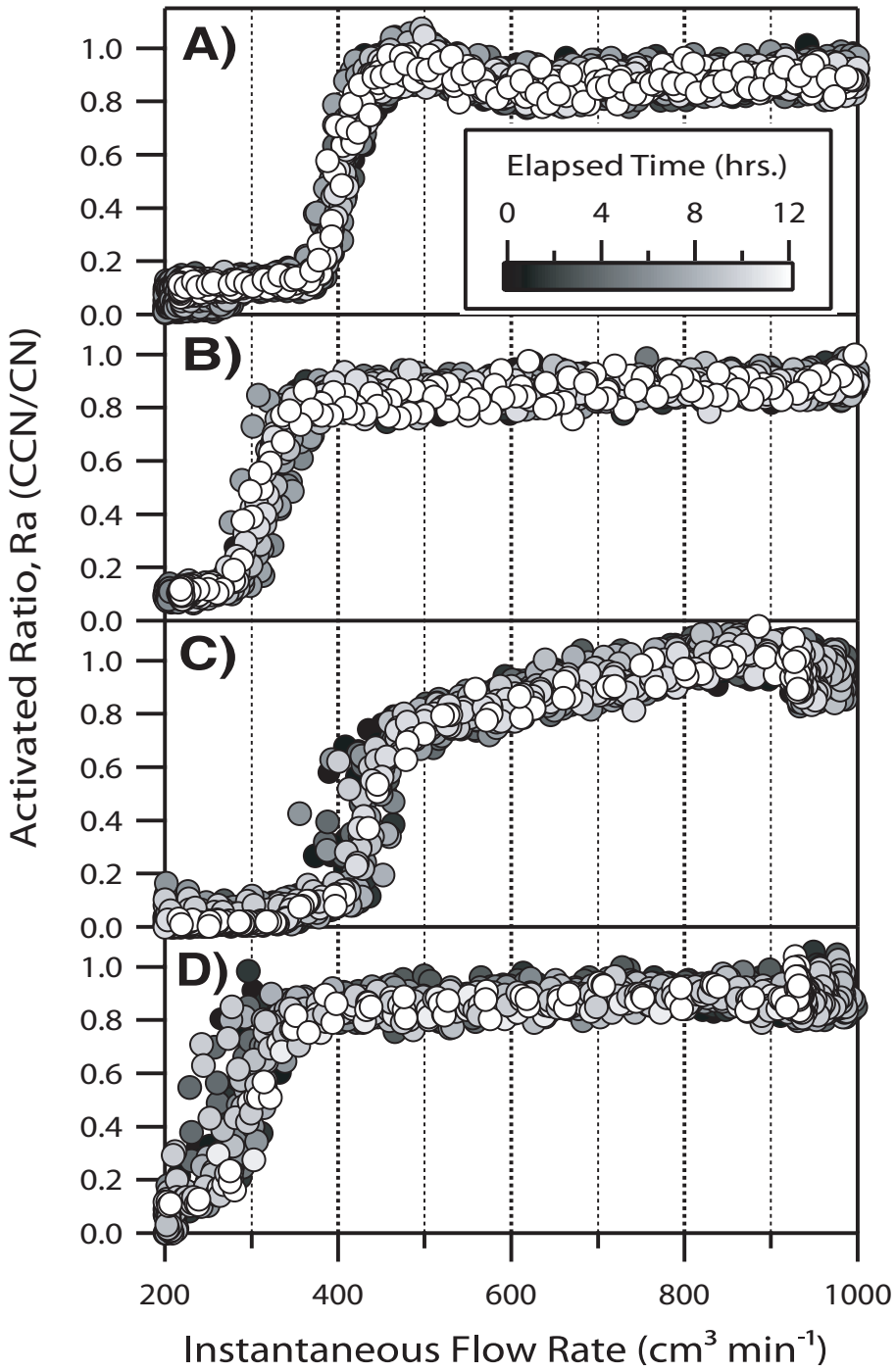


**Figure 2.11:** Compilation of $R_a$ vs. flow rate for classified 50-nm $(NH_4)_2SO_4$ aerosol. Data collected over a 12-hour period for (A) 60-second upscans, (B) 60-second downscans, (C) 20-second upscans, (D) 20-second downscans. $\Delta T_{nom} = 10$ K and $t_{base} = t_{peak} = 20$ s in all scans.

operation in the CFSTGC for both fast and slow scan times.

### 2.4.2 Ambient Aerosol

CCN spectra of ambient aerosol in Atlanta, GA, were measured using SFCA during the period of November to December 2008. Sampling was conducted on the Georgia Tech rooftop measurement platform in Midtown Atlanta (33°46'44.75"N; 84°23'45.15"W; ∼30-40 m elevation). The aerosol sampled at this location is expected to be representative of an urban environment with strong biogenic influences. The inlet stream was split between one CFSTGC operating in SFCA mode, another CFSTGC operating in "conventional" (stepping-$\Delta T$ and constant-$Q$) mode, and a CPC measuring CN concentrations. Activation experiments using calibration aerosol with both instruments operating in stepping-$\Delta T$-mode suggested a 6% deviation between the CCN concentrations measured by both instruments, and this difference was accounted for in the instrument intercomparison. Timeseries $R_a$ data are shown for both instruments in Figure 2.12; SFCA was carried out using two different scan times (60, 10s) and two different values of $\Delta T_{nom}$. Both instruments are in excellent qualitative agreement with identical peaks and troughs in the $R_a$ timeseries throughout the weeks of operation.

A direct quantitative comparison of the SFCA timeseries to the stepping-ΔT-mode timeseries is shown in Figure 2.13. Data from both instruments were averaged over each stepping-ΔT-mode time period. Both the ambient SFCA and ambient stepping-ΔT-mode data shown in Figure 2.13 are in excellent agreement ($R^2$=0.985, 0.977 for the 60 and 10 s scans, respectively). 10 s scans tend to exhibit somewhat larger scatter (inset of Figure 2.13b) than for 60 s scans (inset of Figure 2.13a); the symmetric nature of the scatter and its relation to scantime suggests that it is broadening from the OPC integration time, which can be addressed either during the inversion process or through decreasing the OPC integration time. Nevertheless, Figure 2.13 conclusively shows that SFCA compares well with the well-established and robust technique of varying the instrument temperature difference,

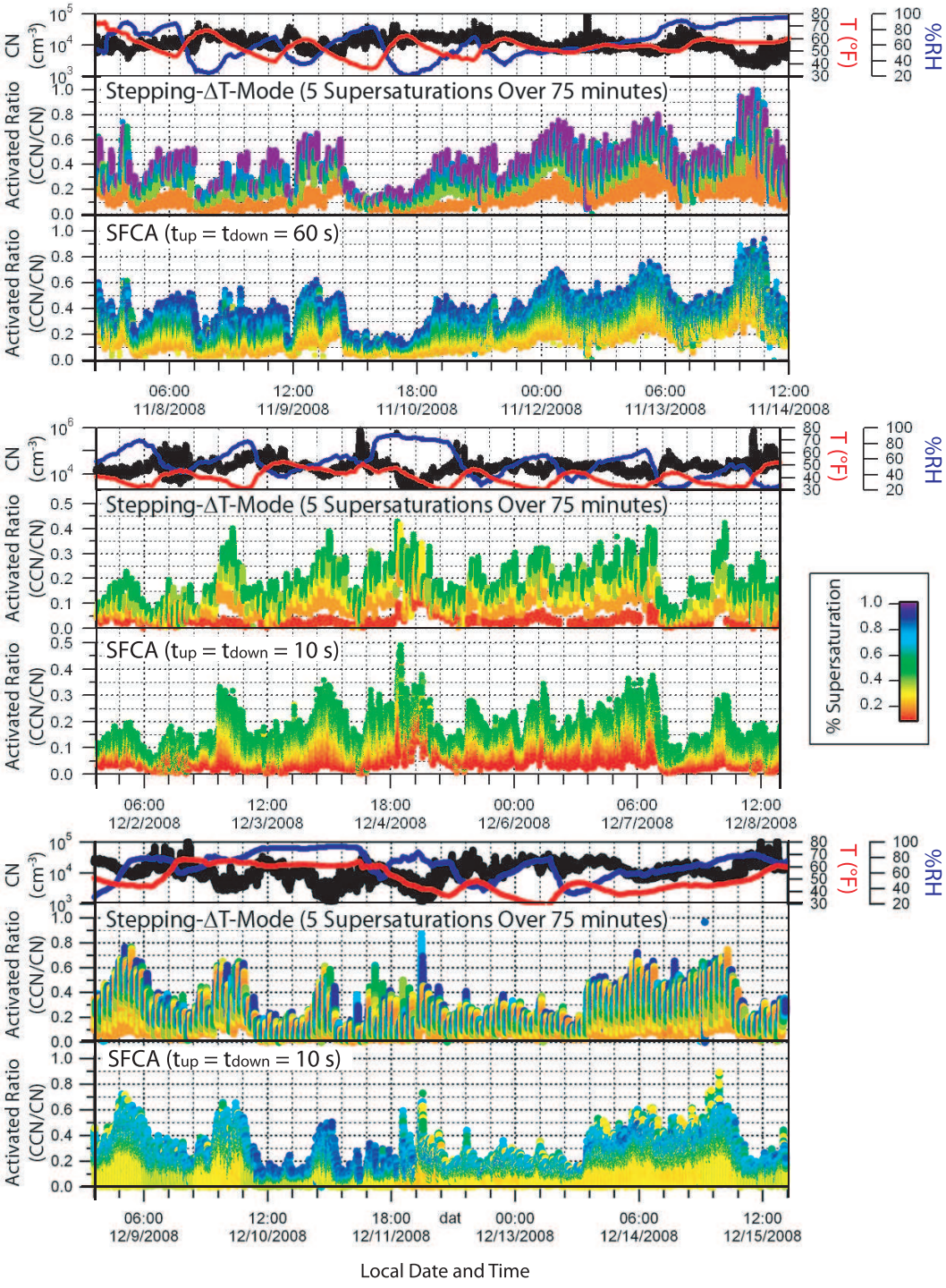


**Figure 2.12:** Continuous measurements of $R_a$ for Atlanta aerosol using both SFCA and stepping-$\Delta T$ methods. Data shown for (top) $\Delta T_{nom} = 10$ K, $t_{up} = t_{down} = 60$ s, $t_{peak} = t_{base} = 20$ s; (middle) $\Delta T_{nom} = 6$ K, $t_{up} = t_{down} = 10$ s, $t_{peak} = t_{base} = 10$ s; and (bottom) $\Delta T_{nom} = 10$ K, $t_{up} = t_{down} = 10$ s, $t_{peak} = t_{base} = 10$ s.

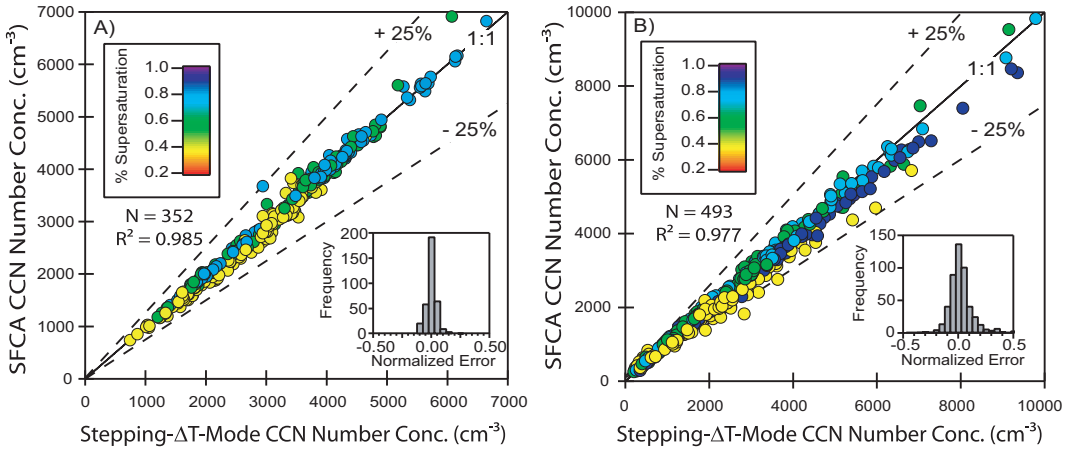


**Figure 2.13:** Comparison plots of A) 60-second-scan and B) 10-second-scan SFCA spectra to the stepping-$\Delta$T mode spectra for November 7-14, 2008 and December 8-15, 2008.

but with much better temporal and supersaturation resolution.

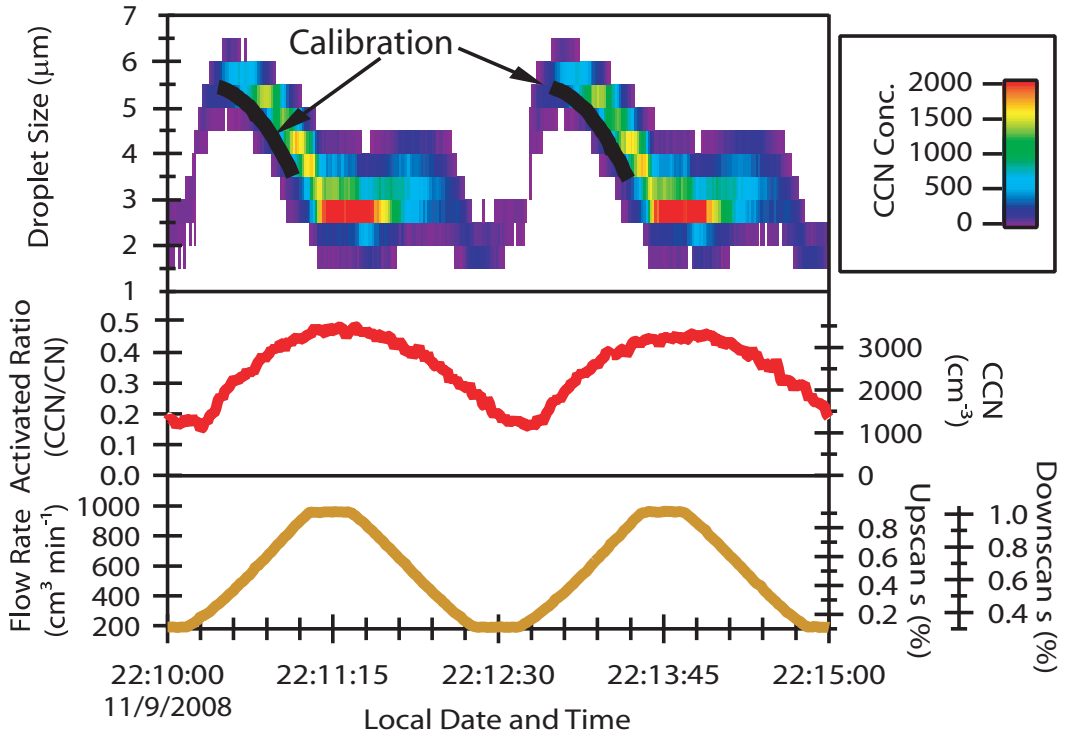


**Figure 2.14:** Exemplary SFCA timeseries showing ambient CCN concentrations and measured droplet sizes over time. The black traces denote the average droplet diameter ($\pm$0.5 $\mu$m) of ammonium sulfate calibration aerosol as a function of upscan supersaturation.

In addition to CCN activation, SFCA provides high-resolution droplet growth information. The average droplet size measured at the OPC can be compared against that of ammonium sulfate calibration aerosol at the same flow rate (superaturation) to evince any kinetic limitation on droplet growth from the presence of organic compounds. An example is shown in Figure 2.14 for successive 60-second scans of ambient Atlanta aerosol taken on 09 November 2008. The droplet size distribution trends with expectations – the initial increase in droplet size caused by increasing supersaturation is followed by a decrease in droplet size where the decreasing residence time at the higher flow rates allows less time for droplet growth. The black curves represent the maximum droplet size obtained for $(NH_4)_2SO_4$ calibration aerosol with $s_c$ equal to instrument $s$; the ambient aerosol grow to sizes roughly consistent with (or even slightly larger than) the inorganic salt ($\pm 0.5\mu$m). Thus, the ambient aerosol displays the same (fast) activation kinetics as calibration aerosol. If slow activation kinetics are observed, then the instrument and droplet growth models could be used to parameterize the delayed droplet growth in terms of changes in $\gamma$ (e.g., *Asa-Awuku et al.*, 2008; *Ruehl et al.*, 2008).

## *2.5 Summary and Conclusions*

Scanning Flow CCN Analysis (SFCA) is a new method that allows rapid, high-resolution measurements of CCN spectra using the CFSTGC design of *Roberts and Nenes* (2005). SFCA is based on varying the instrument flow rate while keeping the instrument pressure and streamwise temperature difference constant. Varying the flow in the growth chamber at a sufficiently slow rate (but still adequate for airborne CCN measurements) allows for instrument operation at "pseudo-steady" state, where droplets grow to detectable sizes, and, instantaneous supersaturation linearly correlates with flow rate and greatly facilitates inversion of the CCN timeseries to a CCN spectrum.

Activation of laboratory-generated inorganic calibration aerosol and ambient aerosol are shown to be in excellent agreement with the instrument simulations and conventional

operation of the CCN counter. SFCA can be employed on existing Droplet Measurement Technologies CFSTGC instruments with a software upgrade. Current hardware allows CCN activity and droplet size spectra to be obtained in as little as 10 seconds with very stable performance, which is adequate for airborne measurements and vastly superior to the 3600-seconds required by the conventional "stepping-$\Delta$T" mode. If operated at lower pressures, even faster scans can be obtained, but would require a transfer function deconvolution to correct for droplet inertial effects and OPC integration time. SFCA is a technique that combines the simplicity and robustness of the CFSTGC with the dynamic range and resolution of a CCN spectrometer. For a wide range of operation conditions, SFCA provides spectra unbiased by shifts in activation kinetics and aerosol composition.

# CHAPTER III

# SCANNING MOBILITY CCN ANALYSIS (SMCA)

This chapter presents Scanning Mobility CCN Analysis (SMCA) as a novel method for obtaining rapid measurements of size-resolved cloud condensation nuclei (CCN) distributions and activation kinetics. SMCA involves sampling the monodisperse outlet stream of a Differential Mobility Analyzer (DMA) operated in scanning voltage mode concurrently with CCN and condensation particle counters. By applying the same inversion algorithm as used for obtaining size distributions with a scanning mobility particle sizer (SMPS), CCN concentration and activated droplet size are obtained as a function of mobility size over the timescale of an SMPS scan (typically 60-120s). Methods to account for multiple charging, non-sphericity effects and limited counting statistics are presented. SMCA is demonstrated using commercial SMPS and CFSTGC instruments with the manufacturer-provided control software. The method is evaluated for activation of both laboratory aerosol and ambient aerosol obtained during the NEAQS-ITCT2k4 field campaign. It is shown that SMCA reproduces the results obtained with a DMA operating in voltage "stepping" mode.

## *3.1 Introduction*

Predictive understanding of aerosol-cloud interactions in climate and hydrological cycle studies (e.g., *Solomon et al.* (2007); *Levin and Cotton* (2009)) requires a global network of cloud condensation nuclei (CCN) measurements. With the advent of the Continuous-Flow Streamwise Thermal Gradient CCN Chamber (CFSTGC; *Roberts and Nenes* (2005)) and its commercialization by Droplet Measurement Technologies (*Lance et al.*, 2006; *Rose*

This chapter published as: Moore, R. H., A. Nenes, and J. Medina (2010), Scanning mobility CCN analysis - A method for fast measurements of size-resolved CCN distributions and activation kinetics, Aerosol Science and Technology, 44, 861-871, doi:10.1080/02786826.2010.498715. 

*et al.*, 2008), this is rapidly becoming a reality.

CCN instruments can be utilized in various ways to complement aerosol-cloud interaction studies. They can be used as "counters", where the concentration of CCN is measured at a given level of supersaturation. This mode of operation is commonly used for "CCN closure" studies, i.e., to assess the ability of thermodynamic theory to predict CCN concentrations from measurements of aerosol size distribution and chemical composition (e.g., *Rose et al.*, 2010; *Jurányi et al.*, 2010; *Bougiatioti et al.*, 2009; *Lance et al.*, 2009; *Cubison et al.*, 2008; *Sorooshian et al.*, 2008; *Wang et al.*, 2008; *Vestin et al.*, 2007; *Medina et al.*, 2007; *Broekhuizen et al.*, 2006, and others). The maximum potential of CCN measurements is realized when CCN instruments, operating in either counting mode or in "spectrometer" mode (*Moore and Nenes*, 2009), are coupled with a differential mobility analyzer (DMA) to obtain size-resolved measurements. These methods provide the CCN concentration across supersaturations and particle sizes, which when coupled with theory, enables the parameterization of composition impacts on cloud droplet formation (e.g., *Rose et al.*, 2010; *Petters et al.*, 2009; *Dusek et al.*, 2010; *Carrico et al.*, 2008; *Petters and Kreidenweis*, 2007; *Wex et al.*, 2007; *Padró et al.*, 2007, 2010; *Padró Martinez*, 2009; *Lance*, 2007), the characterization of chemical ageing and mixing state of aerosol (e.g., *Shinozuka et al.*, 2009; *Cubison et al.*, 2008; *Kuwata et al.*, 2008; *Lance*, 2007; *Padró Martinez*, 2009), and the evaluation of CCN activation kinetics (e.g., *Asa-Awuku et al.*, 2008; *Shantz et al.*, 2008; *Sorooshian et al.*, 2008; *Ruehl et al.*, 2008, 2009). Under certain conditions, size-resolved measurements allow for the inference of average molar volume and surfactant characteristics of the water-soluble carbonaceous aerosol fraction (e.g., *Padró et al.*, 2007; *Asa-Awuku and Nenes*, 2007; *Asa-Awuku et al.*, 2010, 2008; *Engelhart et al.*, 2008; *Moore et al.*, 2008; *Padró et al.*, 2010).

Most studies to date operate the DMA in "stepping mode", where the voltage applied to the DMA is held constant during a CCN measurement; the voltage is increased stepwise for another CCN measurement to cover the entire size range of the DMA (e.g., *Rose*

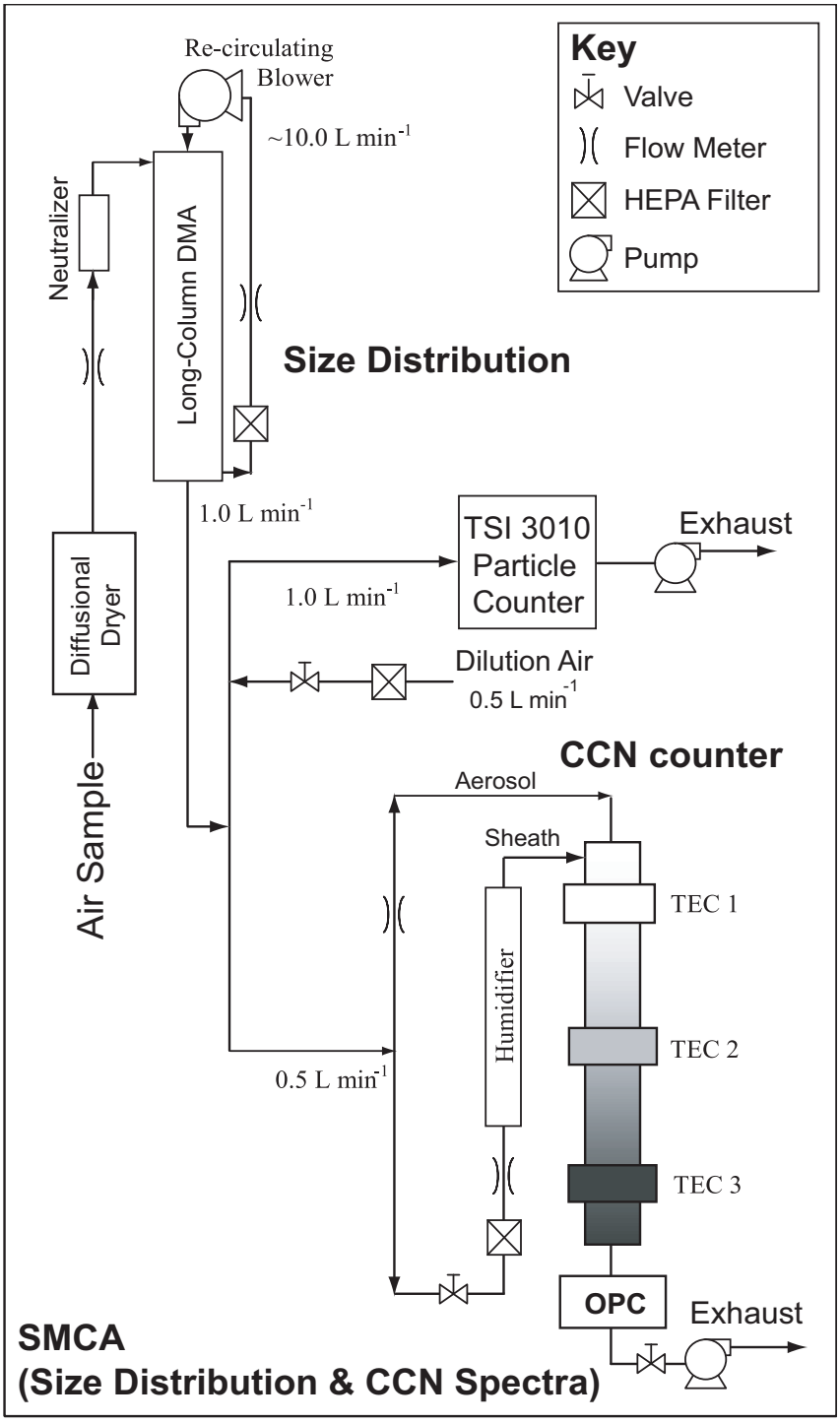


**Figure 3.1:** Schematic of the setup used for the Scanning Mobility CCN Analysis (SMCA).

*et al.*, 2010; *Gunthe et al.*, 2009; *Petters et al.*, 2009; *Asa-Awuku and Nenes*, 2007; *Petters and Kreidenweis*, 2007, and others). The technique described in this manuscript, entitled "Scanning Mobility CCN Analysis" (SMCA), provides an alternative method for performing size-resolved CCN measurements; the DMA is operated as a Scanning Mobility Particle Sizer and the voltage is ramped exponentially, typically over a period of 60-120 seconds (*Wang and Flagan*, 1989). SMCA has been successfully applied in a number of studies (*Padró et al.*, 2007; *Asa-Awuku and Nenes*, 2007; *Asa-Awuku et al.*, 2010, 2008; *Engelhart et al.*, 2008; *Moore et al.*, 2008; *Padró et al.*, 2010) and presented in detail here. SMCA can be applied to commercial SMPS and CFSTGC instruments with the manufacturer-provided control software coupled with simple post-processing routines (available for download from http://nenes.eas.gatech.edu). In subsequent sections, we present SMCA, an overview of the data analysis, and validation of the method with both laboratory aerosol and ambient aerosol sampled during the 2004 ICARTT-ITCT2k4 field campaign.

## *3.2 Description of SMCA*

### 3.2.1 Instrumentation Setup

The instrumentation setup is shown in Figure 3.1. Polydisperse dry aerosol is charge-neutralized using a Kr-85 neutralizer (TSI 3077A) and introduced into a differential mobility analyzer (DMA, TSI 3081L) for classification by electrical mobility. The classified aerosol is then split between a condensation particle counter (CPC, TSI 3010 or 3022a) for measurement of total aerosol (condensation nuclei, CN) concentration, and a Droplet Measurement Technologies Continuous-Flow, Streamwise Thermal-Gradient Chamber (CFSTGC) (*Roberts and Nenes*, 2005; *Lance et al.*, 2006; *Rose et al.*, 2008) to measure CCN concentrations. In order to maintain a sample flow rate of 1 LPM through the DMA, filtered make-up air is supplied to the classified aerosol stream or to the CPC stream (the latter being preferable in cases where low aerosol concentrations limit the counting statistics in the CFSTGC). In this study, the voltage applied to the DMA is exponentially scanned using the

TSI Aerosol Instrument Manager control software, which also manages data acquisition in the CPC and inversion to provide the aerosol number size distribution. The software also provides the raw CN counts reported by the CPC every 0.1 s during each scan cycle. While not further discussed here, any instrument control software could be used to control and invert the SMPS data.

The CFSTGC consists of a cylindrical growth chamber with internally-wetted walls upon which a constant streamwise temperature gradient is applied. The difference between the diffusivity of heat and water vapor generates a supersaturation that depends on the flow rate, the streamwise temperature gradient and the pressure in the chamber. Figure 3.1 illustrates the components and flow diagram of the CFSTGC. The inlet flow is first split into "sheath" and "sample" flows. The latter is directed to the center of the growth chamber, whereas the "sheath" flow is filtered and humidified prior to its entry in the chamber. Both flows travel through the column, exposing aerosol about the centerline to an approximately constant supersaturation (after the decay of entry length effects), a fraction of which activate to form cloud droplets. An optical particle counter (OPC) then counts and sizes the activated droplets at the outlet of the column. The CCN counts are accumulated over a time period of 1s. The relationship between instrument supersaturation and operating conditions (column temperature gradient, flow rate and column pressure) is determined using calibration aerosol, following the procedure of *Lance et al.* (2006), *Rose et al.* (2008), and *Bougiatioti et al.* (2009).

### 3.2.2 Application of SMCA

The DMA voltage is continuously cycled between a minimum and maximum value, and the timeseries of CN and CCN counts are recorded (examples are presented in Figures 3.2a and 3.2b for high and low aerosol concentration, respectively). The particle size distribution is then obtained from the CN timeseries using well-established SMPS inversion techniques

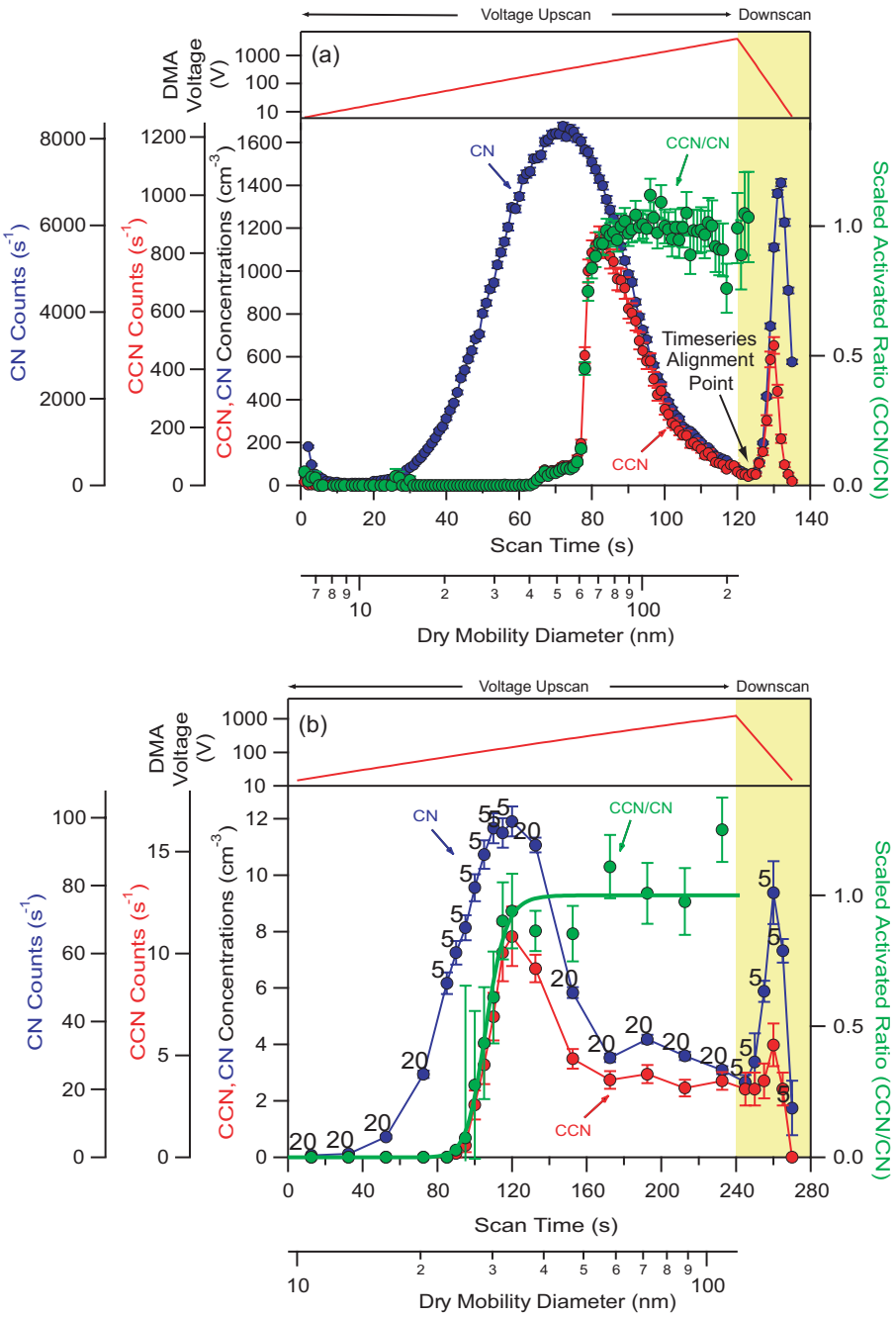


**Figure 3.2:** Example of CCN (red), CN (blue) timeseries and inverted activation curve (green). CCN, CN data are presented in terms of raw counts accumulated over 1s, and the corresponding concentrations. Error bars represent the propagated uncertainty, calculated using Equations 3.5 to 3.6. Results shown for laboratory-generated aerosol with a total number concentration of (a) $4x10^5$ $cm^{-3}$, and (b) 200 $cm^{-3}$. Counting statistics limitations are addressed by averaging (post-measurement) consecutive 1s bins, the number of which is noted beside each point.

(e.g., *Crump and Seinfeld* (1981); *Hagen and Alofs* (1983); *Wang and Flagan* (1989); *Russell et al.* (1995); *Collins et al.* (2002)). In this study, the CN timeseries is inverted using the TSI AIM software (which uses the method of *Wang and Flagan* (1989)). The timeseries of CN, CCN is used to determine the "activation" ratio of CCN to CN concentration, $R_a$, (see right ordinate axis in Figure 3.2) and applied to the inverted aerosol size distribution to obtain the CCN size distribution (discussed in section 3.2.3).

For this study, the centroid mobility diameter obtained from the DMA ranged between 10 and 300 nm, size distribution scans were obtained every 135 or 270 seconds (120/240 seconds for the voltage "upscan", and, 15/30 seconds for the voltage "downscan", respectively), where the longer scan time was applied for low concentration measurements to improve counting statistics. The sample flow rate in the DMA was adjusted to be 1 L $\text{min}^{-1}$ and the sheath-to-aerosol flow was maintained at a 10:1 or 5:1 ratio. The TSI 3010 CPC (used in the field experiments) operates at 1 L $\text{min}^{-1}$, while the TSI 3022a (used in the laboratory experiments) operates at 1.5 L $\text{min}^{-1}$ (with a 0.3 L $\text{min}^{-1}$ internal flow). The CCN counter was operated at a flow rate of 0.5 L $\text{min}^{-1}$ at a sheath-to-aerosol flow ratio of 10:1. The supersaturation at the CCN counter is changed every 3-4 voltage scan cycles in the DMA (by changing either the flow rate or the streamwise temperature gradient). Whenever the temperature gradient is changed, up to 2 minutes are required for the instrument profiles to stabilize.

### 3.2.3 Data Inversion and Multiple Charge Correction

The inversion to obtain CCN and CN size distributions is applied to the data collected during the voltage upscan. The CPC and CCN counts time series are obtained from the AIM software and CFSTGC software, respectively, and are normalized by flow rate to express them in terms of number concentration. The time series are aligned by matching the minimum in counts that occurs during the transition between upscan and downscan (Figure 3.2). Owing to the longer plumbing time associated with the CFSTGC, its minimum

occurs some fixed time after the corresponding CPC signal (here about 15 seconds). After alignment, the CCN time series is mapped into size space using the size-scantime relationship provided by the AIM software (which uses the voltage-time relationship used in the DMA, accounting for the plumbing time between DMA and CPC and assuming that particles carry a single charge). The aerosol number distribution is then inverted, and $R_a$ determined from the CPC/CCN timeseries is used to obtain the CCN number distribution.

Since the timeseries are influenced by multiple charged particles, it is necessary to rebin the CN and CCN counts based on an equilibrium charge distribution. The following procedure is used:

1. The aerosol number size distribution, $n_n(D_p)$, is obtained by inversion of the CPC timeseries (here using the TSI AIM software).

2. The aligned CN and CCN timeseries are binned to a common time grid. The grid spacing by default is 1s (the reporting time of the CFSTGC), although it can vary to ensure sufficient counting statistics.

3. The size-dependent activation efficiency, $R_a^*(D_p) = C_{CCN}(D_p)/C_{CN}(D_p)$, is estimated from the CCN and CN timeseries and the size-scantime relationship provided by the AIM software.

4. The CCN and CN timeseries are then corrected for multiple-charging. Starting from the largest aerosol size bin of the CN timeseries (and moving to each successive smaller bin), the number of particles with +2 and +3 charges are removed and placed in the CN timeseries bin with the correct mobility diameter. The procedure starts from the largest size, because an impactor is placed in front of the sample flow of the DMA, so that the largest size bin in the inverted distributions (corresponding to the 50% cutoff diameter of the impactor) contains only singly-charged particles.

   The number of multiply-charged particles is computed assuming equilibrium charging in the aerosol neutralizer. For particles with $n$=+1,+2 charges, expressions from

*Wiedensohler* (1988) are used to compute the fraction of particles with dry size $D_p$ (here equal to the centroid mobility diameter of each aerosol size bin) and $n$ charges, $f(D_p, n)$,

$$f(D_p, n) = 10^{\left(\sum_{i=0}^{5} a_i(n)(\log D_p)^i\right)} \tag{3.1}$$

where $a_i(n)$ are empirical coefficients presented in *Wiedensohler* (1988). For $n$ =+3, the parameterization presented in *TSI, Incorporated* (2003); *Gunn* (1955); *Gunn and Woessner* (1956) is used,

$$f(D_p, +3) = \Phi \exp \frac{-\left(n - \frac{2\pi\varepsilon_0 D_p kT}{e^2} \ln\left(\frac{Z_{i+}}{Z_{i-}}\right)\right)^2}{4\pi\varepsilon_0 D_p kT/e^2} \tag{3.2}$$

where $\Phi = \frac{e}{\sqrt{4\pi^2\varepsilon_0 D_p kT}}$, $e$ is the elementary charge, $\varepsilon_0$ is the dielectric constant of air, $k$ is the Boltzmann constant, $T$ is absolute temperature, and $Z_{i+}/Z_{i-} = 0.875$ is the ion mobility ratio (*TSI, Incorporated*, 2003).

Calculation of the mobility diameter is done using the fundamental DMA equation (*Wang and Flagan*, 1989):

$$\frac{D_p}{nC_c(D_p)} = \frac{2eV(t)}{3\mu q_s ln\frac{r_1}{r_2}} \tag{3.3}$$

where $C_c(D_p) = 1 + \frac{2\lambda}{D_p}\left[1.257 + 0.4\exp\left(\frac{-1.1D_p}{2\lambda}\right)\right]$ is the size-dependent Cunningham slip correction factor (*Seinfeld and Pandis*, 2006), $V(t)$ is the applied voltage at a given time $t$ during the scan, $\mu$ is the viscosity of air, $q_s$ is the sheath flow rate, and $r_1$, $r_2$ are the inner and outer radii of the DMA annular space, respectively.

5. The CCN timeseries is processed similarly to the CN timeseries, with the difference that the CCN counts in each size bin $j$ is multiplied by $R_a^*(D_{p_j})$.

6. The processed CCN and CN timeseries are used to update $R_a^*(D_p)$; Steps 4-6 are iterated until convergence of $R_a(D_p)$ (typically within 2-3 iterations).

7. The CCN number size distribution at the instrument supersaturation, $n_s(D_p)$, is given by $n_s(D_p) = R_a(D_p)n_n(D_p)$.

The above algorithm is one of numerous approaches presented in the literature to correct for multiply-charged particles in size-resolved CCN measurements using electrical mobility classification. *Frank et al.* (2006) corrected for multiple charging by removing the fraction of particles with +2 or more charges scaled by an activation efficiency determined from an average of five spectra. *Rose et al.* (2008) assumed a constant fraction of doubly-charged particles across the entire size distribution as determined from the hump of the CCN/CN response curve and subtracted from fraction from the CCN and CN distributions. *Petters and Kreidenweis* (2007) fit the CCN and CN response curves to a function that incorporates the size-dependent DMA transfer function, multiple charge fraction, and activation efficiency. By iteratively minimizing the $\chi^2$ statistic, the activation efficiency of the particle distribution can be determined with a substantial fraction of multiply-charged particles. *King et al.* (2009) simulate the instrument response by employing a function similar to *Petters and Kreidenweis* (2007), but with a binary activation efficiency (being unity if activated, or zero if unactivated) based on the size-dependent critical supersaturation computed from Köhler Theory (using measured composition and assumed organic properties). *Petters et al.* (2009) developed a matrix form of the inversion used by *Petters and Kreidenweis* (2007) to calculate the activation efficiency from the measured CCN and CN size distribution without an iterative process. All the above methods do not employ the DMA in scanning voltage mode.

Particle sphericity is often assumed to determine the diameter corresponding to the centroid mobility of each size bin; this may lead to important sizing biases for non-spherical particles (e.g., black carbon, mineral dust, or crystalline inorganics). This issue can be accounted for by using a "dynamic shape factor", which accounts for the difference in hydrodynamic drag force experience by a non-spherical particle compared to a spherical particle of the same mass. Shape factors for pure salts are often known (e.g., 1.08 for

NaCl, *Kämer et al.* (2000)), but its determination for ambient particles may require auxiliary measurements of aerodynamic sizing (e.g., *DeCarlo et al.* (2004); *Kuwata and Kondo* (2009)).

## *3.3 Measurement Uncertainty*

As with all particle detection methods, sufficient counting statistics are required to obtain meaningful distributions. Both the CFSTGC and the CPC accumulate counts, $N$, over a time period $\tau_{accum}$. $N$ is then divided by the volume of aerosol sample, $Q_a$, that flows through the optics during $\tau_{accum}$ to provide the concentration of CN, CCN ($C_{CN}$, $C_{CCN}$). The relative uncertainty in concentration, $\varepsilon_C$, is then determined from the relative counting uncertainty, $\varepsilon_N$, and the flow rate uncertainty, $\varepsilon_{Q_a}$, as

$$\varepsilon_C^2 = \left(\frac{\sigma_C}{C}\right)^2 = \varepsilon_N^2 + \varepsilon_{Q_a}^2 \tag{3.4}$$

where $\sigma_C$ is the absolute concentration uncertainty and $\varepsilon_N$, $\varepsilon_{Q_a}$ are the relative uncertainties of $N$ and $Q_a$, respectively. $Q_a$ is continuously measured in the instrument, so $\varepsilon_{Q_a}$ can be directly determined as $\frac{\sigma_{Q_a}}{Q_a}$. The CFSTGC samples at a lower flow rate (0.018–0.25 L min$^{-1}$) than either of the CPCs in this work. For the CFSTGC, $\varepsilon_{Q_a}$ almost never exceeded 4%, reported flow rate uncertainties for the TSI 3010 CPC and TSI 3022a CPC are 10% and 5%, respectively. Assuming that particles are randomly distributed in space throughout the sampled volume, Poisson statistics can be used to estimate $\varepsilon_N$, since the sample standard deviation equals the square root of the mean ($\varepsilon_N = \frac{\sigma_N}{N} = N^{-1/2}$). Accumulating counts over $\tau_{accum}$ seconds, yields a modified form of Equation 3.4,

$$\varepsilon_C^2 = (CQ_a)^{-1} + \varepsilon_{Q_a}^2 \tag{3.5}$$

Then, the combination of applying Equation 3.5 for $C_{CCN}$ and $C_{CN}$ yields the uncertainty for the activation efficiency, $R_a = \frac{C_{CCN}}{C_{CN}}$, as

$$\varepsilon_{R_a}^2 = (C_{CN}Q_{CN})^{-1} + (C_{CCN}Q_{CCN})^{-1} + \varepsilon_{Q_{CCN}}^2 + \varepsilon_{Q_{CN}}^2 \tag{3.6}$$

**Table 3.1:** Calculated relative uncertainty in CN Concentration, $C_{CN}$, CCN Concentration, $C_{CCN}$, and Activated Ratio, $R_a$, (evaluated at $R_a$=0.5) for selected values of $C_{CN}$.

| $C_{CN}$ (cm$^{-3}$) | $\varepsilon_{C_{CCN}}$ | $\varepsilon_{C_{CN}}$ | $\varepsilon_{R_a}$ |
|---|---|---|---|
| 20 | 0.37 | 0.11 | 0.38 |
| 100 | 0.17 | 0.067 | 0.18 |
| 200 | 0.12 | 0.059 | 0.14 |
| 1000 | 0.065 | 0.052 | 0.083 |
| 2000 | 0.054 | 0.051 | 0.074 |

Table 3.1 provides values of $\varepsilon_{C_{CCN}}$ and $\varepsilon_{C_{CN}}$ for selected values of $C_{CN}$ (evaluated at $R_a = 0.5$). A sample flow rate in the CFSTGC of 0.045 L min$^{-1}$ is assumed (total flow rate of 0.5 L min$^{-1}$, 10:1 sheath-to-aerosol flow ratio) and a 0.3 L min$^{-1}$ internal flow rate is assumed for the TSI 3022a CPC. Thus, for most atmospherically-relevant CN concentrations, $\varepsilon_{C_{CN}}$ is 7% or less, while $\varepsilon_{C_{CCN}}$ is less than 17% and $\varepsilon_{R_a}$ is less than 18%.

The validity of applying Poisson statistics to approximate the concentration uncertainty was confirmed experimentally by activation of classified $(NH_4)_2SO_4$ aerosol of 80-600 nm diameter at CFSTGC supersaturations between 0.16% and 0.39%. A comparison between predicted and observed $\varepsilon_N$ exhibits excellent agreement (not shown).

## *3.4 Evaluation of SMCA*

### 3.4.1 SMCA for laboratory aerosol

SMCA was evaluated using aerosol generated via atomization of an aqueous salt solution, followed by drying of the droplets with silica gel diffusion dryers. The dry polydisperse aerosol was introduced into a DMA, which was operated using both SMCA and "stepping mode". Figure 3.3 displays $R_a$ as a function of mobility diameter, when the DMA is operated in scanning mode (closed symbols) and stepping mode (open symbols). Data is shown for aerosol composed of $(NH_4)_2SO_4$ (top panel) and NaCl (bottom panel). Ordinate error bars represent the standard deviation of 3 scan repetitions (at each size); abscissa

error bars are the half-width of the DMA transfer function ($\pm 5\%$ for the 10:1 sheath-to-aerosol ratio used). Activation curves obtained using SMCA and "stepping mode" of the DMA are largely identical. There is a slight "broadening" of the activation curves at the lower $\Delta T$ (supersaturation) associated with the OPC integration time (which is enhanced at large particle sizes). This issue could be addressed by increasing the voltage scan time at low supersaturations, or accounting for the integration time in the inversion (e.g., *Russell et al.* (1995); *Collins et al.* (2002)). The experiments for obtaining scanning mode curves in Figure 3.3 were performed in approximately 20 minutes.

The activation curves display a characteristic "sigmoidal" shape; the dry diameter, $d_{p50}$, for which 50% activation of the calibration particles act as CCN is called "dry activation diameter". Figure 3.3 shows the activation curves without multiple charge correction, hence the minor secondary activation peak to the left of $d_{p50}$. When multiple charge correction is applied, the secondary peak vanishes, and the slope of the sigmoid steepens (see Figure 3.4). The uncertainty in $d_{p50}$ associated with neglecting multiple charges is approximately 3-4%, consistent with the results of *Rose et al.* (2008) (whom operated the DMA in "voltage-stepping" mode).

$d_{p50}$ corresponds to the particle with critical supersaturation equal to the instrument supersaturation, and should not change if the DMA is operated in "stepping" or "scanning" mode. This is shown in Figure 3.5a, which presents $d_{p50}$ (determined by both methods) for $(NH_4)_2SO_4$ (open symbols) and NaCl (filled symbols) aerosol. Error bars represent the half-width of the DMA transfer function ($\pm 5\%$). The excellent agreement in $d_{p50}$ between both methods implies that calibration of instrument supersaturation should also be in agreement. This is shown in Figure 3.5b; Köhler Theory (*Seinfeld and Pandis*, 2006) is applied to compute the critical supersaturation of particles $s_c$ from knowledge of $d_{50}$ and chemical composition:

$$s_c = \left(\frac{4A^3}{27B}\right)^{1/2} \tag{3.7}$$

where $A = \frac{4M_w\sigma_w}{RT\rho_w}$, $B = \frac{\rho_s M_w \phi_s \nu_s d_{50}^3}{\rho_w M_s}$ and $M_w$, $\sigma_w$, $\rho_w$ are the molar mass, surface tension

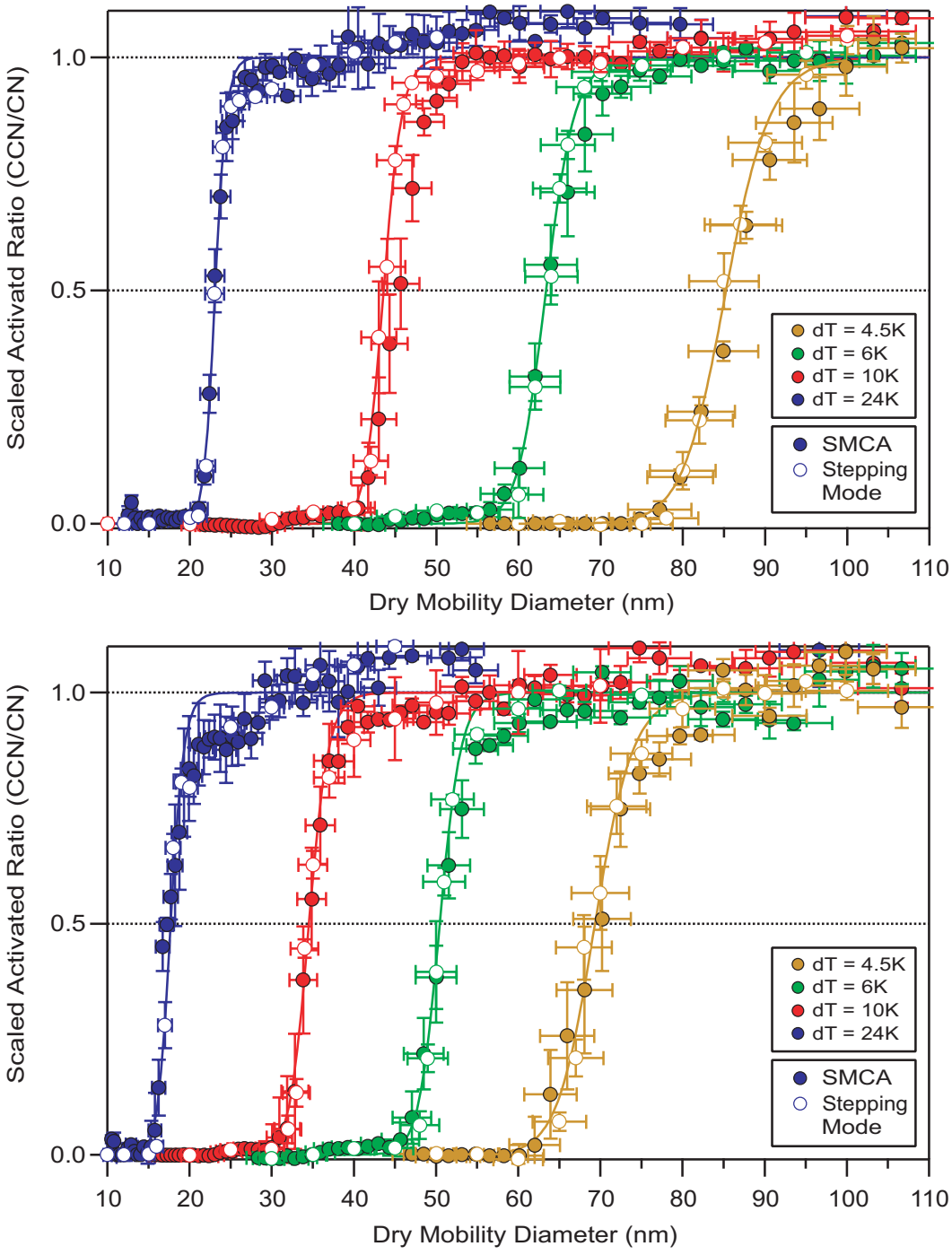


**Figure 3.3:** Example of activation curves obtained by SMCA (filled symbols) and by stepping-mode measurements (open symbols). Top panel is for activation of $(NH_4)_2SO_4$ aerosol, while bottom is for NaCl aerosol. All curves were corrected for multiple charges using the algorithm described in the text. Explanation of error bars is provided in the text.

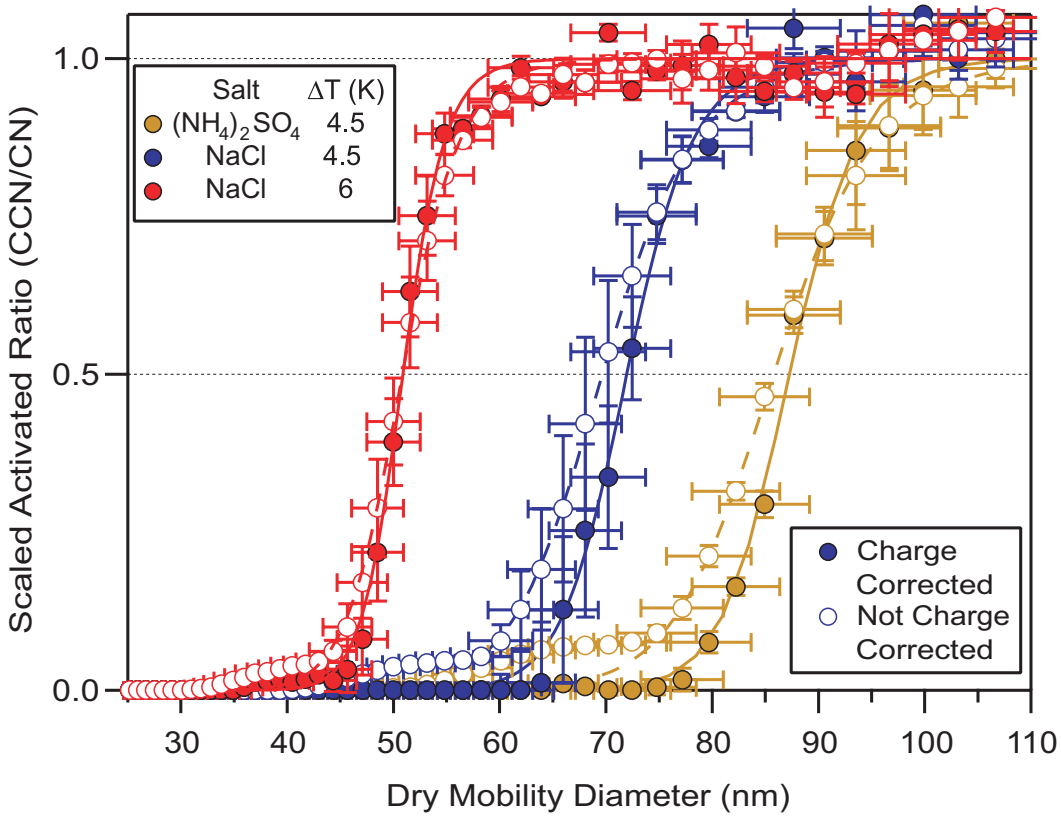


**Figure 3.4:** Activation curves for $(NH_4)_2SO_4$ aerosol obtained by SMCA. Shown are inversions without (open symbols) and with multiple-charge corrections (filled symbols).

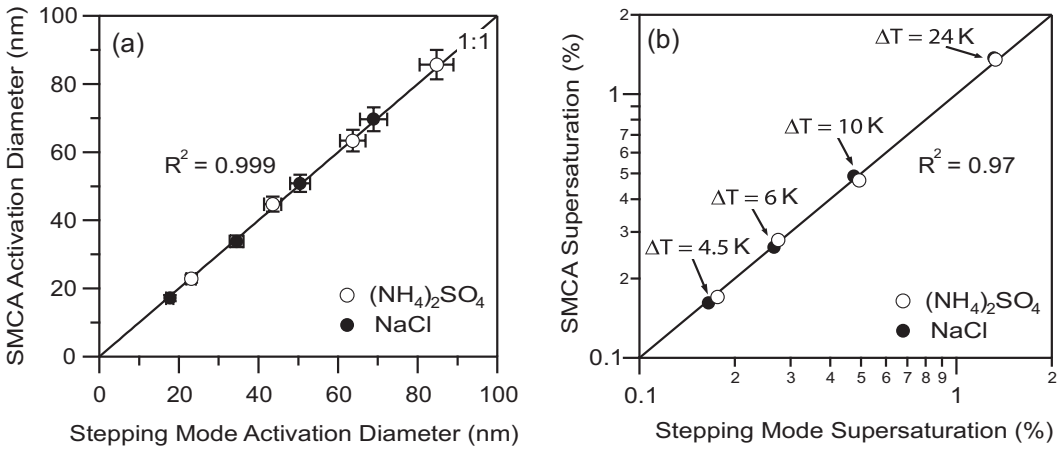


**Figure 3.5:** (a) Dry activation diameter determined by SMCA and stepping mode operation for $(NH_4)_2SO_4$ and NaCl particles. Explanation of error bars is provided in the text. (b) Instrument supersaturation calibration as determined by SMCA and stepping mode operation for $(NH_4)_2SO_4$ and NaCl particles. Results shown for different column temperature gradients.

and density of water, respectively. $\phi_s$, $\nu_s$, and $\rho_s$ are the osmotic coefficient, stoichiometric van't Hoff factor, and density of the solute, respectively. A dynamic shape factor of 1.08 was applied to $d_{50}$ to account for the non-sphericity of NaCl (*Kämer et al.*, 2000). $\phi_s$ accounts for incomplete solute dissociation and was calculated for $(NH_4)_2SO_4$ and NaCl using the ion-interaction approach of *Pitzer and Mayorga* (1973) with parameters taken from *Clegg and Brimblecombe* (1988). Instrument supersaturation calibrated by "stepping" or "scanning" modes are virtually identical; at the lower supersaturation, there is a minor ($\sim$3%) difference in supersaturation from the smearing effect of the long integration time of the CFSTGC OPC.

SMCA also allows for the measurement of the size of activated CCN (droplets) exiting the flow chamber, as a function of particle dry diameter. An example is shown in Figure 3.6, where the (wet) size of the activated CCN detected in the OPC is plotted against dry mobility diameter, determined from SMCA (filled symbols) and "stepping mode" (open symbols) operation of the DMA. Data is shown for a number of supersaturation levels in the CFSTGC. As expected, the droplet size at constant supersaturation increases with aerosol

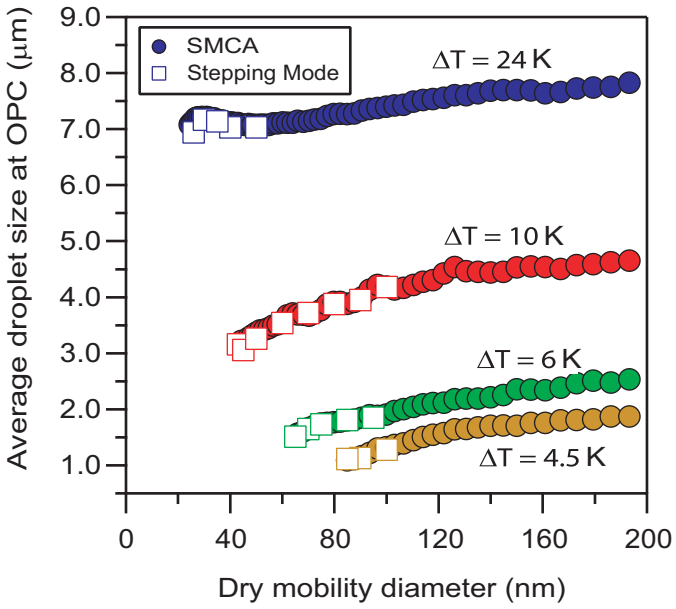


**Figure 3.6:** Size of activated $(NH_4)_2SO_4$ particles measured at the OPC of the CCN instrument, as a function of dry mobility diameter and instrument supersaturation for the data presented in Figure 3.3.

dry diameter (*Lance et al.*, 2006); exposing particles of constant dry diameter to higher supersaturation also increases the droplet diameter at detection (*Lance et al.*, 2006). Diameters using both modes of DMA operation are in excellent agreement.

### 3.4.2 SMCA for ambient aerosol

SMCA was used for ambient aerosol measurements obtained at the University of New Hampshire (UNH) AIRMAP Observing Station (http://airmap.unh.edu) at Thompson Farm. The site is located in Durham, NH, approximately two miles south of the University of New Hampshire (43.11N, 70.95W, elevation 75ft). The aerosol at this location is an internal mixture of organic and inorganic material and is ideal for evaluating SMCA. A detailed description of the station and dataset can be found in *Medina et al.* (2007); data shown here were collected on August $8^{th}$, 2004, during the NEAQS-ITCT2K4 campaign (July-August 2004).

Figure 3.7 presents exemplary aerosol size distributions and activation efficiency curves

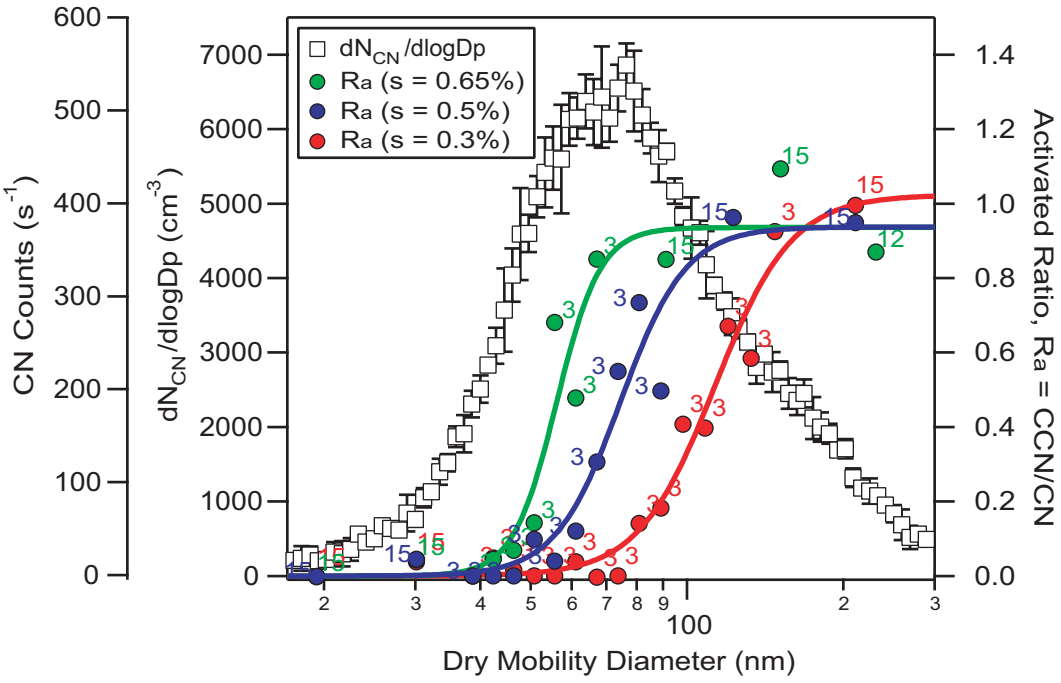


**Figure 3.7:** Example of differential activation spectra obtained by SMCA with multiple-charge correction for aerosol sampled at the AIRMAP Thompson Farm site during the NEAQS-ITCT2K4 campaign. The limited counting statistics are addressed by averaging (post-measurement) consecutive 1s bins, the number of which is noted beside each point.

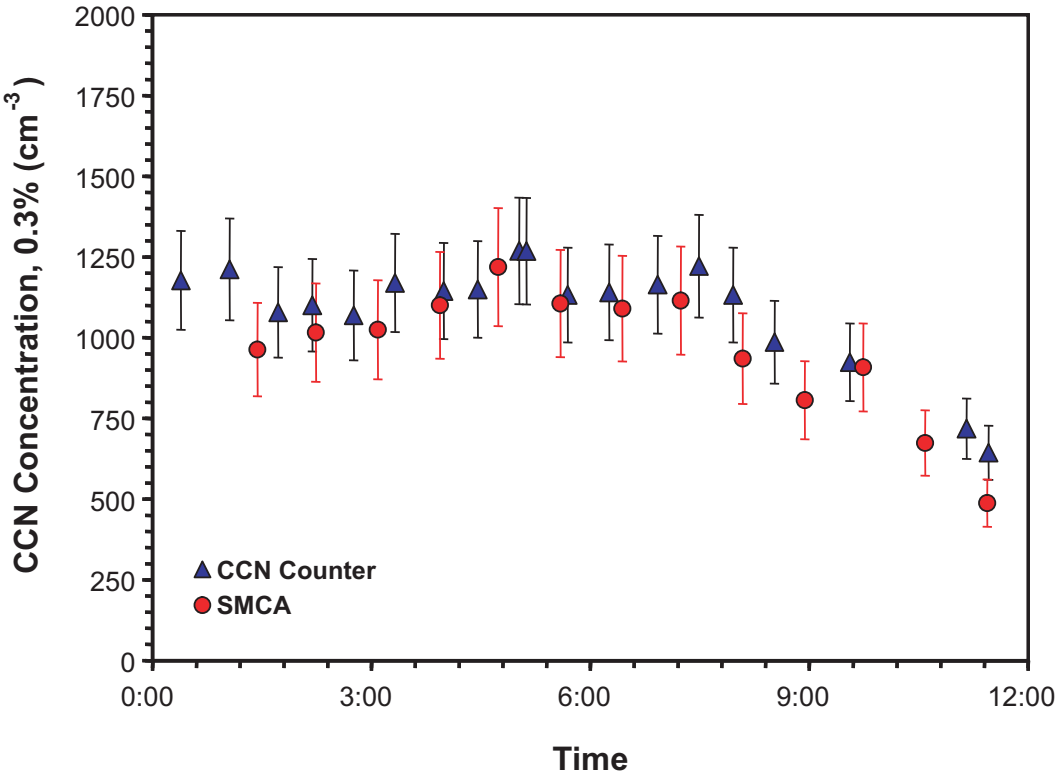


**Figure 3.8:** CCN concentrations at 0.3% supersaturation for in-situ aerosol sampled during the NEAQS-ITCT2K4 campaign. Shown are results obtained from direct measurements of CCN (triangles) and integrated SMCA spectra (circles).

sampled at three different supersaturations. As expected, the CCN distribution increasingly converges towards the total aerosol number size distribution as the instrument supersaturation increases. If particle composition is size-invariant, the CCN distribution would be zero for all sizes less than a single characteristic value (i.e., where the particle critical supersaturation equals the instrument supersaturation), and the sigmoidal activation curve would appear as a step function. This is not the case however in Figure 3.7, as chemical heterogeneity (size-dependent composition and mixing state) broadens the transition towards activation.

We test SMCA by assessing "closure" with another CCN instrument. This is done by comparing total CCN concentrations obtained by integration of the differential size spectra (like those in Figure 3.7) with measurements obtained independently with another CCN

instrument measuring the total aerosol distribution. The CCN concentrations from the integrated SMCA distributions (red symbols) agree with CCN measurements obtained with the other CFSTGC (blue symbols) to within measurement variability (Figure 3.8).

## *3.5 Summary and Conclusions*

We present Scanning Mobility CCN Analysis (SMCA), a novel method for obtaining fast measurements of size-resolved CCN activity and growth kinetics, by coupling a CPC and a CCN counter with the monodisperse outlet stream of a scanning DMA. By applying the same inversion algorithm as is currently used for obtaining size distributions, CCN activity and droplet growth kinetics are obtained as a function of mobility size over the timescale of a SMPS scan. The performance of the new method is evaluated for activation of laboratory-generated aerosol composed of $(NH_4)_2SO_4$, NaCl and for ambient aerosol measured at the AIRMAP Thompson Farm site during the ITCT2K4 field campaign. Overall, SMCA performs remarkably well, as essentially identical CCN properties are seen measured with "scanning" and "stepping" modes of the DMA.

SMCA has been successfully used in studies focused on size-resolved CCN measurements (e.g., *Padró et al.*, 2007; *Asa-Awuku and Nenes*, 2007; *Asa-Awuku et al.*, 2010, 2008; *Engelhart et al.*, 2008; *Moore et al.*, 2008; *Padró et al.*, 2010). The fast time response and ease of setting up SMCA are attractive features, especially if measurements are to be carried out in polluted environments and the laboratory (where counting statistics are most favorable for rapid measurements). SMCA can also be used to study the size-resolved CCN activity in clean environments, at the expense of some temporal (or size) resolution. Finally, SMCA can be applied to commercial SMPS and CFSTGC instruments with the manufacturer-provided control software coupled with a simple post-processing routines (available for download from http://nenes.eas.gatech.edu) to align the instrument response curves, correct for multiple charges, and correct for the non-sphericity of the aerosol.

# CHAPTER IV

# KÖHLER THEORY ANALYSIS OF MARINE DISSOLVED ORGANICS

The CCN-relevant properties and droplet growth kinetics are determined for marine organic matter isolated from seawater collected near the Georgia coast. The organic matter is substantially less CCN active than $(NH_4)_2SO_4$, but droplet growth kinetics were similar. Köhler Theory Analysis (KTA) is used to determine the average organic molar masses of two samples, which are 4370±24% and 4340±18% kg kmol$^{-1}$. KTA is used to infer surface tension depression, and is in excellent agreement with direct measurements. For the first time it is shown that direct measurements of surface tension are relevant for CCN activation, and this study highlights the power of KTA.

## *4.1 Introduction*

Oceanic surface waters contain a substantial amount of dissolved organic matter (DOM) that is transferred to the aerosol phase during the process of sea spray generation. The ocean surface layer contains large amounts of surfactants (*Cavalli et al.*, 2004), which can influence the ability of marine aerosol to act as cloud condensation nuclei (CCN). Measurements of primary marine aerosol composition have observed a size-dependent enrichment of organics (particularly water-insoluble species) in submicron aerosol (*O'Dowd et al.*, 2004; *Oppo et al.*, 1999). Despite their potential importance, the CCN-relevant properties of marine organics are largely unknown. This is because DOM is difficult to isolate, as its concentration in bulk seawater is orders of magnitude lower than inorganic salts (*Ogawa*

This chapter published as: Moore, R. H., E. D. Ingall, A. Sorooshian, and A. Nenes (2008), Molar mass, surface tension, and droplet growth kinetics of marine organics from measurements of CCN activity, Geophysical Research Letters, 35, L07801, doi:10.1029/2008GL033350. 

*and Tanoue*, 2003). Recently, *Vetter et al.* (2007) developed a method to remove most of the salt in seawater samples via a combination of electrodialysis and reverse osmosis, thus enabling direct characterization of marine DOM.

Köhler Theory Analysis (KTA, *Padró et al.*, 2007) is a technique to infer the molar volume, surfactant characteristics, and droplet growth kinetics of organic aerosol constituents, all of which are important for linking organic aerosol with cloud formation. KTA has been previously evaluated for aerosol composed of $C_3$-$C_9$ organics mixed with $(NH_4)_2SO_4$ (*Padró et al.*, 2007), for water-soluble organics in biomass burning aerosol (*Asa-Awuku et al.*, 2008), and for secondary organic aerosol formed from the ozonolysis of biogenic volatile organic carbon (*Asa-Awuku et al.*, 2010). *Asa-Awuku et al.* (2010) first extended KTA to infer surface tension as well, which is useful when sample size prohibits direct measurement of surface tension; this aspect of KTA is further developed here.

In this study, we measure the CCN-relevant properties of marine DOM and then use KTA to infer its average molar mass and surface tension depression characteristics. The potential impact of marine surfactants on droplet growth kinetics is also explored. To evaluate KTA, inferred values of surface tension are compared against direct measurements using the pendant drop technique.

## *4.2 Experimental*

### 4.2.1 Sample Collection

Seawater samples were collected near the Georgia Coast on board the Research Vessel Savannah during an October 2006 research cruise in the Atlantic Ocean. 200-l samples from the Gulfstream current (31°32.5'N, 79°13.8'W, 84 m depth) and the Ogeechee River estuary (31°56.6'N, 81°9.1'W, 2 m depth) were collected in Niskin bottles and filtered to remove suspended particulates greater than 0.45 $\mu$m with a polypropylene filter. The estuarine sample was collected under tidal conditions. Inorganic salt concentrations were similar in both samples ($3.7\times10^4$ ppm in the Gulfstream sample and $3.1\times10^4$ ppm in the

estuarine sample); however, more organics were initially present in the estuarine sample than the Gulfstream sample (4.36 ppm and 0.95 ppm, respectively).

The DOM in each sample was subsequently concentrated using the electrodialysis/reverse osmosis (ED/RO) technique of *Vetter et al.* (2007). In this method, ED is first used to remove the majority of the inorganic salts and is followed by RO to remove excess water. This cycle is repeated until a desired concentration of DOM is attained, after which the sample is freeze-dried. Typical DOM recoveries range from 64-93% (*Vetter et al.*, 2007), and water conductivities were reduced by over 99.98%. During the process, all $Cl^-$ is depleted, and the remaining inorganic fraction is primarily $Na_2SO_4$ and $(NH_4)_2SO_4$.

### 4.2.2 Chemical Composition of Samples

The water-soluble organic carbon (WSOC) content of both samples was measured with a total organic carbon (TOC) analyzer (Sievers Model 800 Turbo). Additionally, inorganic ions ($SO_4^{2-}$, $Cl^-$, $NO_3^-$, $Na^+$, $NH_4^+$, $Ca^{2+}$, $Mg^{2+}$, and $K^+$) were measured using a dual ion chromatography (IC) system (Dionex ICS-2000). TOC concentrations of the Gulfstream and estuarine dry samples are 0.111 kgC $kg^{-1}$ and 0.249 kgC $kg^{-1}$, respectively. From the IC measurements, the major inorganic species present in the DOM extract are $Na_2SO_4$ and $(NH_4)_2SO_4$. The solution pH is neutral, suggesting that the organics do not substantially dissociate.

### 4.2.3 Surface Tension Measurements

Surface tension measurements were performed using the pendant drop method with a KSV CAM 200 goniometer. Each droplet was allowed to equilibrate for 20-30 seconds, allowing sufficient time for organics to partition between the bulk and surface layers (*Taraniuk et al.*, 2007). The droplet shape was fit to the Young-Laplace equation to obtain the surface tension, $\sigma$, at the liquid-air interface. The temperature (approximately 297 K) was monitored throughout each set of measurements using a 50 k$\Omega$ thermistor (Digikey ERT-D2FHL503S). Seven pendant drops were photographed at ten frames per second for each

surface tension measurement.

Multiple solutions of each sample (done by preparing ∼2000 ppm samples, which are successively diluted down to 100 ppm) were prepared to determine $\sigma$ as a function of dissolved carbon concentration, $C$. The data are fit to the Szyskowski-Langmuir (SL) adsorption isotherm (*Langmuir*, 1917):

$$\sigma = \sigma_w - \alpha T \ln(1 + \beta C) \tag{4.1}$$

where $\sigma_w$ is the surface tension of water (i.e., an "infinite dilution" sample), $T$ is the absolute temperature, and $\alpha$ and $\beta$ are empirical constants obtained from least-squares fits to the data. While the SL isotherm is an adsorption model for one compound, it is able to model the complex DOM/salt system reasonably well (Figure 4.2). $\alpha$ and $\beta$, were determined to be 2.952 mN m$^{-1}$ K$^{-1}$ and $2\times10^{-6}$ l mg$^{-1}$.

### 4.2.4 CCN Activity and Droplet Growth Kinetics Measurements

The experimental setup used for CCN activity measurements is described in detail elsewhere (e.g., *Asa-Awuku et al.*, 2008; *Padró et al.*, 2007). Aerosol is generated by atomizing an aqueous solution of each of the seawater samples. The particles are dried and introduced into a scanning mobility CCN analyzer (SMCA, *Moore et al.*, 2010), for characterization of size-resolved CCN activity and growth kinetics. SMCA uses a differential mobility analyzer (DMA, TSI 3081), operating in voltage-scanning mode, to classify the aerosol. The monodisperse stream is then introduced simultaneously into a Droplet Measurement Technologies Continuous-Flow Streamwise Thermal Gradient CCN Counter (DMT-STGC, *Roberts and Nenes*, 2005) and a condensation particle counter (CPC, TSI 3022). The time-series of the DMT-STGC and CPC counts are inverted to obtain curves of CCN/CN as a function of mobility diameter (while maintaining instrument supersaturation at a constant value). The dry diameter, $d_p$, for which 50% of particles are activated (neglecting multiply-charged particles) represents the aerosol that activates at the instrument supersaturation, $s_c$.

The DMT-STGC uses an optical particle counter (OPC) to obtain the size distribution of activated droplets exiting the instrument column.

The CCN activity of aerosol containing the estuarine sample and a known amount of added $(NH_4)_2SO_4$ was also measured in order to see if a "salting out" effect could be observed. The effect occurs at relatively high electrolyte concentrations ($\sim$50 wt%, dry concentration), when the salts enhance surfactant partitioning to the droplet surface, dramatically reducing the surface tension and increasing the CCN activity (*Asa-Awuku et al.*, 2010). Two samples were prepared to total salt concentrations of approximately 60 and 90 wt%. The 60 wt% salt sample was also used as an independent mixture to infer molar mass and surface tension depression.

For all CCN measurements, the flow rate of air through the column was maintained at 0.5 l $min^{-1}$ (10:1 sheath-to-aerosol ratio), which corresponds to a residence time of 15 seconds. The DMT-STGC instrument supersaturation was varied from 0.2% to 1.4%.

## *4.3 Results and Discussion*

### 4.3.1 CCN Activity

The CCN activation curves for both samples and pure $(NH_4)_2SO_4$ are shown in Figure 4.1. For a CCN composed of soluble non-surfactant compounds, Köhler theory suggests that the "critical supersaturation", $s_c$, scales with $d_p$ to the $-3/2$ power (*Köhler*, 1936). However, for aerosol containing surfactants, this scaling will change, tending to be lower at smaller $d$ and approaching $-3/2$ at larger $d$. This is because at smaller particle diameters, the high concentration of WSOC depresses $\sigma$, which lowers $s_c$ more than would be expected from the solute effect alone; at larger $d$, the WSOC concentration is insufficient to induce this effect (*Padró et al.*, 2007).

The activation curve of the Gulfstream sample aerosol (blue circles) is almost identical to $(NH_4)_2SO_4$ (yellow triangles), despite the presence of $\sim$40 wt% surface-active DOM. It is likely that the surface tension depression from the organic fraction compensates for the

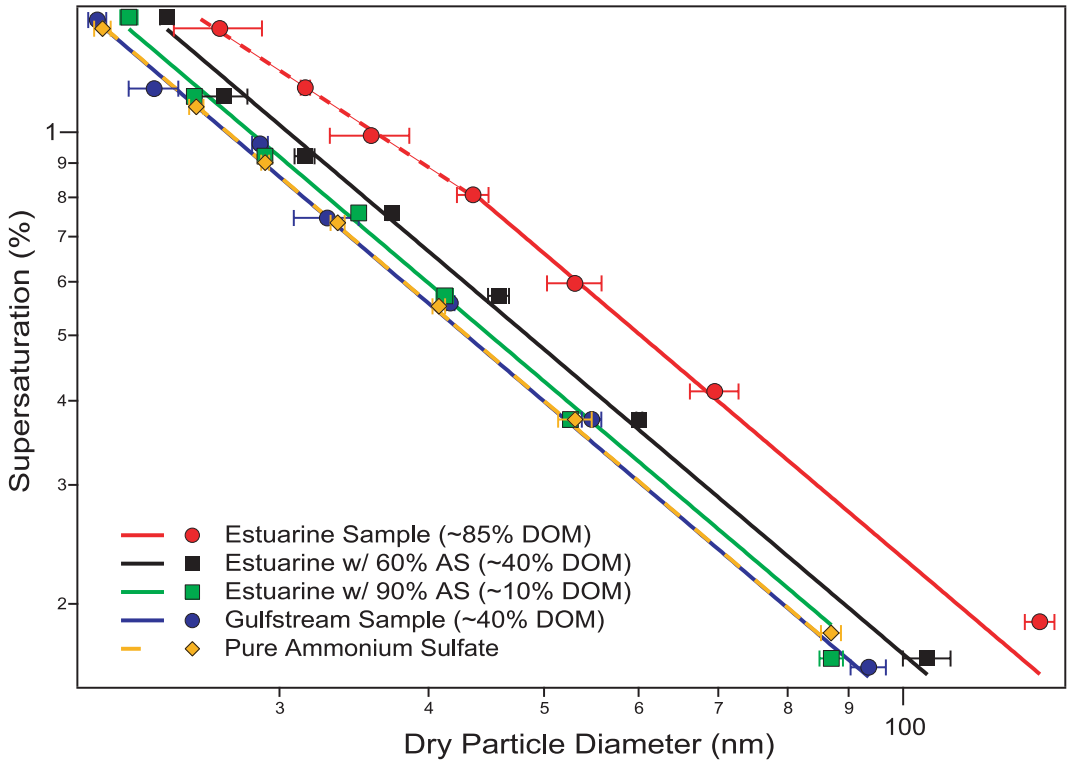


**Figure 4.1:** Critical supersaturation versus dry particle diameter for all samples considered.

decreased soluble mole fraction. The estuarine sample aerosol contains ∼85 wt% organic matter and is much less CCN active than $(NH_4)_2SO_4$ (red circles in Figure 4.1). Additionally, the activation curve deviates from the $-3/2$ exponential power law fit (as indicated by the dotted line) at low dry particle diameters and high $s_c$, where the concentration of organic matter is high enough to significantly affect the droplet surface tension ($C > 1000$ mg $l^{-1}$, from Figure 4.2).

### 4.3.2 Köhler Theory Analysis (KTA)

The organic molar mass and surface tension depression were inferred from the CCN activity measurements using KTA, method $b_2$ (*Padró et al.*, 2007; *Asa-Awuku et al.*, 2008, 2010). For each $s_c/d_p$ measurement, the fitted CCN activity (FCA) parameter, $\omega$, is calculated from

$$\omega = s_c d_p^{3/2} \tag{4.2}$$

KTA entails expressing FCA in terms of its constituents, assuming the aerosol is composed of N components (*Padró et al.*, 2007):

$$\omega = 2\left(\frac{4M_w\sigma}{3RT\rho_w}\right)^{3/2}\left[\sum_{i=1}^{N}\left(\frac{\rho_w}{M_w}\right)\left(\frac{M_i}{\rho_i}\right)\frac{1}{\varepsilon_i\nu_i}\right]^{1/2} \tag{4.3}$$

where $M_w$, $\rho_w$ are the molar mass and density of water, respectively, $R$ is the universal gas constant, and $M_i$, $\rho_i$, $\varepsilon_i$, $\nu_i$ are the molar mass, density, volume fraction, and effective van't Hoff factor of component $i$, respectively. Denoting the organic fraction as component "$j$" and rearranging Equation 4.3 to solve explicitly for $M_j$ and $\sigma$ yields

$$M_j = \frac{\rho_j\varepsilon_j\nu_j}{\frac{256}{27}\left(\frac{M_w}{\rho_w}\right)^2\left(\frac{1}{RT}\right)^3\sigma^3\omega^{-2} - \sum_{i\neq j}^{N}\frac{\rho_i}{M_i}\varepsilon_i\nu_i} \tag{4.4}$$

$$\sigma = \left[\frac{\left(\frac{\rho_j}{M_j}\right)\varepsilon_j\nu_j + \sum_{i\neq j}^{N}\frac{\rho_i}{M_i}\varepsilon_i\nu_i}{\frac{256}{27}\left(\frac{M_w}{\rho_w}\right)^2\left(\frac{1}{RT}\right)^3\omega^{-2}}\right]^{1/3} \tag{4.5}$$

$\sigma$ corresponds to the value at activation, and the surfactant carbon concentration is given by (*Padró et al.*, 2007),

$$C_{act} = \frac{27}{8}x_{c,j}\varepsilon_j\rho_j\frac{d_p^3 s_c^3}{A^3} \tag{4.6}$$

where $A = \frac{4M_w\sigma}{RT\rho_w}$ and $x_{c,j} = 0.29$ is the mass fraction of carbon in the DOM, estimated from the Redfield ratio (C:N:P = 106:16:1) (*Schulz and Zabel*, 2006; *Redfield et al.*, 1963). In applying Equations 4-6, we assume an organic density, $\rho_j$, of 1400 kg m$^{-3}$ (*Schulz and Zabel*, 2006), an effective van't Hoff factor of 1 for the organics (*Dinar et al.*, 2007), and 2.5 for $(NH_4)_2SO_4$ and $Na_2SO_4$ (*Padró et al.*, 2007).

To compute $M_j$ and $\sigma$ from KTA, the following procedure is used: First, the average organic molar mass, $M_j^*$, is estimated for each $s_c/d_p$ pair (Equation 4.4) initially assuming the surface tension of pure water. Equations 4.5 and 4.6 are used to estimate $\sigma$ for the $s_c/d_p$ data of the sample plus 60% $(NH_4)_2SO_4$. The updated $\sigma$ values are used to reevaluate $M_j^*$

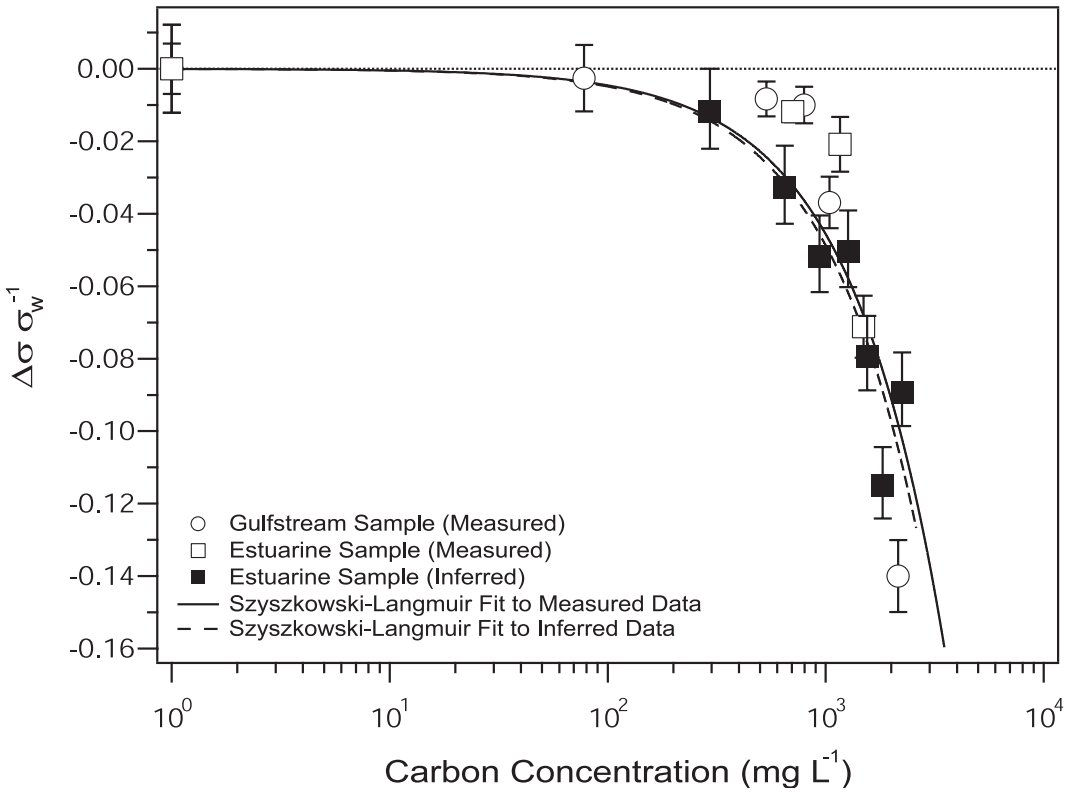


**Figure 4.2:** Fractional surface tension depression with respect to pure water. Shown are direct measurements (open symbols) and values inferred from KTA (closed symbols).

and this process is iterated until the $\sigma$ and $M_j^*$ values converge. This procedure allows the concurrent inference of $M_j$ and $\sigma$ (as a function of WSOC concentration) from the CCN activity data alone.

$M_j$ is estimated to be 4370±26% kg kmol$^{-1}$ and 4340±6% kg kmol$^{-1}$ for the Gulfstream and estuarine samples, respectively, (the reported uncertainty is one standard deviation from the mean $M_j$ over all $s_c/d_p$ pairs). The sensitivities of $M_j$ to each of the independent parameters is computed with the method of *Padró et al.* (2007) (Table 4.1). Using this method, the total estimated uncertainties of $M_j$ for the estuarine and Gulfstream samples are 18% and 24%, respectively. As expected, the Gulfstream sample uncertainty exceeds the estuarine sample uncertainty, since the lower organic mass increases the $M_j$ sensitivity to most of the independent parameters (*Padró et al.*, 2007).

Both molar masses are consistent with each other and fall in the mid-range of the

**Table 4.1:** Molar mass uncertainty, $\Delta M_j$, from parameter uncertainty, $\Delta x$, for the estuarine (Gulfstream) samples.

| | $\omega(\mathrm{m}^{3/2})$ | $\rho_j$ (kg m$^{-3}$) | $\nu_j$ | $x_{c,j}$ (%) |
|---|---|---|---|---|
| Base $x$ Value | | 1400 | 1 | 0.29 |
| $\Delta x$ | 1.47(2.16) $\times 10^{-15a}$ | 400[b] | 0.2[c] | 0.044[b] |
| $\Delta M_j$, % | 3.7 (6.9) | 10 (17) | 0.2 (0.1) | 15 (16) |
| Total molar mass uncertainty, % | | | | 18 (24) |

[a] One standard deviation from the mean FCA value.

[b] *Schulz and Zabel* (2006)

[c] *Dinar et al.* (2007)

high molar-mass fraction that comprises 30-35% of the marine surface DOM (*Ogawa and Tanoue*, 2003). The inferred $M_j$ is also consistent with that of a theoretical Redfield-based molecule, $(CH_2O)_{106}(NH_3)_{16}H_3PO_4$ (*Schulz and Zabel*, 2006). While most of the DOM is recovered, it is expected that the small amount of DOM not recovered during the ED/RO process would be low-molar-mass species that can permeate the ED membranes easiest; therefore, higher molar-mass DOM in the sample may be enriched in the process and the $M_j$ of the sample (and hence, that inferred using KTA) may be greater than $M_j$ of in-situ marine DOM.

The inferred $\sigma$ is in excellent agreement with the SL fit to direct measurements (Figure 4.2). The agreement is still excellent if other functions for fitting the data are used; the variability in inferred $M_j$ remains within the reported uncertainty (not shown). Since the inferred values are derived independently of the direct measurements, their agreement shows conclusively that diffusion of surface-active molecules to the droplet surface is sufficiently rapid to achieve equilibrium surface tension depression. *Taraniuk et al.* (2007) and *Asa-Awuku and Nenes* (2007) showed that humic-like organic species ($\sim$500 kg kmol$^{-1}$) in growing droplets are in equilibrium; we find this to apply for marine DOM with a tenfold higher molar mass (hence, $\sim \sqrt{10}$ times lower diffusivity). The latter finding is consistent

with the analysis of *Asa-Awuku and Nenes* (2007), as a diffusivity of $2\times10^{-10}$ ($= \frac{6\times10^{-10}}{10^{1/2}}$, with $6\times10^{-10}$ being the diffusivity of HULIS, *Taraniuk et al.*, 2007) implies that the organic concentration at the droplet surface is more than 90% of its equilibrium value for the supersaturation range considered here.

While the inferred and measured surface tension agree, the surfactants require tenfold higher concentrations to give the same effect as organics isolated from marine aerosol (*Cavalli et al.*, 2004). This difference reflects the enrichment of marine aerosol in organic surfactants from the process of bubble bursting. Hence, the samples investigated here are representative of natural marine DOM, but should be interpreted as the lower limit of CCN activity of primary marine organic aerosol.

### 4.3.3 Droplet Growth Kinetics

The mean droplet sizes for each sample measured by the DMT-STGC OPC at varying values of $s_c$ are shown in Figure 4.3. All samples studied exhibit growth similar to that of pure $(NH_4)_2SO_4$ for most supersaturations. For the three middle supersaturations (0.6%, 0.8%, and 1.0%) it appears that both seawater samples grow to larger droplet sizes than for pure $(NH_4)_2SO_4$. Since it is not expected that organics would enhance droplet growth, the observed discrepancy may be caused by slight shifts in the laser scattering during the sizing measurement, resulting from the presence of a compressed film. $(NH_4)_2SO_4$ growth could also be depressed because of water vapor depletion in the column during the calibrations; however, this is unlikely since the total CCN concentrations were relatively low ($\sim$500 $cm^{-3}$) and constant for all supersaturations. Laser shifts over long time periods are unlikely, as the results are reproducible. The data suggest that the dissolved organics, compared to pure $(NH_4)_2SO_4$, do not significantly alter the droplet growth kinetics (i.e., the water vapor mass transfer coefficient).

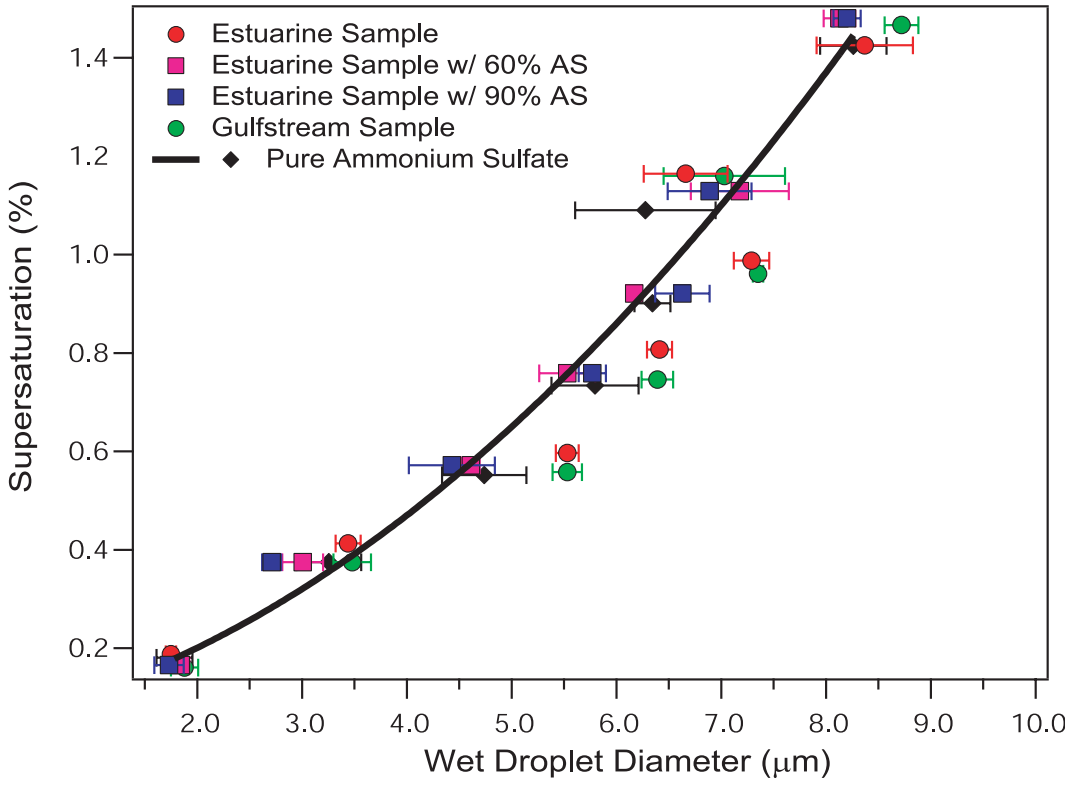


**Figure 4.3:** Activated droplet sizes for CCN with $S_c = S_{instrument}$.

## *4.4 Summary and Conclusions*

In this study, measurements of CCN activity, droplet growth kinetics, and WSOC/ionic composition of marine DOM were used to infer its CCN-relevant properties. Köhler Theory Analysis (KTA) determined the molar masses of the organic matter in the Gulfstream sample and estuarine sample to be 4370±24% and 4340±18%, respectively. This is consistent with the high-molar-mass marine DOM typically found in surface ocean waters. KTA was used to infer the organic surface tension depression, and was found to be in excellent agreement with direct measurements using the pendant drop technique. This shows that very large organic molecules are able to diffuse to the surface of a growing droplet and establish an equilibrium surface tension depression; in fact, direct equilibrium surface tension measurements adequately describe droplet surface tension at activation. Furthermore, KTA is proven to be a powerful technique that can be used to infer organic surface tension

depression using small amounts of aerosol generated from a dilute solution. Finally, while the dissolved organics form compressed surface films that can substantially change surface tension, they exhibited similar growth to pure $(NH_4)_2SO_4$.

# CHAPTER V

# HYGROSCOPICITY AND COMPOSITION OF ALASKAN ARCTIC CCN

This chapter presents a comprehensive characterization of cloud condensation nuclei (CCN) sampled in the Alaskan Arctic during the 2008 Aerosol, Radiation, and Cloud Processes affecting Arctic Climate (ARCPAC) project, a component of the POLARCAT and International Polar Year (IPY) initiatives. Four distinct air mass types were sampled including relatively pristine Arctic background conditions as well as biomass burning and anthropogenic pollution plumes. Despite differences in chemical composition, inferred aerosol hygroscopicities were fairly invariant and ranged from $\kappa$ = 0.1-0.3 over the atmospherically-relevant range of water vapor supersaturations studied. Analysis of the individual mass spectral *m/z* 43 and 44 peaks show the organic aerosols sampled to be well-oxygenated, consistent with long-range transport and aerosol aging processes. However, inferred hygroscopicities are less than would be predicted based on previous parameterizations of biogenic oxygenated organic aerosol, suggesting an upper limit on organic aerosol hygroscopicity above which $\kappa$ is less sensitive to the O:C ratio. Most Arctic aerosol act as CCN above 0.1% supersaturation, although the data suggest the presence of an externally-mixed, non-CCN-active mode comprising approximately 0-20% of the aerosol number. CCN closure was assessed using measured size distributions, bulk chemical composition measurements, and assumed aerosol mixing states; CCN predictions tended toward over-prediction, with the best agreement ($\pm$ 0-20%) obtained by assuming the aerosol to be

This chapter published as: Moore, R. H., R. Bahreini, C. A. Brock, K. D. Froyd, J. Cozic, J. S. Holloway, A. M. Middlebrook, D. M. Murphy, and A. Nenes (2011), Hygroscopicity and composition of Alaskan Arctic CCN during April, 2008, Atmospheric Chemistry and Physics Discussions, 11, 21789-21834, doi:10.5194/acpd-11-21789-2011. 

externally-mixed with soluble organics. Closure also varied with CCN concentration, and the best agreement was found for CCN concentrations above 100 $cm^{-3}$ with a 1.5- to 3-fold overprediction at lower concentrations.

## *5.1 Introduction*

The Arctic is particularly sensitive to climatic changes because of the complex feedbacks between surface temperature and surface albedo, among other factors. Trace gas and aerosol species have the potential to modify this feedback through their interaction with shortwave and longwave radiation, and, are thus, an important area of active research. A number of long-term measurements around the Arctic have indicated that these species vary seasonally, and their concentrations peak during late winter and early spring when mid-latitude anthropogenic pollution is transported northward and injected into the vertically-stratified springtime Arctic atmosphere (*Quinn et al.*, 2007; *Shaw*, 1995).

Termed "Arctic haze", these pollution layers can persist for days or weeks and have been attributed mostly to anthropogenic sources in northern Europe and Asia (*Law and Stohl*, 2007). Recent work indicates that biomass burning emissions may contribute more to the haze layers than previously thought (*Warneke et al.*, 2010; *Quinn et al.*, 2008a; *Stohl et al.*, 2007, 2006), possibly because industrial emissions contributing to the haze have steadily decreased over past decades (*Quinn et al.*, 2007), or because of improved instrumental capabilities for detecting and attributing the biomass burning contribution.

Aerosol species can impact the Arctic energy balance directly by absorbing and scattering sunlight, and also indirectly, through their ability to act as cloud condensation nuclei (CCN) and modify cloud properties. It is known that increased CCN loadings produce more numerous, and smaller cloud droplets, which reflect more incoming shortwave, solar radiation back into space, thereby cooling the Earth's surface (*Twomey*, 1977a). However, it has been suggested by a number of studies that this cooling effect is more than offset in the Arctic by changes in longwave cloud emissivity (*Alterskjær et al.*, 2010; *Garrett and Zhao*,

2006; *Lubin and Vogelmann*, 2006; *Shupe and Interieri*, 2004; *Garrett et al.*, 2002). This is because of decreased solar insolation during the Arctic winter-spring and because low-level Arctic clouds tend to be diffuse and optically-thin. Additionally, the high albedo of surface snow and ice limits the potential cooling associated with light scattering from these clouds. Smaller cloud droplets also inhibit ice crystal riming and droplet collision-coalescence processes, which increase the cloud lifetime against precipitation (*Lance et al.*, 2011; *Borys et al.*, 2003, 2000; *Albrecht*, 1989). Thus, accurate in-situ observations of aerosol and cloud properties are essential for models to account for these "indirect effects" of aerosols on Arctic clouds and climate.

In past decades, measurements of CCN have been made on a variety of ground-based and airborne platforms throughout the Arctic by exposing particles to a specified water vapor supersaturation and counting the number of droplets that are formed. *Hoppel et al.* (1973) used a thermal-gradient diffusion cloud chamber to measure vertical profiles of CCN above the Yukon Valley, approximately 100 miles north of Fairbanks, Alaska, during February. A distinct vertical gradient was observed and CCN concentrations were found to increase by about a factor of three above 2-km altitude (from $\sim$100 CCN cm$^{-3}$ near the surface) and exhibited increased sensitivity to supersaturation.

*Shaw* (1986) performed CCN measurements of episodic Arctic haze in central Alaska during January-February, also using a thermal diffusion chamber, and found that particles behaved like soluble salts, with approximately 10-30 CCN cm$^{-3}$ measured at $\sim$ 0.3-0.5% supersaturation.

*Hegg et al.* (1995) studied CCN during seven research flights in April, 1992, which were conducted 350 km north of Alaska during the Arctic Leads Experiment (LEADEX). CCN concentrations were generally less than 100 cm$^{-3}$ with a mean of 47 $\pm$ 19 cm$^{-3}$, while the Aitken mode particle concentration varied from 135 to 4600 cm$^{-3}$. Most aerosols did not act as CCN even at 1% supersaturation (the mean CCN-active fraction was 0.15 $\pm$ 0.08). This unexpectedly-low CCN-active fraction was attributed to the prevalence of

smaller, Aitken mode particles. Concurrent $SO_4^{2-}$ measurements did not correlate with CCN concentrations at 0.3% supersaturation (r=0.046), but improved at 1% supersaturation (r=0.640), suggesting that the sulfate was present in the smaller particles.

*Hegg et al.* (1996) made measurements of aerosol size, volatility, and CCN activity near Prudhoe Bay, Alaska, during June, 1995. At 1% supersaturation, they found mean CCN concentrations of 0 to 178 $cm^{-3}$, corresponding to CCN-active fractions of around 0.10, similar to those of *Hegg et al.* (1995). The CCN-active fraction was found to correlate weakly with the aerosol mass fraction volatile at 320°C (e.g., sulfate and organic species), suggesting that compositional effects were important in modulating CCN concentrations (*Hegg et al.*, 1996).

*Bigg and Leck* (2001) measured CCN from an icebreaker in the central Arctic Ocean during July to September using a CCN-remover-type instrument (*Ji et al.*, 1998), and found CCN concentrations of 1-1000 $cm^{-3}$ at 0.25% supersaturation, with median daily concentrations of 15-50 $cm^{-3}$. The highest concentrations were observed over open water and were reduced to less than 200 $cm^{-3}$ after 24 hrs. transport over the ice pack. Assuming that all particles were composed of ammonium sulfate generally overpredicted CCN concentrations by 30%. Single-particle electron microscopy indicated that the majority of particles were internally-mixed, but also showed the presence of organic species or other non-hygroscopic, non-volatile aerosol inclusions that likely led to the overprediction bias.

*Yum and Hudson* (2001) measured the vertical distribution of CCN concentrations (0.04-0.8% superaturation) approximately 500 km north of the Alaskan coast as part of the Arctic Clouds Experiment (ACE) and Surface Heat Budget of the Arctic Ocean (SHEBA) projects in May, 1998. They found that both CCN and CN increased with altitude, on average, from less than 100 $cm^{-3}$ in the boundary layer to 150-200 $cm^{-3}$ aloft. Average CCN concentrations at all altitudes increased from roughly 10 $cm^{-3}$ at 0.02% supersaturation to 100 $cm^{-3}$ at 0.1% supersaturation and 200-300 $cm^{-3}$ at 0.8% supersaturation, and the

authors attributed the relatively high CCN-active fraction of 0.63 and the slope of the CCN-supersaturation spectrum as indicative of aged aerosol with few small particles (*Yum and Hudson*, 2001), in contrast to the prevalent small particles and low CCN activation ratios observed by *Hegg et al.* (1995).

More recently, *Kammermann et al.* (2010) measured summertime CCN and aerosol hygroscopic growth during the Abisco campaign at the Stordalen mire, Sweden, and saw CCN concentrations ranging from 30-700 $cm^{-3}$ with mean CCN-active fractions of 7-27% at 0.1-0.7% supersaturation. Inferred values of the hygroscopicity parameter, $\kappa$ (*Petters and Kreidenweis*, 2007), obtained from the CCN measurements, were found to range from 0.07 at the highest supersaturation to 0.21 at the lowest supersaturation. CCN concentration closure was assessed by using $\kappa$ values obtained from the hygroscopic growth measurements to predict CCN, and agreement was typically achieved to within $\pm 11\%$.

In summary, measurements of Arctic CCN over the past decades have found concentrations to be highly variable, in part due to seasonal changes, but typically on the order of a few tens to hundreds of CCN $cm^{-3}$, which constitute only 7-63% of total particles present even at supersaturations as high as 0.7-1%. Both CCN and total particle concentrations have been observed to increase with altitude, underscoring the need for additional airborne studies to complement surface measurements. Additionally, the aerosol mixing state remains poorly-characterized with some limited evidence for size-variant aerosol chemistry and the presence of a small non-hygroscopic aerosol mode.

In this paper, we present observations of the CCN activity and hygroscopic properties of Arctic aerosol sampled during Spring 2008 and quantify the uncertainty in CCN predictions based on simplified models of aerosol mixing state and chemical composition relevant for global climate models. We also examine the relationship between aerosol hygroscopicity and oxidation state. It has been suggested that more-oxidized organic aerosol are more hygroscopic (*Jimenez et al.*, 2009), and we explore this relationship in the context of well-aged, Arctic air masses.

## *5.2 Observational Data Set*

### 5.2.1 Study Location

An extensive description of the ARCPAC mission and aerosol instrumentation is given by *Brock et al.* (2011a), so only a brief summary is included here. Measurements were made aboard the National Oceanic and Atmospheric Administration WP-3D aircraft based out of Fairbanks, AK (64° 48' 54" N, 147° 51' 23" W). A total of eight research flights were conducted from April 3rd-23rd, 2008, including two transit flights into and out of Alaska. We restrict our analysis, here, to five of the research flights conducted entirely within the Alaskan Arctic (April 12th, 15th, 18th, 19th, and 21st). As described by *Brock et al.* (2011a), these flights extended from western Alaska near Nome, northeast to the Beaufort Sea, and intercepted four distinct types of air masses (background, biomass burning plumes, anthropogenic pollution plumes, and pristine air in the Arctic boundary layer), which will be discussed in detail in Section 5.3.1. A map of the flight tracks is shown in Figure 5.1.

### 5.2.2 Chemical Composition Measurements

Mass loadings of non-refractory, sub-micron aerosol species were obtained from a compact time-of-flight aerosol mass spectrometer (C-ToF-AMS) with a pressure-controlled inlet (*Bahreini et al.*, 2008; *DeCarlo et al.*, 2006; *Drewnick et al.*, 2005). The C-ToF-AMS focuses the sample aerosol stream into a narrow beam, which is impacted on a hot plate. Particles are vaporized and ionized before being detected with a compact time of flight mass spectrometer. The instrument was operated in either "particle time of flight" mode or in "mass spectrum" mode. In the former mode, the narrow particle beam is periodically interrupted by a rotating chopper, and the particle time-of-flight across the vacuum chamber is detected and related to size. Size-resolved mass distributions were averaged to five-minute intervals to improve counting statistics. In the latter mode, the chopper is alternated in and out of the beam line so that the differential mass spectrum is obtained at 0.1

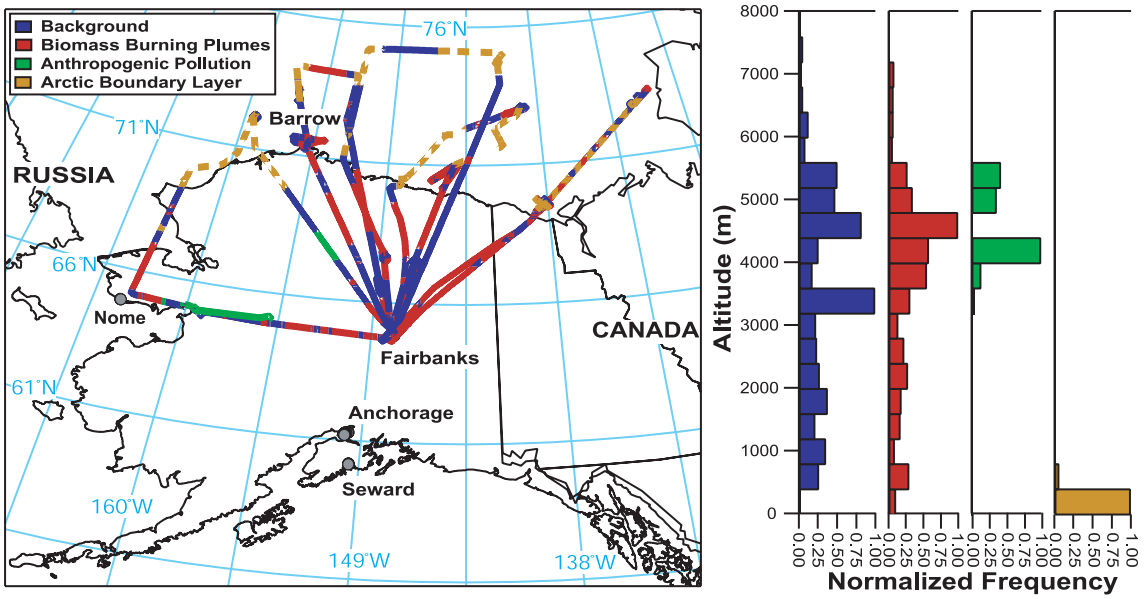


**Figure 5.1:** (Left) Aircraft trajectories for the research flights on April 12th, 15th, 18th, 19th, and 21st, colored by air mass type. Due to vertical profiling, some air mass types overlap. (Right) Vertical profiles showing the altitudes at which each air mass type was frequently encountered.

Hz with good counting statistics, but for the entire particle size distribution. Mass loadings for sulfate, nitrate, ammonium, and organic aerosol constituents were then calculated from the mass spectra following the procedure of *Allan et al.* (2003), with relative uncertainties of $\pm$34-38% (*Bahreini et al.*, 2009).

The C-ToF-AMS provides information about the mass fraction of non-refractory chemical constituents, but gives relatively little information on refractory aerosol (e.g., sea salt, mineral dust, elemental carbon) and the aerosol mixing state. Such information is obtained using a particle analysis by laser mass spectrometry (PALMS) instrument (*Murphy et al.*, 2006; *Thomson et al.*, 2000). The PALMS instrument ablates and ionizes single particles (0.15-0.75 $\mu$m diameters) using a laser, and analyzes the resulting ions with a time-of-flight mass spectrometer. The positive- or negative-ion mass spectral patterns of each particle are then used to classify the particle as one of six different compositional types according to the dominant constituent in each particle. The compositional types are biomass/biofuel, sulfate/organic, sea salt, mineral dust, elemental carbon, and unclassified. The unclassified

compositional type refers to particles that could not be identified by the automated data processor, although subsequent inspection of these spectra showed them to be consistent with the distribution of other particle types. In addition, elemental carbon was found to constitute less than 1% of particle number. Consequently, we neglect the unclassified and elemental carbon particle type categories in this analysis. Particle number concentrations of each type were computed with a 60-second resolution and an estimated uncertainty of 15%, relative.

### 5.2.3 Particle Size Distribution Measurements

Dry particle size distribution measurements (0.003 to 8.3 $\mu$m diameters) were obtained at 1 Hz from a white-light optical particle counter (WLOPC), an ultra-high sensitivity aerosol size spectrometer (UHSAS), and a nucleation mode aerosol size spectrometer (NMASS). An impactor with 1 $\mu$m cutoff diameter was located upstream of the UHSAS. The NMASS consists of five condensation particle counters, with 0.004, 0.008, 0.015, 0.030, and 0.055 $\mu$m cutoff diameters. Fine particle size distributions (0.003 to 1 $\mu$m diameters) were then calculated by coupling these five size bins to the UHSAS distribution using a nonlinear inversion algorithm (*Brock et al.*, 2000). The calibrated uncertainty of the fine particle concentrations is approximately $\pm$ 20%, although an additional bias of 5-10% was noted during aircraft ascent and descent (*Brock et al.*, 2011a).

### 5.2.4 CCN Measurements

CCN measurements were made using a Droplet Measurement Technologies (DMT) stream-wise thermal-gradient cloud condensation nuclei counter (CCNC, *Lance et al.*, 2006; *Roberts and Nenes*, 2005), which was located downstream of the 1-$\mu$m-cutoff-diameter impactor. The CCNC consists of a cylindrical flow tube with wetted walls, on which a linear stream-wise temperature gradient is applied. Owing to the greater mass diffusivity of water vapor than the thermal diffusivity of air, a supersaturation is generated, which is maximum at the centerline of the flow tube. The supersaturation depends on the applied temperature

gradient, flow rate, pressure, and, to a lesser extent, the temperature at the instrument inlet (*Roberts and Nenes*, 2005). During ARCPAC, the instrument was operated at a constant flow rate (0.75 L $min^{-1}$) and pressure (450 hPa). A flow orifice and active control system were used to ensure that the pressure remained constant, despite changes in ambient pressure with altitude. In the rare instances when the ambient pressure decreased below 450 hPa, the instrument pressure fluctuated freely with the ambient pressure. All CCN and total particle concentration measurements during ARCPAC are reported here at standard temperature and pressure (STP, 1013 hPa and 273.15 K).

During the research flights, the CCNC instrument supersaturation was varied between 0.1% and 0.6% in a stepwise manner by changing the streamwise temperature gradient, $\Delta T$. Supersaturation, $s$, scales linearly with $\Delta T$ (at constant flow rate and pressure), and this relationship was determined using ammonium sulfate calibration aerosol and Scanning Mobility CCN Analysis (SMCA, *Moore et al.*, 2010). This technique couples the CCNC to an aerosol generation system and scanning mobility particle sizer (SMPS). Ammonium sulfate aerosol are size-classified by the SMPS before being introduced into the CCNC, and particles above a critical dry diameter, $D_{p,c}$, act as CCN and are detected by the CCNC. Köhler theory (*Köhler*, 1936), is then used to determine $s$ from the measured $D_{p,c}$ for each $\Delta T$ following the procedure of *Rose et al.* (2008) and *Moore et al.* (2010). Parameters for computing the osmotic coefficient using the ion-interaction approach of *Pitzer and Mayorga* (1973) were obtained from *Clegg and Brimblecombe* (1988). The secondary activation peak associated with doubly-charged particles was removed. The effect of the width of the DMA tranfer function and particle non-sphericity were not considered; however, the error associated with these assumptions is less than 3%, relative (*Rose et al.*, 2008), which is less than the variability of $s$ from the calibrations throughout the field measurements ($\pm$0.04%, absolute). The instrument operating temperature was operated well above the ambient temperatures encountering during ARCPAC, which may cause some particles to

partially volatilize prior to activation (*Asa-Awuku et al.*, 2009); however, insufficient information was available to deduce this effect. The total uncertainty in the reported CCN number concentration derived from counting statistics and small variations in temperature, pressure, and flow rate is 7-16% for CCN concentrations above 100 $cm^{-3}$ STP, which were typical.

## *5.3 Results and Discussion*

### 5.3.1 Air Masses Sampled

During the five research flights from April 12th-21st, the WP-3D aircraft sampled aerosol from four distinct air mass types (*Brock et al.*, 2011a), characterized as:

1. *Background:* Air masses where both carbon monoxide and acetonitrile mixing ratios were less than 170 ppbv and 100 pptv, respectively, and that did not contain layers with enhanced aerosol and trace gas concentrations. Organics constitute 51% of aerosol volume, on average, with the remaining volume divided between ammonium nitrate, ammonium sulfate, ammonium bisulfate, and sulfuric acid by an average ratio of approximately 0:2.5:4:3.5, respectively.

2. *Biomass Burning Plumes:* Air masses where both carbon monoxide and acetonitrile mixing ratios were greater than 170 ppbv and 100 pptv, respectively. Often layers with enhanced aerosol and trace gas concentrations were present. Organics constitute 70% of aerosol volume, on average, with the remaining volume divided between ammonium nitrate, ammonium sulfate, ammoninum bisulfate, and sulfuric acid by an average ratio of approximately 1:4:4:1, respectively.

3. *Anthropogenic Pollution:* Air masses where the carbon monoxide mixing ratio exceeded 170 ppbv, but where the acetonitrile mixing ratio was less than 100 pptv. This case was only observed on April 15th for a short period of time. Organics constitute

40% of aerosol volume, on average, with the remaining volume divided between ammonium nitrate, ammonium sulfate, ammoninum bisulfate, and sulfuric acid by an average ratio of approximately 0:1.5:7:1.5, respectively.

4. *Arctic Boundary Layer:* Air masses over sea ice and below the inversion layer, where ozone mixing ratios were less than 20 ppbv and/or photochemically-active bromine was enhanced, indicating sea-ice surface interaction. Organics constitute 25% of aerosol volume, on average, with the remaining volume divided between ammonium nitrate, ammonium sulfate, ammoninum bisulfate, and sulfuric acid by an average ratio of approximately 0:1.2:6.4:2.3, respectively.

A detailed description of additional aerosol properties as well as the source and transport characteristics for each air mass type is given by *Brock et al.* (2011a).

Aerosol volume fractions reported above were calculated from the the C-ToF-AMS mass loadings, assuming internally-mixed aerosol, tabulated inorganic species densities, and an organic density of 1400 kg $m^{-3}$. Partitioning of the inorganic aerosol fraction between neutral and acidic sulfate species for each air mass was calculated using the molar ratio of ammonium ions to sulfate and nitrate ions, $R_{SO_4}$, and mass balance as per *Nenes et al.* (1998). Nitrate constitutes a small fraction of aerosol volume in all air mass types and is assumed to be completely neutralized. For $R_{SO_4} > 2$, the sulfate is present as ammonium sulfate, while for $1 < R_{SO_4} < 2$, the sulfate is present as a mixture of ammonium sulfate and ammonium bisulfate. Finally, for $R_{SO_4} < 1$, the sulfate is present as a mixture of ammonium bisulfate and sulfuric acid. The ion balance indicates that much of the aerosol sampled during ARCPAC is partially acidic.

Figure 5.1 shows the geographical distribution of the different air mass types sampled by the WP-3D. Background and biomass burning air masses coexist throughout northern Alaska at all altitudes sampled, but were sampled most frequently between 3.5 and 5.5 km. Only a few anthropogenic pollution plumes were intercepted at similar altitudes to the

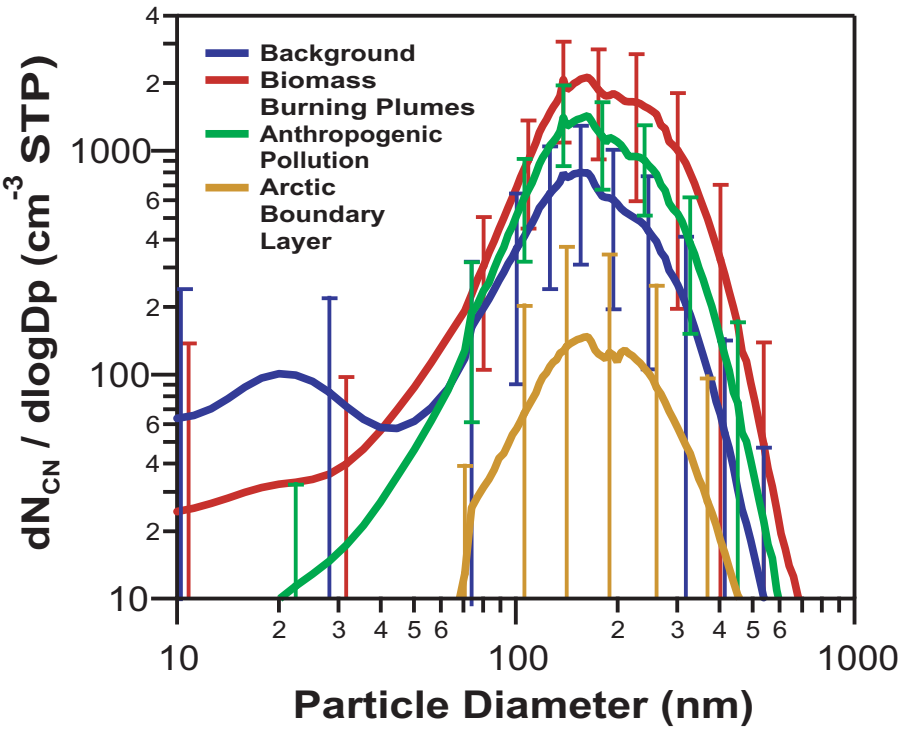


**Figure 5.2:** Average dry particle size distributions for each air mass type sampled during April 12th-21st. Error bars denote one standard deviation from the mean.

biomass burning layers. It is important to note that the sampling strategy of the aircraft is reflected somewhat in this frequency distribution, as different air masses were specifically targeted during some research flights.

The average size distributions for the air mass types are shown in Figure 5.2. Error bars denote the standard deviation in particle number concentration. The size distributions for all air mass types are dominated by the accumulation mode, with average geometric mean diameters of approximately 170 nm for all air mass types except for the biomass plumes, which were more variable ($D_g$ = 189 $\overset{\times}{\div}$ 1.19 nm) (*Brock et al.*, 2011a).

A much smaller nucleation mode ($D_g < 50$ nm) is also commonly present for the background case, but is reflected only as a very slight increase in the average concentration at smaller sizes in Figure 5.2. Although the small features at the lower end of the size

distributions ($<$ 80 nm) in Figure 5.2 may not be statistically significant due to uncertainties in the lowest NMASS size bins, the background nucleation mode remains even after averaging over the five research flights, suggesting that it is likely real. Size distributions similar to the background case have been observed previously for the springtime Arctic atmosphere at Svalbard for well-aged, continental air masses transported northward from the mid-latitudes (e.g., *Ström et al.*, 2003; *Covert and Heintzenberg*, 1993; *Heintzenberg*, 1980). Meanwhile, *Shaw* (1983, 1984) report a more significant nucleation mode for springtime Alaskan Arctic haze aerosol with concentrations on the order of those of the accumulation mode, which was also seen by *Hegg et al.* (1995) but at tenfold lower particle concentrations over the Arctic Ocean. Measurements also indicate that these Aitken and nucleation modes become increasingly dominant during the summer months as larger particles are removed via deposition and local sources become important (*Korhonen et al.*, 2008; *Heintzenberg et al.*, 2006; *Ström et al.*, 2003; *Hegg et al.*, 1996). Thus, the aerosols sampled during ARCPAC are representative of large, well-aged springtime Arctic pollution aerosol with a significant biomass burning influence. The strong biomass burning contribution even throughout the background air mass type means that while this background is representative of the Alaskan Arctic during Spring 2008, it is not necessary representative of the Arctic as a whole. In subsequent sections we evaluate the relative impacts of particle size and chemical composition on the CCN activity of these air mass types.

### 5.3.2 CCN Activity

Vertical profiles of measured CCN concentration, $N_{CCN}$, and fine particle condensation nucleus (CN) concentration, $N_{CN}$, for each air mass type are shown in Figures 5.3 and 5.4, respectively. Fine particle concentrations were generally in the range of 100-1500 cm$^{-3}$, and show little systematic dependence with altitude, except for the Arctic boundary layer air type, where $N_{CN}$ increases by a factor of four with height over the first kilometer in altitude. Particle concentrations in the biomass burning plumes generally exceeded the background

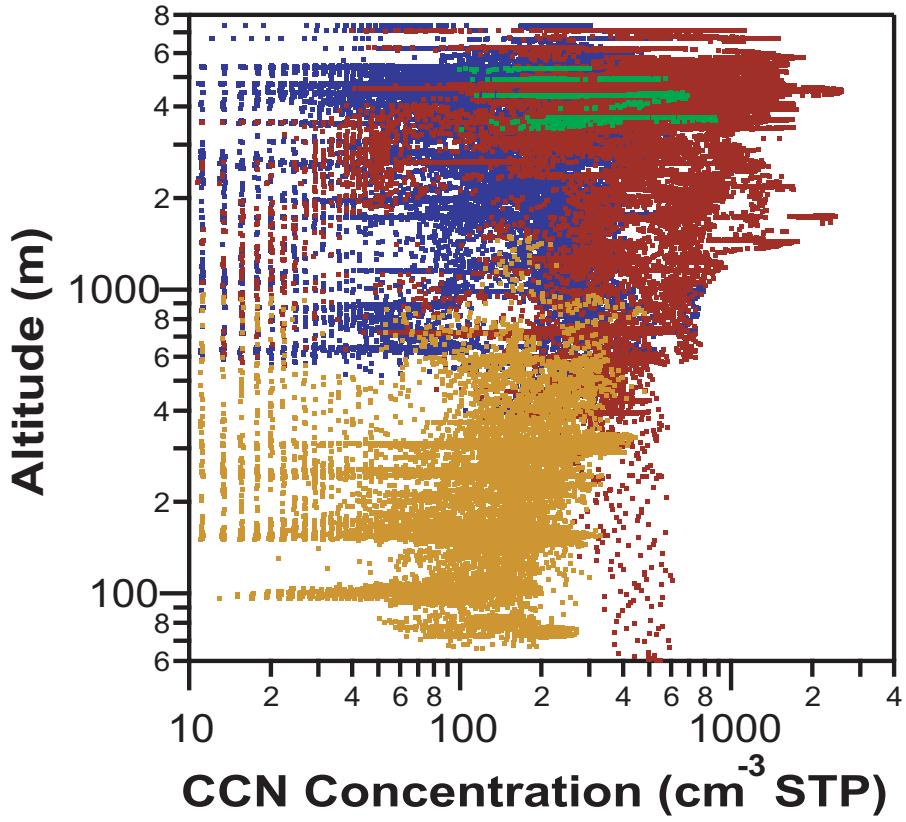


**Figure 5.3:** Vertical profiles of CCN concentrations measured during ARCPAC. Data shown are 1 Hz measurements and are color-coded by air mass type as in Figures 5.1 and 5.2.

by roughly two-fold, and even larger enhancements can be observed in layers between 1500-3000 m (April 19th) and at 4500 m (April 21st). This structure is largely reflected in the CCN concentrations, which range from a few tens of particles per cm$^3$ to concentrations on the order of $N_{CN}$. While a small amount of this variability can be attributed to the range of water vapor supersaturations studied (0.1-0.6%), low CCN concentrations were measured frequently at high supersaturations and vice versa.

As a quantitative comparison between CCN and CN, activation curves showing the fraction of CCN-active particles ($R_a = N_{CCN}/N_{CN}$), across the entire aerosol size distribution and as a function of instrument supersaturation, were computed for each air mass type and are shown in Figure 5.5. The circles and fitted trend lines in Figure 5.5 denote the median

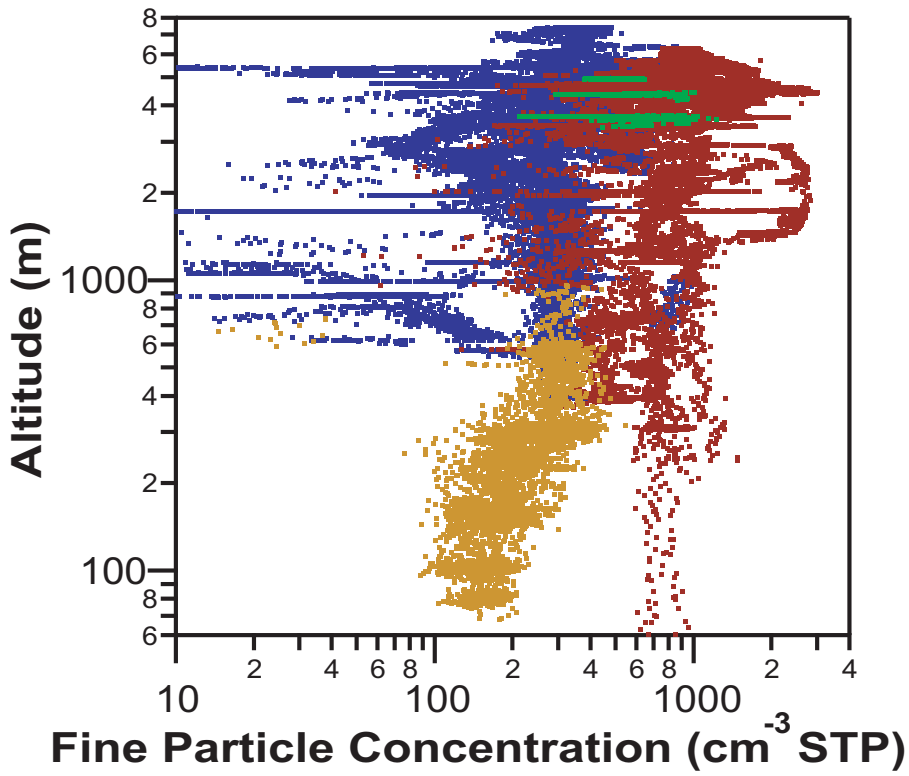


**Figure 5.4:** Vertical profiles of fine particle (CN) concentrations measured during AR-CPAC. Data shown are 1 Hz measurements and are color-coded by air mass type as in Figures 5.1 and 5.2.

activated fraction at each supersaturation, while the shaded area denotes the interquartile range. Dark, black lines denote the theoretical activated fractions calculated for constant aerosol hygroscopicity, $\kappa$, using the average size distribution for each air mass type (discussed in Section 5.3.3). It can be seen that the activation curves are very similar across air mass types with a majority of particles acting as CCN around 0.1% supersaturation. Much of the similarity of these CCN activation curves can be attributed to the similarity of the aerosol size distributions; that is, size effects are more dominant than chemical effects in determining CCN activity (*Dusek et al.*, 2006; *Twomey*, 1977b).

Compositional effects appear to become important at the 0.3-0.6% supersaturation range, where the activated fraction reaches a maximum, whose median value is less than unity. This suggests the presence of an externally-mixed, non-CCN-active aerosol fraction that

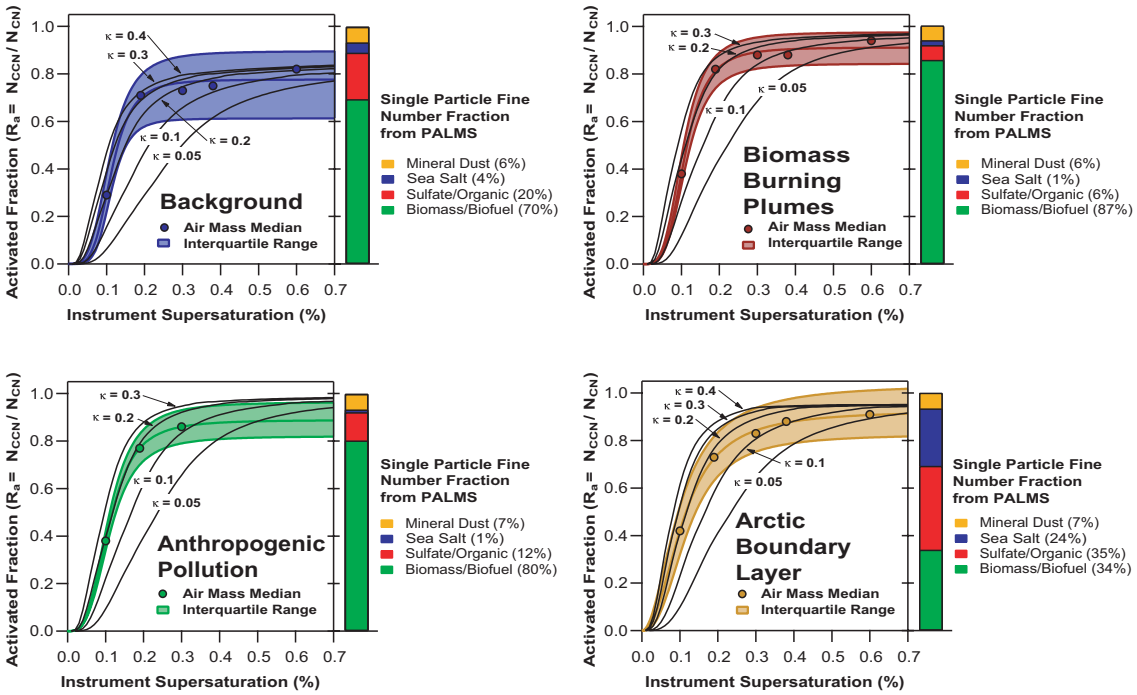


**Figure 5.5:** Median CCN activated fraction ($R_a = N_{CCN}/N_{CN}$) as a function of instrument supersaturation for each air mass sampled during April 12th-21st. Thick, colored curves are sigmoidal fits of the form $R_a = a_0/(1 + (s/a_1)^{-a_3})$, where $a_0$, $a_1$, and $a_2$ are fitting constants, and the shaded region in the figure is the interquartile range. Thin, black lines denote constant values of the hygroscopicity parameter, $\kappa$, computed based on the average size distribution for each air mass type. The stacked bars show the number fraction of each particle type from the PALMS instrument for particle diameters of 150-750 nm.

constitutes approximately 0-20% of the aerosol number, and as much as 40% for the background air mass type where increased numbers of nucleation-mode particles were sometimes observed; although, the combined measurement uncertainties of $N_{CCN}$ and $N_{CN}$ (7-16% and 20%, respectively), make this a weaker conclusion. For the background case, the maximum activated ratio is lower than the other cases because of the sub-40-nm nucleation mode, whose particles are too small to act as CCN regardless of their composition. Measurements of the sub-750-nm, single-particle number fractions from the PALMS, which are also shown in Figure 5.5, indicate a non-negligible dust fraction for all air mass types which would likely contribute to this non-CCN-active fraction, as well as less-oxidized organic species present as sulfate/organic or biomass/biofuel particle types. Previous studies have also detected the presence of a small, externally-mixed and less-hygroscopic aerosol mode either through humidified tandem differential mobility analyzer (HTDMA) measurements (e.g., *Herich et al.*, 2009; *Covert and Heintzenberg*, 1993) or from inferences based on volatility measurements (e.g., *Engvall et al.*, 2008; *Hegg et al.*, 1996).

Past airborne and ground-based studies of springtime Arctic CCN have reported average concentrations in the range of 0-300 cm$^{-3}$ and average activated fractions, $R_a$, of 0.15-0.63 for supersaturations of 0.3-1% (*Yum and Hudson*, 2001; *Hegg et al.*, 1995; *Shaw*, 1986). *Hegg et al.* (1996) and later *Kammermann et al.* (2010) measured Arctic CCN during the summer and found higher CCN concentrations of 0-675 cm$^{-3}$ and $R_a$ of 0.10-0.17 on average. This study finds 95$^{th}$-percentile CCN concentrations of 100-550 cm$^{-3}$ at 0.15-0.42% supersaturations for the background and Arctic boundary layer air mass types, which would be expected to be most representative of normal springtime Arctic conditions among the four air types encountered during ARCPAC. These increased CCN concentrations appear to be more consistent with measurements of the summertime Arctic than with the springtime studies; however CN concentrations remain consistent with past springtime studies while the CCN-active number fractions measured in this study are much higher. Thus, the enhancement in CCN likely results from the dearth of smaller particles for all air

mass types except portions of the background. The $95^{th}$-percentile CCN concentrations at 0.15-0.42% supersaturations for the anthropogenic pollution and biomass burning air mass types were 300-800 cm$^{-3}$ and 500-1500 cm$^{-3}$, respectively.

### 5.3.3 Inferring Hygroscopicity

The ability of a particle to act as a CCN depends on its size and chemical composition and on the ambient water vapor supersaturation. This relationship is described by Köhler theory (*Köhler*, 1936), and a single parameter representation of this theory has been recently developed and widely-adopted (*Petters and Kreidenweis*, 2007). The critical water vapor supersaturation that a particle must be exposed to to act as a CCN, $s_c$, is given by

$$s_c \approx \sqrt{\frac{4}{\kappa D_p^3}\left(\frac{4\sigma M_w}{3RT\rho_w}\right)^3} \tag{5.1}$$

where $D_p$ is the dry particle diameter, $\kappa$ is the hygroscopicity parameter (*Petters and Kreidenweis*, 2007), $R$ is the gas constant, $T$ is the absolute temperature, $\sigma$ is the surface tension of the solution droplet, and $M_w$ and $\rho_w$ are the molar mass and density of water, respectively. Although organic surfactants present in atmospheric aerosols can depress the droplet surface tension below that of pure water (*Asa-Awuku et al.*, 2009; *Decesari et al.*, 2003; *Facchini et al.*, 1999), most field measurement studies, including this one, assume the surface tension of water in Equation 5.1 for simplicity.

An alternate and equivalent way of expressing Equation 5.1 is to state that when particles with a given $\kappa$ are exposed to a constant water vapor supersaturation, those particles larger than some critical dry diameter, $D_{p,c}$ will act as CCN. Thus, we can infer $\kappa$ directly from measurements of CCN and the particle size distribution by first determining $D_{p,c}$ by integrating the particle size distribution to match the measured CCN concentration at a specified supersaturation,

$$N_{CCN} = \int_{D_{p,c}}^{\infty} n_{CN} dD_p \tag{5.2}$$

where $N_{CCN}$ is the measured CCN number concentration and $n_{CN}$ is the particle size distribution function. The derived $D_{p,c}$ for each supersaturation is then substituted into Equation 5.1 to find $\kappa$. Implicit in this method is the assumption that the aerosols larger than $D_{p,c}$ are internally-mixed. Given that $\kappa$ is most sensitive to size around $D_{p,c}$, we expect that the $\kappa$ derived in this way is most characteristic of particles with size $D_{p,c}$.

Inferred median $\kappa$ values from the CCN and size distribution measurements are plotted against their corresponding values of $D_{p,c}$ in Figure 5.6; error bars denote the interquartile range of inferred values. Also shown for comparison are predicted $\kappa$ values from size-averaged and size-resolved C-ToF-AMS compositions calculated as

$$\kappa = \sum_i \epsilon_i \kappa_i \tag{5.3}$$

where $\epsilon_i$ and $\kappa_i$ are the volume fraction and pure-component hygroscopicity of species $i$, respectively. Values of $\kappa_i$ were found from

$$\kappa_i = (\rho_i / M_i)(M_w / \rho_w)\nu_i \tag{5.4}$$

where $\rho_i$, $M_i$, and $\nu_i$ are the density, molar mass, and van't Hoff factor of the pure solute, respectively. An organic $\kappa$ of 0.11 was assumed, which corresponds to a theoretical organic species with a molar mass of 0.200 kg mol$^{-1}$, density of 1400 kg m$^{-3}$, and a van't Hoff factor of unity.

It is apparent from Figure 5.6 that the CCN-derived hygroscopicities are substantially lower than those suggested by the non-refractory aerosol composition, and these values also show a strong size-dependence. This apparent discrepancy could reflect size-dependent chemistry, where less-soluble organics are enhanced in the smaller particles relative to the larger particles measured by the C-ToF-AMS. For example, *Kammermann et al.* (2010) found similar $\kappa$ values of 0.07-0.21 for accumulation mode aerosol ($D$ = 50-200 nm) sampled in the remote subarctic Stordalen mire in northern Sweden using a DMT CCNC and a hygroscopicity tandem differential mobility analyzer (HTDMA). Alternatively, the lower

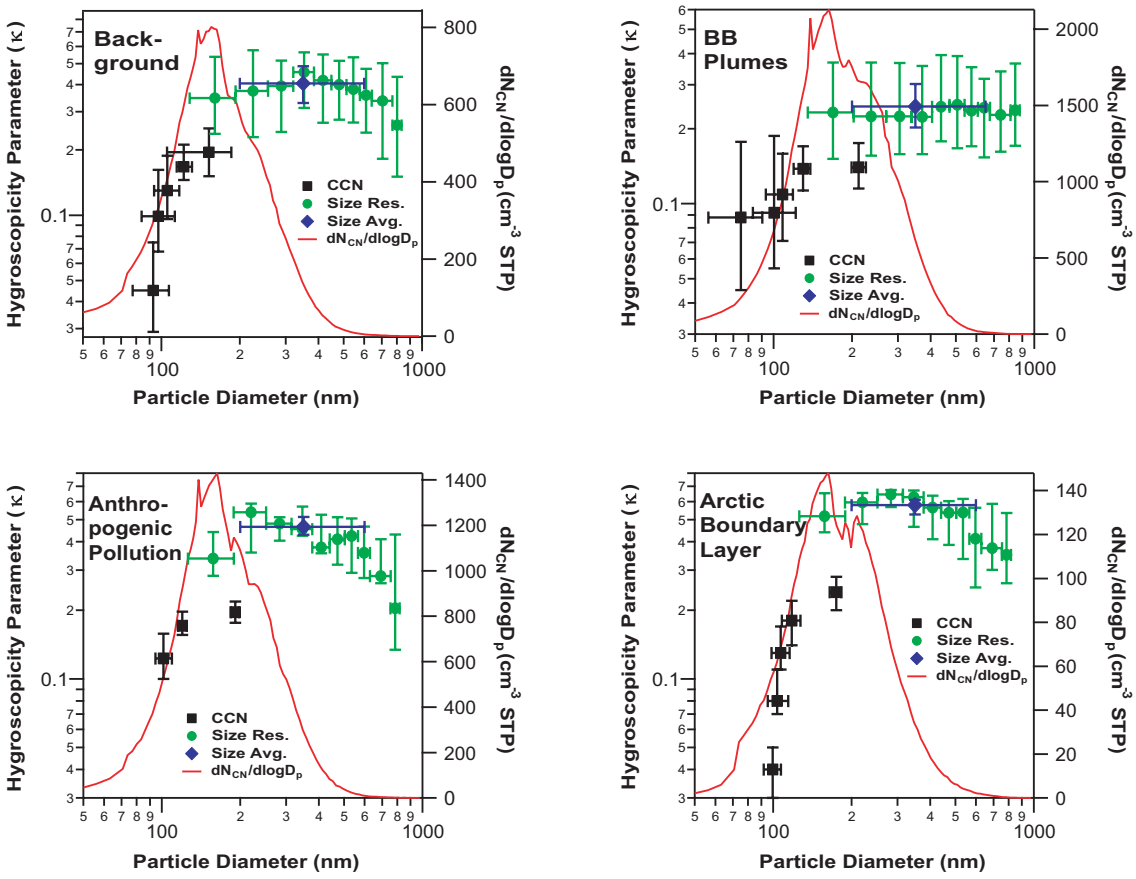


**Figure 5.6:** Inferred values of the hygroscopicity parameter, $\kappa$, obtained from the measured CCN concentrations and size distributions and plotted against the critical activation diameter, $D_{p,c}$ (squares). Also shown are $\kappa$ values calculated for particle compositions obtained from size-resolved (circles) and size-averaged (diamonds) C-ToF-AMS measurements. Markers denote the median values for each air mass type, while error bars denote the interquartile range. The solid line shows the average particle size distribution from Figure 5.2.

$\kappa$ could reflect the presence of an externally-mixed, non-CCN-active aerosol mode such as insoluble organics or even mineral dust, which constitutes $\sim 6\%$ by number (Figure 5.5). Since the hygroscopicities shown in Figure 5.6 were calculated assuming an internally-mixed aerosol, the presence of this less-CCN-active mode would serve to decrease $\kappa$. This is especially true for the lowest values of the CCN-derived $\kappa$ ($s > 0.3\%$), where all of the CCN-active particles have already activated and the effect of a less-hygroscopic mode would disproportionately affect predictions made assuming an internal mixture. The derived hygroscopicities of 0.1-0.3 in this study are consistent with those of aged pyrogenic aerosol (*Andreae and Rosenfeld*, 2008), which is not surprising given the influence of biomass burning aerosol, present in all air mass types sampled.

### 5.3.4 Hygroscopicity and Organic Oxygenation

It was also observed during ARCPAC that the geometric mean diameter of the aerosol size distribution varied with carbon monoxide mixing ratio for the biomass burning and background air types (Figure 8 in *Brock et al.*, 2011a), and it was suggested that dilution of the biomass burning aerosols may evaporate some semi-volatile organic species present in these particles (*Brock et al.*, 2011a). An alternate explanation would be that the plumes were emitted with lower gas-phase concentrations or were diluted early in transport, leading to less secondary aerosol production and smaller particles. CCN and large particle concentrations were also found to correlate linearly with CO (*Lance et al.*, 2011). It would be expected that the least volatile organic species would be the most oxidized, and hence most CCN-active species, while the semi-volatile organics would be less-oxidized and therefore less CCN-active (*Jimenez et al.*, 2009). To test this assumption, Figure 5.7 shows the average aerosol size distribution and hygroscopicities plotted versus the CO mixing ratio for all biomass burning plumes encountered during ARCPAC. A notable decrease in the aerosol geometric mean diameter and number concentration is apparent with decreasing CO, and

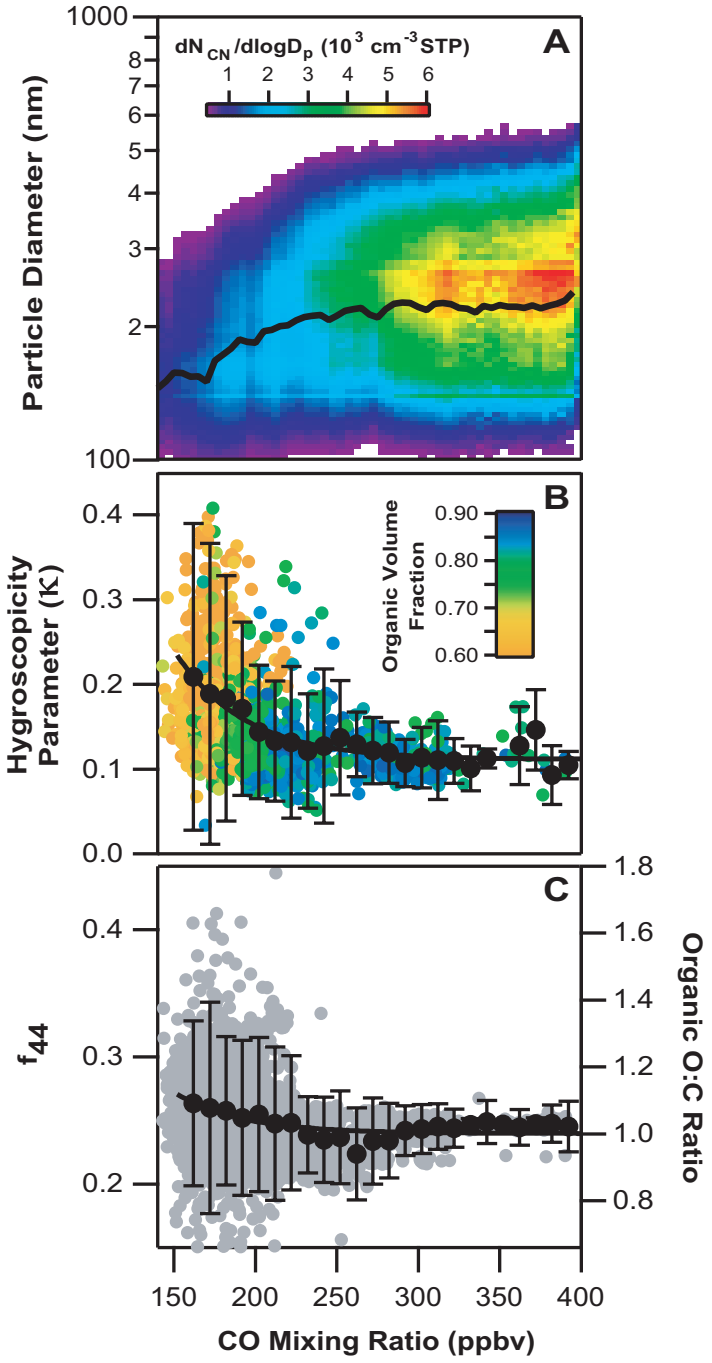


**Figure 5.7:** (a) Average particle size distribution for all biomass burning plumes sampled, colored by number concentration, and plotted versus CO mixing ratio. The black trace denotes the distribution geometric mean diameter. (b) CCN-derived biomass burning aerosol hygroscopicity, colored by aerosol organic volume fraction from the C-ToF-AMS, and plotted versus CO mixing ratio. (c) $f_{44}$ ratio obtained from the C-ToF-AMS (averaged to 5-minute intervals) plotted versus CO mixing ratio. The black-circles in (b) and (c) denote the mean $\kappa$ and error bars represents one standard deviation from the mean.

this trend coincides with an increase in the average $\kappa$ from 0.1 to 0.2 and increased variability of $\kappa$. While the decrease in organic volume fraction, and corresponding increase in the higher-$\kappa$ inorganic fraction is sufficient to explain this behavior, a slight shift in the degree of organic oxidation toward more-oxidized aerosol was also observed. The C-ToF-AMS mass fraction of the *m/z* 44 peak (mostly the $CO_2^+$ fragment of highly oxygenated organics such as, e.g., di-acids and esters) to total organic mass, $f_{44}$, is correlated with the organic O:C ratio (*Aiken et al.*, 2008; *Zhang et al.*, 2005a), which, in turn, relates to the organic hygroscopicity (*Jimenez et al.*, 2009). This is shown for the biomass burning plumes in Figure 5.7c. The relationship between $f_{44}$ and the O:C ratio was calculated using the correlation of *Aiken et al.* (2008). In biomass burning plumes an average $f_{44}$ of $\sim$ 0.26 $\pm$ 0.03 was observed, and the average $f_{44}$ increased very slightly from 0.24 $\pm$ 0.02 to 0.27 $\pm$ 0.06 as CO decreased from $\sim$ 400 ppbv to 150 ppbv. The very small change in $f_{44}$ and $\kappa$ with CO lends support to the early dilution / reduced SOA formation explanation versus evaporation of less-oxidized, semi-volatile species during later plume dilution.

Figure 5.8 shows the 95% simultaneous confidence ellipses for $f_{44}$ and $f_{43}$, where $f_{43}$ is the ratio of the *m/z* 43 peak (mostly $C_3H_7^+$ and $C_2H_3O^+$ fragments) to the total organic mass. The center of each ellipse denotes the mean values of $f_{43}$ and $f_{44}$. Also shown in Figure 5.8 is the triangular bounding region reported by *Ng et al.* (2010) that encompasses ambient and chamber data for oxygenated organic aerosol (OOA). While *Ng et al.* (2010) define $f_X$ as the ratio of *m/z* $X$ to only the oxygenated organic aerosol mass and this study uses the total organic mass measured by the C-ToF-AMS, direct comparison is reasonable because of the expected dominance of OOA (versus hydrocarbon-like organics) in the aged air masses sampled during ARCPAC. This assumption may explain why the ARCPAC confidence ellipses are shifted slightly toward larger $f_{43}$ values relative to the triangular region.

Most organic aerosols sampled during ARCPAC exhibited $f_{44} > 0.15$, indicative of well-oxygenated species (O:C $\sim$ 0.8-1.2 using the correlation of *Aiken et al.* (2008)).

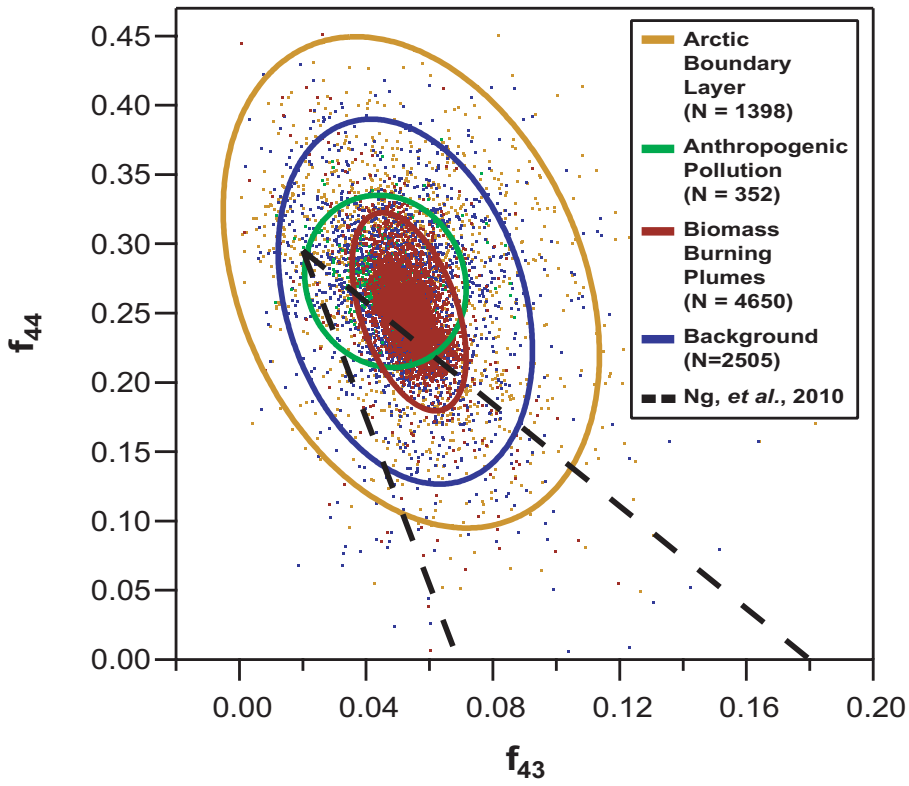


**Figure 5.8:** Oxidation state of the aerosol expressed as $f_{44}$ versus $f_{43}$, following *Ng et al.* (2010). Points denote the 10-second-averaged observations for each air mass type, and the ellipses denote the 95% confidence regions. Dashed lines are the parameterized triangular bounding region reported by *Ng et al.* (2010) for SOA chamber oxidation and ambient measurements.

Model atmospheric compounds with O:C ratios in this range include succinic, glutaric, and malic acids, although these model species have slightly lower molar masses (0.118 kg $mol^{-1}$, 0.132 kg $mol^{-1}$, and 0.134 kg $mol^{-1}$, respectively) than the average organic molar mass inferred from $\kappa$ during ARCPAC ($\sim$ 0.200 kg $mol^{-1}$). *Jimenez et al.* (2009) have shown that the organic hygroscopicity varies linearly with the O:C ratio for biogenic organics in smog chambers and for a number of field studies. Extrapolating the *Jimenez et al.* (2009) parameterization to O:C $\sim$ 1.0 implies an organic $\kappa$ of $\sim$ 0.43, which is significantly greater than the hygroscopicities inferred here. This suggests that increased organic oxygenation via aging processes may increase hygroscopicity only up to a point ($\kappa \sim$ 0.2-0.3), after which the organic hygroscopicity is less sensitive to the O:C ratio. Despite uncertainties with regard to the aerosol mixing state, the high O:C ratios and lower hygroscopicities observed here may suggest, apart from the different aerosol sources, a different secondary organic aerosol formation pathway than purely gas-phase oxidation chemistry. The ubiquity of Arctic clouds and recent modeling simulations showing oxalate concentrations of 20-30% that of sulfate in the Arctic suggest that this formation pathway may be through aqueous phase chemistry (*Myriokefalitakis et al.*, 2011), which can produce both organic acids in cloud droplets and multi-functional humic-like substances with O:C ratio $\sim$ 1 in wet aerosols (*Lim et al.*, 2010; *Ervens et al.*, 2004).

### 5.3.5 Sensitivity of CCN to Composition Effects

While being consistent with previous studies of pyrogenic aerosol, the hygroscopicities inferred in Section 5.3.3 are notably lower than expected from the C-ToF-AMS measurements, especially at higher supersaturations. However, given that most particles have activated already above about 0.1% supersaturation (see Figure 5.5), it is unclear how important these differences in $\kappa$ are for CCN concentrations. Here, we assess the sensitivity of CCN concentrations to composition effects using parameters typical of those measured during ARCPAC.

The sensitivity of CCN concentrations to changes in chemical composition can be computed analytically by, first, using Equation 5.1 to find the sensitivity of $D_{p,c}$ to $\kappa$, and then determining the sensitivity of CCN concentration to changes in $D_{p,c}$ determined by the steepness of the size distribution function:

$$\frac{\partial N_{CCN}}{\partial \kappa} = \left(\frac{\partial D_{p,c}}{\partial \kappa}\right)\left(\frac{\partial N_{CCN}}{\partial D_{p,c}}\right) \tag{5.5}$$

Differentiating Equation 5.1 yields

$$\frac{\partial D_{p,c}}{\partial \kappa} = \frac{-D_{p,c}}{3\kappa} \tag{5.6}$$

For simplicity, we assume here that the aerosol size-distribution is lognormal as

$$n_{CN} = \frac{N_{CN}}{\sqrt{2\pi} D_p \ln \sigma_g} \exp\left(\frac{-\ln^2(D_p/D_g)}{2\ln^2 \sigma_g}\right) \tag{5.7}$$

where $D_g$ is the geometric mean diameter of the size distribution and $\sigma_g$ is the geometric standard deviation. Substituting Equation 5.7 into Equation 5.2 and differentiating with respect to $D_{p,c}$ gives

$$\frac{\partial N_{CCN}}{\partial D_{p,c}} = \frac{-N_{CN}}{\sqrt{2\pi} D_{p,c} \ln \sigma_g} \exp\left(\frac{-\ln^2(D_{p,c}/D_g)}{2\ln^2 \sigma_g}\right) \tag{5.8}$$

Finally, substituting Equations 5.6 and 5.8 into Equation 5.5 and incorporating $\kappa$ and $N_{CN}$ into the left-hand-side yields

$$\frac{\partial R_a}{\partial \ln \kappa} = \frac{1}{3\sqrt{2\pi} \ln \sigma_g} \exp\left(\frac{-\ln^2(D_{p,c}/D_g)}{2\ln^2 \sigma_g}\right) \tag{5.9}$$

Equation 5.9 is expressed in terms of the size distribution constants and $D_{p,c}$, which depends on $s$ and $\kappa$. Thus, for a given $\kappa$, we can express $\partial R_a / \partial \ln \kappa$ across the range of relevant supersaturations. This is shown in Figure 5.9 for $D_g$ = 170 nm and $\sigma_g$ = 1.5, which are values representative of the average size distributions for the background, anthropogenic pollution, and Arctic boundary layer air mass types (*Brock et al.*, 2011a)

The log-normal nature of $\partial R_a / \partial \ln \kappa$ can be interpreted as that $R_a$ is most sensitive to composition effects when $D_{p,c}$ is near the maximum of the size distribution, where a small change in $D_{p,c}$ translates into a larger change in CCN than at the tails of the distribution. This is also true in $s$-space for a constant value of $\kappa$. The curves for $\kappa$ = 0.1-0.2 shown in Figure 5.9 indicate that CCN concentrations are most sensitive to composition effects near $s \sim$ 0.1-0.2, because this combination of $s$ and $\kappa$ produces values of $D_{p,c} \sim D_g$.

The dashed curve in Figure 5.9 shows the approximate CCN sensitivity of an externally-mixed aerosol with the same log-normal size distribution as before, but now with 50% inorganic particles ($\kappa$ = 0.6) and 50% organic particles ($\kappa$ = 0.1), by number. This is computed as the sum of the individual modal sensitivity distributions weighted by the number fraction of each mode. The externally-mixed case shows a similar sensitivity to that of the internally-mixed case with $\kappa$ = 0.2, but with a slightly wider distribution in $s$-space.

This analysis implies that weakly-forced Arctic stratiform clouds with maximum supersaturations of around 0.1-0.2% are at the peak of sensitivity to aerosol chemical composition effects.

### 5.3.6 CCN Closure

In this section, we use chemical compositions from the C-ToF-AMS and the measured size distributions to quantify the uncertainty associated with CCN predictions and to test the impacts of mixing state and solubility assumptions commonly employed in models. Such "CCN closure" analyses are commonplace in the literature and typical reported overprediction uncertainties range from 0-20% (e.g., *Asa-Awuku et al.*, 2011; *Rose et al.*, 2010; *Wang et al.*, 2010a; *Bougiatioti et al.*, 2009; *Broekhuizen et al.*, 2006; *Rissler et al.*, 2004; *VanReken et al.*, 2003, and others).

The C-ToF-AMS was not operational during the April 12th flight, so we restrict our analysis to the flights on April 15th, 18th, 19th, and 21st. Only the April 19th flight examined supersaturations above 0.3%, so we also restrict our analysis here to water vapor

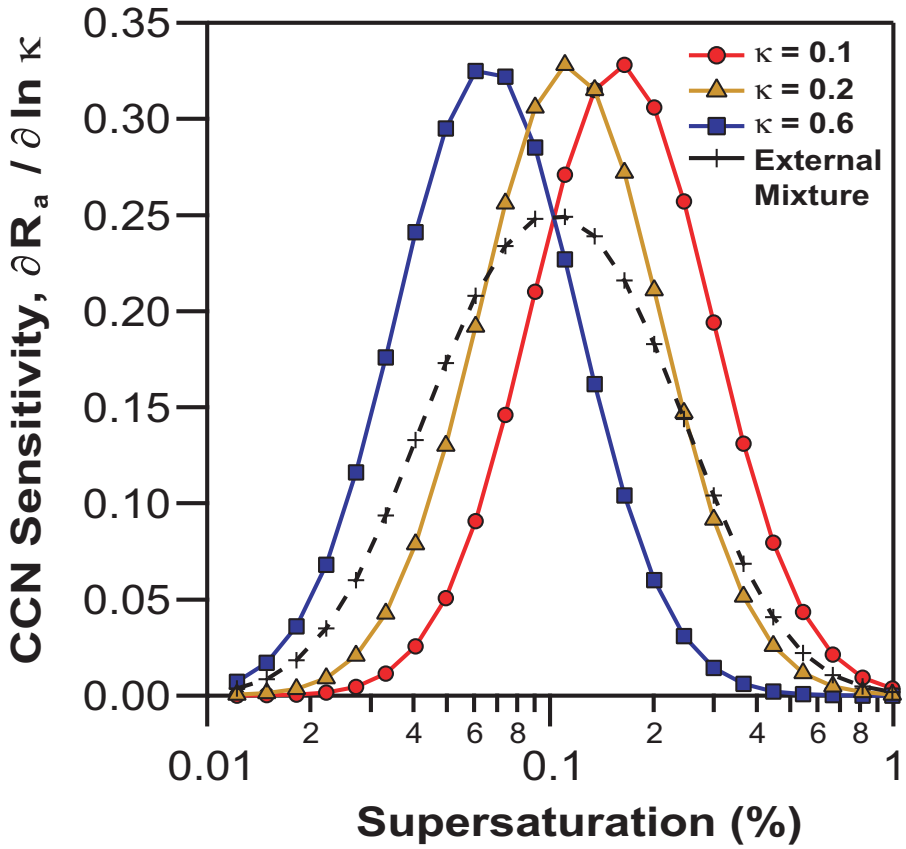


**Figure 5.9:** Sensitivity of $R_a$ to $\kappa$ as a function of superaturation. Solid traces were computed assuming an internal mixture and constant values of $\kappa$, while the dashed trace represents an external mixture of 50% inorganic aerosol ($\kappa$ = 0.6) and 50% organic aerosol ($\kappa$ = 0.1), by number.

supersaturations of 0.1, 0.2, and 0.3%. Finally, because of relatively low aerosol mass loadings at particle diameters less than 150-200 nm, the resolution of the C-ToF-AMS is too noisy to assess closure using size-resolved composition measurements as has been performed by some previous studies in more polluted environments (e.g., *Asa-Awuku et al.*, 2011; *Medina et al.*, 2007), and size-invariant chemistry is assumed for this analysis. From Figure 5.6 it can be seen that the size-averaged and size-resolved compositions yield similar values of $\kappa$ over the diameter range of 200-800 nm, as this is where the mass distribution is located, which would seem to support the size-invariance assumption; however, it is an open question whether the measured particle composition at these sizes is the same as at

**Table 5.1:** Percent overprediction $(\Phi - 1)\times 100\%$ in CCN number concentration from different organic solubility and mixing state assumptions. Data from the CCNC, C-ToF-AMS, and size distributions were averaged over 10-second periods, and N reflects the number of 0.1-Hz data points used to calculate each mean and standard deviation.

| | | Internal Mixture | | External Mixture | | Size |
|---|---|---|---|---|---|---|
| | | Soluble | Insoluble | Soluble | Insoluble | Dependent |
| Air Mass Type | N | Organics | Organics | Organics | Organics | Mixture[a] |
| Anthropogenic Pollution | | | | | | |
| $s$ = 0.1 ± 0.04 (%) | 93 | 81±22 | 73±22 | 20±20 | 9±22 | 44±20 |
| $s$ = 0.2 ± 0.04 (%) | 77 | 20±10 | 19±10 | -7±8 | -31±11 | -7±8 |
| $s$ = 0.3 ± 0.04 (%) | 53 | 13±9 | 13±9 | -1±8 | -35±9 | -1±8 |
| Biomass Burning Plumes | | | | | | |
| $s$ = 0.1 ± 0.04 (%) | 1088 | 47±27 | 18±25 | -12±16 | -65±21 | 17±18 |
| $s$ = 0.2 ± 0.04 (%) | 540 | 16±10 | 9±10 | -4±9 | -70±14 | -4±9 |
| $s$ = 0.3 ± 0.04 (%) | 267 | 12±8 | 9±7 | 3±9 | -67±12 | 3±9 |
| Background | | | | | | |
| $s$ = 0.1 ± 0.04 (%) | 471 | 95±79 | 79±77 | 21±45 | -4±48 | 48±51 |
| $s$ = 0.2 ± 0.04 (%) | 298 | 34±37 | 30±33 | 3±26 | -30±30 | 3±27 |
| $s$ = 0.3 ± 0.04 (%) | 282 | 19±13 | 17±13 | 3±11 | -47±21 | 3±11 |
| Arctic Boundary Layer | | | | | | |
| s = 0.1 ± 0.04 (%) | 76 | 61±18 | 55±21 | 15±19 | 1±28 | 35±18 |
| s = 0.2 ± 0.04 (%) | 64 | 38±13 | 37±13 | 17±13 | 3±18 | 19±14 |
| s = 0.3 ± 0.04 (%) | 41 | 41±9 | 41±9 | 29±9 | 10±16 | 29±9 |
| All Air Mass Types | | | | | | |
| s = 0.1 ± 0.04 (%) | 1715 | 62±52 | 39±53 | 0±31 | -42±43 | 27±34 |
| s = 0.2 ± 0.04 (%) | 955 | 23±24 | 18±23 | -1±17 | -50±31 | 0±18 |
| s = 0.3 ± 0.04 (%) | 623 | 17±13 | 15±13 | 5±12 | -51±26 | 5±12 |

[a]Particles with $D_p > 200$ nm assumed to be internally mixed, while particles with $D_p < 200$ nm are externally mixed. Organics are assumed to be soluble.

smaller sizes.

CCN concentrations are predicted as follows. First, C-ToF-AMS mass loadings are used to find the volume fractions of organics, ammonium nitrate, ammonium sulfate, ammonium bisulfate, and sulfuric acid, where the inorganic species are partitioned as described in Section 5.3.1. Then, Equations 5.3 and 5.4 are used to find the overall hygroscopicity of the aerosol, which is used in Equation 5.1 to find the critical activation diameter, $D_{p,c}$, above which particles will act as CCN.

In applying Equations 5.1, 5.3, and 5.4, it is necessary to make an assumption about

the aerosol mixing state. For example, one can assume that the aerosols are internally mixed with a composition that yields one $D_{p,c}$ for the entire population, and $N_{CCN}$ is found directly from Equation 5.2.

Alternatively, one can assume that the aerosol are externally mixed, where each particle contains either only organic species or only inorganic species, and the number fraction of each particle type is described by the overall volume fractions. In this case, two distinct particle populations exist, each with their own $D_{p,c}$. Since the organic species are less hygroscopic than the inorganic species, $D_{p,c,org} > D_{p,c,inorg}$, and

$$\begin{aligned} N_{CCN} &= \int_{D_{p,c,inorg}}^{D_{p,c,org}} (1-\epsilon_{org}) n_{CN} dD_p \\ &\quad + \int_{D_{p,c,org}}^{\infty} n_{CN} dD_p \end{aligned} \tag{5.10}$$

Equation 5.10 treats all particles (both organic and inorganic) larger than $D_{p,c,org}$ as CCN, while only the inorganic fraction of particles with diameters between $D_{p,c,inorg}$ and $D_{p,c,org}$ are counted as CCN.

In addition, it is necessary to make an assumption regarding the hygroscopicity of the organic species. In this analysis we test two cases: one where the organic particle fraction can be assumed to be slightly soluble ($\kappa$ = 0.11) and one where the organic particle fraction is assumed to be completely insoluble ($\kappa$ = 0). Given the aged nature of the organics, the latter assumption is unlikely, but still a useful sensitivity scenario. Closure is reported in this section in terms of a CCN prediction error ratio, $\Phi = N_{CCN,predicted}/N_{CCN}$.

CCN predictions tended toward overprediction, and the average percent overprediction for each supersaturation and air mass type are shown in Table 5.1. Overall, the largest discrepancies between predicted and measured concentrations were observed at $s$ = (0.1 $\pm$ 0.4)%. This is consistent with Figures 5.5 and 5.9; a small change in $\kappa$ at $\sim$ 0.1% supersaturation would cause a large change in the activated fraction, and hence CCN concentration. Assuming the aerosol to be internally-mixed with soluble organics produced the largest

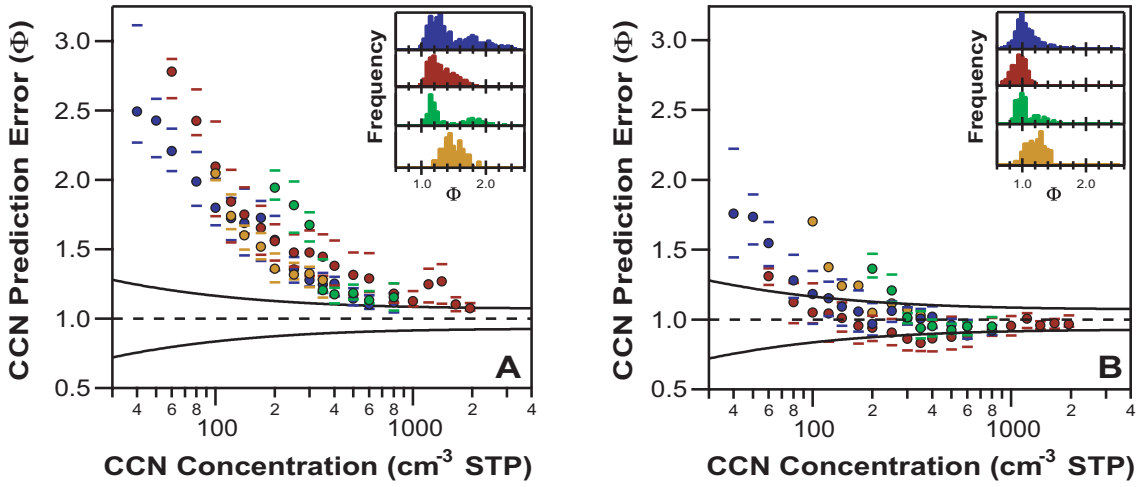


**Figure 5.10:** CCN prediction error for 0.1-0.3% supersaturation versus measured CCN concentrations. Predictions were computed assuming that the aerosol is (a) internally-mixed, or (b) externally-mixed. Organic species are assumed to be soluble with $\kappa$ = 0.11. Markers denote the median error for each air mass type (colored as in Figures 5.1-5.5), and bars denote the interquartile range. The dotted line at $\Phi$=1 denotes perfect agreement and the solid bounding curves denote the CCN measurement uncertainty. The inset shows the frequency distribution of $\Phi$ for all 0.1 Hz data points.

overprediction of the four models tested, and treating the organics as insoluble reduced this overprediction only slightly. Assuming the aerosol to be externally-mixed with soluble organics resulted in a reasonable overall closure ($\Phi \sim$ 1-1.2 for all air mass types), which was worsened substantially by assuming that organics were insoluble ($\Phi \sim$ 0.5 for all air mass types).

Thus, assuming Arctic aerosol to be composed of an external mixture of soluble organic and inorganic particles allowed prediction of CCN concentrations to within roughly 0-20%, on average. This was also true for the individual air mass types, except for within the Arctic boundary layer, where assuming insoluble organics further improved closure. The good closure obtained from assuming an externally-mixed aerosol is somewhat unexpected, considering the long lifetime of these particles in the atmosphere, during which time, particle coagulation, gas condensation, and photochemistry would be expected to shift the aerosol population toward a more internally-mixed state. One explanation for this result is that the

organic species are significantly less-soluble ($\kappa < 0.11$), or even insoluble, and that the aerosol mixing state is some combination of internally- and externally-mixed aerosol.

The PALMS data products show clearly that the fine mode aerosols are an external mixture of different particle types from different sources (Figure 5.5 here and Figure 7 in *Brock et al.* (2011a)), while examination of single particle spectra show that most particles are compositionally internally mixed with both secondary sulfate and organic species. Thus, the internal and external mixture cases explored here bound reality and constrain the CCN activity of the real aerosol population. As an intermediate case, a size-dependent mixing state scenario was examined, where particles greater than a specified threshold diameter are assumed to be internally mixed, while particles smaller than the threshold diameter are treated as externally mixed. Organic species present across the entire size distribution are treated as slightly soluble as before. During ARCPAC, the mass spectra signal-to-noise ratio was very low for particle diameters below 150-200 nm, and so we use 200 nm as the threshold diameter in this scenario. The average overprediction assuming a size-dependent mixing state is shown in Table 5.1. Comparing this closure scenario to the internal mixture and external mixture cases with soluble organics shows the overprediction to be the same as the externally-mixed case at 0.2-0.3% supersaturations. Meanwhile the closure overprediction for $s = (0.1 \pm 0.04)\%$ falls between the two bounding cases. This is consistent with the peak sensitivity uncovered in Section 5.3.5, and provides a closure prediction estimate that is more consistent with the PALMS observations.

FLEXPART modeling of the transport of the biomass burning and anthropogenic pollution plumes indicates an Asian source with transport times of 4-9 days, while the background and Arctic boundary layer air mass types may reside in the Arctic atmosphere for a longer time (*Brock et al.*, 2011a; *Fisher et al.*, 2010; *Warneke et al.*, 2009). We speculate, then, that the biomass burning and anthropogenic plumes undergo aging and mixing processes during transport that result in an internally-mixed, well-oxidized-organic-dominated

aerosol type that is injected into the stratified Arctic atmosphere, where further mixing processes are somewhat suppressed. Meanwhile, the background and Arctic boundary layer air mass types are dominated by an existing population of predominantly-inorganic aerosol. The fact that PALMS shows a significant biomass burning signature for all air mass types indicates that mixing of air types is not completely suppressed, however, and aging processes blur the distinction between different particle types.

CCN prediction error was also found to vary with number concentration, as shown in Figures 5.10a and 5.10b for the internally-mixed and externally-mixed cases, respectively (and assuming soluble organics). The median overprediction increases for both cases as CCN concentration decreases, which cannot be fully-explained by the increase in measurement uncertainty associated with decreased CCN counting statistics (solid curves in Figure 5.10). Higher AMS composition uncertainties at low particle concentrations may also contribute somewhat to this uncertainty. Additionally, analysis of PALMS spectra obtained during periods of low CCN concentration ($< 70$ cm$^{-3}$) in the background air masses suggests a relatively larger role of mineral dust with less soluble material than present at higher CCN concentrations. This would not be reflected in the closure calculation and may also explain the increased overprediction. CCN concentrations below 100 cm$^{-3}$ were somewhat infrequent during ARCPAC and had little influence on the overall predictions reported in Table 5.1, as reflected by the low occurrence of large $\Phi$ values in the inset frequency plots in Figure 5.10. However, the range of 0-300 CCN cm$^{-3}$ for springtime Arctic aerosol reported by previous studies suggests that the CCN prediction uncertainties associated with more pristine conditions occurring in the absence of strong biomass burning conditions may be even greater. Given the susceptibility of Arctic stratus to composition effects, under low CCN concentrations, such errors become important.

## *5.4 Summary and Conclusions*

Measurements of CCN and aerosol properties obtained during the ARCPAC project in April, 2008, are presented and analyzed. We find that size effects dominate the CCN activity because of the accumulation mode size distribution, and that most particles act as CCN above 0.1% supersaturation. However, we also find that aerosol chemistry and mixing state have important secondary effects, particularly in the prediction of CCN number concentration, which is shown to be sensitive to compositional assumptions near 0.1% supersaturation. Assuming the aerosol to be internally-mixed significantly overpredicts CCN concentration, and the best closure (0-20% overprediction error) is obtained assuming externally-mixed aerosol with soluble organics. Closure worsens for low CCN concentratrations ($< 100$ cm$^{-3}$), where CCN are overpredicted by a factor of 1.5-3. While these low concentration periods were infrequent during ARCPAC, and thus do not substantially affect the overall closure, past studies have frequently reported CCN concentrations in this range. Consequently, CCN prediction errors might be expected to be even greater for those conditions.

While this study indicates that aerosol mixing state plays a significant role in determining CCN activity, many current models treat aerosols solely as internal mixtures for computational efficiency. Consequently, we also quantify the CCN activity in terms of the size-dependent hygroscopicity parameter, $\kappa$, which was found to vary with supersaturation (and, hence, $D_{p,c}$) from 0.04 at the highest supersaturations ($s$ = 0.4-0.6%) to 0.15-0.3 at the lowest supersaturations ($s$ = 0.1-0.3%). This observed size-dependence captures the size-dependent chemistry and mixing state effects not explicitly treated by the single-parameter model.

Strong biomass burning plumes originating in Asia and advected into the Arctic atmosphere during this study made this dataset particularly useful for examining a wide variety of Arctic pollution sources; however, mixing of the biomass emissions across air types means that extrapolating these results to more pristine springtime conditions without a

significant biomass burning signature should be done with care. Recent work suggests, however, that biomass burning may be a larger contributor to Arctic haze than previously thought, and a warming climate will likely increase the prevalence of severe fire years in the future (*Warneke et al.*, 2010; *Stocks et al.*, 1998).

# CHAPTER VI

# HYGROSCOPICITY AND COMPOSITION OF CALIFORNIA CCN

This chapter presents an overview and analysis of cloud condensation nuclei (CCN) sampled in California by a NOAA WP-3D aircraft during the 2010 CalNex project. Four distinct geographical regions are characterized, including the Los Angeles basin, the San Joaquin and Sacramento Valleys, and the eastern Pacific Ocean west of southern California. Median size distributions in the Central Valley were unimodal ($D_g \sim 25$ nm) with a larger fraction of organic species and smaller fraction of nitrate species in the Sacramento Valley aerosol than in the San Joaquin Valley aerosol. Size distributions in the Los Angeles basin and marine outflow were bimodal ($D_g \sim 30$, 90-100 nm) with similar organic fractions and some replacement of nitrate with sulfate in the marine outflow. Both fine particle and CCN concentrations were found to decrease above 2 km altitude, with CCN concentrations ranging from $\sim$10-$10^4$ cm$^3$ STP, while fine particle concentrations (0.004-1 $\mu$m diameters) ranged from $\sim 10^3$-$10^5$ cm$^{-3}$ STP. Values of the hygroscopicity parameter, $\kappa$, inferred from the CCN measurements varied from 0.1-0.25, with the highest values in the marine outflow and the lowest values in the Sacramento Valley. The $\kappa$ values agreed well with the predictions based on size-resolved aerosol composition, but were overpredicted by almost twofold when size-averaged composition is used. CCN closure was assessed for simplified compositional and mixing state assumptions, and it was found that assuming the aerosol to be internally mixed overpredicted CCN concentrations by 30-75% for all air mass types except within the Sacramento Valley, where good closure ($<$10%) was achieved by assuming insoluble organics. Assuming a partially externally-mixed aerosol fraction or incorporating size-resolved composition data improved closure in the other three regions, consistent with

This chapter to be submitted for publication as: Moore, R. H., K. Cerully, C. A. Brock, A. M. Middlebrook, and A. Nenes, Hygroscopicity and Composition of California CCN During Summer, 2010.

the bimodal nature of the aerosol size distribution.

## *6.1 Introduction*

The central and southern portions of California experience some of the most severe air quality problems in the United States. This is due to intense local emissions sources combined with topographically-influenced air flow that contains these emissions within the low-lying valleys and basins throughout the region between Los Angeles and Sacramento. Much work has been conducted in the past decades to understand the magnitude and spatiotemporal distribution of this pollution. A strong seasonal variation has been observed by multiple studies indicating that the highest particle concentrations are reached during the winter when strong temperature inversions limit vertical mixing and ventilation of the Los Angeles basin and San Joaquin valleys. During the summer, a more westerly flow driven by diabatic heating in Mojave Desert draws air inland, which significantly decreases local particle concentrations, relative to those observed during winter (e.g., *Chow et al.*, 2006; *Rinehart et al.*, 2006; *Dillon et al.*, 2002; *Green et al.*, 1992, and references therein). The prevailing westerly winds enter the Central Valley through the Carquinez Strait east of San Francisco, and move northward into the Sacramento Valley and southward into the San Joaquin Valley; infrequently, air enters the San Joaquin Valley through additional entrance points to the south. Similar to the sea breeze influence in the Los Angeles basin, these winds can induce a west-east pollution gradient with higher aerosol concentrations accumulating on the upslope side of the Sierra Nevada and San Gabriel mountain ranges.

It is known that increased concentrations of soluble aerosols affect cloud properties and lifetime by increasing droplet number and reducing the mean cloud droplet sizes (*Twomey*, 1977a; *Albrecht*, 1989). Recent work has suggested that these aerosol indirect effects on clouds can also suppress orographic precipitation on the windward side the southern Sierra Nevada mountains (*Rosenfeld et al.*, 2008; *Givati and Rosenfeld*, 2004). This implies that clouds are able to persist long enough to be transported over the crest of the mountains

before either raining out or evaporating on the leeward side (*Rosenfeld et al.*, 2008), with important implications for regional water cycling. While urban pollution plumes were found to be important sources of these enhanced aerosol concentrations, *Rosenfeld et al.* (2008) also report that non-urban primary and secondary aerosol sources likely play an important role.

In addition to inland transport, coastal pollution sources also can be transported out over the eastern Pacific ocean and influence the structure of stratocumulus cloud decks near the coast (e.g., *Hegg et al.*, 2009; *Furutani et al.*, 2008; *Roberts et al.*, 2006). These observed effects of aerosols on clouds and precipitation motivated the need to better understand the ability of California aerosol to affect droplets by contributing cloud condensation nuclei (CCN). The ability of a particle to act as a CCN depends on both its size and chemical composition, which are, in turn, dependent on aerosol microphysical processes and primary emissions sources.

Major summertime emissions sources in the San Joaquin Valley and Los Angeles basin include secondary production of nitrate and organic aerosol (36-38% by mass), motor vehicle emissions (13-25%), fugative dust (16-19%), and agricultural and animal husbandry operations (4-5%) (*Chen et al.*, 2007). Wintertime emissions sources are more heavily affected by secondary nitrate aerosol production and residental wood burning (*Chen et al.*, 2007). *Neuman et al.* (2003) found evidence of gas-phase $NO_3$ depletion associated with secondary gas-to-particle production of $NH_4NO_3$ aerosol in the San Joaquin Valley and Los Angeles basin during April and May, 2002, which was not observed in the Sacramento Valley or over the coastal Pacific Ocean. This highlights the importance of agricultural ammonia emissions from local animal husbandry operations as the dominant source of atmospheric bases; *Sorooshian et al.* (2008) and *Zhang and Anastasio* (2001) also observed smaller sources of organic nitrogen (e.g., amines and amino acids) in the San Joaquin Valley that could neutralize $NO_3^-$. The timescale of secondary nitrate and organic aerosol production is thought to be much less than the boundary layer mixing timescale, which

results in horizontal and vertical aerosol concentration gradients in the Los Angeles basin and Central Valley (*Neuman et al.*, 2003; *Collins et al.*, 2000). Consequently, using measurements at one or several locations to represent an entire global model grid cell ($\sim$ 100 km by 100 km) can lead to substantial uncertainties (*Collins et al.*, 2000).

In this study, we seek to comprehensively characterize the compositional and size-dependence of CCN activation and hygroscopicity of California aerosol over a wide horizontal and vertical sampling area during May-June, 2010. Average aerosol size, composition, and hygroscopic properties are presented, relevant for scales typical of a global models. Thus, this work will complement previous, more-focused studies of Los Angeles CCN measured near local sources (*Cubison et al.*, 2008), of Central Valley CCN affected by the plume from a large commercial cattle operation (*Sorooshian et al.*, 2008), of the coastal CCN gradient west of Los Angeles (*Furutani et al.*, 2008), and of eastward CCN transport in the southern Sacramento Valley (*Rosenfeld et al.*, 2008).

## *6.2 Observational Data Set*

### 6.2.1 Study Location

Measurements were made aboard a National Oceanic and Atmospheric Administration WP-3D aircraft based out of Ontario, California (34°3'10"N, 117°37'40"W). Eighteen research flights were conducted throughout the Los Angeles basin, San Joaquin and Sacramento Valleys, and coastal regions of California during the CalNex campaign from May 4th – June 20th, 2010 (Table 6.1). A map of the flight tracks is shown in Figure 6.1.

### 6.2.2 Chemical Composition Measurements

Non-refractory aerosol chemical compositions were obtained from a compact time-of-flight aerosol mass spectrometer (C-ToF-AMS) with a pressure-controlled inlet (*Bahreini et al.*, 2008; *DeCarlo et al.*, 2006; *Drewnick et al.*, 2005). The C-ToF-AMS operates by focusing the sample aerosol stream onto a hot plate to vaporize the non-refractory aerosol components, which are subsequently ionized and detected by the time-of-flight mass spectrometer.

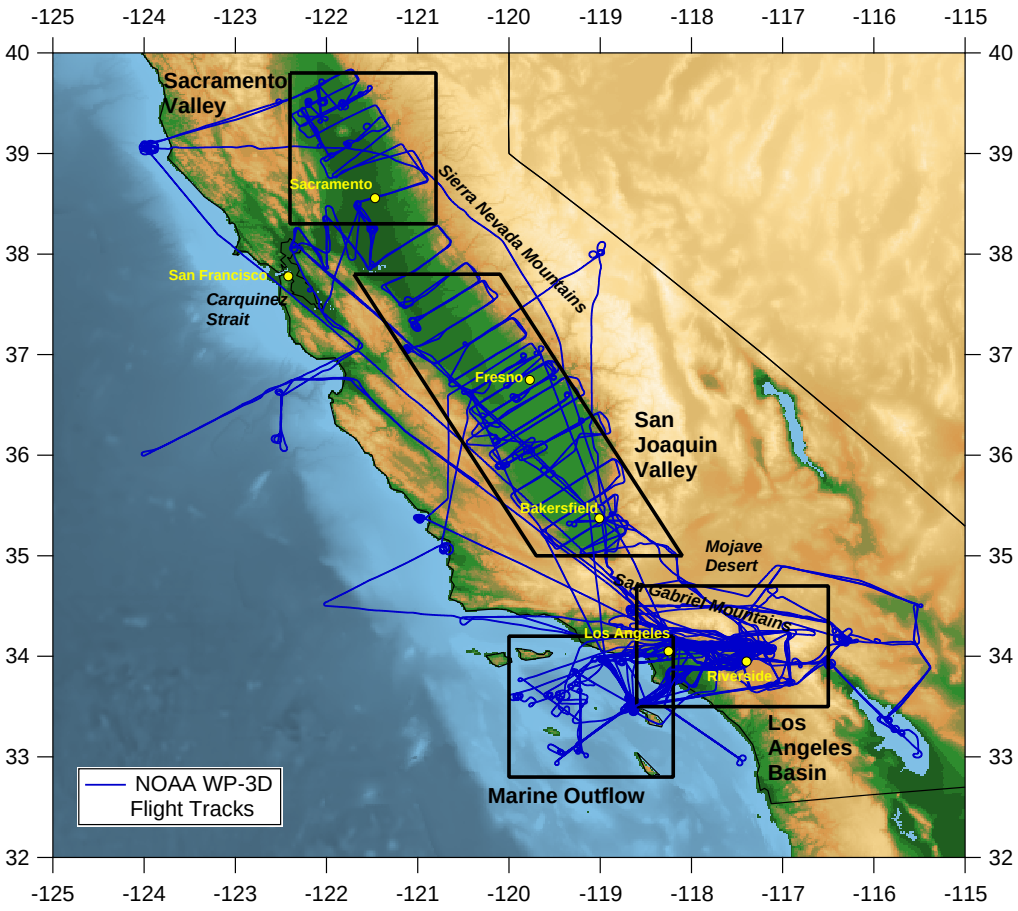


**Figure 6.1:** Overview of NOAA WP-3D flights during CALNEX.

**Table 6.1:** Research flights during 2010 CalNex.

| Research Flight | Date | Local Time (PDT, UTC-7 hrs.) | Flight Location and Description |
|---|---|---|---|
| 1 | 4 May | 11:40-16:27 | Los Angeles basin |
| 2 | 7 May | 10:04-16:58 | Transects across the Central Valley |
| 3 | 8 May | 11:05-18:09 | Los Angeles basin |
| 4 | 11 May | 10:03-17:13 | Rice fields near Sacramento and coastal inflow through the Carquinez Strait |
| 5 | 12 May | 10:00-18:48 | Transects across the Central Valley |
| 6 | 14 May | 10:01-16:12 | Los Angeles basin and upwind over the Pacific Ocean coast |
| 7 | 16 May | 10:58-18:42 | Los Angeles basin and upwind over the Pacific Ocean coast |
| 8 | 19 May | 10:27-17:11 | Los Angeles basin |
| 9 | 21 May | 08:27-11:26 | Ship plume interception and upwind of the Los Angeles basin |
| 10 | 24 May | 16:07-22:00 | Los Angeles basin to coast and Central Valley |
| 11 | 30 May | 18:58-00:45 | Los Angeles basin during nighttime |
| 12 | 31 May | 21:59-03:54 | Los Angeles basin during nighttime |
| 13 | 2 Jun | 00:58-07:08 | Los Angeles basin during early morning |
| 14 | 3 Jun | 00:58-07:41 | Los Angeles basin during early morning |
| 15 | 14 Jun | 10:55-18:16 | Rice fields near Sacramento and inflow through the Carquinez Strait |
| 16 | 16 Jun | 11:02-17:57 | Transects across the Central Valley |
| 17 | 18 Jun | 11:03-18:08 | Transects across the Central Valley, flow through the Carquinez Strait, and westward profile of coastal emissions gradient over the Pacific Ocean |
| 18 | 20 Jun | 10:57-18:04 | Los Angeles basin |

The instrument can be operated in either "time of flight" mode or in "mass spectrum" mode, where the former involves periodically interrupting the aerosol stream with a rotating chopper to measure the size-dependent particle time-of-flight across the vacuum chamber, while the latter alternates the chopper in and out of the beam line to obtain size-averaged differential mass spectra. Both methods of operation yield mass spectra at 0.1 Hz, although, the size-resolved mass distributions were averaged over five-minute intervals to improve counting statistics. Mass loadings ($\mu$g cm$^{-3}$) of sulfate, nitrate, ammonium, and organic aerosol constituents were then obtained from the mass spectra via the procedure of *Allan et al.* (2003), with relative uncertainties of $\pm$34-38% (*Bahreini et al.*, 2009).

### 6.2.3 Particle Size Distribution Measurements

The dry aerosol size distribution (0.003 to 8.3 $\mu$m diameters) was measured using a white-light optical particle counter (WLOPC), an ultra-high sensitivity aerosol size spectrometer (UHSAS), and a nucleation mode aerosol size spectrometer (NMASS). The NMASS consists of five condensation particle counters with 0.004, 0.008, 0.015, 0.030, and 0.055 $\mu$m cutoff diameters, and the fine particle size distributions (diameters $< 1$ $\mu$m) were obtained

by coupling these five size bins to the UHSAS distribution using a nonlinear inverison algorithm (*Brock et al.*, 2000). The calibrated uncertainty of the fine particle concentrations is approximately $\pm$ 20%.

### 6.2.4 CCN Measurements

CCN measurements were conducted using a Droplet Measurement Technologies streamwise, thermal-gradient cloud condensation nuclei counter (CCNC, *Roberts and Nenes*, 2005; *Lance et al.*, 2006), which was located downstream of a 1-$\mu$m-cutoff-diameter impactor. The CCNC consists of a cylindrical tube with wetted walls, on which a linear streamwise temperature gradient is applied in the axial direction. Since the diffusivity of water vapor is greater than the thermal diffusivity of air, a water vapor supersaturation is generated in the flow tube, which is maximum at the centerline. Particles are introduced at the column centerline, and those that activate to form droplets are counted and sized by an optical particle counter at the base of the column.

The CCNC supersaturation profile mainly depends on the applied temperature gradient, flow rate, and pressure (*Roberts and Nenes*, 2005). During CALNEX, the instrument was operated as a CCN spectrometer using the Scanning Flow CCN Analysis (SFCA) technique of *Moore and Nenes* (2009). SFCA entails dynamically scanning the instrument flow rate over time to produce a nearly-instantaneous change in supersaturation, while maintaining a constant applied temperature gradient and pressure. A flow orifice and active flow control system were employed to maintain a constant instrument pressure of 500 hPa, while the applied temperature gradient was kept constant at 12 K. Upscan and downscan ramp times of 15 seconds were used, and CCN counts were integrated over each second to obtain 1-Hz CCN concentrations.

Supersaturations were calibrated in terms of the CCNC internal temperature gradient, the instantaneous flow rate, and the overall flow rate range (i.e., the minimum and maximum flow rate in each scan). The relationship between supersaturation and instantaneous

flow rate was found following the procedure of *Moore and Nenes* (2009), where size-classified ammonium sulfate aerosol from a differential mobility analyzer (DMA) were introduced into the CCNC, and the DMA voltage was varied in a stepwise manner so that approximately three CCNC flow scans were obtained at each particle size. Sigmoidal activation curves of CCN versus flow rate are obtained, and the inflection point of the sigmoid is used as the critical activation flow rate, $Q_c$, which corresponds to the critical supersaturation, $s_c$, above which particles act as CCN. For each particle size, $s_c$ is obtained from Köhler theory (*Köhler*, 1936), as in *Rose et al.* (2008) and *Moore et al.* (2010). The molality-dependent osmotic coefficient of ammonium sulfate used in Köhler theory is computed using the ion-interaction approach of *Pitzer and Mayorga* (1973) with parameters obtained from *Clegg and Brimblecombe* (1988). The absolute uncertainty of the calibrated CCNC supersaturation is estimated to be $\pm 0.04\%$, while the uncertainty in CCN number concentration from counting statistics and fluctuations in temperature, pressure, and flow rates during flight operation is estimated to be 7-16% for CCN concentrations above 100 $cm^{-3}$ STP, which is comparable to the uncertainty of the instrument operating in constant flow mode (*Moore et al.*, 2011). The overall flow rate range was found to be sensitive to the large changes in the ambient air temperature ($\sim$10°C) encountered throughout the CalNex mission and would gradually shift toward larger values as the aircraft cabin temperature increased during flight. This temperature-dependence was found to impact the calibrated supersaturations during the flow downscans, while only weakly-influencing the calibrated supersaturations during the upscans. Consequently, calibration curves for multiple flow ranges were obtained to account for these effects, and only flow upscan data are used for this analysis.

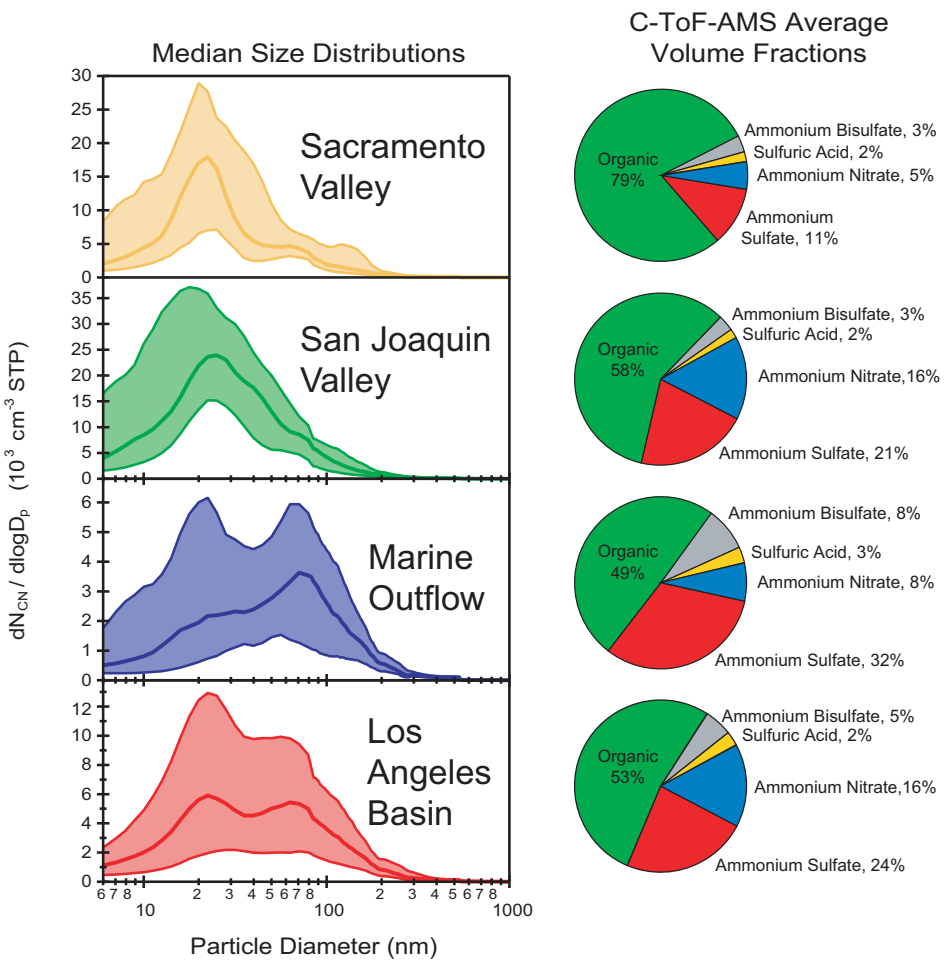


**Figure 6.2:** (Left) Median size distributions for each geographical region. Shaded area denotes the interquartile range. (Right) Average aerosol volume fractions obtained from the C-ToF-AMS.

## *6.3 Results and Discussion*

### 6.3.1 Regional Air Types

During the eighteen research flights from May 4th – June 20th, the WP-3D aircraft sampled aerosol in four distinct geographical regions: the Los Angeles basin, the marine coastal environment west of Los Angeles, the San Joaquin Valley, and the Sacramento Valley. Figure 6.1 shows the aircraft flight trajectories during CalNex, as well as the geographical regions used for this analysis.

The median particle size distributions and mean aerosol volume fractions for each sampling region are shown in Figure 6.2. Distinct aerosol modes are present at 30 nm and 90 nm in the Los Angeles basin, with a similar but slightly larger bimodal distribution in the marine outflow from the basin ($D_g$ = 30, 100 nm). A similar bimodal size distribution was seen by *Cubison et al.* (2008) for measurements in Riverside, California, during Summer, 2005. They attribute small mode organics observed with an aerosol mass spectrometer to be externally-mixed with a larger, aged, internally-mixed mode of organics and inorganics (*Cubison et al.*, 2008), consistent with measurements in other urban and non-urban settings (e.g., *Murphy et al.*, 2006; *Zhang et al.*, 2005b). Median size distributions in the San Joaquin and Sacramento valleys were found to be primarily unimodal ($D_g \sim 25$ nm).

The average aerosol volume fractions shown in Figure 6.2 were calculated from the C-ToF-AMS mass loadings assuming the aerosol to be internally mixed. Inorganic species densities were obtained from tabulated values and an organic density of 1400 kg $m^{-3}$ is assumed (*Lance et al.*, 2009). Neutral and acidic sulfate species were differentiated using the molar ratio of ammonium ions to sulfate ions, $R_{SO4}$, and mass balance as per *Nenes et al.* (1998). For $R_{SO4} > 2$, sulfate is fully neutralized by the available ammonium and is present as ammonium sulfate, while for $1 < R_{SO4} < 2$, the sulfate is present as ammonium sulfate and ammonium bisulfate. For $R_{SO4} < 1$, the sulfate is a mixture of ammonium bisulfate and sulfuric acid. Nitrate was found to constitute a significant fraction of the aerosol volume and is likely neutralized since $HNO_3$ is volatile at the ambient temperatures typically encountered during CALNEX. In a limited number of cases constituting less than 10% of the sampling time in the Los Angeles basin and San Joaquin Valley, the measured ammonium mass was insufficient to fully neutralize both the measured sulfate and nitrate mass loadings. This suggests either the presence of other cations not explicitly resolved by the C-ToF-AMS (e.g., aminium salts) or the presence of externally mixed acidic sulfate. The "excess nitrate" that cannot be neutralized by ammonium does not contribute significantly to the overall aerosol compositions shown in Figure 6.2, but was found to comprise less

than 6% of aerosol volume during some periods in the Los Angeles basin and San Joaquin Valley. Given the uncertainty of the C-ToF-AMS measurements and external mixing effects, this estimate likely represents an upper limit. *Sorooshian et al.* (2008) measured the aerosol composition downwind of a large bovine source in the San Joaquin Valley and found a significant contribution from amines even in the presence of ammonia. Excess nitrate mass loadings reportedly reached 0.89-1.72 $\mu$g m$^{-3}$ within the source plume, but were close to zero for background conditions in the valley (*Sorooshian et al.*, 2008). Organic species dominate all mass types ($\sim$49-79% by volume), with smaller contributions from ammonium sulfate and ammonium nitrate. Overall, unneutralized sulfate and excess nitrate species constitute only 8-14% of aerosol volume on average.

### 6.3.2 CCN Activity

Vertical profiles of the measured CCN concentration, $N_{CCN}$, and fine particle condensation nucleus (CN, 0.004-1 $\mu$m diameters) concentration, $N_{CN}$, are shown in Figure 6.3. Fine particle concentrations range from 500-100,000 cm$^{-3}$ STP, and concentrations exhibit a decreasing trend above about 1-2 km altitude. CCN concentrations follow a similar trend, but with at least ten-fold lower concentrations, typically ranging from a few tens to several thousand particles per cm$^3$ STP. The overall trends of the vertical profiles observed in each sampling region are similar.

SFCA provides fast measurements of CCN concentrations over 0.25-0.65% supersaturation, $s$, during a 15-second flow scan, and these values were fit to a sigmoidal function of the form:

$$N_{CCN}(s) = \frac{a_0}{1 + \left(\frac{s}{a_1}\right)^{a_2}} \tag{6.1}$$

where $a_0$, $a_1$, and $a_2$ are empirical fitting constants. The fit function was then used to find the differential CCN distribution, $dN_{CCN}/ds$ over the range of 0.2-0.7% supersaturation for each flow upscan. This indirect procedure has the advantage of smoothing out any

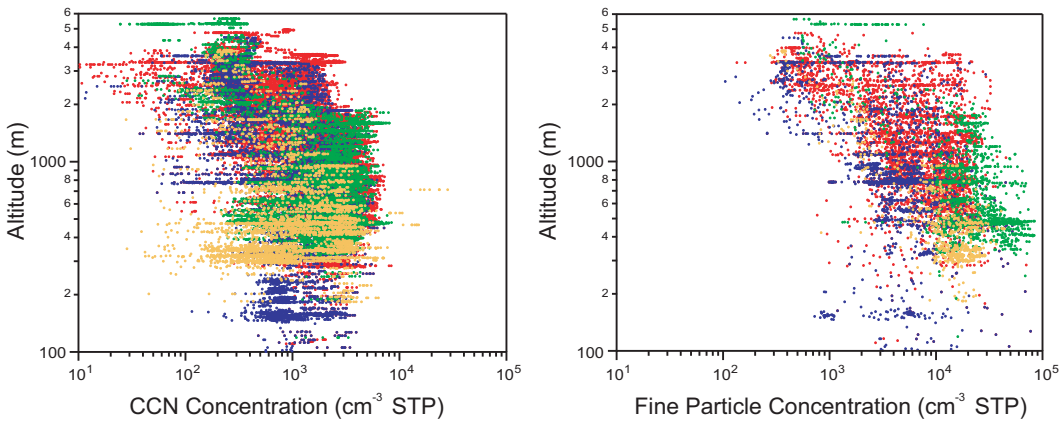


**Figure 6.3:** Vertical profiles of CCN concentrations at 0.25-0.65% supersaturation (left) and submicron, fine particle concentrations (right) measured during CALNEX. Data are color-coded by sampling region as in Figure 6.2.

Poisson counting statistics uncertainty for the 1 Hz CCN concentrations, and is analagous to concentration averaging over 10-second and 30-second periods employed by *Moore et al.* (2011) and *Asa-Awuku et al.* (2011) for constant flow operation of the instrument.

Figure 6.4 shows the average CCN and particle size distributions as a function of C-ToF-AMS organic volume fraction for each sampling region. The geometric mean supersaturation of the CCN distribution varies between 0.35-0.40% for all sampling regions, while the breadth of the distribution is more variable. Most of the CCN distribution falls within 0.2-0.4% supersaturation in the Los Angeles basin and marine outflow regions, although broadening toward higher supersaturations occurs at the highest organic loadings. The bimodal structure seen in Figure 6.2 for these regions is also reflected in the size distribution when the organic volume fraction, $\epsilon_{org}$ is below 0.6. As $\epsilon_{org}$ increases, the size distribution transitions to a unimodal shape. This may reflect particle aging and secondary organic aerosol formation that blurs the distinction between a smaller mode of "fresh", primary particles and a larger mode of well-aged background aerosol similar to that observed by *Cubison et al.* (2008). Although total fine particle concentrations peak at the highest $\epsilon_{org}$ for the marine region, $dN_{CCN}/ds$ decreases in magnitude and broadens considerably, which, perhaps, reflects coastal sources of organic-rich and less-CCN-active pollution

aerosol.

The particle size distributions shown in Figure 6.4 for the San Joaquin and Sacramento Valleys are much more concentrated and unimodal. A more pronounced increase in particle size with increasing $\epsilon_{org}$ is observed, which is consistent with condensational growth of small, freshly-emitted or nucleated particles. The $dN_{CCN}/ds$ distributions in the valleys are much broader than in the Los Angeles basin, although the increase in geometric mean supersaturation between the regions is relatively small. This CCN polydispersity peaks at $\epsilon_{org} \sim$ 0.5-0.7 in the San Joaquin Valley and 0.7-0.75 in the Sacramento Valley, suggesting external mixing of hygroscopic and less-hygroscopic aerosol modes.

In summary, while there is some variation in the regional size distribution, most particles are present in the 10-100 nm size range, which constrains the range of supersaturations required for CCN activation, consistent with the well-known principle that size is more important than composition in determining CCN activity (*Dusek et al.*, 2006; *Twomey*, 1977a). Composition does play an important role, however, which is reflected in the broadening of the CCN spectrum at high aerosol organic fraction. This is seen most clearly in the Central Valley, particularly the Sacramento Valley, where the aerosol organic fraction is greatest.

### 6.3.3 Inferring Hygroscopicity

The compositional and size-dependence of CCN activation is described by Köhler theory (*Köhler*, 1936), and a single parameter representation of this theory has been widely-adopted in recent years (*Petters and Kreidenweis*, 2007). The critical water vapor supersaturation, $s_c$, required for a particle to act as a CCN is given by

$$s_c \approx \sqrt{\frac{4}{\kappa D_{p,c}^3}\left(\frac{4\sigma M_w}{3RT\rho_w}\right)^3} \tag{6.2}$$

where $D_{p,c}$ is the corresponding critical dry particle diameter, $\kappa$ is the hygroscopicity parameter, $R$ is the universal gas constant, $T$ is the absolute temperature, $\sigma$ is the surface tension of the solution droplet at the point of activation, and $M_w$ and $\rho_w$ are the molar

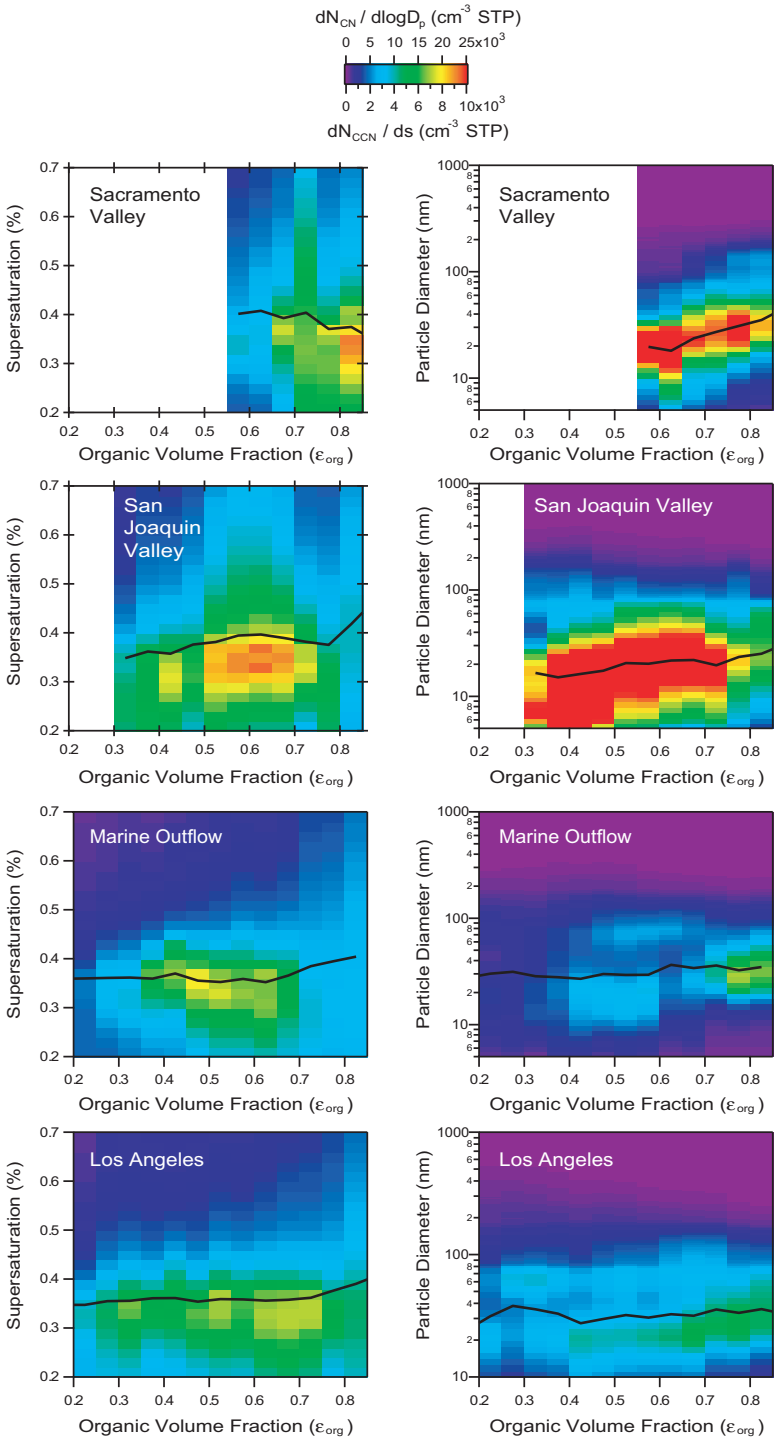


**Figure 6.4:** Average CCN supersaturation distributions (left) and particle size distributions (right) plotted versus the C-ToF-AMS organic volume fraction. Solid traces denote the geometric mean supersaturation and geometric mean diameter.

mass and density of water, respectively. Here, the surface tension of pure water is assumed following the convention of *Petters and Kreidenweis* (2007).

As in *Moore et al.* (2011), Equation 6.2 can be rearranged to state that when particles of a given $\kappa$ are exposed to a constant water vapor supersaturation, those larger than the critical dry diameter, $D_{p,c}$ will act as CCN. Thus, $\kappa$ can be determined by finding $D_{p,c}$ from integrating the the particle size distribution to match the measured CCN concentration at a given supersaturation,

$$N_{CCN} = \int_{D_{p,c}}^{\infty} n_{CN} dD_p \tag{6.3}$$

where $N_{CCN}$ is the measured CCN number concentration, $D_p$ is the dry particle diameter, and $n_{CN}$ is the particle size distribution function. The derived values of $D_{p,c}$ are then used in Equation 6.2 to find $\kappa$.

Figure 6.5 shows the median, CCN-derived $\kappa$ values plotted versus $D_{p,c}$ for each supersaturation measured. Although, the CCN measurements are not size-resolved, it is expected that $\kappa$ would be most characteristic of the aerosol size range near $D_{p,c}$, since that is where CCN concentrations would be most sensitive to small changes in $\kappa$. The error bars in Figure 6.5 denote the interquartile range of observed values. Also shown for comparison are $\kappa$ values calculated from the size-resolved and bulk (i.e., size-averaged) C-ToF-AMS compositions as

$$\kappa = \sum_i \epsilon_i \kappa_i \tag{6.4}$$

where $\epsilon_i$ and $\kappa_i$ are the volume fraction and pure-component hygroscopicity of species, $i$, respectively. Pure-component inorganic $\kappa$ values are computed as in *Moore et al.* (2011), and an organic $\kappa$ of either 0 or 0.11 is assumed. The C-ToF-AMS size-resolved compositions yield much better agreement with the CCN-derived $\kappa$ than is achieved with the bulk compositions. Assuming the organic species to be insoluble or slightly soluble has a small effect on the size-resolved $\kappa$ predictions, but the CCN-derived $\kappa$ seems to agree best with

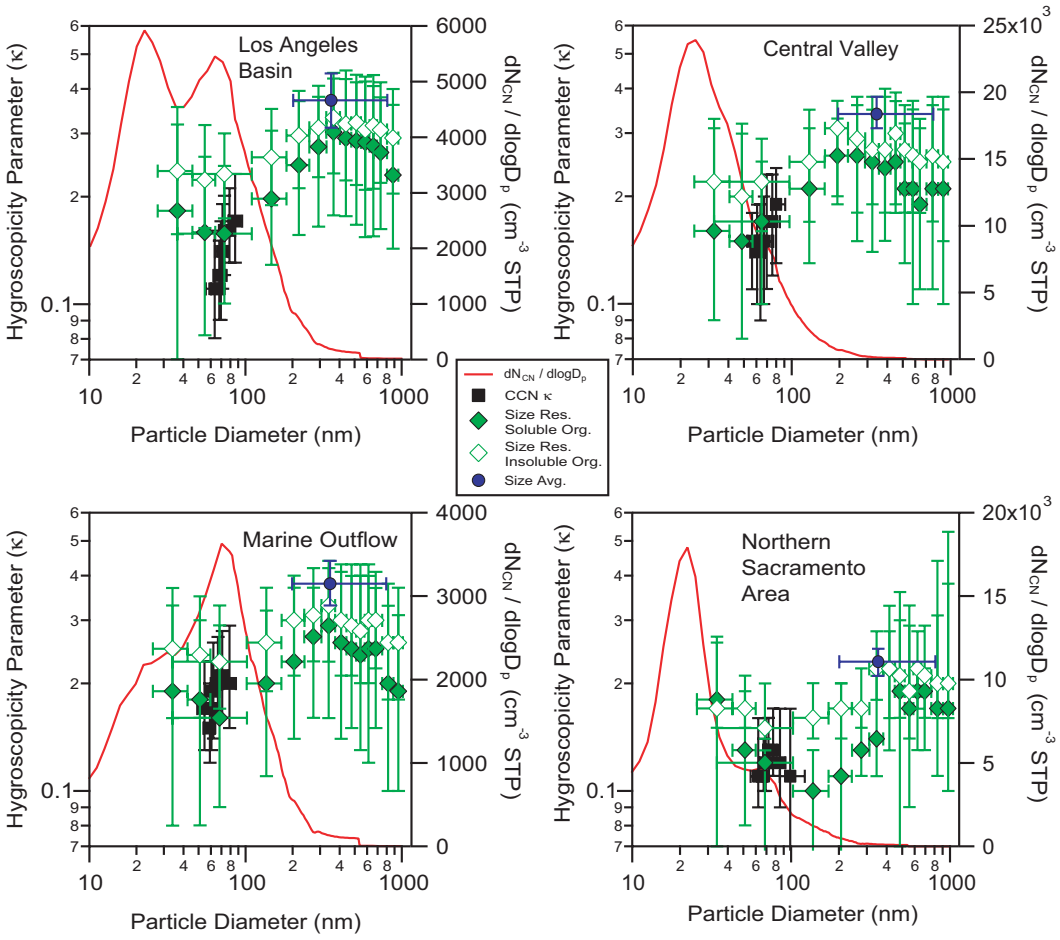


**Figure 6.5:** Aerosol hygroscopicity, $\kappa$, inferred from the measured CCN concentrations and aerosol size distributions, plotted against the critical activation diameter, $D_{p,c}$ for each supersaturation (0.25-0.65%)(squares). Shown for comparison are $\kappa$ values calculated from size-resolved (diamonds) and size-averaged (circles) C-ToF-AMS measurements. Markers denote the median values for each air mass type, while error bars denote the interquartile range. The solid line shows the median particle size distribution from Figure 6.2.

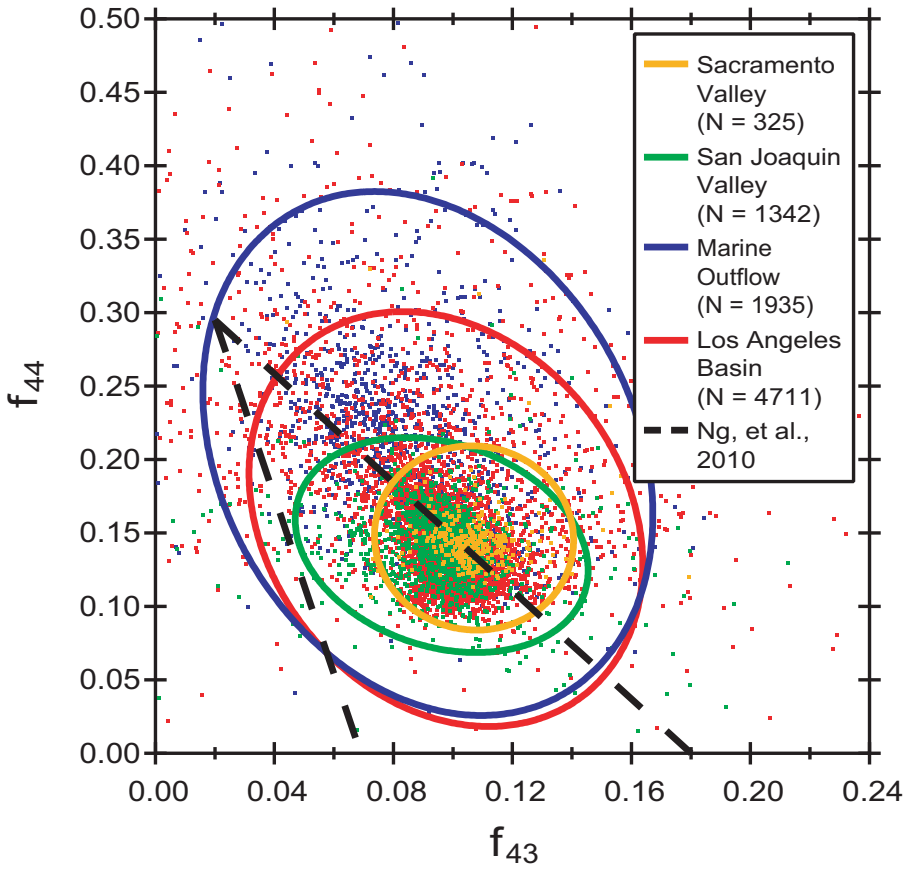


**Figure 6.6:** Oxidation state of the aerosol expressed as $f_{44}$ versus $f_{43}$, following *Ng et al.* (2010). Points denote the 30-second-averaged observations for each sampling region, and the ellipses denote the 95% confidence regions. Dashed lines are the parameterized triangular bounding region reported by *Ng et al.* (2010) for SOA chamber oxidation and ambient measurements.

the predictions based on insoluble organics. This may point to an externally-mixed aerosol with both fresh (non-hygroscopic) and aged (more hygroscopic) organic species. Aerosol mixing state influences will be considered in the CCN closure study in Section 6.3.6. Hygroscopicities derived from bulk C-ToF-AMS chemistry significantly overpredict those measured by the CCNC by almost twofold, which is consistent with *Cubison et al.* (2008), who found size-dependent aerosol compositions were necessary to accurately reproduce the CCN concentrations observed in Riverside, CA.

### 6.3.4 Organic Oxygenation

Figure 6.5 shows that the CCN-derived $\kappa$ is more consistent with size-resolved C-ToF-AMS predictions assuming insoluble organics, although mixing state effects would be expected to also play a role. Past studies have found organic aerosol hygrosocopicity to vary with the degree of oxygenation (e.g., *Jimenez et al.*, 2009; *Duplissy et al.*, 2011; *Chang et al.*, 2010), with more-oxidized organics expected to be less-volatile and more hygroscopic. The C-ToF-AMS $m/z$ 43 and 44 peaks can be used to characterize the organic oxygenation since $m/z$ 44 is mostly the $CO_2^+$ fragment of highly oxygenated organics (e.g., dicarboxylic acids and esters) and $m/z$ 43 is mostly $C_3H_7^+$ and $C_2H_3O^+$ fragments. The ratio of each peak to the total organic aerosol mass ($f_{44}$ and $f_{43}$, respectively) is then a proxy for the total oxygenation of the organic aerosol with higher $f_{44}$ values correlated with higher O:C (*Aiken et al.*, 2008; *Zhang et al.*, 2005b) and hygroscopicity (*Jimenez et al.*, 2009).

Figure 6.6 shows the 95% simultaneous confidence ellipses for $f_{43}$ and $f_{44}$ for each sampling region, where the center of each ellipse denotes the mean $f_{43}$ and $f_{44}$ values. Also shown is the triangular bounding region reported by *Ng et al.* (2010) that describes the range of observations for ambient and chamber oxygenated organic aerosol (OOA). *Ng et al.* (2010) define $f_X$ as the ratio of $m/z$ $X$ to only the OOA aerosol mass, while this study uses the total organic mass. These different definitions are unlikely to bias the comparision between the range of $f_{44}$ values, but would be expected to shift the $f_{43}$ values in this study to higher values than seen by *Ng et al.* (2010) since $m/z$ 43 incorporates both oxygenated and non-oxygenated fragments.

It can be seen from Figure 6.6 that the organic oxygenation of aerosol in the San Joaquin and Sacramento Valleys is less variable than that observed in the Los Angeles basin and marine outflow. Typical $f_{44}$ values were $\sim$0.1-0.2, which corresponds to an approximate O:C ratio of $\sim$0.45-0.85 (*Aiken et al.*, 2008) and organic $\kappa$ of $\sim$0.06-0.2 (*Jimenez et al.*, 2009). This range of organic $\kappa$ agrees very well with the CCN-derived $\kappa$ in Figure 6.5, reflecting the dominance of organic species at small aerosol sizes. An open question is whether the

O:C ratio derived from size-averaged C-ToF-AMS measurements is truly representative of the smaller Aitken-mode particles that determine CCN activity. These results indicate that approximating the CCN-sensitive small aerosol mode with size-dependent composition and size-averaged organic oxygenation properties gives a reasonable prediction of the observed CCN hygroscopicity.

### 6.3.5 Sensitivity of CCN to Composition Effects

While quantifying the aerosol hygroscopicity is important for parameterizing CCN activation and growth, it is also important to assess the overall sensitivity of CCN to $\kappa$. To do these, we examine the theoretical sensitivity of the CCN activated ratio, $R_a$, which is defined as the CCN concentration normalized by the total fine particle concentration. Following *Wang et al.* (2008) and *Moore et al.* (2011), we assume that the aerosol size distribution for each region (shown in Figure 6.2) can be represented well by the sum of two, lognormal aerosol modes. The sensitivity of $R_a$ is then given as

$$\frac{\partial R_a}{\partial \ln \kappa} = \frac{n_{CN}}{3} \tag{6.5}$$

where $n_{CN}$ is the size distribution function given as

$$n_{CN} = \sum_{i}^{2} \frac{1}{\sqrt{2\pi} \ln \sigma_{g,i}} \exp\left(\frac{-\ln^2(D_{p,c}/D_{g,i})}{2\ln^2 \sigma_{g,i}}\right) \tag{6.6}$$

and $D_{g,i}$ and $\sigma_{g,i}$ are the geometric mean diameter and geometric standard deviation of each mode, $i$. Since $D_{p,c}$ is related to $\kappa$ and $s_c$ in Equation 6.2, we can express $\partial R_a/\partial \ln \kappa$ across the range of possible supersaturations. This is shown in Figure 6.7 for sampling region, using bimodal fits to the median size distributions shown in Figure 6.2.

As discussed by *Moore et al.* (2011), the shape of $\partial R_a/\partial \ln \kappa$ implies that $R_a$ is most sensitive to composition changes when $D_{p,c}$ is near the maximum of the size distribution. As discussed in the preceding section, California CCN exhibit $\kappa \sim$ 0.1-0.2, and the sensitivity curves in Figure 6.7 for these values suggest that aerosol in the Los Angeles basin

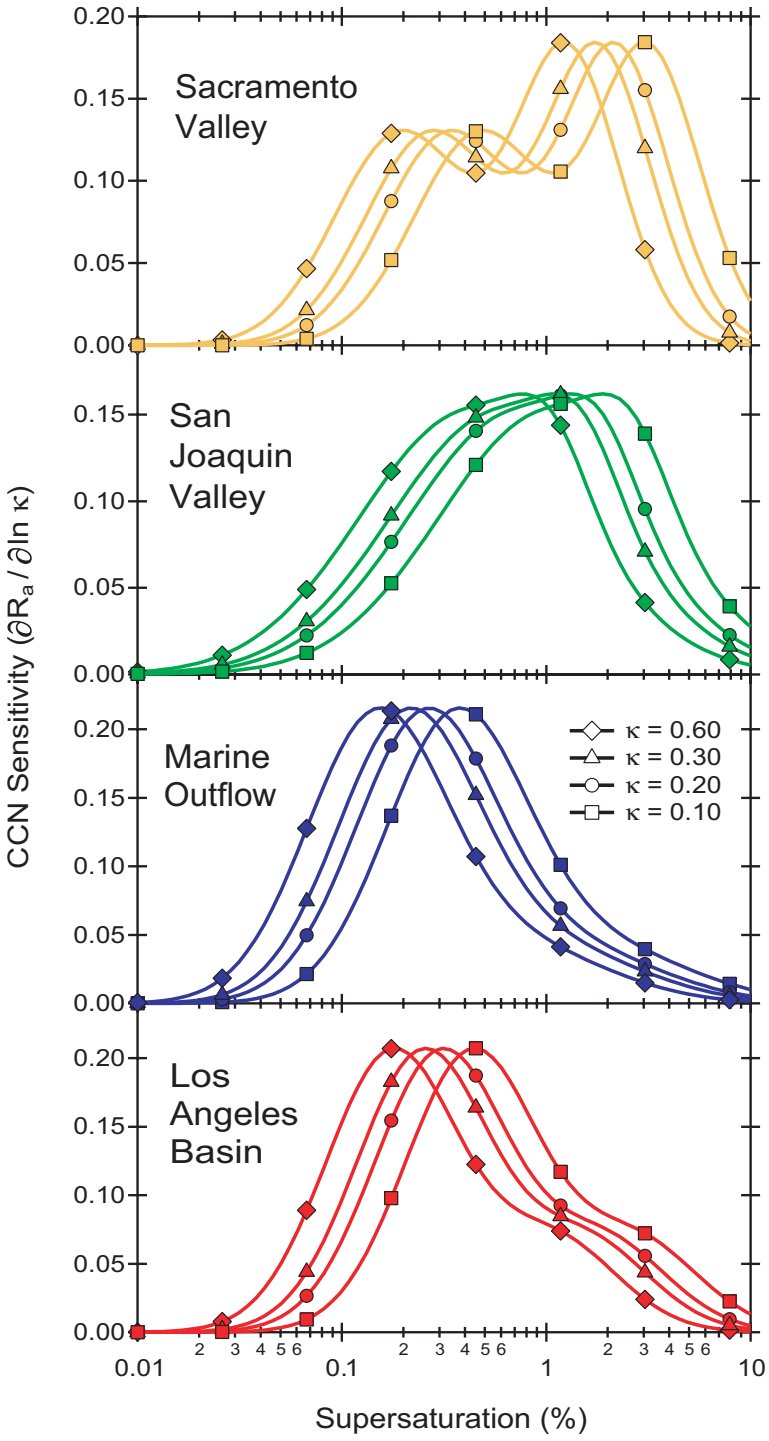


**Figure 6.7:** Sensitivity of the activated ratio, $R_a$ to $\kappa$ as a function of supersaturation. Curves for each sampling region were computed assuming an internal mixture and constant values of $\kappa$, while using a bimodal fit to the median size distributions shown in Figure 6.2.

and marine outflow are at peak sensitivity to compositional effects between 0.25-0.4% supersaturation, while aerosol in the Sacramento and San Joaquin Valleys are more sensitive to $\kappa$ above 0.35% supersaturation.

These estimates are based only on the measured, median size distributions for each sampling region. Yet, the derived range of supersaturations where $R_a$ is sensitive to $\kappa$ agrees very well with the range over which SFCA-measured $dN_{CCN}/ds$ values are highest (Figure 6.4). This implies that California convective and stratiform clouds with supersaturations on the order of 0.2-0.4% are particularly sensitive to aerosol chemical composition effects. This analysis also implies that much of the average CCN supersaturation distribution can be captured assuming a constant aerosol size distribution and a constant value of $\kappa \sim$ 0.1-0.2.

### 6.3.6 CCN Closure

In addition to quantifying the measured size and compositional impacts on CCN activity in terms of $\kappa$, we also seek to quantify the uncertainty associated with using common simplifying assumptions typical of those in large scale models. Termed "CCN closure", this type of error analysis has been performed for a wide range of urban and rural sites (e.g., *Asa-Awuku et al.*, 2011; *Moore et al.*, 2011; *Rose et al.*, 2010; *Ervens et al.*, 2010; *Wang et al.*, 2010a; *Bougiatioti et al.*, 2009; *Lance et al.*, 2009; *Cubison et al.*, 2008; *Broekhuizen et al.*, 2006; *Rissler et al.*, 2004; *VanReken et al.*, 2003, and others).

The CCN concentrations are computed following *Moore et al.* (2011), where the C-ToF-AMS compositional data are first used to find the volume fractions of organics, ammonium nitrate, ammonium sulfate, ammonium bisulfate, and sulfuric acid. These volume fractions are then used to find the aerosol $\kappa$ (Equation 6.4) and the critical activation diameter, $D_{p,c}$, above which all particles act as CCN (Equation 6.2).

In applying these equations, it is necessary to make assumptions regarding the aerosol mixing state (e.g., internal versus external), organic hygroscopicity (e.g., $\kappa_{org}$=0 or $\kappa_{org}$=0.11),

and whether the aerosol composition varies with particle size (e.g., size-dependent or size-invariant). In this study, we examine seven scenarios as follows:

1. *Ammonium Sulfate:* All particles are composed of ammonium sulfate ($\kappa$=0.6)

2. *Internal Mixture, Soluble Organics:* All particles have the same composition as determined by the size-averaged, C-ToF-AMS-derived volume fractions. Organics are soluble with $\kappa$ = 0.11.

3. *Internal Mixture, Insoluble Organics:* All particles have the same composition as determined by the size-averaged, C-ToF-AMS-derived volume fractions. Organics are insoluble with $\kappa$ = 0.

4. *External Mixture, Soluble Organics:* Particles are composed of pure components (e.g., organic particles, ammonium sulfate particles, etc.), and the number of each type is determined by the size-averaged, C-ToF-AMS-derived volume fractions. Organics are soluble with $\kappa$ = 0.11.

5. *External Mixture, Insoluble Organics:* Particles are composed of pure components (e.g., organic particles, ammonium sulfate particles, etc.), and the number of each type is determined by the size-averaged, C-ToF-AMS-derived volume fractions. Organics are insoluble with $\kappa$ = 0.

6. *Internal Mixture, Size-Dependent Composition, Soluble Organics:* Particles in each size distribution bin have the same composition as determined by the size-resolved, C-ToF-AMS-derived volume fractions, but the particle compositions in different size bins may not be the same. Organics are soluble with $\kappa$ = 0.11.

7. *Internal Mixture, Size-Dependent Composition, Insoluble Organics:* Particles in each size distribution bin have the same composition as determined by the size-resolved, C-ToF-AMS-derived volume fractions, but the particle compositions in different size bins may not be the same. Organics are insoluble with $\kappa$ = 0.

Closure was assessed for each scenario in terms of a CCN prediction error ratio, $\Phi = N_{CCN,predicted}/N_{CCN}$. CCN predictions tended toward overprediction, and the mean percent overprediction $(\Phi-1)\times100\%$ for each sampling region and instrument supersaturation are shown in Table 6.2. The scenarios are arranged in columns with increasing complexity from left to right. Assuming the aerosol to be pure ammonium sulfate substantially overpredicts CCN concentrations in all sampling regions, while a modest improvement is gained by incorporating C-ToF-AMS compositions, assuming an internally-mixed aerosol population. Good agreement is found for internally-mixed aerosol with insoluble organics in the Sacramento Valley ($\Phi \sim$ 0.92-1.01); although, given the large measured organic volume fractions and expected sources of secondary organic aerosol in this region, assuming the organics to be insoluble seems unlikely.

Treating the aerosol as externally mixed overpredicts CCN concentrations if organics are assumed to be soluble and underpredicts CCN concentrations if organics are assumed to be insoluble. The Central Valley is an exception, with good closure ($\Phi \sim$ 0.99-1.08) obtained for the San Joaquin Valley, again for the insoluble organics case. Finally, incorporating size-dependent compositions improves closure to within $\pm$10-25% for most sampling regions, which is similar to predictions using size-averaged composition data ($\Phi \sim$ 0.8-1.2), despite the increased complexity.

Figure 6.8 shows the variation of prediction error ratios with measured CCN concentration, and it can be seen that the internally-mixed scenario assuming soluble organics consistently overpredicts CCN over the range of concentrations ($\Phi \sim$ 1.1-2.0), while the externally-mixed, insoluble organics scenario gives a lower overall $\Phi$ but with more scatter ($\sim$ 0.5-1.5). For both scenarios, the median prediction error ratio increases with deceasing CCN concentration beyond what can be explained by decreased CCN counting statistics. Although some of this uncertainty may be associated with increased C-ToF-AMS composition uncertainties at low particle concentrations. The concentration dependence also

**Table 6.2:** Percent overprediction $(\Phi - 1) \times 100\%$ in CCN number concentration from different organic solubility and mixing state assumptions. Data from the CCNC, C-ToF-AMS, and size distributions were averaged over 30-second periods, and N reflects the number of data points used to calculate each mean and standard deviation.

| | | | Internal Mixture | | External Mixture | | Size-Dep. Int. Mix. | |
|---|---|---|---|---|---|---|---|---|
| Air Mass Type | N | Ammonium Sulfate | Soluble Organics | Insoluble Organics | Soluble Organics | Insoluble Organics | Soluble Organics | Insoluble Organics |
| Los Angeles Basin | | | | | | | | |
| $s$ = 0.33 ± 0.04 (%) | 1940 | 125±204 | 73±129 | 54±117 | 51±110 | 0±85 | 37±86 | 18±85 |
| $s$ = 0.38 ± 0.04 (%) | 4268 | 93±110 | 54±60 | 40±55 | 35±53 | -13±44 | 27±40 | 6±43 |
| $s$ = 0.43 ± 0.04 (%) | 4306 | 83±88 | 49±42 | 36±37 | 33±37 | -18±35 | 26±33 | 6±35 |
| $s$ = 0.48 ± 0.04 (%) | 4323 | 83±82 | 51±46 | 39±38 | 36±37 | -18±35 | 30±34 | 10±35 |
| $s$ = 0.53 ± 0.04 (%) | 4344 | 85±77 | 54±45 | 42±41 | 40±40 | -17±36 | 35±35 | 16±36 |
| $s$ = 0.58 ± 0.04 (%) | 4218 | 84±71 | 56±41 | 45±41 | 42±36 | -16±37 | 39±36 | 20±37 |
| $s$ = 0.63 ± 0.04 (%) | 4098 | 76±63 | 49±57 | 39±37 | 37±49 | -20±34 | 35±34 | 18±35 |
| San Joaquin Valley | | | | | | | | |
| $s$ = 0.33 ± 0.04 (%) | 591 | 152±145 | 75±107 | 45±88 | 57±92 | 8±59 | 48±86 | 28±75 |
| $s$ = 0.38 ± 0.04 (%) | 1283 | 143±278 | 75±230 | 47±183 | 56±191 | 4±91 | 42±70 | 23±68 |
| $s$ = 0.43 ± 0.04 (%) | 1303 | 139±310 | 72±268 | 47±220 | 57±230 | 2±97 | 42±70 | 23±65 |
| $s$ = 0.48 ± 0.04 (%) | 1314 | 138±115 | 70±90 | 46±79 | 56±80 | 1±49 | 43±66 | 23±62 |
| $s$ = 0.53 ± 0.04 (%) | 1320 | 143±98 | 74±70 | 49±63 | 60±64 | 3±46 | 48±63 | 28±60 |
| $s$ = 0.58 ± 0.04 (%) | 1163 | 140±86 | 68±47 | 43±42 | 56±48 | 1±47 | 42±59 | 24±60 |
| $s$ = 0.63 ± 0.04 (%) | 1037 | 136±84 | 63±44 | 37±38 | 51±48 | -1±49 | 37±58 | 19±59 |
| Sacramento Valley | | | | | | | | |
| $s$ = 0.33 ± 0.04 (%) | 132 | 389±537 | 36±60 | -2±44 | 21±53 | -56±33 | 10±59 | -14±77 |
| $s$ = 0.38 ± 0.04 (%) | 319 | 195±215 | 24±31 | -6±29 | 11±26 | -59±25 | 7±37 | -19±51 |
| $s$ = 0.43 ± 0.04 (%) | 320 | 140±101 | 19±25 | -8±25 | 11±22 | -60±21 | 4±31 | -20±43 |
| $s$ = 0.48 ± 0.04 (%) | 317 | 124±78 | 22±24 | -4±23 | 14±21 | -59±20 | 7±29 | -15±39 |
| $s$ = 0.53 ± 0.04 (%) | 320 | 120±72 | 25±24 | -1±23 | 18±21 | -58±20 | 9±28 | -10±35 |
| $s$ = 0.58 ± 0.04 (%) | 318 | 116±63 | 28±23 | 1±22 | 21±21 | -57±21 | 13±29 | -6±38 |
| $s$ = 0.63 ± 0.04 (%) | 321 | 105±55 | 24±22 | -2±21 | 17±20 | -58±20 | 8±27 | -13±45 |
| Marine Outflow Near LA Basin | | | | | | | | |
| $s$ = 0.33 ± 0.04 (%) | 657 | 81±97 | 50±80 | 37±76 | 31±71 | -8±57 | 20±62 | 1±61 |
| $s$ = 0.38 ± 0.04 (%) | 1455 | 61±88 | 33±43 | 22±39 | 17±38 | -21±33 | 9±42 | -10±41 |
| $s$ = 0.43 ± 0.04 (%) | 1505 | 56±104 | 29±32 | 20±28 | 17±30 | -24±29 | 8±26 | -11±31 |
| $s$ = 0.48 ± 0.04 (%) | 1466 | 55±90 | 29±31 | 20±26 | 18±30 | -25±29 | 9±26 | -8±31 |
| $s$ = 0.53 ± 0.04 (%) | 1464 | 58±105 | 31±32 | 23±26 | 21±30 | -24±29 | 13±25 | -4±29 |
| $s$ = 0.58 ± 0.04 (%) | 1463 | 58±77 | 34±32 | 25±26 | 24±30 | -23±30 | 16±25 | 0±29 |
| $s$ = 0.63 ± 0.04 (%) | 1457 | 53±66 | 29±30 | 21±24 | 21±28 | -26±28 | 14±24 | -2±27 |

appears to be slightly more pronounced for the external mixture, insoluble organics scenario than for the internally-mixed, soluble organics case. The greatest underpredictions are seen for the Sacramento Valley, where CCN concentrations were highest when $\epsilon_{org}$ was high (Figure 6.4). Consequently, the significant underprediction observed at high concentrations may occur from assuming insoluble organics.

This analysis shows that the assumed aerosol mixing state and organic solubility are important for predicting CCN in California, and that the aerosol are likely to be at least partially externally mixed with both soluble and insoluble organics; however, it is not possible

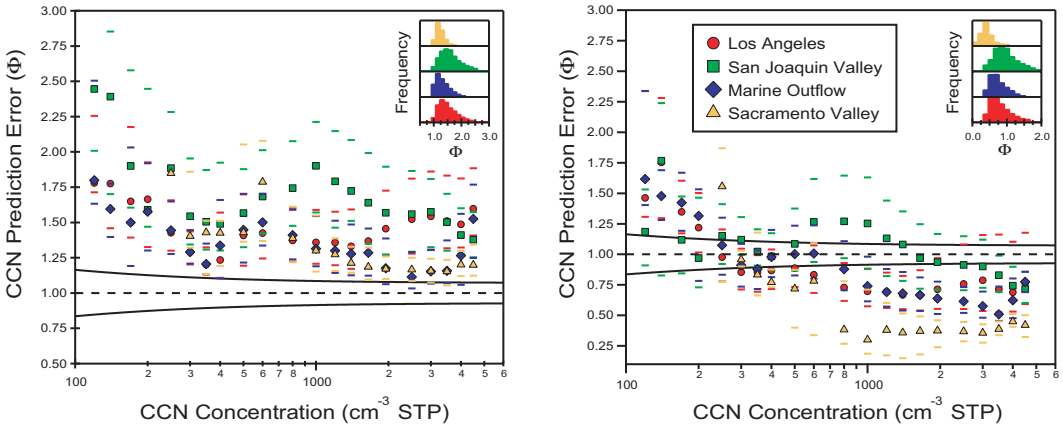


**Figure 6.8:** CCN prediction error for 0.30-0.65% supersaturation versus measured CCN concentrations. Predictions were computed assuming that the aerosols is internally-mixed with $\kappa_{org}$=0.11 (left) and externally-mixed with $\kappa_{org}$=0 (right). Markers enote the median error for each sampling region, while the bars denote the interquartile range. The dotted line at $\Phi$ = 1 denotes perfect agreement and the solid bounding curves indicate the CCN measurement uncertainty. The inset plots show the frequency distribution of $\Phi$ for all 30-second-averaged data points.

to deconvolute these effects. *Asa-Awuku et al.* (2011) and *Wang et al.* (2010a) were able to achieve closure to within similar uncertainties ($\sim$ 20%) for urban aerosol in the vicinity of Houston, TX, and Mexico City, Mexico, respectively. The latter study notes that agreement was predicated on most aerosol having $\kappa > 0.1$ (*Wang et al.*, 2010a). *Cubison et al.* (2008) performed CCN closure for aerosol sampled in Riverside, California, and report substantially higher prediction uncertainties ($\Phi \sim$ 4-6) for similar size-averaged scenarios as employed here (*Ervens et al.*, 2010), which were attributed to the influence of fresh emissions of non-CCN-active elemental carbon and small particles (*Cubison et al.*, 2008). Ship-based measurements in the ship channel near Houston, TX, also showed large CCN overpredictions ($\Phi \sim$ 1.7-2.4) in a recent closure study, which again were explained by close proximity to local emissions sources (*Quinn et al.*, 2008a; *Ervens et al.*, 2010). Thus, while these results are broadly representative of the regional aerosol near Los Angeles and the Central Valley of California, they do not seem to capture the increased uncertainty associated with localized fresh emissions sources that may be important for assessing air quality

impacts. Given the relatively low resolution of large scale models, however, the more regional nature of these measurements may be more appropriate for future assessments of climate prediction uncertainties.

## *6.4 Summary and Conclusions*

Measurements of CCN and aerosol properties obtained during the CalNex project in May-June, 2010, are presented and analyzed. Assuming the aerosol to be internally-mixed was found to significantly overpredict CCN concentration by 30-75% for all sampling regions except the Sacramento Valley, where good closure ($<$10%) was achieved assuming insoluble organics. Assuming the aerosol to be externally-mixed with insoluble organics underpredicted CCN concentrations, on average. This suggests that California aerosol is likely to be only partially externally mixed, which is consistent with the observed biomodal size distributions and with the coexistence of both fresh and aged aerosol.

We also quantify the compositional dependence of CCN activity in terms of the hygroscopicity parameter, $\kappa$, which was found to vary between 0.1-0.2 with very little supersaturation or size dependence. CCN-derived $\kappa$ and those calculated from size-resolved C-ToF-AMS compositions were found to agree very well; although, using size-averaged C-ToF-AMS compositions overpredicted $\kappa$ by almost twofold. Calculations based on the median size distributions for each sampling region suggest that CCN concentrations are at peak sensitivity to compositional effects for supersaturations between 0.2-0.6%, which is agrees remarkably well with the measured $dN_{CCN}/ds$ distributions, which were also centered in this range. This suggests that using regional aerosol properties is sufficient for capturing the overall trend in CCN concentrations; although, this likely does not account for small scale features such as fresh emissions plumes.

# CHAPTER VII

# HYGROSCOPICITY AND GROWTH KINETICS OF SECONDARY ORGANIC AEROSOL FROM THE DEEPWATER HORIZON OIL SPILL

Secondary organic aerosol (SOA) resulting from the oxidation of organic species emitted by the Deepwater Horizon oil spill were sampled during two survey flights conducted by a National Oceanic and Atmospheric Administration (NOAA) WP-3D aircraft in June 2010. A new technique for fast measurements of cloud condensation nuclei (CCN) supersaturation spectra called Scanning Flow CCN Analysis (SFCA) was deployed for the first time on an airborne platform. Retrieved CCN spectra show that most particles act as CCN above (0.3$\pm$0.05)% supersaturation, which increased to (0.4$\pm$0.1)% supersaturation for the most organic-rich aerosol sampled. The aerosol hygroscopicity parameter, $\kappa$, was inferred from both measurements of CCN activity and from humidified-particle light extinction, and varied from 0.05-0.10 within the emissions plumes. However, $\kappa$ values were lower than expected from chemical composition measurements, indicating a degree of external mixing or size-dependent chemistry, which was reconciled assuming bimodal, size-dependent composition. The CCN droplet effective water uptake coefficient, $\gamma_{cond}$, was inferred using a comprehensive instrument model, and no significant delay in droplet activation kinetics from the presence of organics was observed, despite a large fraction of hydrocarbon-like SOA present in the aerosol.

This chapter submitted for publication as: Moore, R. H., T. Raatikainen, J. M. Langridge, R. Bahreini, C. A. Brock, J. S. Holloway, D. A. Lack, A. M. Middlebrook, A. E. Perring, J. P. Schwarz, J. R. Spackman, and A. Nenes (submitted), CCN spectra, hygroscopicity, and droplet activation kinetics of secondary organic aerosol resulting from the 2010 Deepwater Horizon oil spill, Environmental Science and Technology.

## 7.1 Introduction

The explosion and loss of the Deepwater Horizon (DWH) oil platform on 20 April 2010 resulted in the release of millions of barrels of oil into the waters of the Gulf of Mexico during April-July, 2010 (*Crone and Tolstoy*, 2010). While a large portion of the oil-gas mixture remained dissolved or dispersed in the water column, a substantial portion reached the water surface and evaporated into the atmosphere over a period of hours to days (*Ryerson et al.*, 2011; *de Gouw et al.*, 2011). Volatile organic carbon (VOC) and intermediate volatility organic carbon (IVOC) species are oxidized in the atmosphere, which lowers their volatility causing them to nucleate new particles or condense onto existing aerosol particles. Termed secondary organic aerosol (SOA), these particles are an important but uncertain contributor to adverse air quality and climate change (*de Gouw and Jimenez*, 2009; *Hallquist et al.*, 2009).

This chapter presents a detailed characterization of the hygroscopic and droplet-forming properties of SOA formed in the vicinity of the DWH site during two survey flights conducted by the National Oceanic and Atmospheric Administration (NOAA) WP-3D aircraft on 8 and 10 June 2010. These survey flights provide a unique case study of hydrocarbon-derived SOA that has experienced relatively little atmospheric oxidative processing and whose concentrations exceed those of the more oxidatively-aged organic aerosol background. Both fresh and aged SOA coexist in urban environments, although the latter species are usually much more abundant (*Zhang et al.*, 2007), and, hence, may obscure the influence of the former on measured cloud condensation nuclei (CCN) activation and droplet growth.

## 7.2 Methodology

The observational data were obtained on two survey flights conducted near the site of the DWH oil platform (28°44'12"N, 88°23'13"W) on 8 and 10 June 2010. Data were filtered to include only those sampled within the lower portion of the marine boundary layer at

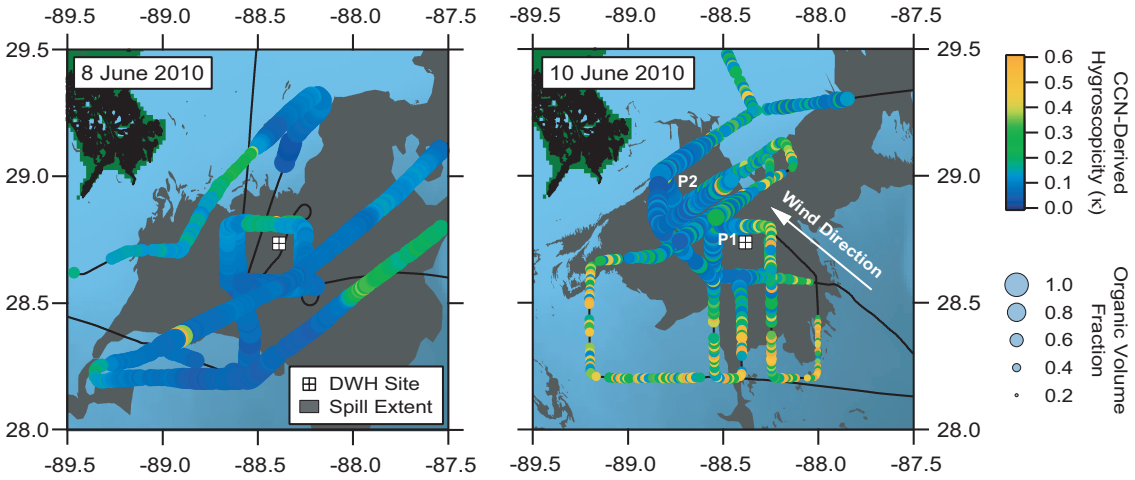


**Figure 7.1:** Aircraft trajectories for the survey flights on 8 June (left) and 10 June (right) when the aircraft was sampling near the DWH spill site. Markers are colored by the CCN-derived hygroscopicity and sized by the aerosol organic volume fraction. The gray shaded area represents the satellite-derived extent of surface oil (both fresh and aged) (*NOAA-NESDIS*, 2010). Winds on June 8th were light and variable, but were more sustained from the southeast on 10 June. P1 and P2 denote the separate plume interceptions on 10 June described by (*de Gouw et al.*, 2011). The ordinate and abscissa denote degrees latitude and longitude, respectively.

between 50 and 150 meters altitude above sea level. Intermittent periods with elevated CO mixing ratios (>150 ppbv), indicative of combustion sources, were rarely observed but were also excluded from the dataset in order to focus solely on the SOA signature. This filtering process also excludes the interception of the plume from a surface oil burn southwest of the DWH site on 8 June (*Perring et al.*, 2011). Flight tracks near the DWH site are shown in Figure 7.1, while the entire, unfiltered flight tracks are provided in the supporting information (Section 7.5).

### 7.2.1 CCN and Aerosol Measurements

CCN concentration measurements were obtained using a Droplet Measurement Technologies (DMT) stream-wise thermal-gradient cloud condensation nuclei counter (CCNC) (*Roberts and Nenes*, 2005; *Lance et al.*, 2006), which exposes an aerosol to a specified water vapor

supersaturation and counts and sizes the droplets that form. Since the supersaturation in the instrument is sensitive to pressure fluctuations, the pressure inside the growth chamber was kept constant at 500 hPa using a flow orifice and active control system. On 8 June, the CCNC was operated at a constant flow rate (0.5 L $min^{-1}$) and a single supersaturation of 0.33% for the duration of the flight, while on 10 June, the CCNC supersaturation was dynamically scanned over a range of supersaturations (0.2-0.7%) every 15 seconds using Scanning Flow CCN Analysis (SFCA) (*Moore and Nenes*, 2009). Supersaturations were calibrated in terms of the CCNC internal temperature gradient and flow rate using size-classified ammonium sulfate aerosol and Köhler theory (*Köhler*, 1936; *Rose et al.*, 2008; *Moore et al.*, 2010). The supersaturation absolute uncertainty is estimated to be $\pm$0.04%.

Subsaturated hygroscopicity measurements were obtained from a cavity ringdown (CRD) spectrometer measuring aerosol extinction at 532 nm wavelength under both dry (10%RH) and humidified (70-95%RH) conditions (*Langridge et al.*, 2011).

Fine mode dry particle size distribution measurements (0.004 to 1 $\mu$m diameter) were obtained every second from an ultra-high sensitivity aerosol size spectrometer (UHSAS) and a nucleation mode aerosol size spectrometer (NMASS). The NMASS consists of five condensation particle counters (0.004, 0.008, 0.015, 0.030, and 0.055 $\mu$m cutoff diameters) that are coupled to the UHSAS distribution using a nonlinear inversion algorithm to obtain the complete size distribution (*Brock et al.*, 2000, 2011a).

Non-refractory, sub-micron aerosol chemical composition was measured using a compact time-of-flight aerosol mass spectrometer (C-ToF-AMS) with a pressure-controlled inlet (*Bahreini et al.*, 2008; *DeCarlo et al.*, 2006; *Drewnick et al.*, 2005). The instrument was operated in "mass spectrum" mode to obtain bulk (i.e., size-averaged) mass spectra with a 0.1 Hz resolution and in "time-of-flight" mode to obtain size-resolved mass spectra, which were then averaged over 5 minute periods to improve signal-to-noise. The mass spectra were integrated to calculate the total mass loadings for sulfate, nitrate, ammonium, and organic aerosol components. Mass loadings of elemental carbon were obtained from a single

particle soot photometer (SP2) and were found to be much smaller than the non-refractory mass measured by the C-ToF-AMS (*Perring et al.*, 2011; *Schwarz et al.*, 2008).

### 7.2.2 Coupled CCNC Instrument Model

An important feature of the DMT CCNC is the ability to measure the size distribution of activated droplets leaving the flow chamber; this makes it possible to infer information about activation kinetics. To first order, this can be done by qualitatively comparing the measured droplet size distribution to that obtained for calibration aerosol (e.g., $(NH_4)_2SO_4$ or NaCl) at the same instrument operating conditions (flow rate, pressure, and applied temperature gradient). If the measured mean droplet size exceeds that for calibration aerosol, slow activation kinetics can be ruled out, while a lower measured mean droplet size may suggest slow kinetics. Termed Threshold Droplet Growth Analysis, this procedure has been applied in a number of past studies with success (*Lathem and Nenes*, 2011). However, in addition to the basic instrument operating parameters, droplet sizes are also dependent on the aerosol size distribution, and to a lesser extent, the aerosol number concentration in the growth chamber (*Lathem and Nenes*, 2011). We use a detailed numerical model to deconvolve these dependencies, allowing the quantification of composition impacts on droplet activation kinetics in terms of an empirical water uptake coefficient, $\gamma_{cond}$, that accounts for gas- and particle-phase mass transfer resistances, solute dissolution kinetics, and for the sticking probability of a water vapor molecule colliding with a growing water droplet.

The coupled CCNC instrument and droplet growth model (*Lance et al.*, 2006; *Lathem and Nenes*, 2011), together with recent improvements by *Raatikainen et al.* (A Coupled Instrument and Droplet Growth Model for Inferring CCN Activation Kinetics From the DMT CCNC, manuscript in preparation, 2011) is used here to numerically solve the coupled momentum, mass, and energy balance equations for an aerosol population traversing the CCNC flow field. Model predictions of both the droplet number concentration and size distribution leaving the CCNC growth chamber are compared to the measurements in

order to determine the value of $\gamma_{cond}$ that gives the best agreement between predicted and measured droplet sizes.

### 7.2.3 Analysis

The ability of a particle to act as a CCN depends on its size, chemical composition, and on the ambient water vapor supersaturation (*Köhler*, 1936). This compositional dependence is commonly parameterized in terms of a hygroscopicity parameter, $\kappa$, in Köhler theory (*Petters and Kreidenweis*, 2007)

$$\kappa = \frac{4}{s^2 D_{p,c}^3} \left( \frac{4\sigma M_w}{3RT\rho_w} \right)^3 \tag{7.1}$$

where $s$ is the water vapor supersaturation, $D_{p,c}$ is the particle critical dry diameter (above which all particles act as CCN), $\sigma$ is the surface tension of the solution droplet, $R$ is the gas constant, $T$ is the absolute temperature, and $M_w$ and $\rho_w$ are the molar mass and density of water, respectively. In this study, the surface tension of pure water is assumed. Following *Moore et al.* (2011), $\kappa$ is calculated by integrating the aerosol size distribution above some $D_{p,c}$ so that the integrated concentration matches the measured CCN concentration at a specified supersaturation. This value of $D_{p,c}$ is then used in Equation 7.1 to find $\kappa$.

While the hygroscopicity parameter is unable to unambiguously account for complex aerosol mixing state or surface tension impacts, using the above approach offers a simple way to parameterize composition for global models and is applicable to other measures of water uptake, such as in subsaturated conditions. While $\kappa$ is expected to be similar for both water vapor saturation ratios less than and greater than unity, solution non-ideality or surface tension effects in the former may yield a derived subsaturated $\kappa$ that is somewhat lower than for supersaturated cloud droplets, which are more dilute (*Petters and Kreidenweis*, 2007; *Cerully et al.*, 2011).

The subsaturated humidity dependence of the CRD aerosol extinction was used to derive the aerosol humidification factor, $\gamma_{ext}$, as

$$\frac{\sigma_{RH}}{\sigma_{RH_{ref}}} = \left[\frac{1 - RH}{1 - RH_{ref}}\right]^{\gamma_{ext}} \tag{7.2}$$

where $\sigma_{RH}$ is the measured aerosol extinction at relative humidity, RH. The humidification factor represents the dependence of aerosol extinction on RH, which results from changes in the particle size and refractive index upon humidification. Thus, $\gamma_{ext}$ and $\kappa$ are related quantities and one can employ Mie theory with a number of assumptions to independently derive $\kappa$ from $\gamma_{ext}$. These calculations were performed using the CRD data together with the measured dry particle distribution and a prescribed refractive index (RI) of 1.45 - $0i$. Further details regarding the calculation approach and sensitivity to the RI assumption are presented in the supporting information (Section 7.5).

## *7.3 Results and Discussion*

### 7.3.1 CCN Activity and Hygroscopicity

Figure 7.1 shows the collocated spatial distribution of the CCN-derived $\kappa$ and the organic aerosol volume fraction for the low-level flight legs near the DWH site. Greater variability in $\kappa$ for adjacent points far from the DWH site on 10 June exceeds that seen on 8 June, which may reflect size-dependent aerosol composition because the changing instrument supersaturation during SFCA operation on 10 June also changes the size range over which CCN measurements are most sensitive (i.e., diameters near $D_{p,c}$). Winds on 8 June were light with variable direction, while a more sustained southeasterly flow was present on 10 June. This gives rise to a distinct plume of low-hygroscopicity, organic aerosol to the northwest of the DWH site on the 10th. *de Gouw et al.* (2011) examined the gas- and aerosol-phase composition on this day for a plume transect near the DWH site (P1) and a transect farther downwind (P2). They found a narrow plume of VOCs surrounded by a much broader plume of hydrocarbon-like SOA, with the organic aerosol concentration and size distribution both increasing from P1 to P2 (*de Gouw et al.*, 2011). Transport calculations based on wind speed and direction suggest that the enhancement in SOA results

from less-volatile IVOC precursors (likely $C_{14}$ to $C_{16}$ compounds), which evaporate over a period of hours to days after surfacing and are chemically transformed to SOA within a few hours in the atmosphere (*de Gouw et al.*, 2011). The importance of a sustained wind direction in dispersing the oil emissions is apparent from the lack of an appreciable organic fraction south of the DWH site on the 10th, but a wider impacted area on the 8th. Satellite imagery of the spill extent (gray shaded region in Figure 7.1) on both days does not necessary coincide with enhancements in gas- or aerosol-phase species, suggesting that the "highly-aged" portion of the oil slick consists of low volatility compounds, which do not contribute appreciably to SOA.

The changes in the total particle size distribution ($dN_{CN}/dlogD_p$) and CCN supersaturation distribution ($dN_{CCN}/ds$) across different organic aerosol fractions are shown in Figure 7.2. The solid trace denotes the geometric means and the circles denote the mean values for P1 and P2. A small accumulation mode of a few thousand particles per $cm^3$ is present at all organic fractions with a significant Aitken mode appearing at organic fractions above 60%. The mean size of the Aitken mode increases by roughly three-fold over the observed range of organic fractions, consistent with condensational growth from semi-volatile organic vapors. A large Aitken mode is also present in Figure 7.2 between 30%-40% organics, which reflects the sampling of freshly nucleated particles in the absence of organic condensation on existing large particles just upwind of the DWH site (*Brock et al.*, 2011b). For organic volume fractions less than 75-80%, the peak of the CCN distribution is around (0.30±0.05)% supersaturation, which broadens considerably and shifts to approximately (0.4±0.1)% supersaturation at the highest organic fractions.

The increase in critical supersaturation coincides with an increase in the mean particle diameter, which implies a significant decrease in the particle hygroscopicity since increasing particle size tends to strongly decrease the critical supersaturation. This is shown by the inverse correlation between $\kappa$, $\gamma_{ext}$, and organic volume fraction in Figure 7.3a,b. The overall $\kappa$ for an aerosol containing $n$ components is calculated as

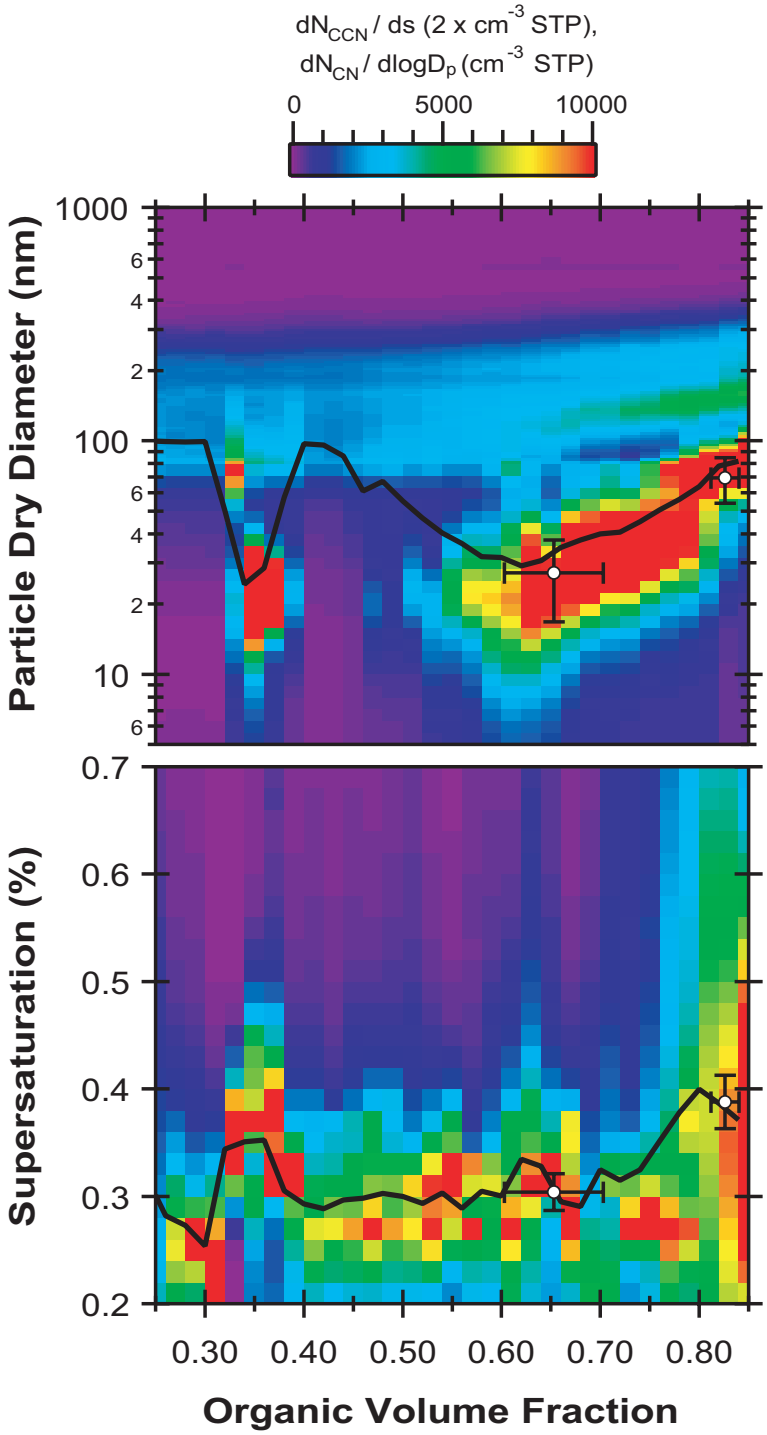


**Figure 7.2:** Average particle size distributions (top) and CCN supersaturation distributions (bottom) plotted versus the C-ToF-AMS organic volume fraction for the 10 June flight. Solid traces denote the geometric mean diameter and supersaturation in the top and bottom figures, respectively, calculated for a single mode. Circles show the mean values for the intercepted plume at P1 and P2 ($\pm$ 1 standard deviation).

$$\kappa = \sum_{i}^{n} \epsilon_i \kappa_i \tag{7.3}$$

where $\epsilon_i$ and $\kappa_i$ are the volume fraction and hygroscopicity of the $i$-th aerosol component, respectively. Two-component mixing lines were calculated from Equation 7.3 assuming a constant inorganic hygroscopicity, $\kappa_{inorg}$, of 0.6 and a constant organic hygroscopicity, $\kappa_{org}$, of either 0 or 0.1 (dashed traces in Figure 7.3a). It can be seen from Figure 7.3a that the observed aerosol hygroscopicity lies below even the $\kappa_{org}$=0 mixing line, which likely reflects size-dependent composition or a partially externally-mixed aerosol population not captured by these simple, but commonly-employed mixing rules. Extrapolating the piece-wise linear fit of the median $\kappa$ data in Figure 7.3a to $\epsilon_{org}$=1 yields an effective $\kappa_{org}$=0.05. In modeling the condensational growth rate of SOA near the DWH site, *Brock et al.* (2011b) assumed an intermediate-volatility organic species with a molar mass of 0.292 kg mol$^{-1}$ and density of 1000 kg m$^{-3}$. Using these values and a unit van't Hoff factor to estimate $\kappa_{org} = (M_w/\rho_w)(\rho_{org}/M_{org})$, yields a value of 0.06 consistent with the CCN-derived estimate.

A number of ambient and SOA chamber studies have shown that the pure organic hygroscopicity increases with increasing organic oxygenation (*Jimenez et al.*, 2009; *Chang et al.*, 2010; *Duplissy et al.*, 2011). The C-ToF-AMS mass fraction of the *m/z* 44 peak to total organic mass, $f_{44}$, is correlated with the organic O:C ratio (*Aiken et al.*, 2008; *Zhang et al.*, 2005a), and the relationship between $\kappa_{org}$ and $f_{44}$ or O:C has been reported for some previous measurements (*Chang et al.*, 2010; *Duplissy et al.*, 2011). From Figure 7.3c, it can be observed that aerosol composed almost entirely of SOA are less-oxidized than aerosol composed only partially of SOA. This trend reflects the varying contribution of the low-O:C, fresh SOA and the higher-O:C, aged background organic aerosol to the total aerosol composition, where the former dominate at high $\epsilon_{org}$ near the DWH site and the latter dominate at lower $\epsilon_{org}$ outside of these SOA plumes. Using two parameterizations for $\kappa_{org}$ and

a constant $\kappa_{inorg}$=0.6 yields the dark shaded regions shown in Figure 7.3a, which considerably overpredict the aerosol hygroscopicity parameter by a similar amount as the $\kappa_{org}$=0.1 mixing line.

As shown in Figure 7.2, a distinct accumulation size mode is present throughout the survey flights with a more prominent Aitken size mode associated with the organic-rich aerosol near the DWH site. Consequently, size-resolved C-ToF-AMS chemical composition was used to look for compositional differences between the two modes, which may explain the overprediction shown in Figure 7.3a. As discussed in the supporting information (Section 7.5), a lower size-resolved, organic volume fraction $\epsilon_{SR,org}$ was observed for the accumulation mode ($\sim$0.4-0.8) versus the Aitken mode ($\sim$0.85-1). While the larger-sized particles affect the bulk (i.e., size-averaged) C-ToF-AMS composition more so than the smaller particles, the Aitken-mode-dominated number size distribution is a more important determinant of CCN activity. Using the average composition for each mode, $\kappa$ was calculated for both the accumulation mode and the Aitken mode aerosol assuming $\kappa_{org}$=0.05 and $\kappa_{inorg}$=0.6. The overall $\kappa$ is then obtained from a CCN number-weighted average of the two modes and is shown as the blue shaded region in Figure 7.3, where it can be seen that predictions of $\kappa$ based on a two-mode, size-dependent composition are in much better agreement with observations than those obtained from bulk (i.e., size-averaged) composition, both using the same simple mixing rule assumptions.

A comparison between the supersaturated, CCN-derived $\kappa_{CCN}$ and the subsaturated, CRD-derived $\kappa_{CRD}$ is shown for the entire June 8th flight in the lower part of Figure 7.4. For most of the flight, $\kappa_{CRD}$ is approximately 50% less than $\kappa_{CCN}$ (Figure 7.7), although the data are highly correlated assuming a constant 50% bias ($R^2$ = 0.75). A similar discrepancy ($\sim$30-50%) has been previously observed for comparision of CCN-derived hygroscopicities and those inferred from subsaturated measurements with an humified tandem differential mobility analyzer (HTDMA) (*Cerully et al.*, 2011; *Roberts et al.*, 2010). This suggests that while the humidification of organic-rich aerosol has a small effect on their

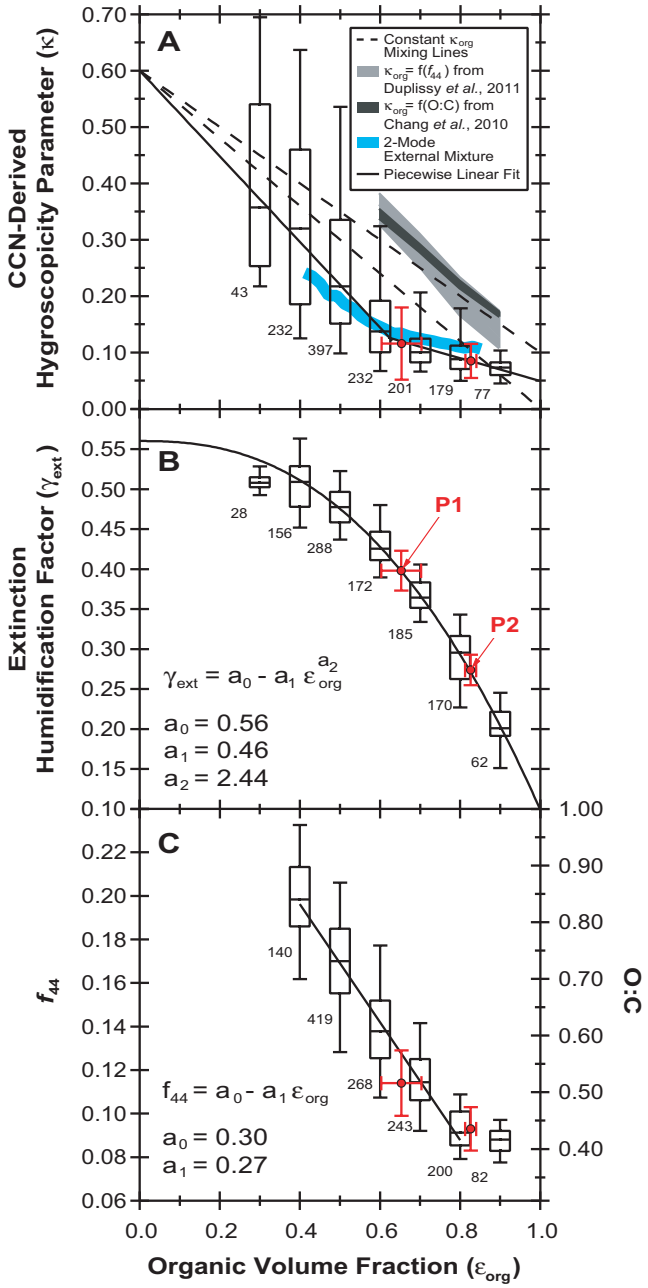


**Figure 7.3:** Distribution of (a) CCN-derived hygroscopicity, (b) extinction humidification factor, and (c) $f_{44}$ ratio and O:C ratio (from the *Aiken et al.* (2008) correlation) plotted versus C-ToF-AMS organic volume fraction. Boxes denote the median and interquartile range for all observations from both flights between 50 and 150 meters altitude, while the numbers beside each box denote the number of 0.1 Hz points used in the calculation. Solid traces are fits to the median data. Circles show the mean values for the intercepted plume at P1 and P2 on June 10th ($\pm$ 1 standard deviation). Shaded areas and dashed traces in (a) are $\kappa$ predictions from different compositional assumptions.

size and light scattering ($\kappa_{CRD} \sim$ 0.01-0.05), these particles have a greater contribution to CCN activation ($\kappa_{CCN} \sim$ 0.05-0.10).

### 7.3.2 Droplet Activation Kinetics

Figure 7.4 presents the droplet size distribution of activated CCN in the CCNC (normalized by the total number of droplets), the number-averaged mean droplet size, and the modeled mean droplet size for aerosol with an effective water uptake coefficient, $\gamma_{cond}$, of 0.2. It can be seen that the temporal variability is strongly correlated for the measured and modeled mean droplet sizes when accounting for supersaturation depletion effects from moderate CCN concentrations in the CCNC growth chamber ($\sim$1000-3000 cm$^{-3}$ STP) (*Lathem and Nenes*, 2011). Neglecting the depletion effects leads to a larger mean droplet size and much less variability in the predictions, which is not in agreement with observations. This is because, even though supersaturation depletion has a limited effect on the measured CCN concentration, it can have an observable effect on the measured droplet size distribution. The simulated traces were corrected by a constant 2.3 $\mu$m bias, which gives the best agreement between the $\gamma_{cond}$=0.2 simulated and observed droplet sizes (see Section 7.5). Simulations of ammonium sulfate calibration aerosol reveal a 2.1 $\mu$m model overprediction bias, which is in good agreement with the correction bias applied here. Regression analysis of the modeled versus measured mean droplet sizes indicates that a constant value of $\gamma_{cond}$ between 0.1 and 0.2 reproduces the observed droplet size variability for the entire dataset.

While it is known that droplet formation is less sensitive to changes in $\gamma_{cond}$ in the range of 0.1-1 versus lower values (*Nenes et al.*, 2002), the exact value of $\gamma_{cond}$, even for pure water droplets, remains uncertain with reported values in the range of 0.04 to 1 (*Davis*, 2006; *Li et al.*, 2001; *Shaw and Lamb*, 1999; *Mozurkewich*, 1986). The most realistic value is probably between 0.06 and 0.3 (*Fountoukis et al.*, 2007; *Li et al.*, 2001; *Shaw and Lamb*, 1999). As the inferred coefficients in this study are similar to the reference values for pure water, this suggests that the fresh SOA generated near the DWH site do not promote

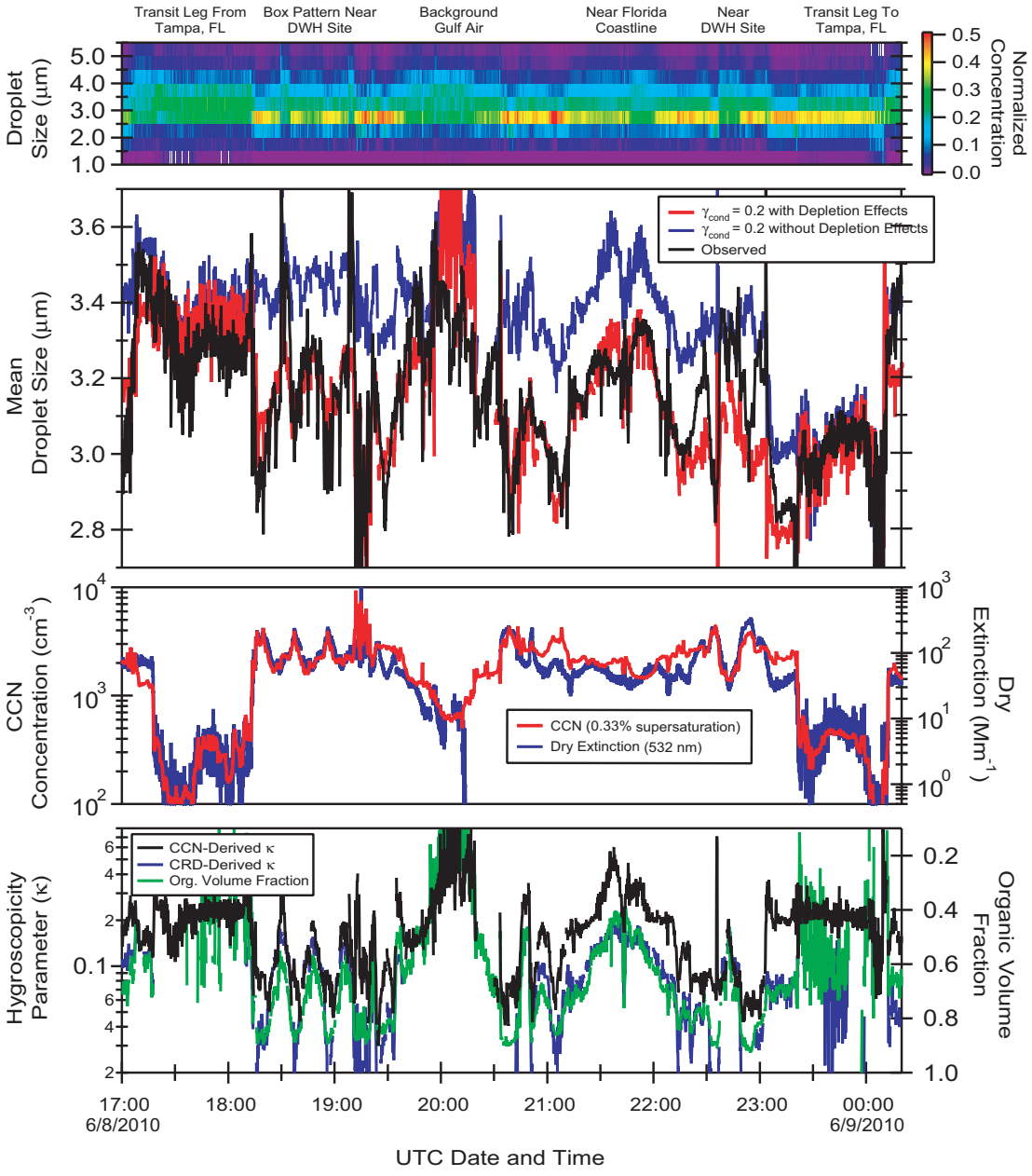


**Figure 7.4:** Timeseries of measured and modeled droplet sizes of activated CCN in the CCNC during the June 8th flight. Shown for comparison are the aerosol organic volume fraction and hygroscopicities derived from the supersaturated CCN and subsaturated cavity ring down measurements.

kinetic delays upon condensation on ambient CCN. Given the relatively low hygroscopicity and hydrocarbon-like nature of the organic species (O:C ratios $\sim$ 0.4-0.5 around the plume), this is a somewhat unexpected result. Previous work has shown that hydrophobic organic compounds may retard water uptake through slow dissolution, which reduces the amount of solute in the droplet and shifts the water vapor-liquid equilibrium more towards the gas-phase than if all of the solute had immediately dissolved (*Asa-Awuku and Nenes*, 2007). Alternatively, organics may form compressed films on the droplet surface, which increases the condensational mass transfer resistance (*Rubel and Gentry*, 1984). A number of past studies have found distinctly slower activation kinetics for smog-chamber SOA resulting from the photo-oxidation of $\beta$-caryophyllene (*Asa-Awuku et al.*, 2008), aerosol above the Pacific marine boundary layer (*Ruehl et al.*, 2009), biogenic aerosol in rural Canada (*Shantz et al.*, 2010), and both urban and rural aerosol at ground-based locations around the United States (*Ruehl et al.*, 2008). *Lance et al.* (2009) examined airborne measurements of CCN in Houston, TX, during the 2006 GoMACCS campaign and found no evidence for slow activation kinetics (*Lance et al.*, 2009), contrary to *Ruehl et al.* (2009) and *Asa-Awuku et al.* (2011), who did observe delayed CCN activation from concurrent ground-based and airborne platforms. Since some of these studies were carried out with size-selected aerosol (i.e., a small fraction of the overall CCN concentration was sampled at a time), supersaturation depletion effects may not have caused the apparent kinetic delays. A potential difference may be the phase state of the aerosol (e.g., glassy/amorphous versus partially-deliquesced) and its impact on water uptake kinetics. Given that most kinetic delays were reported for dry aerosol may lend some support to this hypothesis. A previously-deliquesced aerosol state is consistent with the current results as even a small amount of residual water could inhibit glassy transition and promote rapid activation kinetics. If true, this suggests that condensation of even the most hydrophobic SOA onto existing inorganic CCN may not impact activation kinetics. This finding is relevant for the growth of newly-formed particles in the atmosphere, which have been hypothesized to

form as $H_2SO_4$ seeds and grow to CCN-relevant sizes primarily through the condensation of SOA from IVOCs and VOCs (*Kulmala and Kerminen*, 2008; *Smith et al.*, 2008; *Wang et al.*, 2010b).

## *7.4 Conclusions*

CCN and hygroscopicity measurements of the SOA formed from Deepwater Horizon oil spill emissions are presented and parameterized in terms of aerosol composition. Particles composed almost entirely of organic species were observed to be relatively unoxidized (O:C ratio $\sim$ 0.4-0.5), and exhibited hygroscopicities, $\kappa$, of 0.05-0.1. Hygroscopicity increased with decreasing organic fraction at a rate less than that suggested by simple mixing rules, but which was consistent with size-dependent composition across the Aitken and accumulation size modes. The validity of the derived $\kappa$ is supported by the overall good correlation between supersaturated, CCN-derived $\kappa_{CCN}$ and subsaturated, CRD-derived $\kappa_{CRD}$. The derived $\kappa_{CRD}$ was approximately 50% less than $\kappa_{CCN}$, indicating that while the SOA are CCN-active, subsaturated hygroscopic growth is more limited. Finally, fast measurements of CCN spectra resulting from the first airborne deployment of Scanning Flow CCN Analysis (SFCA) indicate that most aerosol act as CCN above approximately 0.30%$\pm$0.05% supersaturation, with a higher and broader range of critical supersaturations observed for the most organic-rich aerosol (0.4%$\pm$0.1% supersaturation).

A coupled instrument and droplet growth model was used to invert the droplet distribution measured by the CCNC, and activation kinetics were parameterized in terms of an effective water uptake coefficient, $\gamma_{cond}$. Regression analysis suggests that the best correlation between predicted and measured droplet sizes ($R^2 \sim 0.51$) occurs for $\gamma_{cond}$=0.1-0.2 when CCN-concentration-dependent water vapor depletion effects are considered. When water vapor depletion effects are neglected, the correlation worsens significantly, which may lead to underestimation of $\gamma_{cond}$. Based on the inferred $\gamma_{cond}$, we conclude that the large presence of organics in the CCN encountered in the humid, marine boundary layer

near the Gulf of Mexico do not retard droplet activation kinetics.

## *7.5 Supporting Information*

### 7.5.1 Flight Overview Maps

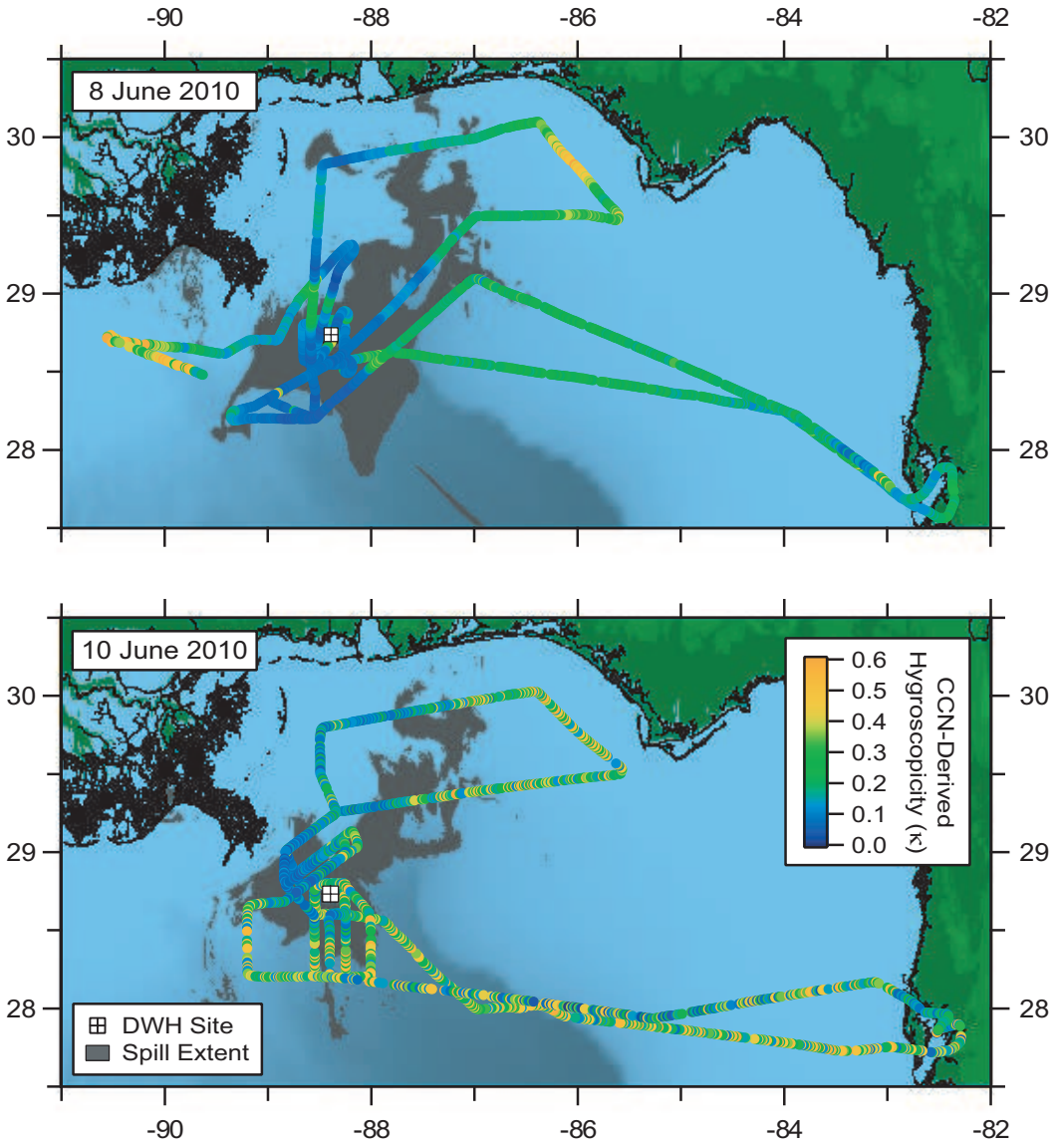


**Figure 7.5:** Complete aircraft trajectories for the survey flights on 8 June (top) and 10 June (bottom). Both flights originate and end in Tampa, Florida. Markers are colored by the CCN-derived hygroscopicity. The gray shaded area represents the extent of surface oil (*NOAA-NESDIS*, 2010). The ordinate and abscissa denote degrees latitude and longitude, respectively.

### 7.5.2 CRD-Derived Hygroscopicity

The data from the cavity ringdown (CRD) spectrometer were used to infer the hygroscopicity parameter, $\kappa$, as follows:

1. The extinction-derived humidification factor, $\gamma_{ext}$, was used to calculate the change in extinction between a dry particle at 10%RH and a humidified particle at 85%RH, $f(85\%RH)$, as

$$f(85\%RH) = \frac{\sigma_{85\%RH}}{\sigma_{10\%RH}} = \left[\frac{1-0.85}{1-0.10}\right]^{\gamma_{ext}} \tag{7.4}$$

   where $\sigma_{RH}$ is the is the aerosol extinction at relative humidity, RH.

2. Mie theory equations (*Bohren and Huffmann*, 1983) were iteratively solved to find the hygroscopic growth factor, $g(85\%RH) = \frac{D_p(85\%RH)}{D_p(10\%RH)}$, consistent with the observed $f(85\%RH)$, where $D_p(RH)$ is the RH-dependent particle diameter. The Mie theory calculations were performed at the CRD laser wavelength of 532 nm and used the fine particle size distribution ($D_p < 2$ $\mu$m) with a prescribed complex refractive index (RI) of 1.45 - $0i$ that is characteristic of alkane and aromatic species (*Riazi and Al-Sahhaf*, 1995). At each iteration step, the humidified particle refractive index is calculated by volume-weighting the dry particle refractive index with that of water (1.33 - $0i$).

3. The hygroscopicity parameter, $\kappa$, is then calculated as (*Petters and Kreidenweis*, 2007)

$$\kappa = \left(g^3 - 1\right)\left(\frac{\exp(\frac{A}{D_p g})}{\frac{RH}{100}} - 1\right) \tag{7.5}$$

   where $A = (4M_w\sigma_w)/(RT\rho_w)$, $R$ is the ideal gas constant, $T$ is the absolute temperature of the measurement, and $\sigma_w$, $M_w$ and $\rho_w$ are the surface tension, molar mass, and density of water, respectively.

**Table 7.1:** Pure component densities and refractive indices used to compute $\kappa_{CRD}$.

| Component | Density (kg m$^{-3}$) | Refractive Index |
|---|---|---|
| Ammonium Sulfate | 1769[a] | $1.53-0.00i$[a,b] |
| Ammonium Nitrate | 1725[a] | $1.61-0.00i$[a] |
| Organic Carbon | 1400[c] | $1.45-0.00i$[d] |
| Elemental Carbon | 1800[e] | $1.95-0.79i$[e] |
| Water | 996[a] | $1.33-0.00i$[a] |

[a] *Green and Perry*, (*Green and Perry*, 2008)
[b] *Toon et al.*, (*Toon et al.*, 1976)
[c] *Alfarra et al.*, (*Alfarra et al.*, 2006)
[d] *Riazi and Al-Sahhaf*, (*Riazi and Al-Sahhaf*, 1995)
[e] *Bond and Bergstrom*, (*Bond and Bergstrom*, 2006)

Implicit in this method is the assumption that the aerosol are internally-mixed and can be described well by a single, complex refractive index. To test the sensitivity of the derived $\kappa_{CRD}$ to the RI assumption, the measured aerosol composition from a compact time of flight aerosol mass spectrometer (C-ToF-AMS) and a single particle soot photometer (SP2) was used to compute an RI based on a volume-weighted average of the pure component refractive indices (Table 7.1). As shown in Figure 7.6a, the derived $\kappa_{CRD}$ is insensitive to the assumed RI over the range of observed values (Figure 7.6b,c) with the uncertainty in $\kappa_{CRD}$ from this assumption estimated to be less than 0.02, absolute. While elemental carbon has the potential to significantly impact aerosol extinction because of its large RI, the low mass loadings observed during the the 8 June flight do not appear to have a large influence (Figure 7.6b,c). The observed insensitivity of $\kappa_{CRD}$ to the refractive index assumption may not be true for some heterogeneous environments with large local sources of elemental carbon, however, the finding is consistent with at least one previous study (*Ervens et al.*, 2007).

Figure 7.7 shows a direct comparison between $\kappa_{CCN}$ and $\kappa_{CRD}$ for the June 8 flight, with the corresponding timeseries shown in Figure 7.4 of the main article. Overall, the

CRD-derived hygroscopicity is approximately two-fold lower than the CCN-derived hygrosopicity, with $\kappa_{CCN}$ ranging from 0.05-0.6, while $\kappa_{CRD}$ varies from 0.01-0.2. A linear fit between the two quantitities gives a slope of 0.47 and a coefficient of determination, $R^2$ = 0.75. An interesting feature of Figure 7.7 is that a clear minimum value of $\kappa_{CCN}$ is apparent between 0.05-0.10, despite wider variation in $\kappa_{CRD}$. Similarly, $\kappa_{CRD}$ reaches a maximum value of 0.15-0.20, despite much wider variation in $\kappa_{CCN}$. These asymptotic limits coincide with high and low organic volume fractions, and seem to imply that organic species reduce subsaturated hygroscopic growth more so than CCN activation.

### 7.5.3 Size-Dependent CCN Composition

Figure 7.8 shows the size-resolved organic aerosol volume fraction ($\epsilon_{SR,org}$) plotted versus the bulk (i.e., size-averaged) organic volume fraction ($\epsilon_{org}$). The Aitken mode aerosol contains mostly organics ($\epsilon_{SR,org}\sim$0.85-1), but its influence is eclipsed by the more-massive accumulation mode aerosol resulting in lower values of bulk $\epsilon_{org}$. A 100-nm cutsize was used to differentiate the two modes, and the average composition in each mode was used to determine the modal $\kappa = \epsilon_{SR,org}\kappa_{org} + \epsilon_{SR,inorg}\kappa_{inorg}$, assuming $\kappa_{org}$=0.05 and $\kappa_{inorg}$=0.6. As shown the lower part of Figure 7.8, the accumulation mode $\kappa$ is roughly two-fold greater than the Aitken mode $\kappa$. The modal $\kappa$ were linearly regressed against the bulk $\epsilon_{org}$, and were combined in an aerosol number-weighted average to find the overall aerosol hygroscopicity, shown as filled circles in Figure 7.8. Using a number-weighted average versus a volume-weighted average is analogous to assuming the two modes are externally mixed rather than internally mixed.

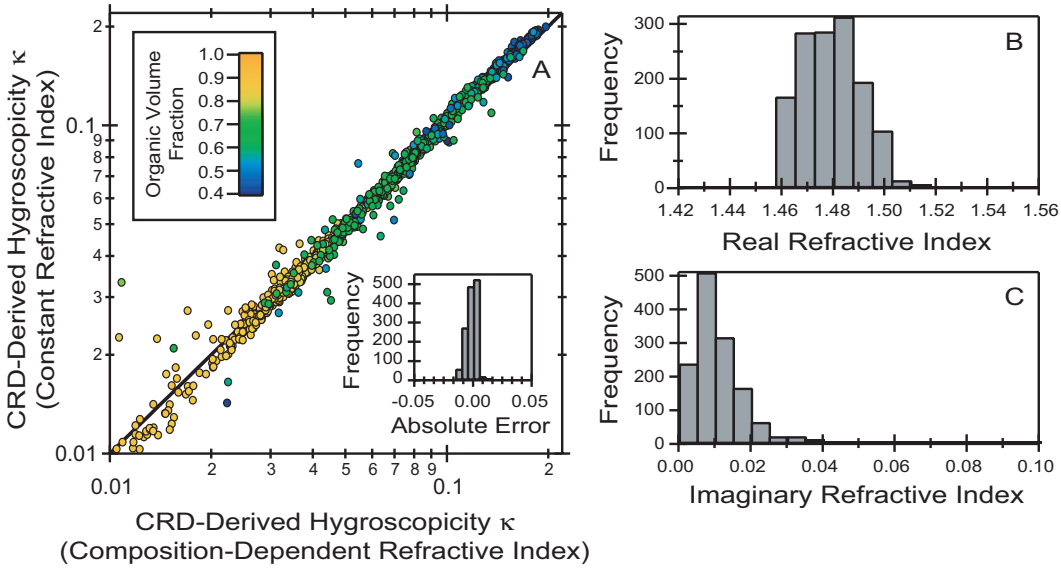


**Figure 7.6:** (a) Comparison plot of the CRD-derived hygroscopicity for the 8 June flight calculated assuming constant and composition-dependent refractive indices. Data from the high altitude transit legs are excluded. (b,c) Frequency of occurrence of the real and imaginary parts of the composition-dependent refractive index during the 8 June flight.

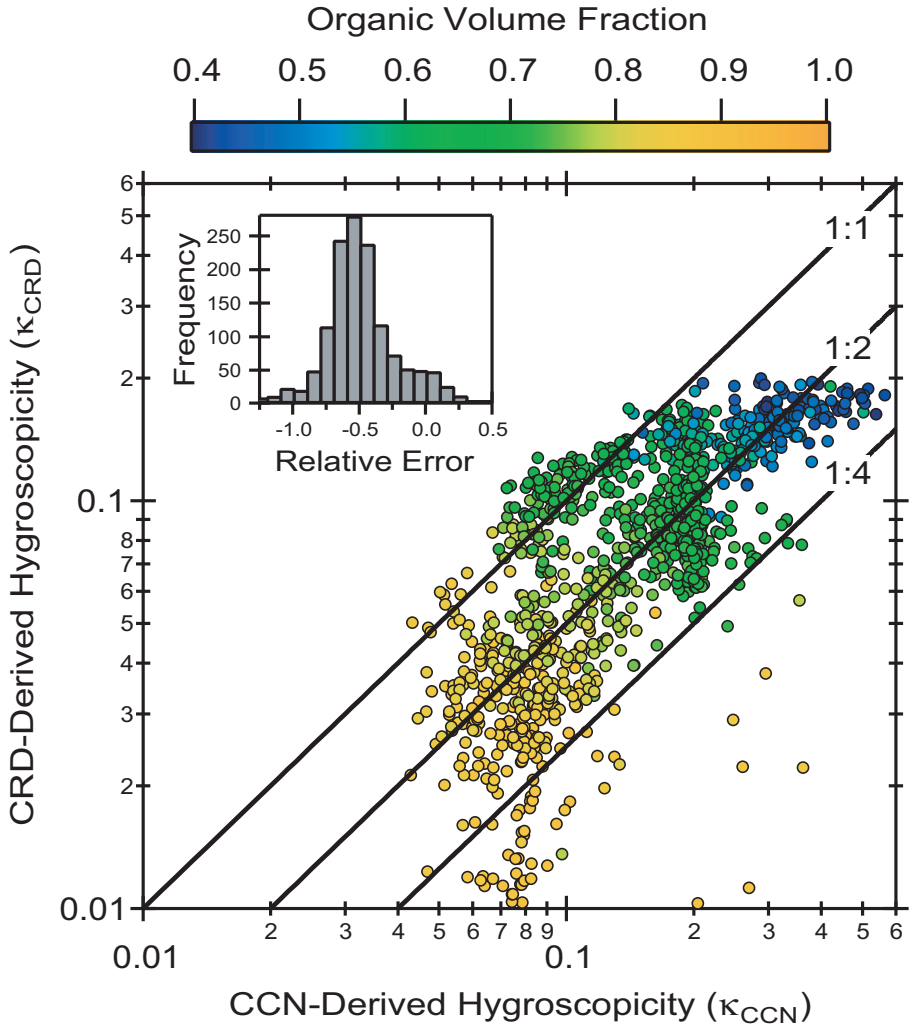


**Figure 7.7:** Comparison plot of the CRD-derived and CCN-derived hygroscopicity parameters observed during the 8 June flight.

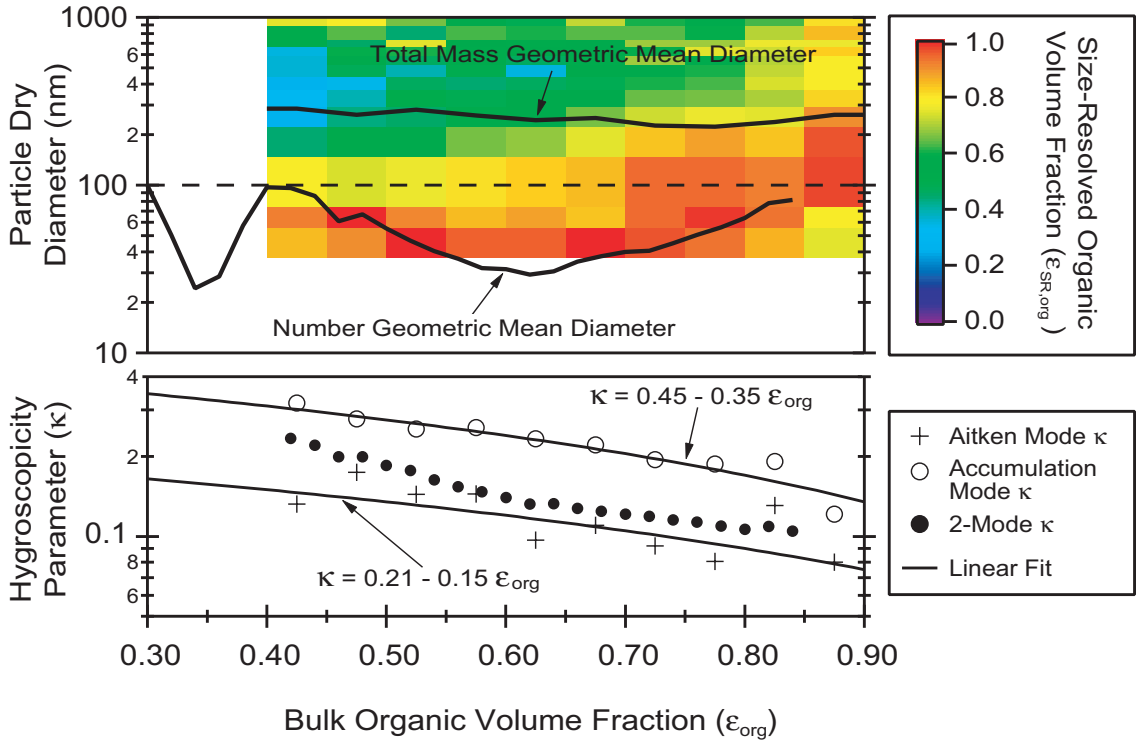


**Figure 7.8:** Average size-resolved organic volume fraction ($\epsilon_{SR,org}$) from the C-ToF-AMS (top) and calculated modal hygroscopicity parameters ($\kappa$) (bottom) plotted versus the bulk (i.e., size-averaged) C-ToF-AMS organic volume fraction $\epsilon_{org}$ for both flights. The 2-Mode $\kappa$ is an aerosol number-concentration-weighted average of the linear fits to the Aitken and accumulation mode $\kappa$.

### 7.5.4 Coupled CCNC and Droplet Growth Model

A detailed description of the coupled CCNC instrument and droplet growth model is given by *Raatikainen et al.* (A Coupled Instrument and Droplet Growth Model for Inferring CCN Activation Kinetics From the DMT CCNC, manuscript in preparation, 2011), so only a brief description is included here. A simplified form of the coupled model was employed here, which assumes parabolic velocity fields while solving the water vapor and energy conservation equations. Neglecting explicit calculation of the velocity fields has a negligible effect on the simulation results, but substantially decreases the necessary computational time (*Raatikainen et al., in preparation*). The model has been successfully applied in the past to simulate the instrument behavior for both steady-state and transient operation (*Moore and Nenes*, 2009; *Rose et al.*, 2008; *Lance et al.*, 2006). Recent work by *Lathem and Nenes* (2011) has shown that moderately high CCN concentrations in the growth chamber can slightly decrease the centerline supersaturation profile. This effect appears to be unimportant for measurements of CCN concentrations below $10^4$ cm$^{-3}$ (*Lathem and Nenes*, 2011), which is the typical mode of operation. However, supersaturation depletion can have a detectable effect on the OPC-measured droplet size distribution when the CCN concentrations exceed several hundred per cm$^3$. The model can be used to simulate the CCN droplet size distributions, both with and without such supersaturation depletion effects as a function of the effective water uptake coefficient, $\gamma_{cond}$. The optimal value of $\gamma_{cond}$ is then found by iteratively matching the simulated and measured droplet size distributions.

As described in detail by *Raatikainen et al., in preparation*, a number of uncertainties exist that challenge the simulations. For example, aerosol mixing state and size-dependent composition give rise to a polydisperse hygroscopicity distribution, which is poorly-constrained. Additionally, there are various instrument non-idealities (e.g., column thermal resistance, possible OPC sizing biases, incomplete wetting of the column wall and overall mass transfer coefficient changes, non-linearity of the wall temperature profile). To

quantify the impact of these effects, CCN droplet distributions for ammonium sulfate calibration aerosol were compared to those predicted by the model, and it was found that the model simulations overpredict the measured mean droplet size by approximately 2.1 $\mu$m, which agrees well with the correction bias of 2.3 $\mu$m uncovered for $\gamma_{cond}$=0.2 (Table 7.2) and applied to the June 8th simulation timeseries in Figure 7.4.

Figure 7.9 shows 1:1 comparison plots for the uncorrected simulated mean droplet size ($\bar{D}_{p,sim}$) versus the OPC measured mean droplet size ($\bar{D}_p$), and the linear regression coefficients are listed in Table 7.2. It can be seen that forcing the regression slope to unity has a negligible effect on the coefficient of determination for all simulations except those where supersaturation depletion effects are neglected. Simulations assuming $\gamma_{cond}$=0.05-1 show the best correlation with observations ($R^2 \sim 0.51$), and the overprediction bias for the $\gamma_{cond}$=0.1-0.2 simulations is most similar to the 2.1 $\mu$m bias identified from calibrations. The correlation worsens significantly for $\gamma_{cond}$ <0.05 or when depletion effects are neglected. Thus, the regression analysis indicates that CCN near the Deepwater Horizon oil spill do not exhibit slow activation kinetics and derived values of $\gamma_{cond}$ are consistent with those for ammonium sulfate calibration aerosol and previously reported values for pure water droplets (*Li et al.*, 2001; *Shaw and Lamb*, 1999).

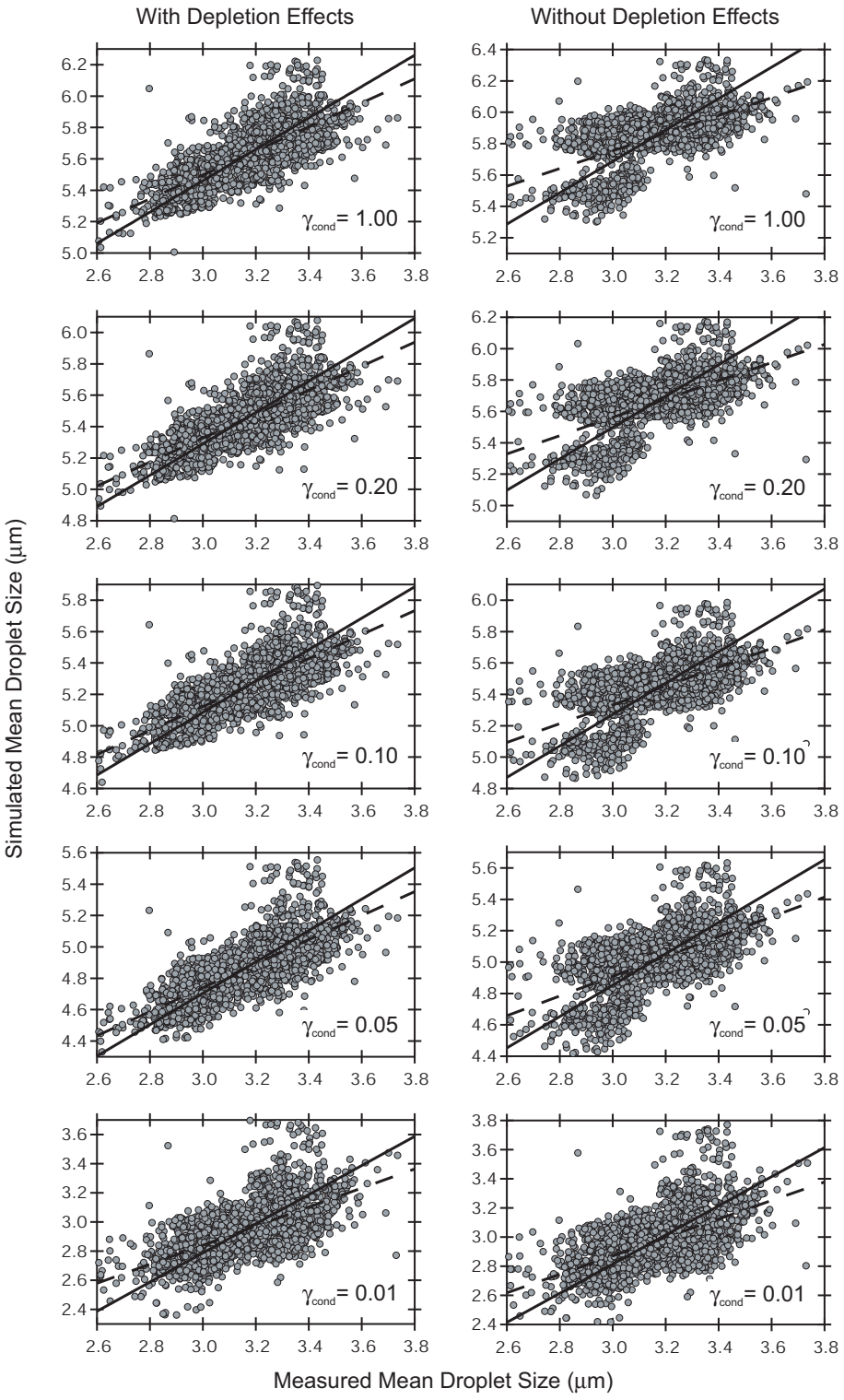


**Figure 7.9:** Comparison plots of the simulated CCN droplet sizes obtained from the instrument model versus the measured mean droplet sizes during the 8 June flight. Solid traces are a 1-parameter linear fit (constant bias), and dashed traces are a 2-parameter linear fit (slope and bias). Regression coefficients are listed in Table 7.2.

**Table 7.2:** Linear regression coefficients between modeled and observed mean droplet sizes for model simulations with varying water uptake coefficients and with supersaturation depletion effects considered or turned off. Both 1-parameter ($\bar{D}_{p,sim} = \bar{D}_p +$ Bias) and 2-parameter ($\bar{D}_{p,sim} =$ Slope $\times \bar{D}_p +$ Bias) are listed.

| Model Simulation | | 1-Parameter Fit | | 2-Parameter Fit | | |
|---|---|---|---|---|---|---|
| $\gamma_{cond}$ | Depletion Effects? | Bias | $R^2$ | Slope | Bias | $R^2$ |
| 1.00 | Yes | 2.46 | 0.49 | 0.76 | 3.20 | 0.53 |
| 0.20 | Yes | 2.29 | 0.50 | 0.76 | 3.03 | 0.53 |
| 0.10 | Yes | 2.09 | 0.49 | 0.76 | 2.83 | 0.54 |
| 0.05 | Yes | 1.70 | 0.49 | 0.76 | 2.45 | 0.53 |
| 0.04 | Yes | 1.53 | 0.47 | 0.76 | 2.28 | 0.52 |
| 0.03 | Yes | 1.25 | 0.44 | 0.75 | 2.03 | 0.50 |
| 0.02 | Yes | 0.78 | 0.39 | 0.73 | 1.63 | 0.46 |
| 0.01 | Yes | -0.21 | 0.26 | 0.65 | 0.88 | 0.37 |
| 0.008 | Yes | -0.53 | 0.22 | 0.62 | 0.67 | 0.35 |
| 0.005 | Yes | -1.11 | 0.04 | 0.52 | 0.41 | 0.29 |
| 1.00 | No | 2.69 | 0.15 | 0.56 | 4.06 | 0.36 |
| 0.20 | No | 2.50 | 0.18 | 0.58 | 3.82 | 0.36 |
| 0.10 | No | 2.27 | 0.20 | 0.60 | 3.53 | 0.36 |
| 0.05 | No | 1.85 | 0.24 | 0.63 | 3.02 | 0.36 |
| 0.04 | No | 1.66 | 0.25 | 0.64 | 2.79 | 0.36 |
| 0.03 | No | 1.36 | 0.25 | 0.65 | 2.46 | 0.35 |
| 0.02 | No | 0.85 | 0.26 | 0.66 | 1.91 | 0.35 |
| 0.01 | No | -0.19 | 0.22 | 0.63 | 0.97 | 0.34 |
| 0.008 | No | -0.51 | 0.19 | 0.61 | 0.72 | 0.33 |
| 0.005 | No | -1.10 | 0.04 | 0.52 | 0.42 | 0.29 |

# CHAPTER VIII

# HYGROSCOPICITY, MIXING STATE, AND VOLATILITY OF ATLANTA CCN

The diurnal variation of CCN-derived hygroscopicity and mixing state are presented for measurements conducted in Atlanta during March, 2009. The CCN-active fraction decreases by 20-50% during the morning rush hour, while aerosol hygroscopicity and a metric for chemical homogeneity both increase during the day and peak in the early afternoon, indicative of photochemical oxidative aging. Measurements of aerosol volatility and resulting changes in CCN activity from treatment with a thermal-denuder are also presented for typical Aitken-mode, background aerosol and for aerosol resulting from a new particle formation (NPF) event. It was found that 40-nm particles formed from freshly-nucleated particles are highly-hygroscopic and of limited volatility, consistent with neutralized and unneutralized sulfate species. Organics likely comprise a larger fraction of the background aerosol, which is reflected in the larger amount of volume evaporated in the thermal denuder and the overall lower derived values of the CCN hygroscopicity parameter, $\kappa$ of 0.3-0.45 versus 0.55-0.7 during the NPF event.

## *8.1 Introduction*

The Atlanta metropolitan area is characterized by a large concentration of anthropogenic point and mobile emissions sources juxtaposed with a strong, regional biogenic emissions

This chapter to be submitted for publication as: Moore, R. H. and A. Nenes, Diurnal Variability in the CCN Activity and Mixing State of Atlanta Aerosol During Spring, 2009.

and Moore, R.H, J. Scheckman, B. Williams, J. Jiang, P. McMurry, J. Zhao, J. Smith, and A. Nenes, Volatility and Hygroscopicity of Atlanta CCN During New Particle Formation Events in Summer, 2009

background from surrounding forest and pasture land. This environment has important implications for the regulation of ambient air quality, since the abundant sources of natural volatile organic carbon (VOC) species make the city a $NO_x$-limited environment for controlling ozone, whose concentrations frequently exceed values set by the National Ambient Air Quality Standards (NAAQS). Fine mode particle concentrations (diameters $< 2.5$ $\mu$m) are also often out of compliance with the NAAQS. A number of past studies conducted in the Atlanta area have shown the aerosol to be composed of roughly 50% organic species and 50% inorganic sulfate species (*Lim and Turpin*, 2002), and 50-60% of the organic carbon mass is water soluble (WSOC) (*Sullivan and Weber*, 2006). The majority of the Atlanta WSOC has been linked to biogenic VOCs (*Weber et al.*, 2007), which may partition to the particle phase via the tradiational photochemical oxidation pathways or through a two-step aqueous dissolution and heterogeneous reaction chemistry pathway during periods of high ambient relative humidity (*Hennigan et al.*, 2009). Despite this biogenic origin, the secondary organic aerosol (SOA) in Atlanta has also been observed to vary diurnally and correlate with anthropogenic emissions sources (*Hennigan et al.*, 2009; *Weber et al.*, 2007), reflecting the role of daytime photochemistry in both ozone production and SOA formation.

Biogenic SOA accounts for an important fraction of atmospheric aerosol worldwide (*Hallquist et al.*, 2009; *Goldstein and Galbally*, 2007; *Kanakidou et al.*, 2005), and elucidating the chemical production mechanisms and properties of SOA has been an important area of active research in recent years. Of particular interest is the determination of the hygroscopic properties of SOA, because of the ability of atmospheric aerosol to act as cloud condensation nuclei (CCN) and form cloud droplets, which, in turn, influence the Earth's climate. A number of recent laboratory and field measurements of SOA report values of the *Petters and Kreidenweis* (2007) hygroscopicity parameter, $\kappa$, of between 0.1 and 0.2 (e.g., *Engelhart et al.*, 2011; *Dusek et al.*, 2010; *Gunthe et al.*, 2009, and others), and a mean

$\kappa$ of $\sim$0.3$\pm$(0.1-0.2) has been suggested for continental aerosol (*Pringle et al.*, 2010; *Andreae and Rosenfeld*, 2008), which incorporates the contributions of the relatively lower-$\kappa$ organics and higher-$\kappa$ inorganic species to the overall aerosol hygroscopicity.

While a constant $\kappa$ value for continental and marine environments may be suitable for large-scale modeling of aerosol-cloud interactions, it likely does not reflect the variability present at smaller spatial and temporal scales relevant for regional air quality and climate. For example, *Ervens et al.* (2010) evaluated the error associated with using simplified compositional assumptions to predict CCN concentrations close to and far from emissions sources. They found that CCN were overpredicted by almost 2-6-fold near emissions sources, but that agreement between predictions and observations was much better (within 20-60%) farther from these sources.

In this study, we characterize the diurnal variability of the CCN properties of Atlanta aerosol during a characteristic week in Spring, 2009. The city of Atlanta provides the ideal environment for studying the combined influence of regional biogenic and local anthropogenic influences on aerosol hygroscopic properties. In addition, we present results of the CCN activity of ambient aerosol during a particle nucleation and growth event in Summer, 2009. These conditions allow us to quantify the extent to which aerosol hygroscopicity agrees with or varies from the proposed mean $\kappa$ values for continental aerosol.

## *8.2 Observational Data Set*

Measurements were conducted from March-July, 2009, on the rooftop measurement platform of the Ford Environmental Science and Technology building on the Georgia Institute of Technology campus in midtown Atlanta (33°46'45"N, 84°23'45"W, $\sim$30-40 m AGL). For this study, we focus on the week of 8 March – 15 March. Relative humidity varied diurnally between 50-80% and the ambient temperature was 10-25°C during this week, except for a rain event on 14 March. NOAA HYSPLIT backtrajectories for the sample period at the measurement location and 200 m AGL are shown in Figure 8.1, and two distinct periods

are visible: a more southwesterly flow during the beginning of week and a northeasterly during the end of the week when the temperature decreased. The vertical component of the trajectories shows that the air sampled is representative of the surface, which is ideal for evaluating the impact of local emissions sources.

CCN measurements were also conducted during July-August, 2009 as part of the Nucleation and Cloud Condensation Nuclei (NCCN) experiment at the Jefferson Street monitoring site, approximately 3-4 miles west of the Georgia Tech campus (33°46'34"N, 84°24'58"W), which employed a more comprehensive suite of aerosol and gas phase instrumentation than during the Spring period. The NCCN measurements will be the subject of future work, and only a special experiment related to the volatility of CCN-active aerosol is discussed here.

### 8.2.1 CCN and Aerosol Measurements

CCN concentration measurements were obtained using a Droplet Measurement Technologies stream-wise, thermal-gradient cloud condensation nuclei counter (CCNC *Roberts and Nenes*, 2005; *Lance et al.*, 2006), which was located downstream of a differential mobility analyzer (DMA) for size-resolved measurements. The flow rate in the CCNC was dynamically scanned over a 60-second period using the Scanning Flow CCN Analysis (SFCA) technique of *Moore and Nenes* (2009). To keep the sample flow rate through the DMA constant, the CCNC inlet flow rate was controlled using a flow orifice and active control system that maintained a constant CCNC instrument pressure of 600 hPa. The streamwise temperature gradient in the CCNC was kept constant at 14K, and the functional dependence of the instrument supersaturation on flow rate was calibrated using size-classified ammonium sulfate aerosol and Köhler theory (*Köhler*, 1936; *Rose et al.*, 2008; *Moore and Nenes*, 2009). The supersaturation absolute uncertainty is estimated to be $\pm 0.04\%$.

The monodisperse output from the DMA was split between the CCNC and a condensation particle counter (CPC, TSI 3010) to measure the total particle concentration in a setup similar to the Scanning Mobility CCN Analysis (SMCA) technique of *Moore et al.* (2010).

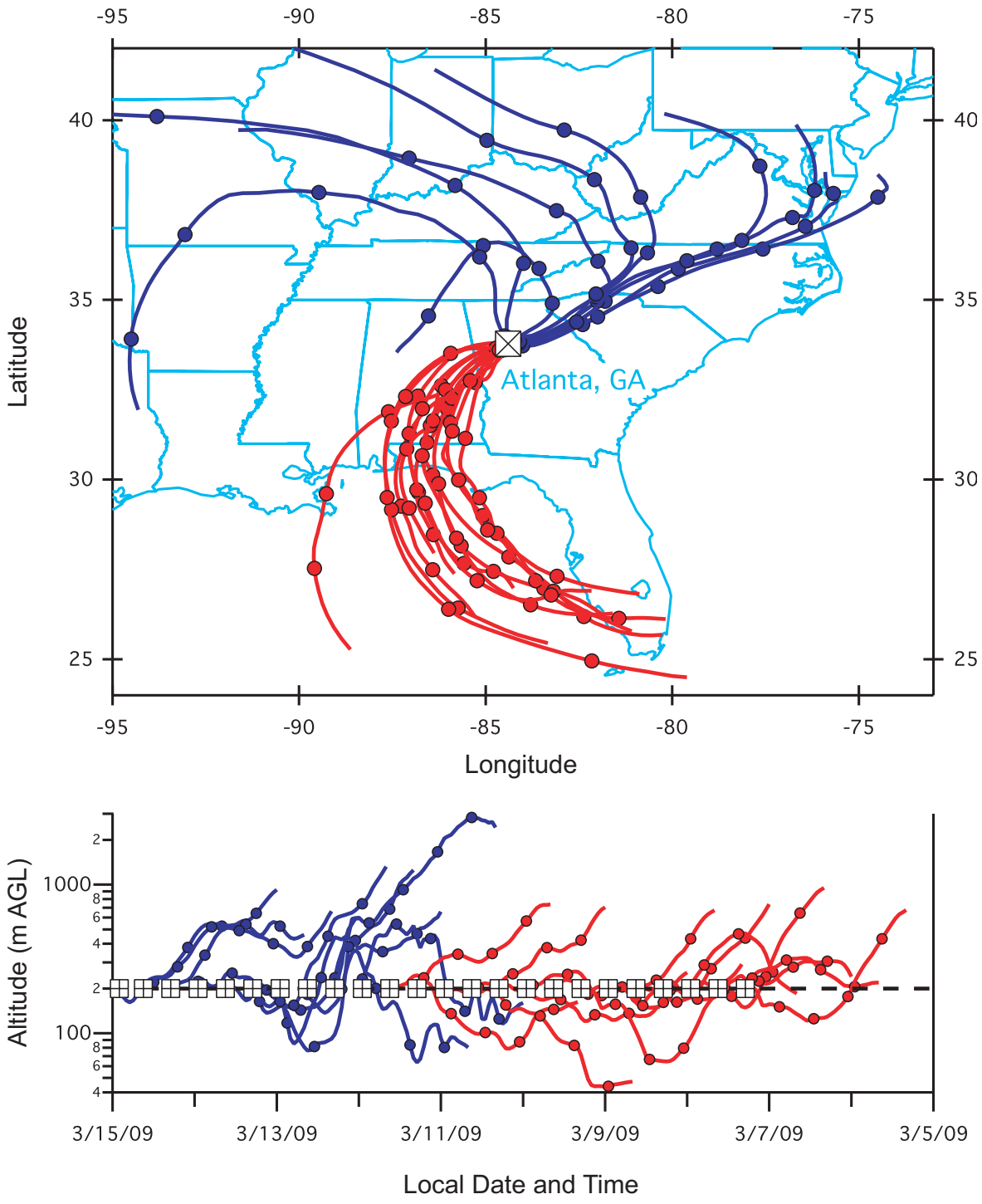


**Figure 8.1:** 48-hour, NOAA HYSPLIT backtrajectories for the 8 March - 15 March period colored by red for the first half of the week and blue for the second half. Boxes denote the sampling location in midtown Atlanta. Trajectories were computed every eight hours using EDAS40 archived meteorological fields. Data obtained from the online HYSPLIT model at `http://www.arl.noaa.gov/ready.php` (*Draxler and Rolph*, 2011; *Rolph*, 2011).

However, instead of dynamically scanning the DMA size range over a short period of time, the DMA size was stepped through 20, 40, 60, 80, and 100 nm diameters over 6-minute intervals. This enables measurement of a complete set of size-resolved CCN spectra each half hour.

During the Summer NCCN measurement period, the CCNC was operated in a similar manner to obtain size-resolved CCN spectra, but the flow orifice was replaced with a custom-built laminar flow control system to achieve the same constant flow through the DMA while operating the CCNC at ambient pressure. Two special experiments were conducted where a thermal-denuder was placed directly downstream of a DMA (set to a constant 40 nm diameter size) and the outflow from the thermal-denuder was then sent to the scanning CCNC to obtain CCN spectra and to a scanning mobility particle sizer (SMPS) to obtain the size distribution. The thermal-denuder was operated at five different elevated temperatures (50-150°C) to evaporate any semi-volatile species present in the aerosol, which adsorb on the denuder walls. The less-volatile aerosol cores are then measured by the CCNC and SMPS.

### 8.2.2 Analysis

The ability of an aerosol to act as a CCN depends on its size, chemical composition, and the ambient water vapor supersaturation. Consequently, size-resolved CCN spectra (i.e., CCN concentrations over a range of supersaturations) allow inferences to be drawn about the composition and mixing state of the aerosol population. A typical CCN spectra is shown in Figure 8.2 for 60 nm ambient particles measured on 12 March. Following *Lance* (2007) and *Cerully et al.* (2011), we fit the CCN spectrum to a sigmoidal function of the form

$$R_a(s) \equiv \frac{N_{CCN}(s)}{N_{CN}} = \frac{E}{1 + (s/s^*)^C} \tag{8.1}$$

where $R_a$ is the activated ratio, $N_{CCN}$ is the CCN number concentration, $N_{CN}$ is the fine particle number concentration, $s$ is the instrument supersaturation, and $E$, $s^*$, and $C$ are

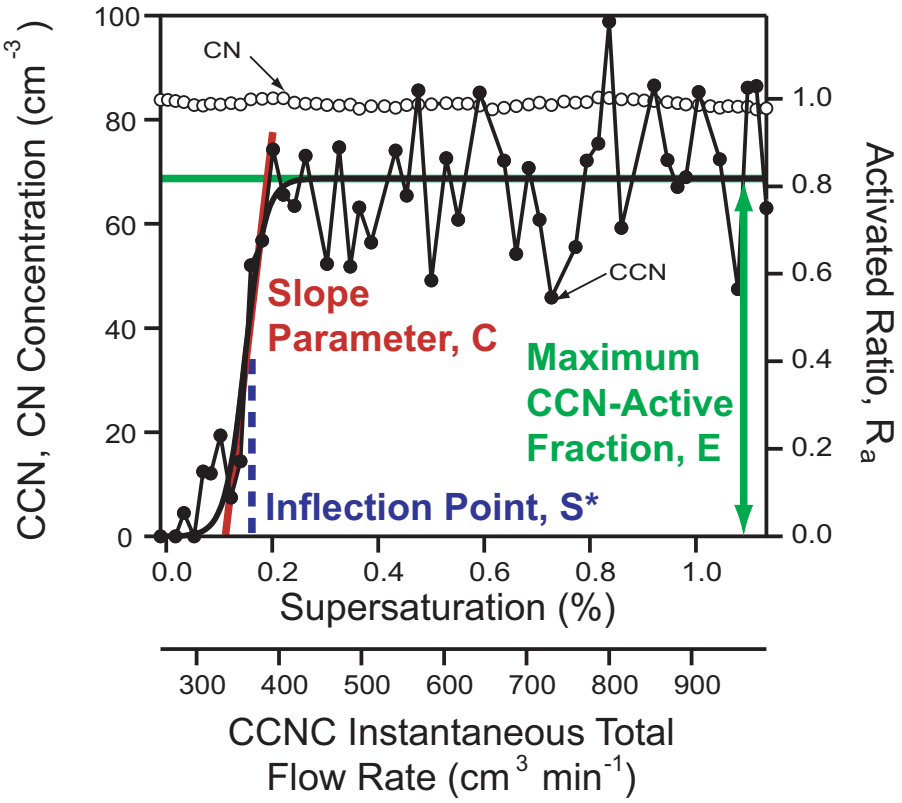


**Figure 8.2:** Exemplary CCN activation curve for ambient 60-nm particles in Atlanta, GA. CCN and CN concentrations are plotted versus supersaturation on the left axis, while the corresponding activated ratio is shown on the right axis. The relationship between calibrated instrument supersaturation and instantaneous instrument flow rate is shown on the abscissa.

empirical fit parameters that describe the maximum CCN-active fraction, the characteristic supersaturation corresponding to the inflection point of the sigmoid, and the slope of the sigmoid, respectively.

Treating $s^*$ as the characteristic critical supersaturation for the aerosol of constant diameter, $d_p$, allows direct computation of the aerosol hygroscopicity, $\kappa$ (*Petters and Kreidenweis*, 2007), using Köhler theory

$$\kappa = \frac{4A^3}{27s^2d_p^3} \tag{8.2}$$

where $A = (4M_w\sigma)/(RT\rho_w)$, $R$ is the universal gas constant, $T$ is the absolute temperature, and $M_w$, $\rho_w$, and $\sigma$ are the molar mass, density, and surface tension of water,

respectively.

## *8.3 Results and Discussion*

### 8.3.1 Diurnal Variation of CCN Hygroscopicity and Mixing State

The timeseries of CCN concentrations measured during the 8 March – 15 March, 2009 are shown in Figure 8.3, where the points are colored by instrument supersaturation. The highest CCN concentrations are observed in the 80-100 nm size range with few particles detected at the smallest diameter even at 1.5% supersaturation, which is reflective of the typical Atlanta aerosol size distribution in the Aitken (i.e., 40-80 nm) and accumulation (i.e., 80-300 nm) size modes. Occasional bursts of small particles are detected even at low supersaturations, which could be from freshly-nucleated particles, although there does not appear to be a sustained growth of the particles into the larger size modes. The fact that 20-nm particles can act as CCN at supersaturations less than 0.5% indicates that these aerosol are highly hygroscopic and may consist of unneutralized sulfate species. The maximum number concentrations in the 100-nm size bin varies from 50 to 150 $cm^{-3}$ throughout the week, although there does not appear to be a systematic diurnal variation of CCN concentrations.

A more pronounced diurnal trend is apparent, however, for the 60-nm, fitted CCN spectra parameters shown in Figure 8.4. Approximately 80% of particles are CCN active, although a substantial decrease in the maximum activated ratio ($E$) is observed during the morning rush hour beginning around 06:00 and lasting until 12:00 local time. This is consistent with the emission of fresh, ultrafine combusion particles from traffic that are too small and/or non-hygroscopic to act as CCN. An interesting feature of the time series is the absence of a similar decrease in $E$ during the evening rush hour. This can be explained by daytime diabatic surface heating that drives buoyancy and increases the height of the well-mixed, planetary boundary layer. This larger mixed layer rapidly dilutes the afternoon/evening emissions more so than during the morning commute when the mixed layer

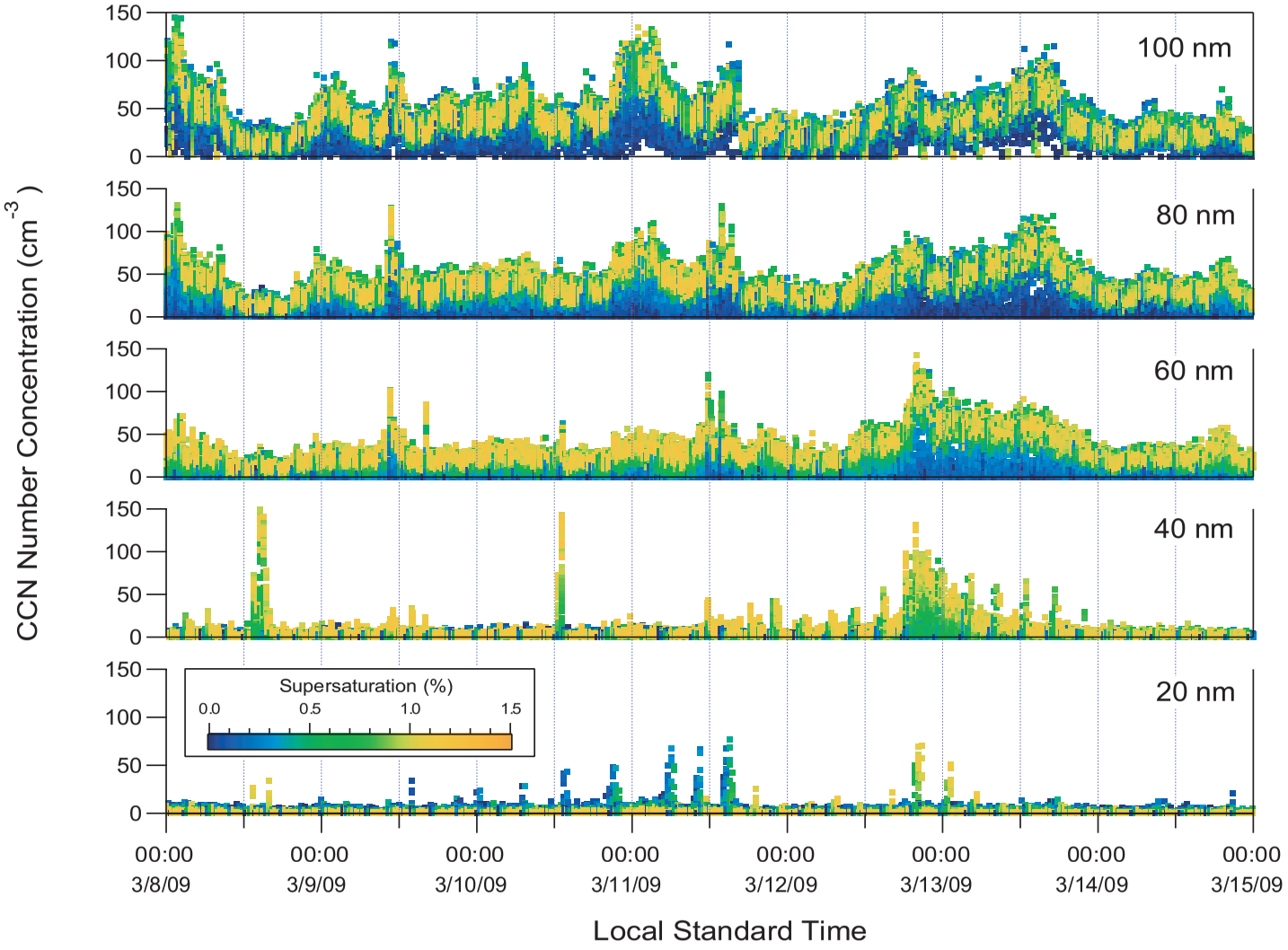


**Figure 8.3:** Timeseries of size-resolved, ambient CCN concentrations colored by instrument supersaturation. Data shown are for 8 March – 15 March, 2009.

height is low. A similar effect was observed by *Gentner et al.* (2009) for whole gasoline source contributions to VOC emissions in Riverside, CA.

The diurnal variation of $s^*$ also shows a slight increase from $\sim$0.6% to $\sim$0.8% at dawn during the morning rush hour, but then decreases to a minimum of $\sim$0.35% as the day progresses. These values of $s^*$ are converted to $\kappa$ using Equation 8.2, and the diurnal trend of $\kappa$ is also shown in Figure 8.4. A nighttime, background $\kappa$ is on the order of 0.2$\pm$0.1, which decreases to 0.1 at dawn before increasing to $\sim$0.4 near midday. The aerosol $\kappa$ peaks around 13:00 local time and gradually decreases to a nighttime minimum around 21:00. Without aerosol composition measurements, it is not possible to attribute this change in $\kappa$ to the influence of organic or inorganic species; although, both likely play a role. For example, the increased mixed layer height in midday can entrain aged, free tropospheric aerosols and power plant sulfate plumes aloft, which are likely to be inorganic-rich. Meanwhile photochemical oxidation of organic species would be expected to increase the organic hygroscopicity as the degree of oxygenation increases (*Duplissy et al.*, 2011; *Chang et al.*, 2010; *Jimenez et al.*, 2009).

Finally, the exponential constant ($C$) in Equation 8.1 corresponds to the slope of the sigmoidal fit function, and is therefore, a metric for the degree of aerosol chemical heterogeneity. Small values of $C$ produce shallow CCN spectra slopes, indicating a more heterogeneous aerosol population that act as CCN across a range of supersaturations. Meanwhile, larger values of $C$ produce steep slopes where most particles act as CCN above a narrow range of supersaturations. The interpretation of the diurnal variation of $C$ seen in Figure 8.4 is less clear than the other CCN spectra parameters. A decrease in the aerosol homogeneity is seen between 06:00 and 09:00 ($C$ decreases), while the midday trend mirrors that of $\kappa$ with increasing homogeneity until a peak around 13:00 before decreasing to a minimum at 21:00. The clarity of the trend is interrupted by the sharp drop in $C$ between 09:00 and 12:00; however, the idea that photochemical aging and physical coagulation processes

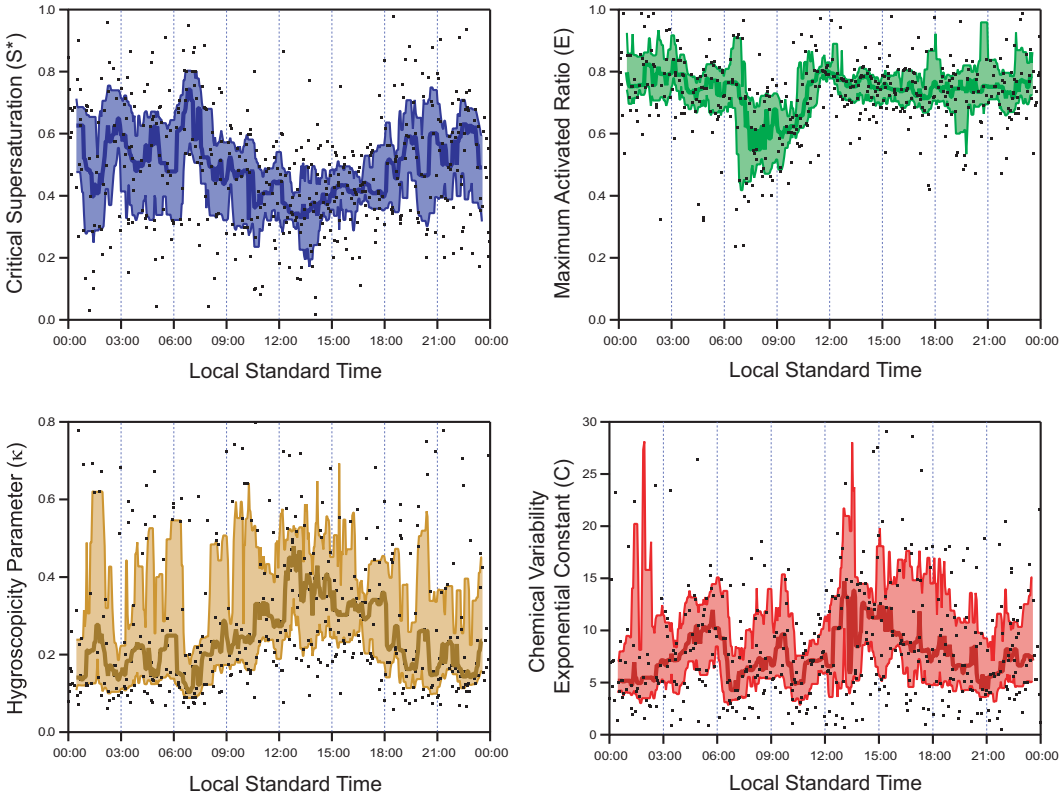


**Figure 8.4:** Diurnal variation in the CCN spectra fitting parameters, $E$, $s^*$, and $C$ for 60 nm particles. Also shown is the diurnal variation of $\kappa$ obtained from $s^*$ using Equation 8.2. Black points denote the measurements from 8 March – 15 March, while the colored traces and shaded regions denote the hourly running median and interquartile range, respectively.

would increase both the aerosol hygroscopicity and homogeneity is consistent with the transition from an external mixture of fresh and aged aerosol toward a more internally-mixed, aged aerosol population.

The diurnal trends shown in Figure 8.4 for 60 nm particles were also determined for 40, 80, and 100 nm particle sizes and are shown in Figure 8.5. Low particle counting statistics prevented fitting many of the 20 nm spectra with good confidence. It can be observed that all sizes exhibit the same decrease in $E$ during the morning rush hour; although, the decrease is more pronounced at the smaller sizes. This is consistent with hypothesis that mobile traffic sources introduce less-hygroscopic ultrafine particles that are poor CCN. A size dependence to the $\kappa$ diurnal variation is also apparent, with larger particles having slightly larger hygroscopicities than the smaller particle sizes. This suggests that Atlanta aerosol exhibit a strong size-dependence in both aerosol mixing state ($E \sim$ 0.4-0.8 from 06:00-12:00 and $\sim$ 0.65-0.9 during all other times) and in aerosol hygroscopicity ($\kappa \sim$ 0.2-0.6 throughout the day). This is consistent with the results of a recent CCN closure study in Atlanta (*Padró et al.*, in review) and in other urban studies (e.g., *Wang et al.*, 2010a; *Ervens et al.*, 2010; *Cubison et al.*, 2008).

### 8.3.2 Volatility and CCN Activity of Newly-Formed Particles

Another source of variability in urban and non-urban aerosol emissions is the nucleation of new particles and their subsequent growth to CCN-relevant sizes. It is currently thought that while new particle formation (NPF) proceeds via condensation of gas-phase sulfuric acid, the growth phase must be dominated by the condensation of secondary organic species in order to reconcile mass-based field observations with theory (*Laaksonen et al.*, 2008; *Kulmala et al.*, 2004). This implies size-dependent aerosol composition with varying amounts of organic species, yet the impact of these organics on the aerosol hygroscopic properties remains poorly characterized. In this section, we use a thermal-denuder to selectively strip away the semi-volatile aerosol components (e.g., less-oxygenated organics)

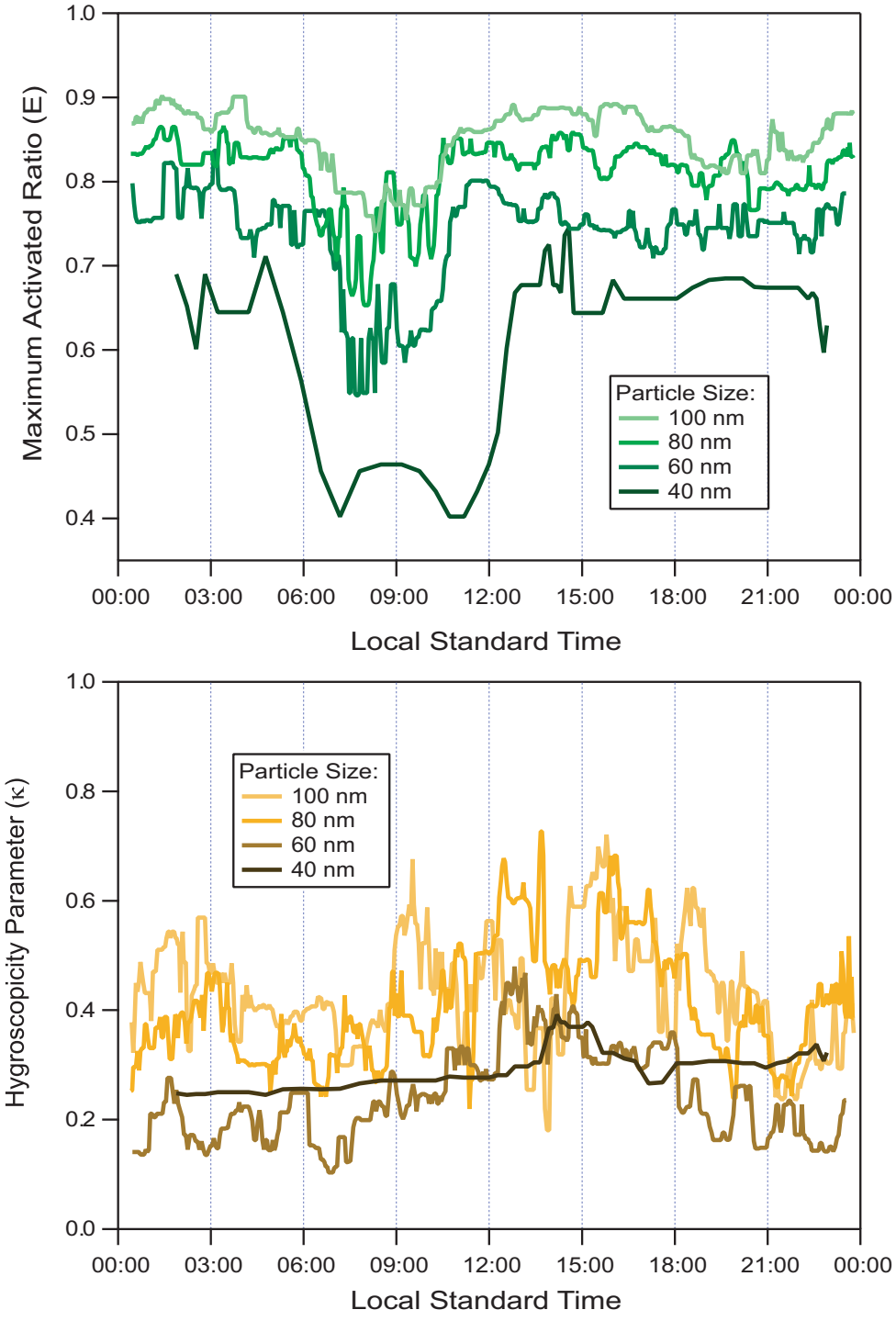


**Figure 8.5:** Hourly running median of $E$ and $\kappa$ for size-classified aerosol between 40 and 100 nm, as in Figure 8.4. Traces are colored by particle size.

leaving only the less-volatile components (e.g., sulfate and more-oxygenated organics).

Two experiments with the thermal-denuder were conducted on 7 August and 27 August 2009, and the measured particle size distributions during both days are shown in Figure 8.6. A burst of small particles is apparent at around 11:20 on 7 August and these particles serve as condensation nuclei for non-volatile and semi-volatile vapors and grow to larger sizes. Meanwhile the experiment on 27 August was conducted during much lower atmospheric particle loadings with diameters centered in the 10-40 nm size range. The DMA upstream of the thermal-denuder in both experiments was set to select only $40\pm4$ nm diameter particles (sheath:aerosol flow ratio of 10:1), and the size distribution and CCN spectra of the denuded aerosol were measured downstream of the thermal-denuder. Figure 8.7 shows lognormal fits to the size distribution data as a function of thermal-denuder temperature for both days. It can be seen that the decrease in aerosol size associated with the NPF aerosol on 7 August is much smaller than that seen for background aerosol on 27 August, which suggests a greater and lessor contribution of less-volatile sulfate species on each day, respectively. Additionally, the size distribution at 150°C is broader for the background aerosol than for the nucleated aerosol indicating a wider range of volatilities (i.e., some particles are more volatile and some particles are less volatile).

The magnitude of the particle size decrease and the increase in the breadth of the size distribution is shown in the left part of Figure 8.8. It can be seen that the decrease in particle diameter for the background aerosol is almost twice that of the aerosol during the NPF event. Aerosol hygroscopicity was determined from the size-resolved CCN spectra using Equations 8.1 and 8.2, and are shown as a function of thermal-denuder temperature in the right portion of Figure 8.8. For both days, $\kappa$ increases by about 0.1-0.2 over the studied temperature range; although, the $\kappa$ for 7 August was much higher than the $\kappa$ on 27 August. The former is more consistent with neutralized or unneutralized sulfate species, while the latter is more consistent with a mixture of soluble organics and inorganics. This finding indicates that newly-formed particles in Atlanta are able to grow to diameters $\sim$ 40 nm

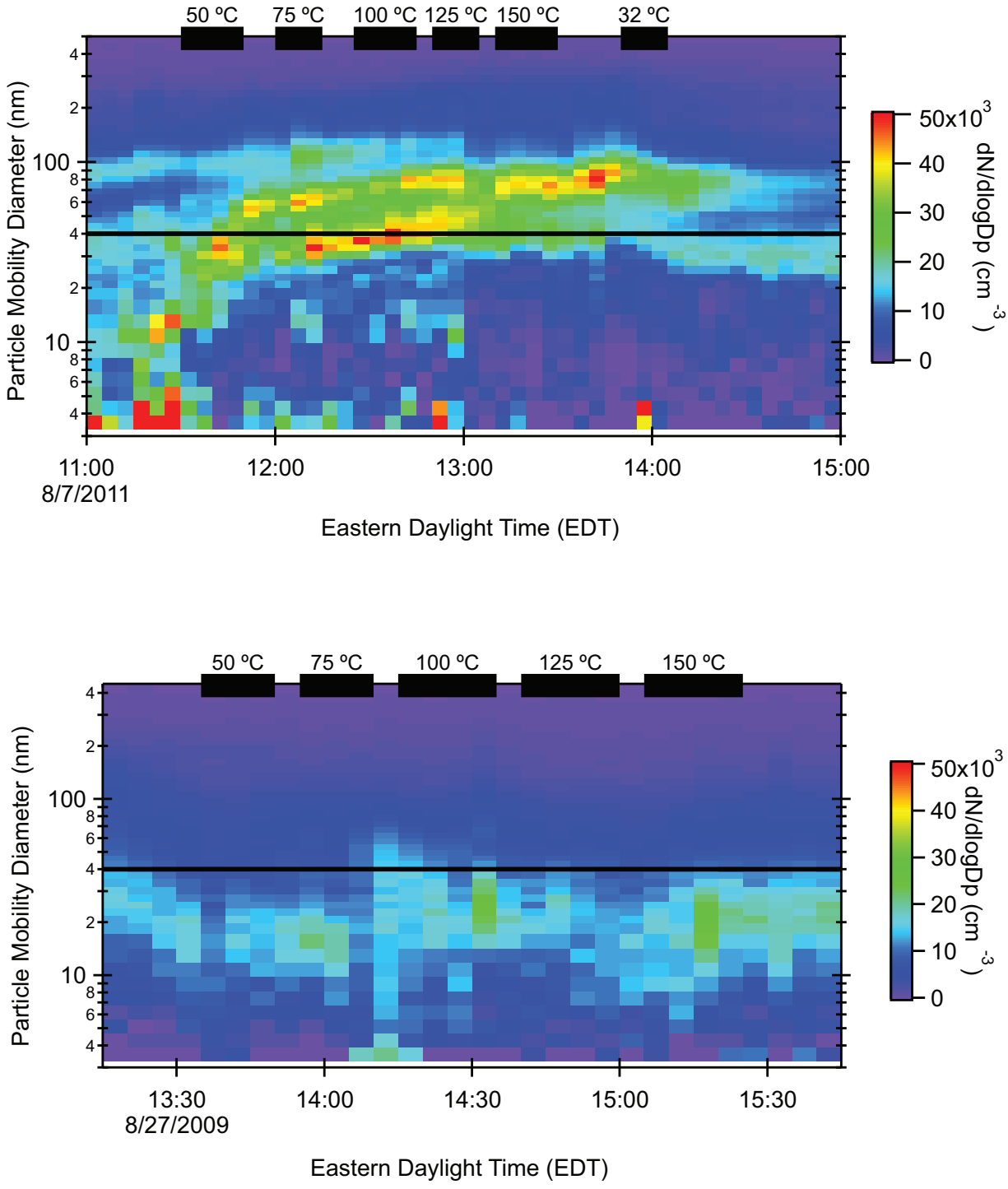


**Figure 8.6:** Measured particle size distributions plotted versus time for the two thermal-denuder experiments during NCCN. The black bars denote the time period for each thermal-denuder temperature setting. The horizontal black line at 40 nm denotes the DMA cut size uses during the experiment.

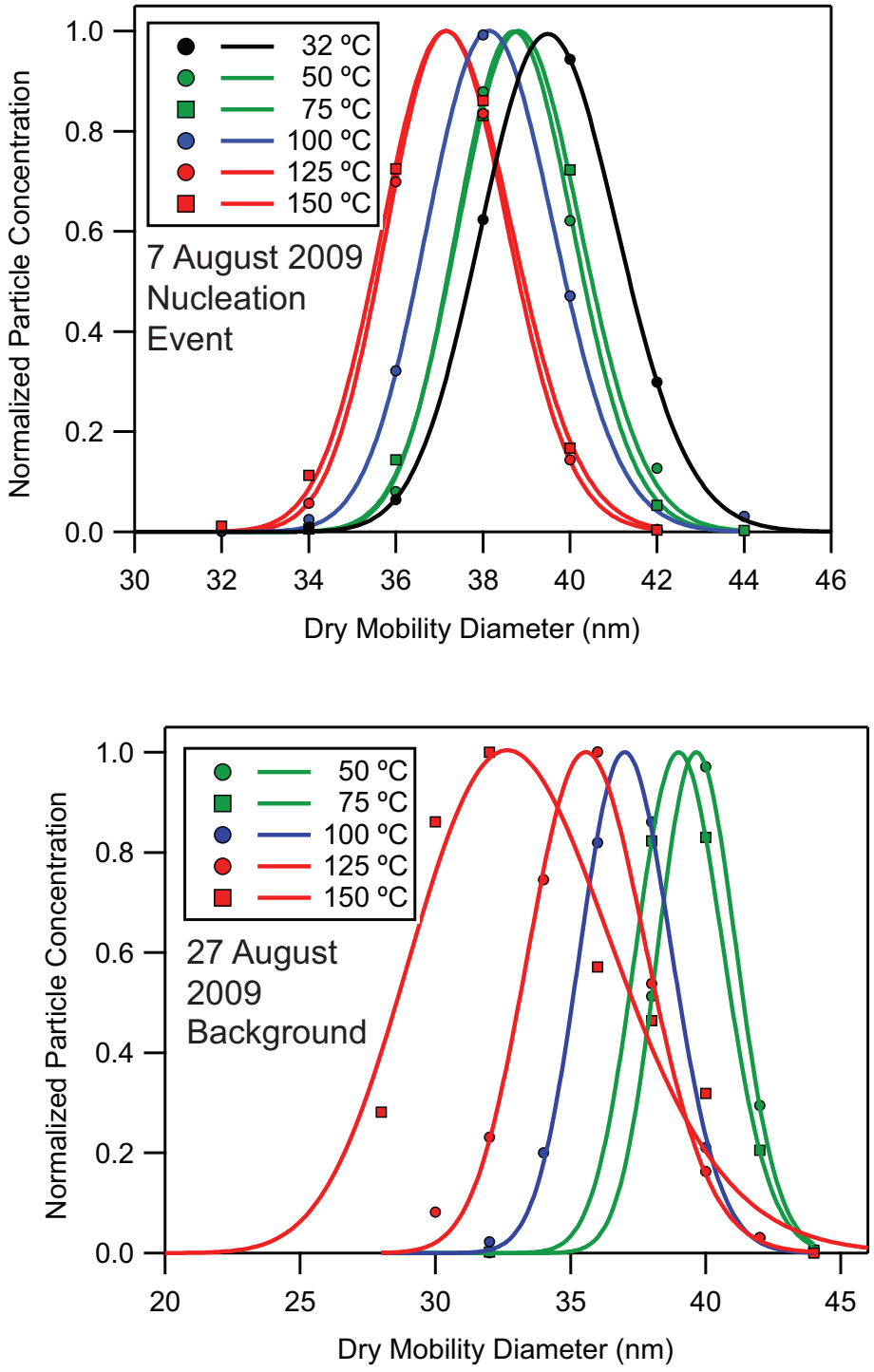


**Figure 8.7:** Size distribution data obtained for 40 nm particles after thermal treatment. Points are measured values, while the lines are lognormal fits to the data.

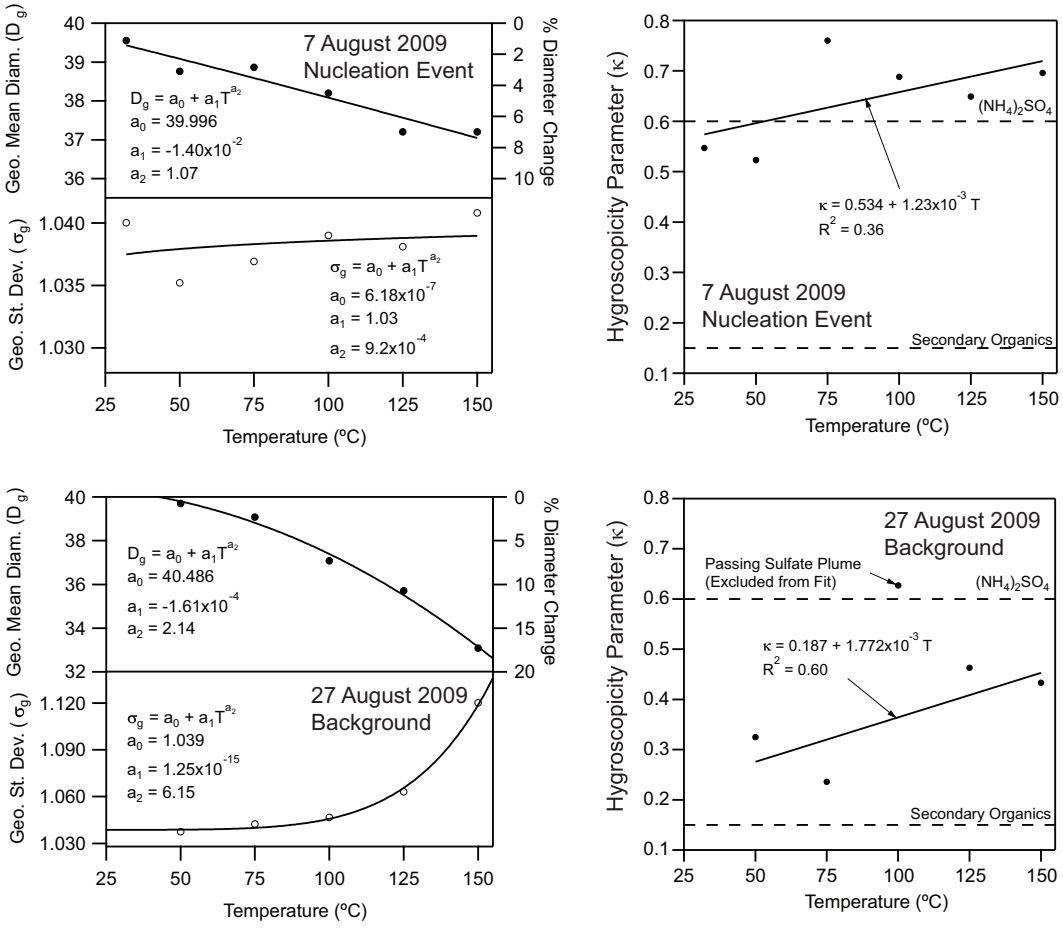


**Figure 8.8:** Measured size distribution parameters and CCN-derived hgyroscopicity for thermal-denuded 40-nm aerosol as a function of thermal-denuder temperature. Dashed lines in the figures at right denote typical $\kappa$ values for pure ammonium sulfate and SOA.

solely from the condensation of sulfate species and without appreciable organic fractions. Aerosol composition measurements on 7 August with a thermal-desorption chemical ionization mass spectrometer (TDCIMS) showed that sulfate salts of ammonium and dimethyl ammonium comprised ∼60% of the total molar composition, consistent with the observed CCN hygroscopicity. TDCIMS compositions were unavailable for the 27 August experiment, but the aerosol composition is likely to be composed of 50% organics and 50% inorganics based on past measurements (*Lim and Turpin*, 2002). This finding is inconsistent with hygroscopicity measurements of nucleated aerosols in other parts of the world showing a decrease in the aerosol hygroscopicity during NPF (e.g., *Dusek et al.*, 2010), which may suggest that the high $SO_4^{2-}$ and $NH_4^+$ concentrations in Atlanta make this area anomalous with regard to the growth of newly formed particles as there is ample inorganic material to grow the particles to larger sizes without a large contribution from semi-volatile organic species.

## *8.4 Summary and Conclusions*

Measurements of the diurnal variation of CCN activity, hygrosopicity, and mixing state are presented for Atlanta aerosol. A distinct increase in the externally-mixed, non-CCN active fraction is apparent during the morning rush hour, while both aerosol hygroscopicity and and chemical homogeneity both decrease during this period before increasing throughout the daytime. This is likely due to photochemical oxidation and coagulation processes that move the aerosol population toward a more internally-mixed and more hygroscopic state. While the mean $\kappa$ was found to agree well with proposed estimates for continental aerosol of $0.3 \pm 0.2$, variation in $\kappa$ between 0.15 and 0.6 throughout the day suggest that neglecting this diurnal variation may result in substantial CCN prediction errors. This makes sense given the large local emissions sources within the city, however, these the spatial extent affected by these trends may be too small to have a significant impact on regional CCN prediction errors.

Additionally, we characterize the aerosol volatility and CCN hygroscopicity during new particle formation events (NPF) and during background conditions. The results suggest that NPF and subsequent growth in Atlanta is driven almost entirely by less-volatile sulfate species, while organics comprise a more substantial aerosol fraction during background conditions. Exposing the aerosol to high temperatures ($\sim$150°C) both decreases the particle size by 8-20%, but also increases $\kappa$ by 0.1-0.2. In the case of the background aerosol, the resulting hygroscopicity is greater than previously reported for the most aged SOA species $\sim$ 0.3 (e.g., *Engelhart et al.*, 2011; *Asa-Awuku et al.*, 2010; *Padró et al.*, 2010; *Engelhart et al.*, 2008), which implies that the aerosol is an internal mixture of both organic and sulfate species.

# CHAPTER IX

# ADJOINT SENSITIVITY OF GLOBAL AND REGIONAL CLOUD DROPLET NUMBER TO CCN PREDICTION UNCERTAINTY

In this chapter, we use the Global Modeling Initiative (GMI) chemical transport model with a cloud droplet parameterization adjoint to quantify the sensitivity of cloud droplet number concentration to uncertainties in predicting CCN concentrations. We use published CCN closure prediction uncertainties for six different simplifying compositional and mixing state assumptions as proxies for modeled CCN uncertainty arising from application of those scenarios. It is found that cloud droplet number concentrations are fairly insensitive to CCN-active aerosol number concentrations over the continents ($\partial N_d/\partial N_{CCN} \sim 20\%$), but the sensitivities approach 100% in pristine regions such as the Alaskan Arctic and remote oceans. Since most of the anthropogenic indirect forcing is concentrated over the continents, this work shows that the application of Köhler theory and attendant simplifying assumptions in models is not a major source of uncertainty in predicting cloud droplet number or anthropogenic aerosol indirect forcing. However, it does highlight the sensitivity of some remote regions to pollution brought into the region via longe-range transport or from seasonal biogenic sources (e.g., phytoplankton as a source of dimethylsulfide in the southern oceans). Since these transient processes are not captured well by current large-scale models, the uncertainties in aerosol-cloud interactions during these events could be much larger than those uncovered here. This motivates additional measurements in these pristine regions, which have recieved little attention to date, in order to quantify the impact of and uncertainty associated with transient processes in effecting changes in cloud properties.

---

This chapter to be submitted for publication as: Moore, R. H., V. A. Karydis, S. L. Capps, and A. Nenes, Adjoint Sensitivity of Global and Regional Cloud Droplet Number to CCN Prediction Uncertainty.

## *9.1 Introduction*

The ability of atmospheric aerosols to act as cloud condensation nuclei (CCN) to form clouds remains one of the largest sources of uncertainty in current global climate modeling efforts (*Solomon et al.*, 2007). This is because aerosols are chemically-complex and are derived from a variety of primary emissions sources and from secondary gas-to-particle conversion in the atmosphere. Given this complexity, there is a need for an extensive global observational dataset that can be used to improve the representation of these processes in models.

Measurements of CCN spectra (i.e., CCN concentrations over a range of water vapor supersaturations) have been made for many decades (e.g., *Twomey*, 1977a; *Hudson*, 1993, and references therein), which have yielded CCN datasets at a few locations worldwide, particularly in marine environments. While providing information on the spatiotemporal variation of CCN concentrations and the total particle size distributions, many of these pioneering studies lacked the detailed aerosol composition information needed to fully explain the observed CCN variability. Recent improvements in instrument capabilities in the past several years have greatly improved the state of the art for measuring the chemical composition and CCN activity of aerosols. This includes the development of the the Particle-Into-Liquid Sampler (PILS, *Weber et al.*, 2001) for measuring water-soluble aerosol composition, the Aerodyne Aerosol Mass Spectrometer (AMS, *Jayne et al.*, 2000; *Jimenez et al.*, 2003) for measuring non-refractory aerosol composition, and the Droplet Measurement Technologies Continuous-Flow, Streamwise, Thermal-Gradient CCN Counter (CCNC, *Roberts and Nenes*, 2005; *Lance et al.*, 2006) for measuring CCN activation and droplet growth. Together with traditional and newer techniques for measuring the aerosol size distribution (e.g., *Wang and Flagan*, 1989; *Flagan*, 2004; *Cai et al.*, 2008; *Olfert et al.*, 2008), these robust and commercially-available instruments have enabled a multitude of field studies that have comprehensively characterized the compositional and size dependence of ambient CCN. With this information, it is now possible to empirically evaluate our theoretical

understanding of aerosol-cloud interactions using *in situ* field data.

CCN concentrations are almost exclusively predicted in models with Köhler theory (*Köhler*, 1936), which has been shown to adequately capture the CCN activity of single- and multi-component aerosol by a large number of laboratory studies (e.g., *Cruz and Pandis*, 1997; *Raymond and Pandis*, 2002, 2003; *Giebl et al.*, 2002; *Padró et al.*, 2007). However, atmospheric aerosols are much more complex than those in the laboratory, so application of Köhler theory-based models and parameterizations must necessarily make simplifying assumptions regarding the aerosol mixing state and composition in order to reduce their computational burden. To evaluate the uncertainty associated with these simplifying assumptions, a number of "CCN closure" studies have been performed, where the aerosol size distributions and chemical compositions measured in the field are used with the simplifying assumption scenarios to predict CCN number concentrations ($N_{CCN}$), which are then compared to concurrent CCN measurements with a CCNC. The deviation between the measured and predicted concentrations is interpreted as the uncertainty introduced by that set of simplifying assumptions.

While quantifying the uncertainty in our predictive understanding of CCN concentrations is important, it represents only one link in our understanding of the aerosol-cloud indirect effects on climate. The second link is the combination of CCN concentrations with cloud dynamics (e.g., ambient liquid water content, updraft velocity, and droplet condensational growth rates) to determine the overall cloud droplet concentration ($N_d$), which, in turn, determines the cloud albedo ($A$) and radiative properties. A few studies have combined ambient measurements of $N_d$ with cloud parcel model simulations using measured $N_{CCN}$ and dynamical parameters to perform "cloud droplet closure" (e.g., *Hallberg et al.*, 1997; *Chuang et al.*, 2000b; *Snider and Brenguier*, 2000; *Snider et al.*, 2003; *Conant et al.*, 2004; *Meskhidze et al.*, 2005; *Fountoukis et al.*, 2007). The agreement between predictions and measurements has generally been quite good despite large observed aerosol variability in some studies, with average $N_d$ predicted-to-measured ratios on the order of 0.71-1.2 and

some larger ratios reported by *Hallberg et al.* (1997).

In addition to these field studies, model simulations are an important tool for examining the sensitivity of $N_d$ to changes in CCN and other parameters by selectively turning on and off certain effects. For example, *Lance et al.* (2004) used a large number of 1-D parcel model simulations to look at the competing influences of aerosol chemistry and cloud updraft velocity in determining $N_d$ under a wide variety of conditions. They found that chemical effects can account for 28-100% of the variability in $N_d$ for both marine and continental environments. *Rissman et al.* (2004) extended the droplet parameterization of *Abdul-Razzak et al.* (1998) to include the effects of surfactants and derived the analytical sensitivities of $N_d$ with respect to the parameterization inputs, and reached a similar conclusion that $N_d$ can be up to 1.5-times as sensitive to aerosol composition and surface tension effects as it is to cloud dynamical effects under certain atmospherically-relevant conditions. *Sotiropoulou et al.* (2006) used a droplet parameterization to propagate the CCN closure uncertainties observed by *Medina et al.* (2007) during the ICARTT campaign to uncertainties in $N_d$. Using a campaign-average, prescribed CCN spectrum and size distribution in the parameterization, they found the uncertainty of $N_d$ to be 50% of that for $N_{CCN}$ over a range of conditions. *Ervens et al.* (2010) also modeled the sensitivity of $N_d$ uncertainty to $N_{CCN}$ uncertainty and found that a 100% overprediction of $N_{CCN}$ leads to only a 15% overprediction in $N_d$. These findings highlight the potential importance of aerosol effects versus cloud dynamic effects, and motivate future work with larger scale, global models to better understand where clouds are most sensitive to aerosol composition effects and where they are not.

Toward this end, *Sotiropoulou et al.* (2007) parameterized the CCN uncertainty from the ICARTT study in terms of supersaturation and used this relationship with the global $N_d$ and $N_{CCN}$ outputs from the NASA Goddard Institute for Space Studies Version II' (GISS II') general circulation model (GCM) to quantify the resulting errors in $N_d$, aerosol

indirect forcing, and autoconversion rate. This is achieved by running two present-day simulations: a base case simulation with normal present day emissions and a perturbed case simulation where the size distribution is varied to alter the CCN concentration according to the ICARTT uncertainty. Their results suggest that a global average CCN prediction error of 10-20% translates into a 7-14% uncertainty in $N_d$ and 10-20% uncertainty in aerosol indirect forcing (*Sotiropoulou et al.*, 2007). While this study gives important first-order constraints on how CCN uncertainty may affect global indirect forcing estimates, the approach does not account for regional differences in the uncertainty of $N_{CCN}$ or how the model pertubation may induce other, non-linear effects in the simulation. A thorough discussion of some of these challenges is presented by *Lee et al.* (2011), who has developed a new statistical method for estimating model sensitivities to input uncertainies.

In summary, while there have been several studies to date examining the sensitivity of cloud droplet number concentration uncertainty to uncertainties in CCN number concentration, there is still no clear estimate of the global magnitude of this sensitivity or how it varies regionally. In this study, we address these questions by combining data obtained from over thirty published CCN closure studies with simulations conducted with the recently-developed adjoint of the *Kumar et al.* (2009) cloud droplet parameterization. The adjoint tracks the sensitivity of model parameters to inputs concurrently with the forward model execution and without perturbing the the simulation parameters. Thus, it is able to find the sensitivity of $N_d$ to $N_{CCN}$ (or a large number of other parameters) with analytical precision and requires only a single model run. In the following sections, we briefly discuss the published datasets and the adjoint model before comparing and contrasting the simulation results with observations. The goal of this work is to improve the understanding of the global and regional sensitivities of modeled cloud droplet number to the CCN concentration uncertainty introduced through simplified model assumptions regarding aerosol mixing state and chemical composition.

## 9.2 Methods

### 9.2.1 CCN Prediction Uncertainty Measurements

In this work, we use CCN prediction uncertainties measured at multiple locations worldwide as a proxy for CCN prediction uncertainty in models employing Köhler theory. Table 9.1 lists the thirty-three closure studies considered, which were selected because they involve ambient measurements of CCN concentration, aerosol size distribution, and aerosol chemical composition. Additionally, they report CCN closure uncertainties for at least one of six common closure scenarios as follows:

1. *Ammonium Sulfate:* All particles are composed of ammonium sulfate ($\kappa$=0.6)

2. *Internal Mixture, Soluble Organics:* All particles have the same composition as determined by the size-averaged, aerosol composition measurements. Organics are soluble with $\kappa$ = 0.11.

3. *Internal Mixture, Insoluble Organics:* All particles have the same composition as determined by the size-averaged, aerosol composition measurements. Organics are insoluble with $\kappa$ = 0.

4. *External Mixture, Soluble Organics:* Particles are composed of pure components (e.g., organic particles, ammonium sulfate particles, etc.), and the number of each type is determined by the size-averaged, aerosol composition measurements. Organics are soluble with $\kappa$ = 0.11.

5. *External Mixture, Insoluble Organics:* Particles are composed of pure components (e.g., organic particles, ammonium sulfate particles, etc.), and the number of each type is determined by the size-averaged, aerosol composition measurements. Organics are insoluble with $\kappa$ = 0.

6. *Internal Mixture, Size-Dependent Composition, Insoluble Organics:* Particles in each size distribution bin have the same composition as determined by the size-resolved,

aerosol composition measurements, but the particle compositions in different size bins may not be the same. Organics are insoluble with $\kappa = 0$.

where the aerosol hygroscopicity is reported using the $\kappa$ parameter of *Petters and Kreidenweis* (2007). These simplified mixing state and composition assumptions are characteristic of those used in large-scale models to improve computational efficiency. In another form of CCN closure, some other studies in the literature use the aerosol hygroscopicity obtained from humidified aerosol growth factor measurements to predict CCN concentrations with typically good agreement (e.g., *Kim et al.*, 2011; *Kammermann et al.*, 2010; *Vestin et al.*, 2007; *Good et al.*, 2010; *Gasparini et al.*, 2006; *Dusek et al.*, 2003; *Covert et al.*, 1998). While important for assessing the uncertainties associated with using the same hygroscopicity to predict both subsaturated and supersaturated water uptake, this type of closure study is less relevant for comparing against mass-composition-based models and is not included here.

The studies shown in Table 9.1 reflect a diverse mixture of urban, rural, and marine sampling on both airborne and ground-based platforms. The majority of published studies focus on locations in North America, and CCN concentrations range from zero to a few thousand particles per $cm^3$ with the highest concentrations observed in the vicinity of local urban emissions sources (e.g., Houston, TX; Riverside, CA; Mexico City, Mexico) and within a targeted ship plume. Most studies report CCN concentration and closure data at a single or a few discrete supersaturations, and the tabulated values reflect the average across all supersaturations. A detailed description of each closure study location, measurements, and data analysis is given by the references in Table 9.1.

The CCN overprediction uncertainties reported by these studies are shown in Table 9.2. Most studies tend toward overprediction with the external mixing scenarios producing lower predicted CCN concentrations than the ammonium sulfate or internal mixing scenarios. As discussed by *Ervens et al.* (2010), some studies report large CCN overpredictions on the order of 2-5-fold, which likely reflects the contribution of local emissions sources

**Table 9.1:** Summary of past CCN closure studies using measured aerosol compositions and size distributions for predictions.

| | Study Location | Dates | GPS Coordinates | | Observed | Observed | Reference |
|---|---|---|---|---|---|---|---|
| | | | Latitude | Longitude | $N_{CCN}$ (cm$^{-3}$) | $s$ (%) | |
| 1 | Alaskan Arctic (ARCPAC) | 04/2008 | 65-76°N | 130-163°W | 100-500 | 0.1-0.3 | *Moore et al.* (2011) |
| 2 | Amazon Rainforest, Brazil (AMAZE-08) | 02/2008-03/2008 | -3-10°N | 50-60°W | 40-200 | 0.10-0.82 | *Gunthe et al.* (2009) |
| 3 | Atlanta, GA (AMIGAS) | 07/2008-08/2008 | 33-34°N | 84-85°W | 500-10,000 | 0.2-1.0 | *Padró et al.* (in review) |
| 4 | Chebogue Point, Canada (ICARTT) | 07/2004-08/2004 | 43-44°N | 62-63°W | 0-4,000 | 0.65 | *Ervens et al.* (2007, 2010) |
| 5 | Duke Forest, NC (Celtic) | 07/2003 | 34-36°N | 75-80°W | 0-3,000 | 0.20-0.33 | *Stroud et al.* (2007) |
| 6 | Ebert, Ontario, Canada (CARE) | 11/2005 | 43-45°N | 79-81°W | 400-5,000 | 0.32 | *Chang et al.* (2007) |
| 7 | Ebert, Ontario, Canada (CARE) | 05/2007-06/2007 | 43-45°N | 79-81°W | 0-10,000 | 0.42 | *Chang et al.* (2010) |
| 8 | Finokalia, Greece (FAME-07) | 06/2007-10/2007 | 33-38°N | 15-25°E | 500-4,000 | 0.21-0.73 | *Bougiatioti et al.* (2009, 2011) |
| 9 | Florida Coast (CRYSTAL-FACE) | 07/2002 | 24-27°N | 80-84°W | 230-380 | 0.20-0.85 | *VanReken et al.* (2003) |
| 10 | Guangzhou, China (PRIDE-PRD2006) | 07/2006 | 21-24°N | 111-115°E | 1,000-10,000 | 0.068-0.47 | *Rose et al.* (2011) |
| 11 | Gulf Coast, Houston, TX (GoMAACS) | 08/2006-09/2006 | 27-29°N | 93-95°W | 3,000-30,000 | 0.44 | *Quinn et al.* (2008b); *Ervens et al.* (2010) |
| 12 | Gulf of Mexico Background Air (CalNex) | 06/2010 | 27-31°N | 84-86°W | | 0.25-0.65 | *Moore et al.* (in review) |
| 13 | Holme Moss, UK | 11/2006-12/2006 | 53-54°N | 4-5°W | 400-1,200 | 0.23 | *Ervens et al.* (2010) |
| 14 | Houston, TX (GoMACCS) | 08/2006-09/2006 | 29-32°N | 93-97°W | 200-15,000 | 0.35-1.0 | *Lance et al.* (2009) |
| 15 | Houston, TX (TexAQS) | 09/2006-10/2006 | 29-34°N | 92-100°W | 200-2,000 | 0.30-0.71 | *Asa-Awuku et al.* (2011) |
| 16 | Jeju Island, Korea (ABC-EAREX) | 03/2005-04/2005 | 32-36°N | 124-128°E | 1,500-3,500 | 0.6 | *Yum et al.* (2007) |
| 17 | Jeju Island, Korea (ABC-EAREX) | 03/2005-04/2005 | 32-36°N | 124-128°E | 400-4,600 | 0.09-0.97 | *Kuwata et al.* (2008) |
| 18 | Jungfraujoch, Switzerland | 05/2008 | 46-47°N | 7-9°E | 0-1,500 | 0.12-1.18 | *Jurányi et al.* (2010) |
| 19 | Los Angeles, CA (CalNex) | 05/2010-06/2010 | 33-35°N | 116-118°W | 0-7,000 | 0.25-0.65 | *Moore et al.* (in preparation) |
| 20 | Mexico City, Mexico (MILAGRO) | 03/2006 | 19-20°N | 98-100°W | 7,000-17,000 | 0.29 | *Wang et al.* (2010a); *Ervens et al.* (2010) |
| 21 | Monterey, CA (MASE) | 07/2005 | 36-39°N | 121-125°W | 300-1,300 | 0.1 | *Ervens et al.* (2010) |
| 22 | Monterey, CA, Above Cloud (MASE) | 07/2005 | 36-39°N | 121-125°W | 0-1,700 | 0.2 | *Wang et al.* (2008) |
| 23 | Monterey, CA, Marine Boundary Layer (MASE) | 07/2005 | 36-39°N | 121-125°W | 0-1,700 | 0.2 | *Wang et al.* (2008) |
| 24 | Pacific (Eastern), N. California Coast (CIFEX) | 04/2004 | 37-44°N | 123-130°W | 200-1,000 | 0.2-0.8 | *Roberts et al.* (2006) |
| 25 | Pacific (Eastern), Los Angeles, CA (CalNex) | 05/2010-06/2010 | 33-34°N | 118-120°W | 50-6,000 | 0.25-0.65 | *Moore et al.* (in preparation) |
| 26 | Riverside, CA (SOAR-I) | 07/2005-08/2005 | 33-34°N | 116-119°W | 11,000-19,000 | 0.27 | *Cubison et al.* (2008); *Ervens et al.* (2010) |
| 27 | San Joaquin Valley, CA (CalNex) | 05/2010-06/2010 | 35-38°N | 118-121°W | 100-8,000 | 0.25-0.65 | *Moore et al.* (in preparation) |
| 28 | Sacramento Valley, CA (CalNex) | 05/2010-06/2010 | 38-40°N | 121-123°W | 50-7,000 | 0.25-0.65 | *Moore et al.* (in preparation) |
| 29 | Ship Channel, Houston, TX (GoMACCS) | 08/2006-09/2006 | 28-30°N | 94-95°W | 400-3,000 | 0.44 | *Quinn et al.* (2008b); *Ervens et al.* (2010) |
| 30 | Ship Exhaust Plume, Monterey, CA (MASE-II) | 07/2007 | 35-36°N | 123-124°W | 200-30,000 | 0.10-0.35 | *Murphy et al.* (2009) |
| 31 | Southern Great Plains ARM Site, OK | 05/2003 | 35-37°N | 96-98°W | 100-11,000 | 2.1-2.8 | *Rissman et al.* (2006) |
| 32 | Thompson Farms, NH (ICARTT) | 08/2004 | 42-44°N | 70-74°W | 100-4,000 | 0.2-0.6 | *Medina et al.* (2007) |
| 33 | Toronto, Canada | 09/2003 | 43-44°N | 79-80°W | 0-3,500 | 0.58 | *Broekhuizen et al.* (2006) |

**Table 9.2:** CCN number concentration percent overprediction ($\Phi$-1)$\times$100% for different closure scenarios reported by the studies in Table 9.1.

| | | | Internal Mixture | | | External Mixture | |
|---|---|---|---|---|---|---|---|
| | Study Location | $(NH_4)_2SO_4$ | Sol. Org. | Insol. Org. | Size-Dep. | Sol. Org. | Insol. Org. |
| 1 | Alaskan Arctic (ARCPAC) | | 57±50 | 49±47 | – | 11±30 | -23±36 |
| 2 | Amazon Rainforest, Brazil (AMAZE-08) | – | 14.1 | – | – | – | – |
| 3 | Atlanta, GA (AMIGAS) | 194 | 157 | 146 | – | 169 | 40 |
| 4 | Chebogue Point, Canada (ICARTT) | – | 40±40 | -10±40 | – | 20±30 | -30±30 |
| 5 | Duke Forest, NC (Celtic) | – | 71 | 20 | – | – | – |
| 6 | Ebert, Ontario, Canada (CARE) | – | -29 | – | -14 | – | – |
| 7 | Ebert, Ontario, Canada (CARE) | – | – | -3 | – | – | – |
| 8 | Finokalia, Greece (FAME-07) | – | 1.8±12 | -2.8±14 | -7±11 | – | – |
| 9 | Florida Coast (CRYSTAL-FACE) | 6 | – | – | – | – | – |
| 10 | Guangzhou, China (PRIDE-PRD2006) | – | 20.7 | – | – | – | – |
| 11 | Gulf Coast, Houston, TX (GoMAACS) | – | 130±190 | 70±100 | – | 140±190 | 90±110 |
| 12 | Gulf of Mexico Background Air (CalNex) | | | | | | |
| 13 | Holme Moss, UK | – | -10±50 | -20±50 | – | 20±60 | 0±50 |
| 14 | Houston, TX (GoMACCS) | 36.5 | – | 2.6 | – | – | – |
| 15 | Houston, TX (TexAQS) | 11.6±9.3 | -3.6±7.7 | -16.1±10.0 | -13.1±8.4 | – | -60.9±6.4 |
| 16 | Jeju Island, Korea (ABC-EAREX) | 27±29 | – | – | – | – | – |
| 17 | Jeju Island, Korea (ABC-EAREX) | 16±18 | – | – | – | – | – |
| 18 | Jungfraujoch, Switzerland | – | 4±3 | – | – | – | – |
| 19 | Los Angeles, CA (CalNex) | 84±97 | 54±57 | 41±51 | 18±85 | 38±49 | -16±42 |
| 20 | Mexico City, Mexico (MILAGRO) | – | 10±20 | -50±20 | 10 | 10±10 | -50±20 |
| 21 | Monterey, CA (MASE) | – | 10±60 | 10±60 | – | 30±60 | 30±60 |
| 22 | Monterey, CA, Above Cloud (MASE) | -54 | 17 | -29 | – | -11 | -78 |
| 23 | Monterey, CA, Marine Boundary Layer (MASE) | -8 | – | -5 | – | – | – |
| 24 | Pacific (Eastern), N. California Coast (CIFEX) | 79 | – | – | – | – | – |
| 25 | Pacific (Eastern), Los Angeles, CA (CalNex) | 58±90 | 32±39 | 23±34 | -5±31 | 20±36 | -23±33 |
| 26 | Riverside, CA (SOAR-I) | – | 500±210 | 360±170 | – | 390±170 | 340±180 |
| 27 | San Joaquin Valley, CA (CalNex) | 141±187 | 71±154 | 45±126 | 28±75 | 56±132 | 2±67 |
| 28 | Sacramento Valley, CA (CalNex) | 150±190 | 25±29 | -3±26 | -14±77 | 16±25 | -59±22 |
| 29 | Ship Channel, Houston, TX (GoMACCS) | – | 320±320 | 300±300 | – | 300±300 | 140±190 |
| 30 | Ship Exhaust Plume, Monterey, CA (MASE-II) | – | – | 23±6 | 16±6 | – | – |
| 31 | Southern Great Plains ARM Site, OK | 92±192 | – | – | – | – | – |
| 32 | Thompson Farms, NH (ICARTT) | – | – | 35.7±28.5 | 17.4±27.1 | – | – |
| 33 | Toronto, Canada | – | – | – | 12 | – | – |
| | Number of Studies | 15 | 21 | 22 | 11 | 14 | 15 |

near the sampling locations that may produce a size-varying, externally-mixed aerosol that cannot be captured well from bulk chemical composition measurements. In some locations (e.g., Houston, TX, and Los Angeles, CA), airborne studies covering a wide horizontal and vertical sampling area report a smaller closure uncertainty than that from ground-based sites in the same area. These conflicting values probably stem from the more local nature of the ground measurements versus the regional nature of airborne measurements. To capture the observed range of variablity, we evaluate the uncertainties from both sets of measurements, recognizing that the former are probably more relevant for small-scale air quality modeling while the latter are probably more appropriate for comparison with coarser-resolution GCM climate predictions.

### 9.2.2 Model Description

Simulations were conducted with the NASA Global Modeling Initiative (GMI) chemical transport model (CTM) using offline wind fields and an online aerosol simulation module coupled with the *Kumar et al.* (2009) droplet activation parameterization and its adjoint. The GMI model (`http://gmi.gsfc.nasa.gov/`) is a modular CTM capable of multi-year, global simulations of aerosol concentrations and compositions (*Rotman et al.*, 2001; *Considine et al.*, 2005). The aerosol module used for this study is that of *Liu et al.* (2005), which uses emissions inputs for $SO_2$, dimethyl sulfide, $H_2O_2$, elemental carbon (EC), organic carbon (OC), mineral dust, and sea salt from *Liu et al.* (2005). The online aerosol module outputs the global distribution of aerosol mass concentrations, which is used to drive the cloud droplet parameterization and its adjoint.

Before running the offline parameterization, the aerosol mass is first classified as one of four, externally-mixed aerosol modes: fossil fuels ($SO_4^{2-}$, OC, and EC), biomass burning (OC and EC), marine ($SO_4^{2-}$ and sea salt), and mineral dust. The aerosol within each mode are assumed to be internally mixed and follow a prescribed size distribution as given by *Chuang et al.* (1997) and *Radke et al.* (1988) for fossil fuel aerosols, *Anderson*

*et al.* (1996) for biomass burning aerosols, *Lance et al.* (2004) for marine aerosols, and *d'Almeida* (1987) for mineral dust aerosols. The aerosol number concentration for each type is then computed using these size distributions and a mass-fraction-weighted average of the component densities (e.g., $SO_4^{2-}$, OC, EC) as described in more detail by *Karydis et al.* (in press).

The aerosol number distributions are then used to drive an offline cloud droplet parameterization (*Kumar et al.*, 2009; *Barahona and Nenes*, 2007; *Fountoukis and Nenes*, 2005; *Nenes and Seinfeld*, 2003) that employs a physically-based method for calculating the aerosol CCN spectrum (i.e., the number of particles that act as CCN as a function of supersaturation) and the maximum supersaturation, $s_{max}$, for ascending cloud parcels in the global model. The total cloud droplet number, $N_d$, is then the value of the CCN spectrum at $s_{max}$ in each model grid cell.

Recently, the adjoint of the cloud droplet parameterization has been developed (*Karydis, V., et al., Elucidating the Relative Significance of Aerosol and Dynamical Parameters on Global Cloud Droplet Number, in preparation*), which continuously tracks the sensitivity of $N_d$ to the parameterization input parameters (i.e, $N_{CCN}$ and compositions) during the forward model run. This allows the simultaneous computation of both the mean parameter values and their sensitivities with analytical precision.

### 9.2.3 Model Application

The model simulation spans the one year period from March 1997 to February 1998, including a one-month spin up time that is not included in the analysis. This simulated time period was selected to complement the modeling study of *Karydis et al.* (in press). Meteorological fields were obtained from the GISS II' global climate model (*Koch and Rind*, 1998; *Rind and Lerner*, 1996), with a horizontal resolution of 4° latitude by 5° longitude and with 23 vertical layers from surface pressure to 0.017 hPa. The meteorological information in the simulation was updated every three hours. For the droplet parameterization

and adjoint, a constant effective water uptake coefficient of 0.06 was assumed (*Fountoukis et al.*, 2007), and realistic updraft velocities were prescribed based on observed values for stratocumulus clouds over land ($w$ = 0.3 m s$^{-1}$) (*Chuang et al.*, 2000b; *Guibert et al.*, 2003; *Meskhidze et al.*, 2005).

## *9.3 Results and Discussion*

### 9.3.1 Global $N_{CCN}$ Distributions

The simulated global annual mean $N_{CCN}$ and $s_{max}$ are shown in Figure 9.1 and are found to be mostly anti-correlated, consistent with the mechanism of increased CCN concentrations in modulating cloud dynamics (i.e., aerosol indirect effects). The highest concentrations (and lowest $s_{max}$) are seen over the eastern United States, Europe, and east Asia from anthropogenic emissions. Higher concentrations are also predicted for the southern hemisphere near and downwind of biomass burning sources. Meanwhile, the lowest concentrations (and highest $s_{max}$ occur in the the pristine southern and subtropical oceans and the Alaska-Canadian Arctic. The simulated global mean CCN concentration is 1967$\pm$5341 for a mean $s_{max}$ of 0.2$\pm$0.1%.

A quantitative comparison between the simulated $N_{CCN}$ at $s_{max}$ and the observed $N_{CCN}$ at varying $s$ is given in Table 9.3. Since the studies are mostly land-based, the simulated $s_{max}$ in these locations is lower than the global average while the simulated $N_{CCN}$ is nearly two-fold higher. For many regions, simulated concentrations agree reasonably well with the observed range of values, although much higher simulated:observed $N_{CCN}$ ratios are found in a number of locations (e.g., the Amazon Rainforest, Duke Forest, Finokalia, the Florida coast, Jeju Island, and others), which may be reflective of seasonal differences or varying local emissions sources that are not captured by either the short-term field study or the simulated annual mean.

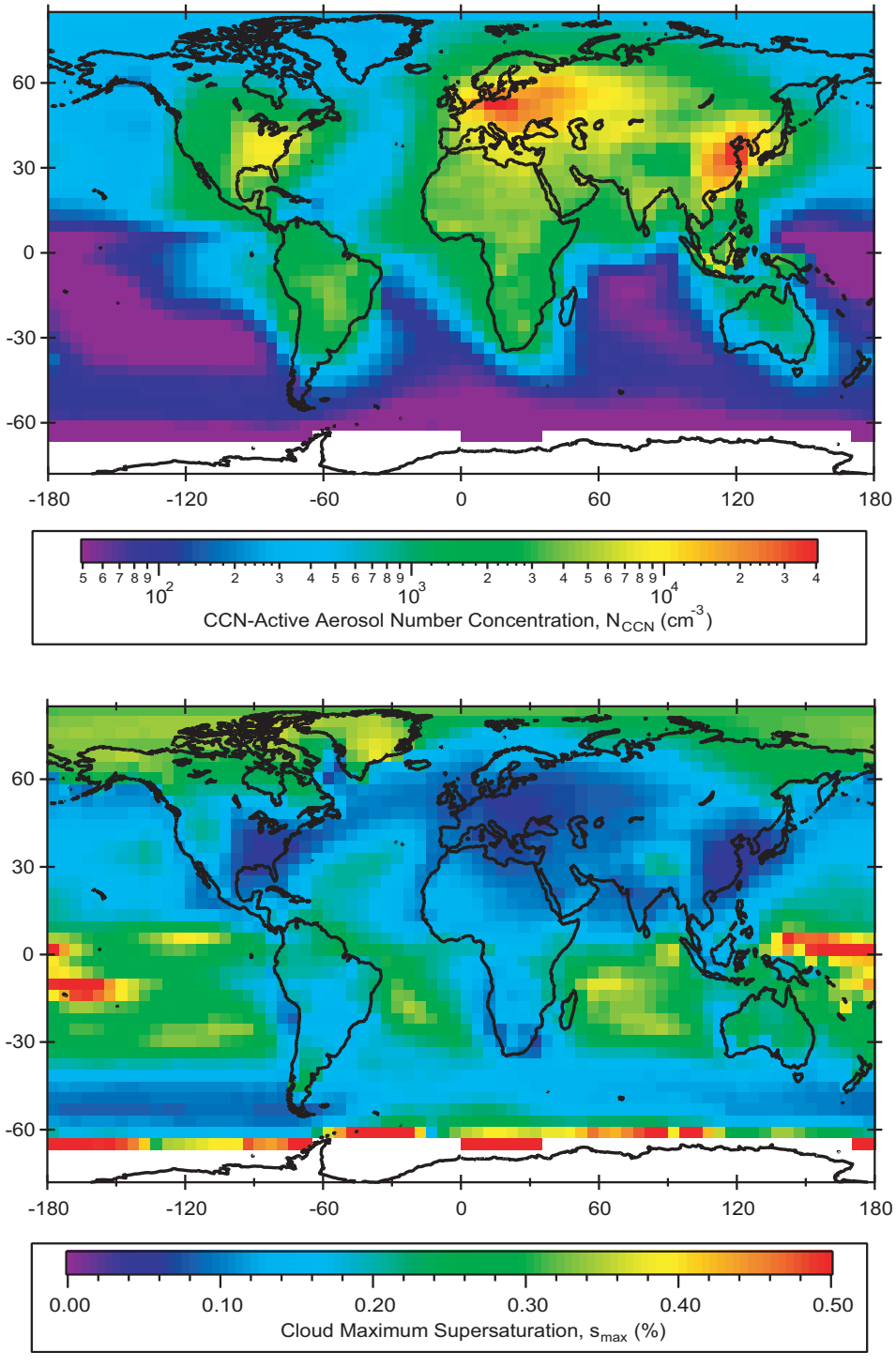


**Figure 9.1:** Simulated global spatial distribution of the annual mean $N_{CCN}$ (top) and $s_{max}$ (bottom).

**Table 9.3:** Comparison of regional observed and simulated CCN number concentrations, $N_{CCN}$, simulated cloud droplet concentrations, $N_d$, and the normalized cloud droplet concentration sensitivities, $(\partial N_d/\partial N_{CCN})(N_{CCN}/N_d)$. All simulation results are annual means.

| | Study Location | Observed $s$ (%) | Observed $N_{CCN}$ (cm$^{-3}$) | Simulated $s_{max}$ (%) | Simulated $N_{CCN}$ (cm$^{-3}$) | Simulated $N_d$ (cm$^{-3}$) | $\left(\frac{\partial N_d}{\partial N_{CCN}}\right)\left(\frac{N_{CCN}}{N_d}\right)$ |
|---|---|---|---|---|---|---|---|
| 1 | Alaskan Arctic (ARCPAC) | 0.1-0.3 | 100-500 | 0.33 | 356 | 245 | 0.74 |
| 2 | Amazon Rainforest, Brazil (AMAZE-08) | 0.10-0.82 | 40-200 | 0.22 | 1,103 | 415 | 0.39 |
| 3 | Atlanta, GA (AMIGAS) | 0.2-1.0 | 500-10,000 | 0.06 | 8,803 | 1,008 | 0.10 |
| 4 | Chebogue Point, Canada (ICARTT) | 0.65 | 0-4,000 | 0.11 | 2,475 | 689 | 0.15 |
| 5 | Duke Forest, NC (Celtic) | s.ss-s.ss | 0-3,000 | 0.06 | 7,691 | 901 | 0.06 |
| 6 | Ebert, Ontario, Canada (CARE) | 0.32 | 400-5,000 | 0.11 | 3,324 | 817 | 0.19 |
| 7 | Ebert, Ontario, Canada (CARE) | 0.42 | 0-10,000 | 0.11 | 3,324 | 817 | 0.19 |
| 8 | Finokalia, Greece (FAME-07) | 0.21-0.73 | 500-4,000 | 0.07 | 8,247 | 845 | 0.03 |
| 9 | Florida Coast (CRYSTAL-FACE) | 0.20-0.85 | 230-380 | 0.08 | 3,557 | 696 | 0.08 |
| 10 | Guangzhou, China (PRIDE-PRD2006) | 0.068-0.47 | 1,000-10,000 | 0.07 | 11,293 | 932 | 0.05 |
| 11 | Gulf Coast, Houston, TX (GoMAACS) | 0.44 | 3,000-30,000 | 0.06 | 5,960 | 744 | 0.005 |
| 12 | Gulf of Mexico Background Air (CalNex) | 0.25-0.65 | | 0.06 | 6,886 | 902 | 0.08 |
| 13 | Holme Moss, UK | 0.23 | 400-1,200 | 0.08 | 6,365 | 672 | -0.05 |
| 14 | Houston, TX (GoMACCS) | 0.35-1.0 | 200-15,000 | 0.06 | 6,710 | 835 | 0.04 |
| 15 | Houston, TX (TexAQS) | 0.30-0.71 | 200-2,000 | 0.07 | 6,755 | 909 | 0.09 |
| 16 | Jeju Island, Korea (ABC-EAREX) | 0.6 | 1,500-3,500 | 0.06 | 10,935 | 943 | 0.05 |
| 17 | Jeju Island, Korea (ABC-EAREX) | 0.09-0.97 | 400-4,600 | 0.06 | 10,935 | 943 | 0.05 |
| 18 | Jungfraujoch, Switzerland | 0.12-1.18 | 0-1,500 | 0.07 | 15,302 | 1,022 | 0.07 |
| 19 | Los Angeles, CA (CalNex) | 0.25-0.65 | 0-7,000 | 0.16 | 1,877 | 626 | 0.20 |
| 20 | Mexico City, Mexico (MILAGRO) | 0.29 | 7,000-17,000 | 0.09 | 4,178 | 831 | 0.13 |
| 21 | Monterey, CA (MASE) | 0.1 | 300-1,300 | 0.15 | 1,472 | 486 | 0.15 |
| 22 | Monterey, CA, Above Cloud (MASE) | 0.2 | 0-1,700 | 0.15 | 1,472 | 486 | 0.15 |
| 23 | Monterey, CA, Marine Boundary Layer (MASE) | 0.2 | 0-1,700 | 0.15 | 1,472 | 486 | 0.15 |
| 24 | Pacific (Eastern), N. California Coast (CIFEX) | 0.2-0.8 | 200-1,000 | 0.13 | 903 | 293 | 0.13 |
| 25 | Pacific (Eastern), Los Angeles, CA (CalNex) | 0.25-0.65 | 50-6,000 | 0.14 | 1,790 | 564 | 0.16 |
| 26 | Riverside, CA (SOAR-I) | 0.27 | 11,000-19,000 | 0.16 | 1,877 | 625 | 0.20 |
| 27 | San Joaquin Valley, CA (CalNex) | 0.25-0.65 | 100-8,000 | 0.18 | 1,721 | 631 | 0.24 |
| 28 | Sacramento Valley, CA (CalNex) | 0.25-0.65 | 50-7,000 | 0.16 | 1,269 | 464 | 0.18 |
| 29 | Ship Channel, Houston, TX (GoMACCS) | 0.44 | 400-3,000 | 0.06 | 6,710 | 835 | 0.04 |
| 30 | Ship Exhaust Plume, Monterey, CA (MASE-II) | 0.10-0.35 | 200-30,000 | 0.11 | 1,441 | 365 | 0.03 |
| 31 | Southern Great Plains ARM Site, OK | 2.1-2.8 | 100-11,000 | 0.07 | 6,426 | 962 | 0.13 |
| 32 | Thompson Farms, NH (ICARTT) | 0.2-0.6 | 100-4,000 | 0.10 | 3,728 | 856 | 0.16 |
| 33 | Toronto, Canada | 0.58 | 0-3,500 | 0.09 | 4,515 | 911 | 0.15 |
| | Mean of All Studies (weighted equally) | | | 0.11±0.06 | 4,708±3,420 | 708±221 | 0.13±0.13 |
| | Mean of All Studies (weighted by area) | | | 0.19±0.11 | 3,430±4,144 | 524±314 | 0.37±0.30 |
| | **Global Mean Values** | | | **0.20±0.10** | **1,967±5,341** | **352±310** | **0.47±0.29** |

### 9.3.2 Global $N_d$ Distribution and Relative Sensitivity of $N_d$ to $N_{CCN}$

Simulated droplet concentrations, $N_d$, are also shown in Table 9.3 and in the upper portion of Figure 9.2. The global distribution of $N_d$ is similar to that of $N_{CCN}$ but with substantially lower concentrations (approximately five-fold on average). This is shown quantitatively in Figure 9.3, where it can been seen that nearly all CCN form droplets at low concentrations, but the impact on $N_d$ of increasing $N_{CCN}$ gradually decreases above $\sim$100 cm$^{-3}$. This implies a concentration-dependent sensitivity of $N_d$ to $N_{CCN}$, which is shown in Figures 9.2 and 9.3. Low values of $N_{CCN}$ correlate with the highest $s_{max}$ and greatest cloud droplet sensitivity, while the highest $N_{CCN}$ correlate with the lowest $s_{max}$ and smallest cloud droplet sensitivity. The sensitivity decreases from nearly unity at 100 cm$^{-3}$ to nearly zero at $10^4$ cm$^{-3}$, however, there is no clear trend in $s_{max}$ within this transition region (Figure 9.3, which likely arises as aerosol concentration effects become more important than cloud dynamics in determining $N_d$.

The $N_d$ sensitivities shown in Table 9.3 indicate that most of the closure studies carried out in the past decade have taken place in moderately to heavily-polluted areas, where $N_d$ is fairly insensitive to changes in $N_{CCN}$ ($\sim$ 5-20%). Two studies in the Alaskan Arctic and the Amazon Rainforest show lower simulated $N_{CCN}$ and higher simulated $s_{max}$ and sensitivity of $N_d$ to $N_{CCN}$ ($\sim$ 40-75%). The global mean sensitivity is 0.47$\pm$0.29.

*Sotiropoulou et al.* (2007) simulated global cloud droplet number concentrations and anthropogenic aerosol indirect forcing using the GISS II' GCM and uncovered a similar geographical distribution as modeled here, but with nearly two-fold lower droplet concentrations in some regions. They found that the spatial pattern of regional aerosol indirect forcing agreed very well with the spatial pattern of $N_d$, which implies that the results of this study are directly relevant for aerosol indirect forcing estimates even though the direct calculation of aerosol indirect forcing with a radiative transfer model was not performed in this study.

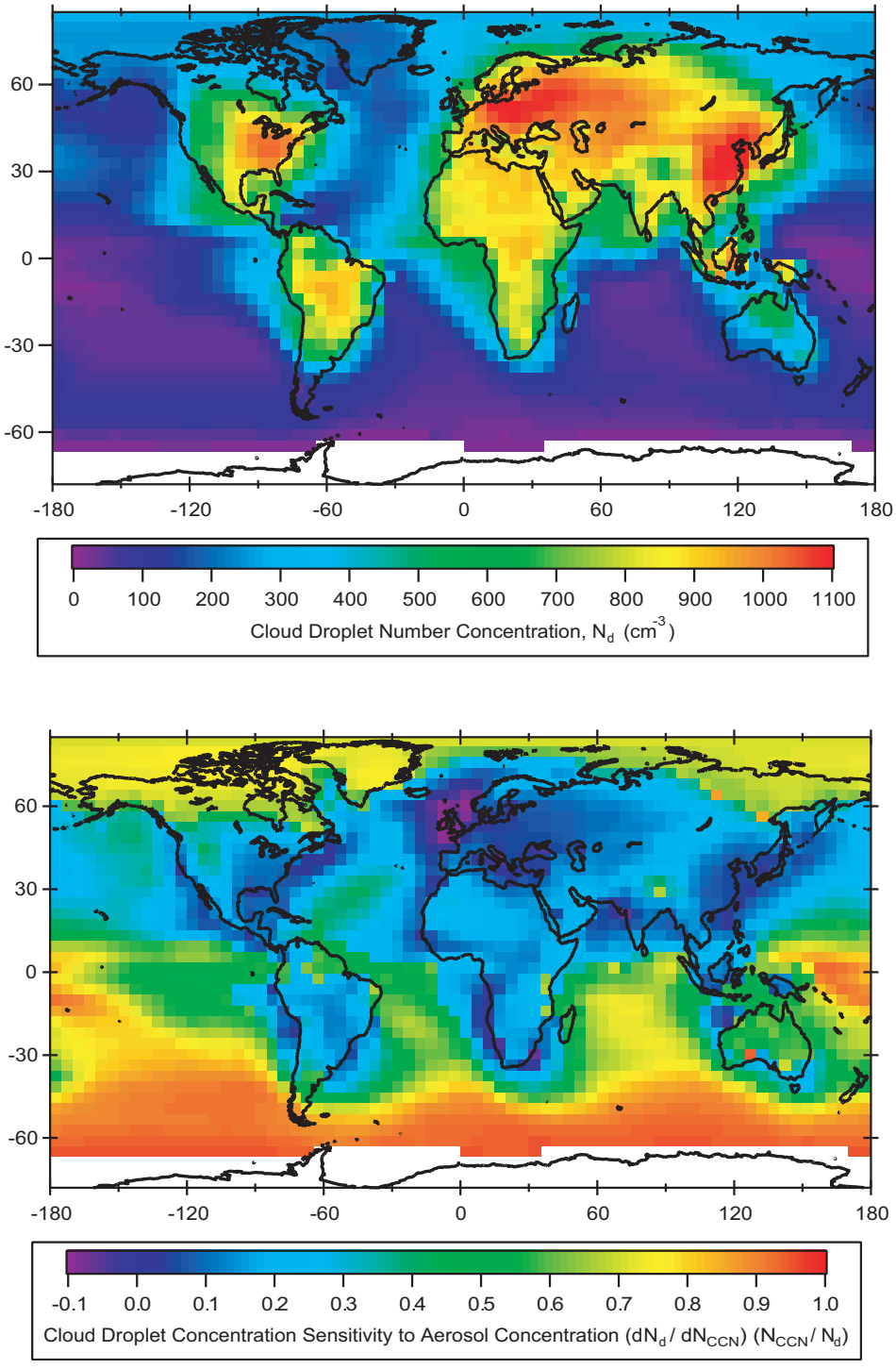


**Figure 9.2:** Simulated global spatial distribution of the annual mean $N_d$ (top) and sensitivity of $N_d$ to $N_{CCN}$ (bottom).

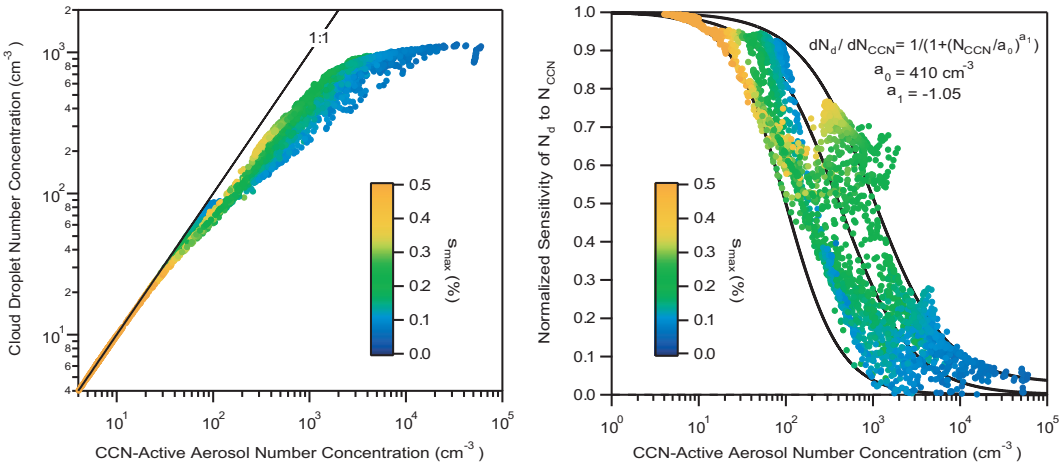


**Figure 9.3:** Simulated $N_d$ (left) and sensitivity of $N_d$ to $N_{CCN}$ (right) plotted versus simulated $N_{CCN}$ for all grid model grid cells. Points are colored by the grid-cell $s_{max}$.

### 9.3.3 Global Cloud Albedo Distribution and Relative Sensitivity of $A$ to $N_{CCN}$

The cloud droplet sensitivity discussed in the previous section provides important information regarding the potential sensitivity of clouds in a given region to changes in aerosol concentrations, but it says nothing about whether or not the clouds would form in the the first place. This is because global and regional cloudiness is driven by air flow dynamics (e.g., vertical updrafts) and moisture fluxes (e.g., liquid water content) in addition to the presence of CCN. Quantifying these individual processes on a global scale is challenging; however, satellite measurements over the past decades have been able to discern global cloudiness with good accuracy. In this study, we use the global annually-averaged cloud albedo ($A$) obtained from the NASA CERES satellite to capture all of these effects. The cloud albedo is found by differencing the total sky and clear sky albedos for 2003 obtained from the NASA Giovanni online data system (*Acker and Leptoukh*, 2007). Since $A$ incorporates both cloudiness fraction and the reflectivity of those clouds, it directly captures the indirect effect of aerosols on clouds. The global distribution of $A$ is shown in the upper portion of Figure 9.4. Synoptic scale dynamics play a large role in the observed distribution of $A$, with higher albedos seen along the equatorial intertropical convergence zone (ITCZ)

and in the mid-latitudes. Meanwhile, the observed cloud albedo is lowest in the subtropical subsidence zones.

In a landmark paper, *Twomey* (1991) defined the cloud albedo susceptibility to cloud droplet number as

$$\frac{\partial A}{\partial N_d} = \frac{A\,(1-A)}{3N_d} \tag{9.1}$$

for a constant amount of liquid water and by making a number of simplifying assumptions regarding the radiative properties of liquid water droplets. Equation 9.1 indicates that $A$ is at peak sensitivity to $N_d$ when $A$=0.5, where $\partial A/\partial N_d = \frac{1}{12}N_d$.

Combining $\partial A/\partial N_d$ obtained from the CERES satellite measurements and Equation 9.1 with $\partial N_d/\partial N_{CCN}$ obtained from the GMI model simulations yields the overall sensitivity of cloud albedo to the CCN-active aerosol fraction, $\partial A/\partial N_{CCN}$, which is shown in the lower portion of Figure 9.4. Overall, the spatial distribution of the albedo sensitivity is very similar to the cloud droplet number sensitivity, except that the former exhibits decreased sensitivity in the subtropical subsidence zones, where there both $N_d$ and cloudiness are low. The most sensitive regions are in the southern oceans, Arctic regions, and eastern Europe and Asia where a doubling of aerosol concentrations can be seen to induce a 6-8% change in albedo, which is very large! The high satellite-derived albedos in the polluted eastern Europe and east Asia appear to compensate for the decreased simulated cloud droplet sensitivity in these regions. An additional interesting feature in Figure 9.4 is the negative sensitivity of albedo to $N_{CCN}$ near Great Britain and along the coasts of the continents. This arises because of the slight negative $\partial N_d/\partial N_{CCN}$ predicted by the model from the addition of coarse mode sea salt aerosol that act as giant CCN (GCCN). The GCCN are large enough to activate at very low supersaturations and remove enough water vapor through their condensational growth that the clouds $s_{max}$ is decreased. This means that fewer droplets form, resulting in an inverse-Twomey effect and a net warming effect. It is important to note that anthropogenic aerosol perturbations are too small to act

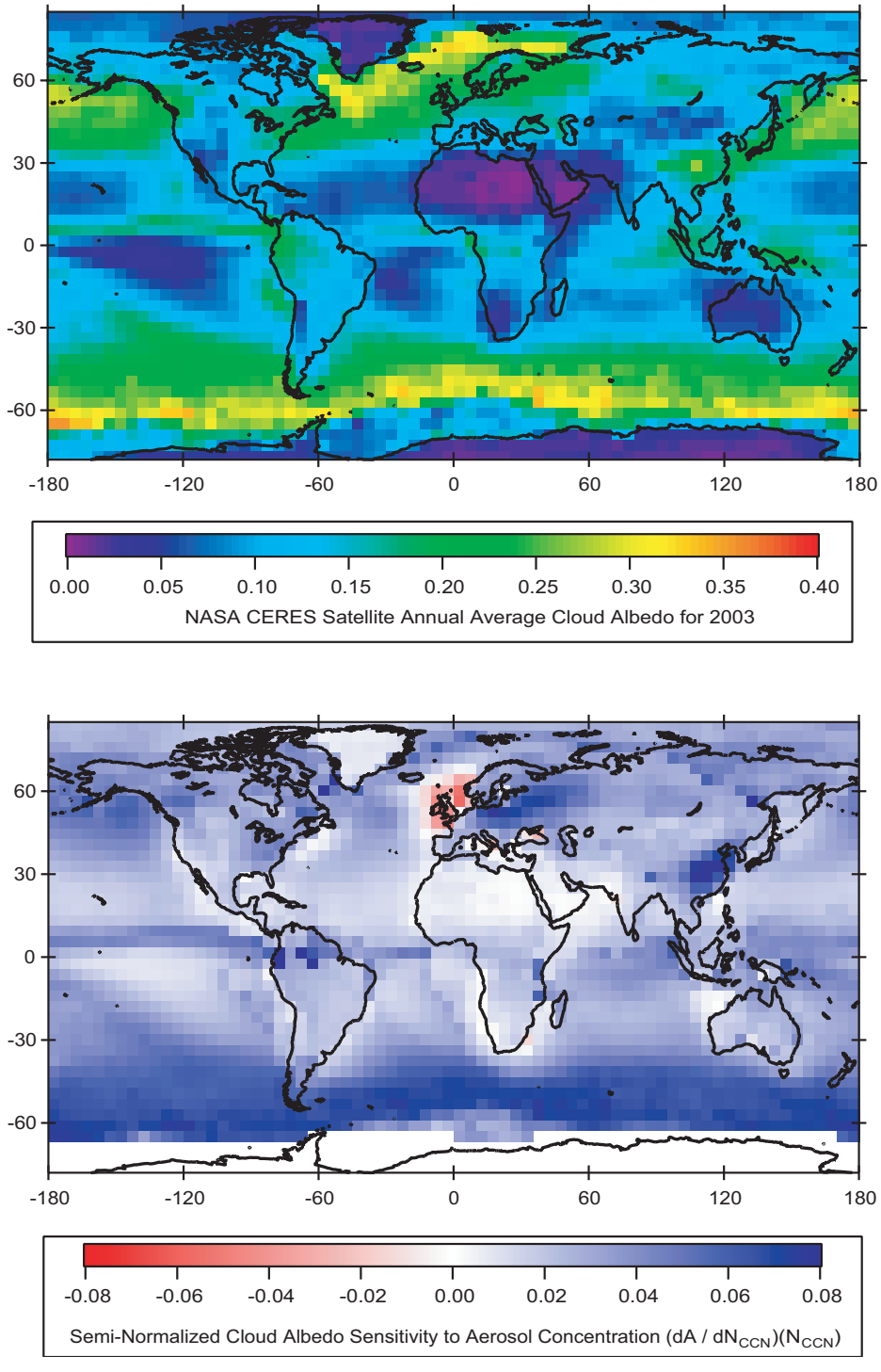


**Figure 9.4:** Global spatial distribution of the annual mean $A$ obtained from the NASA CERES satellite for 2003 (top), and the derived sensitivity of $A$ to $N_{CCN}$ (bottom).

as GCCN, so while this inverse-Twomey effect is relevant for assessing uncertainties in local marine aerosol (i.e., coarse sea salt), it does not capture the cooling impact of episodic anthropogenic emissions transport not considered by the model.

### 9.3.4 Cloud Droplet Number Uncertainties and Implications for the Indirect Effect

In this section, the the CCN closure uncertainties from Section 9.2.1 (Table 9.2) and the modeled cloud droplet sensitivities from Section 9.3.2 (Table 9.3) are combined to estimate the overall $N_d$ uncertainty arising from the application of simplified forms of Köhler theory. Figure 9.5 gives the field measurement uncertainties for four of the size closure scenarios. The left panels show the approximate spatial extent of the thirty-three study areas considered and are colored by the $N_{CCN}$ overprediction uncertainty ($\Delta N_{CCN}$) from Table 9.2. The right panels show the estimated $N_d$ overprediction uncertainty ($\Delta N_d$) calculated as

$$\Delta N_d = \left( \frac{\partial N_d}{\partial N_{CCN}} \right) \Delta N_{CCN} \tag{9.2}$$

The color scale for $\Delta N_{CCN}$ in Figure 9.5 is twice that for $\Delta N_d$, with light blue denoting zero overprediction uncertainty (i.e., perfect agreement between Köhler theory predictions and measurements). For most regions in the continental United States and Europe, $\Delta N_d$ is quite small ($\sim$ 0-20%), despite large variation in $N_{CCN}$, which reflects the relative insensitivity of $N_d$ to $N_{CCN}$ uncovered by the model for continental regions (Figure 9.2). Larger $\Delta N_d$ values are observed in California, in the Alaskan Arctic, and in the Amazon rainforest, although only one closure scenario is considered in the Amazon study. In Los Angeles, the large $\Delta N_d$ reflects the large (nearly five-fold) CCN overprediction uncertainted reported by *Cubison et al.* (2008) and *Ervens et al.* (2010) for all closure scenarios. In the Los Angeles basin and California Central Valley, *Moore et al.* (in preparation) report smaller values of $\Delta N_{CCN}$ that vary from -59 to 79%, which translates into $\Delta N_d \sim$ 0-20%. Reported Arctic CCN uncertainties are considerably lower (*Moore et al.*, 2011), but still have a large effect on $\Delta N_d$ because of the relatively low modeled droplet concentrations

**Table 9.4:** Percent overprediction of CCN concentration ($\Delta N_{CCN}$) and simulated cloud droplet concentration ($\Delta N_d$) averaged over the field studies' domain, with equal weighting given to each study location regardless of area. Reported are the mean $\pm$ one standard deviation across the 33 different data sets. Since individual field studies do not apply all scenarios, the overprediction values cannot be directly compared; however, the domain-averaged sensitivity ratios ($\Delta N_d/\Delta N_{CCN}$) are directly comparable.

| Closure Scenario | N | Measured Mean $N_{CCN}$ Overprediction (%) | Simulated Mean $N_d$ Overprediction (%) | Ratio |
|---|---|---|---|---|
| $(NH_4)_2SO_4$ | 9 | 23±44 | 2±13 | 0.09 |
| Internal Mixture, Soluble Organics ($\kappa_{org}$ = 0.11) | 21 | 77±125 | 18±35 | 0.23 |
| Internal Mixture, Insoluble Organics ($\kappa_{org}$ = 0) | 22 | 45±101 | 11±24 | 0.24 |
| Size-Resolved, Internal Mixture, Insoluble Organics ($\kappa_{org}$ = 0) | 11 | 4±15 | 1±5 | 0.25 |
| External Mixture, Soluble Organics ($\kappa_{org}$ = 0.11) | 14 | 86±122 | 17±30 | 0.20 |
| External Mixture, Insoluble Organics ($\kappa_{org}$ = 0) | 15 | 20±106 | 3±30 | 0.15 |

and relatively high modeled $N_d$ sensitivities in pristine regions.

Table 9.4 shows average uncertainty statistics for the six closure scenarios in this study. These mean values reflect the small sampling bias of being on the North American continent, which limits the generalizability of these numbers to a global scale. Additionally, the number of studies and the locations of those studies employing each closure scenario are different, which prevents direct cross-scenario comparison. However, the ratio of $\Delta N_d/\Delta N_{CCN}$ should be representative of the domain-averaged sensitivities, which can be directly compared despite different sample sizes. We find this ratio to be fairly invariant at 0.09-0.25, with the lowest values for the externally-mixed aerosol scenarios and the largest values for the internally-mixed aerosol cases. This is consistent with estimates of the $N_d$ sensitivity made by *Ervens et al.* (2010) ($\sim$15%) using parcel model, and with average $N_d$ uncertainties of 7-14% reported by *Sotiropoulou et al.* (2007) for the United States and Europe. Interestingly, the average $N_{CCN}$ uncertainties reported in the GCM study were also $\sim$ 10-20%, suggesting a much larger $N_d$ sensitivity than we find here.

*Sotiropoulou et al.* (2007) also used the the GISS II' radiative transfer model to evaluate the impact of CCN uncertainty on the overall cloud indirect forcing. They find that a 10-20% uncertainty in global $N_{CCN}$ results in a 10-20% uncertainty in the global indirect

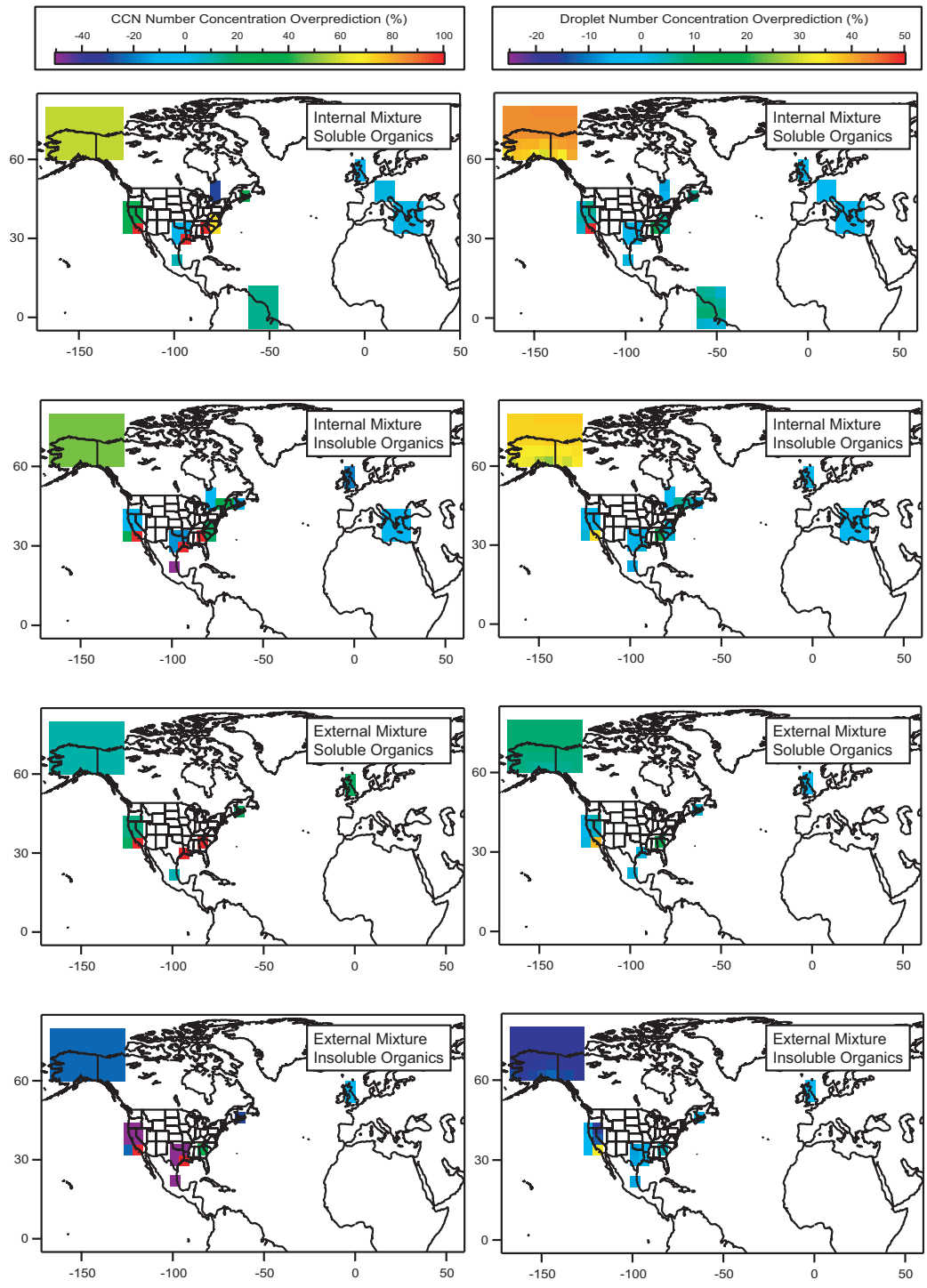


**Figure 9.5:** Regional spatial distribution of measured $N_{CCN}$ uncertainties derived from the closure studies (left) and the $N_d$ uncertainty found by multiplying the measured $\Delta N_{CCN}$ by the simulated $\partial N_d / \partial N_{CCN}$.

effect, comprising 0.1-0.2 W $m^{-2}$ out of the total global mean radiative forcing of -1.00 W $m^{-2}$. While this uncertainty is relatively small on a global scale, regional effects are likely to be more substantial. This is especially true when considering larger CCN prediction uncertainties than the range of 10-20% assumed by *Sotiropoulou et al.* (2007), and which are suggested by some regional CCN closure studies in Table 9.2.

## *9.4 Summary and Conclusions*

Modeling simulations conducted with the GMI chemical transport model and cloud parameterization adjoint are used to interpret and extend the results of thirty-three published CCN closure studies in the literature to estimate the overall uncertainty in cloud droplet number concentration from applying Köhler theory-based parameterizations with simplifying assumptions. We find that the prediction of cloud droplet number is most susceptible to CCN uncertainty at low CCN concentrations ($N_{CCN} < 100$ $cm^{-3}$) and becomes insensitive to uncertainty in $N_{CCN}$ for concentrations above $10^4$ $cm^{-3}$. Thus, pristine areas such as the Arctic and remote oceans are found to be most sensitive ($> 70\%$), while the sensitivity over continental regions is on the order of 10-30%, which is consistent with some previous estimates. While the simplying assumptions employed by past CCN closure studies produce signficant overprediction of $N_{CCN}$ when compared to observations, the impact of these uncertainties on the prediction of $N_d$ is on the order of $\pm 10\%$ over the continental United States, but as high as 30-50% in the Alaskan Arctic and in Los Angeles, CA, where extremely high $N_{CCN}$ prediction uncertainties were observed.

This work shows that the regional sensitivity of $N_d$ to $N_{CCN}$ is important when assessing the uncertainty in cloud droplet number and albedo, and hence indirect forcing, associated with simplified assumptions regarding CCN. Most CCN closure studies to date have been located in continental regions, and future measurements of CCN and aerosol properties should focus on these remote regions to improve the coverage of the global dataset. Much of the past global anthropogenic indirect forcing has been over the continents, and

the results of this study indicate that uncertainties in estimating the global aerosol indirect effect (present day minus pre-industrial) arising from the simplified composition assumptions in models are relatively small. Two questions remain, however, that motivate future research. First, most current models employ prescribed size distributions for aerosol composition modes, which are likely to be a large source of uncertainty; however, the closure studies employed in this study use measured size distribution information. Consequently, size distribution effects are not reflected in the $\Delta N_{CCN}$ proxy. Second, the impact of transient events such as long-range pollution transport or seasonal biogenic emissions sources on changing CCN concentrations remains unclear; the regional sensitivities uncovered in this study indicate that these events could have a substantial climatic impact. This motivates future field measurements directed at measuring CCN in the southern oceans and Arctic, where observations are limited and seasonal variations have been shown to be significant. These datasets would provide important information to quantify the impact and uncertainty associated with transient pollution events on influencing CCN concentrations, and hence, clouds and climate.

# CHAPTER X

# CONCLUSIONS, FUTURE DIRECTIONS, AND RECOMMENDATIONS

## *10.1 Conclusions and Future Directions*

The complexity of aerosol-cloud interactions challenges their accurate representation in large scale models. The methods and analysis presented in this work represent a step toward better understanding the ability of atmospheric aerosols to act as cloud condensation nuclei (CCN) and form cloud droplets. Two new techniques are presented for operating the commercially-available Droplet Measurement Technologies (DMT) streamwise, thermal-gradient, CCN counter that enable size-resolved and supersaturation-resolved measurements over timescales small enough to be relevant for airborne sampling, while increasing the overall size and supersaturation resolution of the measurement. While these represent major advances in the state of the art, continued refinement of the techniques will increase data reliability and further push the lower boundaries of time resolution and minimum detectable concentrations.

In addition, we used laboratory and *in-situ* field measurements to characterize the hygroscopic properties of atmospheric aerosols, particularly the organic components, which are least understood. In Chapter 4, the properties of marine dissolved organic matter, relevant for aerosol generated via sea spray and bubble bursting, were quantified using CCN measurements and Köhler Theory Analysis, as well as bulk solution techniques to find composition and surface tension. It is shown that diffusion of even high-molar-mass organic molecules in growing droplets is sufficiently rapid that the surface tension of these droplets can be described well by equilibrium surface tension measurements. Since the diffusivities of these molecules are expected to be at the low end of those for most atmospheric

organic molecules, this work shows that bulk solution measurements are directly applicable to aerosol-cloud parameterizations, and that Köhler Theory Analysis may provide important surface tension information for a wide variety of chemical engineering applications with sample volumes too small for bulk measurements.

In Chapters 5-8, ambient measurements of urban and non-urban CCN are used to quantify the impact of the aerosol size distribution, mixing state, and chemical composition on CCN hygroscopicity and droplet growth rates. It is shown that size-dependent composition and mixing state are necessary to explain the observed CCN activity. This is due to the influence of local emissions sources or the long-range transport of emissions that form an external mixture with the aged, background aerosol population. In urban environments, such as Atlanta, GA, the mixing state and hygroscopicity exhibit a distinct diurnal dependence, consistent with a mobile source contribution in the morning and a combination of boundary layer dynamics and photochemical transformation throughout mid-day and afternoon. While, attempts to capture this complexity with a single, mean hygroscopicity and CCN-active fraction may be sufficient for large-scale models with relatively coarse resolution, future regional air quality and climate modeling efforts will likely need to account for these changes (e.g., an observed two-fold diurnal change in both $\kappa$ and the CCN-active aerosol number fraction in Atlanta).

Accounting for the size-dependence of aerosol composition and hygroscopicity will be especially important for linking subsaturated hygroscopic growth (relevant for aerosol direct radiative effects) and supersaturated CCN activity (relevant for aerosol indirect radiative effects). This is because light scattering and extinction are most sensitive to the aerosol mass size distribution (typically 0.2-1 $\mu$m diameter size range), while CCN and droplet concentrations are most sensitive to the aerosol number size distribution (typically 0.04-0.2 $\mu$m size range). The composition of the large aerosol mode is easily measured by widely-used instrumentation such as the aerosol mass spectrometer (AMS) or particle-into-liquid sampler (PILS); however, measurements of small-mode aerosol composition

continues to challenge the resolution of these techniques outside of heavily-polluted environments. Thermal-desorption chemical ionization mass spectrometry (TDCIMS) is a promising technique for measuring the small-mode aerosol composition, but requires long sampling times to accumulate a statistically-significant amount of sample ($\sim$5-10 minutes). Given these challenges, the direct measurement of subsaturated and supersaturated aerosol hygroscopicity seems to be the most promising future path toward linking aerosol direct and indirect effects.

The Droplet Measurement Technologies CCN counter (CCNC) using Scanning Flow CCN Analysis (SFCA) provides the means to accomplish this goal with the high temporal and relative-humidity (supersaturation) resolution required for airborne studies. Using a dual-column CCNC (DMT model CCN-200), one column would have the typical, positive, linear temperature gradient to produce a flow-rate-dependent water vapor supersaturation. Meanwhile, the linear temperature gradient in the other column would be inverted following *Ruehl et al.* (2010) to produce a flow-rate-dependent subsaturated relative humidity ($\lesssim$ 99%). Deployment of the dual column instrument would be straightforward with operation the same as the SFCA technique developed in this dissertation, and provide unprecedented information about the link between aerosol hygroscopicity relevant for the direct and indirect effects. As with the CCN measurements outlined in this dissertation, the subsaturated measurements would also implicitly capture complex aerosol mixing state and size-dependent composition impacts, which can be deconvoluted with concurrent measurements of the aerosol size distribution.

In addition to measurements of aerosol hygroscopicity and CCN activity, it is essential that future field work evaluate the conditions under which cloud droplets' growth may be affected by aerosol composition as this can have a profound impact on aerosol indirect effects estimates. The work described in Chapter 7 of this dissertation suggests that relatively un-oxygenated secondary organic aerosol near the Deepwater Horizon oil spill do not exhibit slow droplet growth, despite the ability of these hydrocarbon-like organics

to form surface films that retard droplet growth. This result is surprising since some past studies have found slow growth kinetics, which points to the importance of additional environmental factors (e.g., temperature and relative humidity) that control the hydration and phase state of the aerosol. While no kinetic delays were observed in the warm, humid environment of the Gulf of Mexico, future studies in cooler, continental regions are warranted. Ideally, a global dataset of CCN observations would elucidate the conditions under which models need to account for composition-induced changes in droplet growth kinetics and the conditions under which they do not.

The techniques developed in this dissertation provide the means to comprehensively characterize the aerosol-water interactions relevant for both the aerosol direct and indirect effects. What is lacking is an extensive global dataset of CCN measurements. In directing and planning future field studies focusing on CCN, this work provides some guidance from modeling simulations of cloud sensitivities to aerosol concentration (Chapter 9). Simulations conducted with the NASA GMI chemical transport model and the recently developed adjoint model of the *Kumar et al.* (2009) cloud droplet parameterization indicate that clouds are most susceptible to aerosol concentration uncertainties in the pristine regions such as the Alaska-Canadian Arctic and the southern oceans, and in the polluted regions of Eurasia where cloud albedo is large. However, most studies of CCN properties and prediction uncertainty (i.e., "CCN closure") have been conducted within the North American and European continents, where simulations suggest that clouds are less sensitive to aerosol concentrations. Consequently, future field studies should focus on pristine regions where cloud droplet and albedo sensitivities are largest. In particular, regions susceptible to anthropogenic modification from long-range pollution transport (e.g., the Arctic) or to seasonal variability in biogenic emissions (e.g., the southern oceans) are critical, and have more limited observational datasets to date.

Does the relative cloud insensitivity to aerosol concentrations over continents mean that future CCN measurements are unimportant in these regions? In terms of global climate,

this is probably true given the already high levels of atmospheric aerosols in these locations. However, local emissions sources in the vicinity of urban areas and large point (e.g., power plants) and mobile (e.g., cars, trucks, and ships) sources may have significant local and regional climate implications as seen in, e.g., the Los Angeles basin in Figure 9.5. In these cases, this work (and others) find that a detailed knowledge of aerosol mixing state and chemical composition is needed to predict CCN. As future climate modeling efforts begin to focus more on regional impacts, the need to adequately capture this smaller scale variation becomes important.

## *10.2 Recommendations for Future Work*

While the Scanning Flow CCN Analysis (SFCA) technique (Chapter 2) has been deployed on both ground-based and airborne platforms with good success, hardware improvements and minor adjustments to the flow scan profile would likely fix an observed temperature sensitivity and down scan transient profile. The current implementation of SFCA uses a proportional valve to control the total flow rate, and a fixed, calibrated polynomial relationship between applied valve voltage and total flow rate is used to linearly ramp the flow rate during an SFCA scan. This relationship does not currently account for changes in the air flow temperature and pressure, which would alter the voltage – flow rate relationship. One solution might be to use the built-in pressure transducers at the column inlet to provide a control feedback loop in ramping the valve voltage. A simpler, first-order improvement would be to bypass the proportional valve with a volumetric flow controller (e.g., Alicat Scientific MC-5SLPM) that would internally account for temperature and pressure changes and virtually negate the need for periodic flow calibrations.

Decoupling the flow control system from the DMT software would also enable custom flow scan profiles to be performed easily (e.g., sawtooth, sinusoidal, or other asymmetric upscan/downscan profiles), while taking advantage of the existing well-characterized and robust software for operating the instrument. During low pressure operation or when

streamwise temperature gradients less than ∼10-12K are used with a zig-zag flow profile and fast scan times (< 30-second ramps), transient behavior was observed for the flow downscans where CCN concentrations would decrease rapidly to zero and only recover during the beginning portion of the flow upscan. This likely occurs because of the flow "shock" associated with rapidly transitioning from an accelerating flow field to a decelerating flow field, although the exact cause is still unclear. Future simulations and experimental work on SFCA should explore alternate flow profiles as a potential solution.

The Scanning Mobility CCN Analysis (SMCA) technique (Chapter 3) has been validated over a greater number of laboratory and field studies than SFCA, and data inversion techniques are relatively mature, fast, and robust. While the current Excel-based data analysis processor is suitable (and possibly even superior) for short laboratory experiments and calibrations, it is currently unable to easily handle large datasets spanning multiple days. An important component of the data analysis procedure is the visual alignment of the CCN counter and Scanning Mobility Particle Sizer response curves for each sample scan, and this alignment step has proven difficult to automate. Future development of the SMCA technique should focus on developing algorithms to facilitate this process, after which, automated curve fitting and analysis should be fairly straightforward.

In addition to this instrument and technique development work, a substantial portion of this thesis has focused on characterizing the hygroscopicity and mixing state of ambient CCN over a range of environments (Chapters 5-8). Using the size-resolved SFCA technique for some of these measurements has enabled the direct measurement of differential supersaturation spectra ($dN_{CCN}/ds$), which together with $\kappa$ provides important information for evaluating aerosol-cloud interactions in global models. Using fast measurement techniques, such as SFCA, in future field studies will enable more detailed characterization of not only the mean aerosol hygroscopicity, but also the shape of the observed hygroscopicity probability density function. As this distribution represents the complete picture of

aerosol size, composition, and mixing state influences, it is ideal for future model parameterizations of CCN.

In Chapter 9, the data from these studies and approximately thirty others published in the literature were used to produce a global map of CCN closure uncertainties that can be compared to model simulations. Most of the published closure studies are focused on North America, with relatively few or no measurements in Eurasia, Africa, and remote regions. However, extensive measurements of CCN-derived and composition-derived $\kappa$ have been reported for some of these regions, suggesting that unpublished data is available for closure analysis. In addition to parameterizing $\kappa$, it is important that future studies also use the field data to assess the prediction error associated with simplifying assumptions used by models. Even in continental regions where simulations suggest that cloud droplet number is relatively insensitive to CCN concentrations, there may be some polluted areas with fresh, local sources and several-fold CCN prediction uncertainties that could be significant. Thus, future CCN closure assessments outside of North America are needed to help constrain global model simulations of cloud droplet formation and the aerosol indirect effect. The data analysis products, particularly the closure scenarios, produced in this dissertation for CCN in Alaska, California, Georgia, and the Gulf of Mexico are common to some other studies, which if more widely-adopted would enable even more comprehensive global comparisons to be made with model simulations.

The global impact of aerosol-cloud interactions is too large and complex to be directly observed; however, important advances in improving model confidence and uncertainties can be achieved by combining measurements and modeling; the work outlined in this dissertation represents an important contribution toward that goal.

# REFERENCES


ABDUL-RAZZAK, H., S. J. GHAN, and C. RIVERA-CARPIO (1998), A parameterization of aerosol activation: 1. Single aerosol type., *Journal of Geophysical Research*, *103*, 6123–6131, doi:10.1029/97JD03735. 9.1

ACKER, J. G., and G. LEPTOUKH (2007), Online analysis enhances use of NASA earth science data, *Eos Transactions*, *88*, 14, doi:10.1029/2007EO020003. 9.3.3

ACKERMAN, A. S., O. B. TOON, D. E. STEVENS, A. J. HEYMSFIELD, V. RAMANATHAN, and E. J. WELTON (2000), Reduction of tropical cloudiness by soot, *Science*, *288*, 1042–1047, doi:10.1126/science.288.5468.1042.

AIKEN, A. C., P. F. DECARLO, J. H. KROLL, D. R. WORSNOP, J. A. HUFFMAN, K. S. DOCHERTY, I. M. ULBRICH, C. MOHR, J. R. KIMMEL, D. SUEPER, Y. SUN, Q. ZHANG, A. TRIMBORN, M. NORTHWAY, P. J. ZIEMANN, M. R. CANAGARATNA, T. B. ONASCH, M. R. ALFARRA, A. S. PREVOT, J. DOMMEN, J. DUPLISSY, A. METZGER, U. BALTENSPERGER, and J. L. JIMENEZ (2008), O/C and OM/OC ratios of primary, secondary, and ambient organic aerosols with high-resolution time-of-flight aerosol mass spectrometry, *Environmental Science and Technology*, *42*, 4478–4485, doi:10.1021/es703009q. (document), 5.3.4, 5.3.4, 6.3.4, 7.3.1, 7.3

ALBRECHT, B. A. (1989), Aerosols, cloud microphysics, and fractional cloudiness, *Science*, *245*, 1227–1230, doi:10.1126/science.245.4923.1227. 1.1, 2.1, 5.1, 6.1

ALFARRA, M. R., D. PAULSEN, M. GYSEL, A. A. GARFORTH, J. DOMMEN, A. S. H. PRÉVÔT, D. R. WORSNOP, U. BALTENSPERGER, and H. COE (2006), A mass spectrometric study of secondary organic aerosols formed from the photooxidation of anthropgoenic and biogenic precursors in a reaction chamber, *Atmospheric Chemistry and Physics*, *6*, 5279–5293, doi:10.5194/acp-6-5279-2006. 7.1

ALLAN, J. D., J. L. JIMENEZ, P. I. WILLIAMS, M. R. ALFARRA, K. N. BOWER, J. T. JAYNE, H. COE, and D. R. WORSNOP (2003), Quantitative sampling using an aerodyne aerosol mass spectrometer 1. techniques of data interpretation and error analysis, *Journal of Geophysical Research*, *108*, 4090, doi:10.1029/2002JD002358. 5.2.2, 6.2.2

ALTERSKJÆR, K., J. E. KRISTJÁNSSON, and C. HOOSE (2010), Do anthropogenic aerosols enhance or suppress the surface cloud forcing in the Arctic?, *Journal of Geophysical Research*, *115*, D22204, doi:10.1029/2010JD014015. 5.1

ANDERSON, B. E., W. B. GRANT, G. L. GREGORY, E. V. BROWELL, J. JAMES E. COLLINS, G. W. SACHSE, D. R. BAGWELL, C. H. HUDGINS, D. R. BLAKE, and N. J. BLAKE (1996), Aerosols from biomass burning over the tropical South Atlantic region: Distributions and impacts, *Journal of Geophysical Research*, *101*, 24,117–24,137, doi:10.1029/96JD00717. 9.2.2

ANDREAE, M. O., and D. ROSENFELD (2008), Aerosol-cloud-precipitation interactions. Part 1. the nature and sources of cloud-active aerosols, *Earth-Science Reviews*, *89*, 13–41, doi:10.1016/j.earscirev.2008.03.001. 1.2, 5.3.3, 8.1

ASA-AWUKU, A., and A. NENES (2007), The effect of solute dissolution kinetics on cloud droplet formation: Extended Köhler theory, *Journal of Geophysical Research*, *112*, D22201, doi:10.1029/2005JD00693. 1.2, 1.3, 3.1, 3.1, 3.5, 4.3.2, 7.3.2

ASA-AWUKU, A., A. P. SULLIVAN, C. J. HENNIGAN, R. J. WEBER, and A. NENES (2008), Investigation of molar volume and surfactant characteristics of water-soluble organic compounds in biomass burning aerosol, *Atmospheric Chemistry and Physics*, *8*, 799–812, doi:10.5194/acp-8-799-2008. 1.4, 2.1, 2.3.4, 2.4.2, 3.1, 3.1, 3.5, 4.1, 4.2.4, 4.3.2, 7.3.2

ASA-AWUKU, A., G. ENGELHART, B. LEE, S. PANDIS, and A. NENES (2009), Relating CCN activity, volatility, and droplet growth kinetics of $\beta$-caryophyllene secondary organic aerosol, *Atmospheric Chemistry and Physics*, *9*, 795–812, doi:10.5194/acp-9-795-2009. 5.2.4, 5.3.3

ASA-AWUKU, A., A. NENES, S. GAO, R. C. FLAGAN, and J. H. SEINFELD (2010), Water-soluble SOA from alkene ozonolysis: Composition and droplet activation kinetics inferences from analysis of CCN activity, *Atmospheric Chemistry and Physics*, *10*, 1585–1597, doi:10.5194/acp-10-1585-2010. 2.1, 3.1, 3.1, 3.5, 4.1, 4.2.4, 4.3.2, 8.4

ASA-AWUKU, A., R. H. MOORE, A. NENES, R. BAHREINI, J. S. HOLLOWAY, C. A. BROCK, A. M. MIDDLEBROOK, T. B. RYERSON, J. L. JIMENEZ, P. F. DECARLO, A. HECOBIAN, R. J. WEBER, R. STICKEL, D. J. TANNER, and L. G. HUEY (2011), Airborne cloud condensation nuclei measurements during the 2006 Texas Air Quality Study, *Journal of Geophysical Research*, *116*, D11201, doi:10.1029/2010JD014874. 5.3.6, 6.3.2, 6.3.6, 6.3.6, 7.3.2, 9.1

BAHREINI, R., E. J. DUNLEA, B. M. MATTHEW, C. SIMONS, K. S. DOCHERTY, P. F. DECARLO, J. L. JIMENEZ, C. A. BROCK, and A. M. MIDDLEBROOK (2008), Design and operation of a pressure-controlled inlet for airborne sampling with an aerodynamic aerosol lens, *Aerosol Science and Technology*, *42*, 465–471, doi:10.1080/02786820802178514. 5.2.2, 6.2.2, 7.2.1

BAHREINI, R., B. ERVENS, A. M. MIDDLEBROOK, C. WARNEKE, J. A. DE GOUW, P. F. DECARLO, J. L. JIMENEZ, C. A. BROCK, J. A. NEUMAN, T. B. RYERSON, H. STARK, E. ATLAS, J. BRIOUDE, A. FRIED, J. S. HOLLOWAY, J. PEISCHL, D. RICHTER, J. WALEGA, P. WEIBRING, A. G. WOLLNY, and F. C. FEHSENFELD (2009), Organic aerosol formation in urban and industrial plumes near Houston and Dallas, Texas, *Journal of Geophysical Research*, *114*, D00F16, doi:10.1029/2008JD011493. 5.2.2, 6.2.2

BARAHONA, D., and A. NENES (2007), Parameterization of cloud droplet formation in large-scale models: Including effects of entrainment, *Journal of Geophysical Research*, *112*, D16206, doi:10.1029/2007JD008473. 9.2.2

BIGG, E. K. (1986), Discrepancy between observation and prediction of concentrations of cloud condensation nuclei, *Atmospheric Research*, *20*, 81–86, doi:10.1016/0169-8095(86)90010-4. 2.3.4

BIGG, E. K., and C. LECK (2001), Cloud-active particles over the central Arctic Ocean, *Journal of Geophysical Research*, *106*, 32,155–32,166, doi:10.1029/1999JD901152. 5.1

BIGG, E. K., J. L. BROWNSCOMBE, and W. J. THOMPSON (1969), Fog modification with long-chain alcohols, *Journal of Applied Meteorology*, *8*, 75–82, doi:10.1175/1520-0450(1969)008<0075:FMWLCA>2.0.CO;2. 2.3.4

BOHREN, C. F., and D. R. HUFFMANN (1983), *Absorption and Scattering by Small Particles*, Wiley. 2

BOND, T. C., and R. W. BERGSTROM (2006), Light absorption by carbonaceous particles: An investigative review, *Aerosol Science and Technology*, *40*, 27–67, doi:10.1080/02786820500421521. 7.1

BORYS, R. D., D. H. LOWENTHAL, and D. L. MITCHELL (2000), The relationships among cloud microphysics, chemistry, and precipitation rate in cold mountain clouds, *Atmospheric Environment*, *34*, 2593–2602, doi:10.1016/S1352-2310(99)00492-6. 5.1

BORYS, R. D., D. H. LOWENTHAL, S. A. COHN, and W. O. J. BROWN (2003), Mountaintop and radar measurements of anthropogenic aerosol effects on snow growth and snowfall rate, *Geophysical Research Letters*, *30*, 1538, doi:10.1029/2002GL016855. 5.1

BOUGIATIOTI, A., C. FOUNTOUKIS, N. KALIVITIS, S. N. PANDIS, A. NENES, and N. MIHALOPOULOS (2009), Cloud condensation nuclei measurements in the marine boundary layer of the eastern Mediterranean: CCN closure and droplet growth kinetics, *Atmospheric Chemistry and Physics*, *9*, 7053–7066, doi:10.5194/acp-9-7053-2009. 3.1, 3.2.1, 5.3.6, 6.3.6, 9.1

BOUGIATIOTI, A., A. NENES, C. FOUNTOUKIS, N. KALIVITIS, S. N. PANDIS, and N. MIHALOPOULOS (2011), Size-resolved CCN distributions and activation kinetics of aged continental and marine aerosol, *Atmospheric Chemistry and Physics*, *11*, 8791–8808, doi:10.5194/acp-11-8791-2011. 9.1

BROCK, C. A., F. SCHRÖDER, B. KÄRCHER, A. PETZOLD, R. BUSEN, and M. FIEBIG (2000), Ultrafine particle size distributions measured in aircraft exhaust plumes, *Journal of Geophysical Research*, *105*, 26,555–26,567, doi:10.1029/2000JD900360. 5.2.3, 6.2.3, 7.2.1

BROCK, C. A., J. COZIC, R. BAHREINI, K. D. FROYD, A. M. MIDDLEBROOK, A. MCCOMISKEY, J. BRIOUDE, O. R. COOPER, A. STOHL, K. C. AIKIN, J. A. DE GOUW, D. W. FAHEY, R. A. FERRARE, R.-S. GAO, W. GORE, J. HOLLOWAY,

G. HÜBLER, A. JEFFERSON, D. A. LACK, S. LANCE, R. H. MOORE, D. M. MURPHY, A. NENES, P. C. NOVELLI, J. B. NOWAK, J. A. OGREN, J. PEISCHL, R. B. PIERCE, P. PILEWSKIE, P. K. QUINN, T. B. RYERSON, K. S. SCHMIDT, J. P. SCHWARZ, H. SODEMANN, J. R. SPACKMAN, H. STARK, D. S. THOMSON, T. THORNBERRY, P. VERES, L. A. WATTS, C. WARNEKE, and A. G. WOLLNY (2011a), Characteristics, sources, and transport of aerosols measured in Spring 2008 during the Aerosol, Radiation, and Cloud Processes Affecting Arctic Climate (ARCPAC) project, *Atmospheric Chemistry and Physics*, *11*, 2423–2453, doi:10.5194/acp-11-2423-2011. 5.2.1, 5.2.3, 5.3.1, 5.3.1, 5.3.1, 5.3.4, 5.3.5, 5.3.6, 7.2.1

BROCK, C. A., D. M. MURPHY, R. BAHREINI, and A. M. MIDDLEBROOK (2011b), Formation and growth of organic aerosols downwind of the Deepwater Horizon oil spill, *Geophysical Research Letters*, *38*, doi:10.1029/2011GL048541. 7.3.1, 7.3.1

BROEKHUIZEN, K., R. Y.-W. CHANG, W. R. LEAITCH, S.-M. LI, and J. P. D. ABBATT (2006), Closure between measured and modeled cloud condensation nuclei (CCN) using size-resolved aerosol compositions in downtown Toronto, *Atmospheric Chemistry and Physics*, *6*, 2513–2524, doi:10.5194/acp-6-2513-2006. 3.1, 5.3.6, 6.3.6, 9.1

CAI, Y., D. C. MONTAGUE, W. MOOIWEER-BRYAN, and T. DESHLER (2008), Performance characteristics of the ultra high sensitivity aerosol spectrometer for particles between 55 and 800 nm: Laboratory and field studies, *Journal of Aerosol Science*, *39*, 759–769, doi:10.1016/j.jaerosci.2008.04.007. 9.1

CARRICO, C. M., M. D. PETTERS, S. M. KREIDENWEIS, J. L. C. JR., G. ENGLING, and W. C. MALM (2008), Aerosol hygroscopicity and cloud droplet activation of extracts of filters from biomass burning experiments, *Journal of Geophysical Research*, *113*, D08206, doi:10.1029/2007JD009274. 3.1

CAVALLI, F., M. C. FACCHINI, S. DECESARI, M. MIRCEA, L. EMBLICO, S. FUZZI, D. CEBURNIS, Y. J. YOON, C. D. O'DOWD, J.-P. PUTAUD, and A. DELL'ACQUA (2004), Advances in characterization of size-resolved organic matter in marine aerosol over the North Atlantic, *Journal of Geophysical Research*, *109*, D24215, doi:10.1029/2004JD005137. 4.1, 4.3.2

CERULLY, K. M., T. RAATIKAINEN, S. LANCE, D. TKACIK, P. TIITTA, T. PETÄJÄ, M. EHN, M. KULMALA, D. R. WORSNOP, A. LAAKSONEN, J. N. SMITH, and A. NENES (2011), Aerosol hygroscopicity and CCN activation kinetics in a boreal forest environment during the 2007 EUCAARI campaign, *Atmospheric Chemistry and Physics*, *11*, 15,029–15,074, doi:10.5194/acpd-11-15029-2011. 7.2.3, 7.3.1, 8.2.2

CHANG, R. Y.-W., P. S. K. LIU, W. R. LEAITCH, and J. P. D. ABBATT (2007), Comparison between measured and predicted CCN concentrations at Egbert, Ontario: Focus on the organic aerosol fraction at a semi-rural site, *Atmospheric Environment*, *41*, 8172–8182, doi:10.1016/j.atmosenv.2007.06.039. 9.1

CHANG, R. Y.-W., J. G. SLOWIK, N. C. SHANTZ, A. VLASENKO, J. LIGGIO, S. J. SJOSTEDT, W. R. LEAITCH, and J. P. D. ABBATT (2010), The hygroscopicity parameter ($\kappa$) of ambient organic aerosol at a field site subject to biogenic and anthropogenic influences: relationship to degree of aerosol oxidation, *Atmospheric Chemistry and Physics*, *10*, 5047–5064, doi:10.5194/acp-10-5047-201. 6.3.4, 7.3.1, 8.3.1, 9.1

CHEN, L.-W. A., J. G. WATSON, and J. C. CHOW (2007), Quantifying $PM_{2.5}$ source contributions for the San Joaquin Valley with multivariate receptor models, *Environmental Science and Technology*, *41*, 2818–2826, doi:10.1021/es0525105. 6.1

CHOW, J. C., L.-W. A. CHEN, J. G. WATSON, D. H. LOWENTHAL, K. A. MAGLIANO, K. TURKIEWICZ, and D. E. LEHRMAN (2006), $PM_{2.5}$ chemical composition and spatiotemporal variability during the California Regional $PM_{10}$/$PM_{2.5}$ Air Quality Study (CRPAQS), *Journal of Geophysical Research*, *111*, D10S04, doi:10.1029/2005JD006457. 6.1

CHUANG, P. Y., R. J. CHARLSON, and J. H. SEINFELD (1997), Kinetic limitations on droplet formation in clouds, *Nature*, *390*, 594–596, doi:10.1038/37576. 1.3, 9.2.2

CHUANG, P. Y., A. NENES, J. N. SMITH, R. C. FLAGAN, and J. H. SEINFELD (2000a), Design of a CCN instrument for airborne measurement, *Journal of Atmospheric and Oceanic Technology*, *17*, 1005–1019, doi:10.1175/1520-0426(2000)017<1005:DOACIF>2.0.CO;2. 2.1

CHUANG, P. Y., D. R. COLLINS, H. PAWLOWSKA, J. R. SNIDER, H. H. JONSSON, J. L. BRENGUIER, R. C. FLAGAN, and J. H. SEINFELD (2000b), CCN measurements during ACE-2 and their relationship to cloud microphysical properties, *Tellus*, *52*, 843–867, doi:10.1034/j.1600-0889.2000.00018.x. 9.1, 9.2.3

CLEGG, S. L., and P. BRIMBLECOMBE (1988), Equilibrium partial pressures of strong acids over concentrated saline solutions - i. $HNO_3$, *Atmospheric Environment*, *22*(1), 91–100, doi:10.1016/0004-6981(88)90302-2. 2.4.1, 3.4.1, 5.2.4, 6.2.4

COLLINS, D. R., H. H. JONSSON, H. LIAO, R. C. FLAGAN, J. H. SEINFELD, K. J. NOONE, and S. V. HERING (2000), Airborne analysis of the Los Angeles aerosol, *Atmospheric Environment*, *34*, 4155–4173, doi:10.1016/S1352-2310(00)00225-9. 6.1

COLLINS, D. R., R. C. FLAGAN, and J. H. SEINFELD (2002), Improved inversion of scanning DMA data, *Aerosol Science and Technology*, *36*, 1–9, doi:10.1080/027868202753339032. 3.2.2, 3.4.1

CONANT, W. C., T. M. VANREKEN, T. A. RISSMAN, V. VARUTBANGKUL, H. H. JONSSON, A. NENES, J. L. JIMENEZ, A. E. DELIA, R. BAHREINI, G. C. ROBERTS, R. C. FLAGAN, and J. H. SEINFELD (2004), Aerosol–cloud drop concentration closure in warm cumulus, *Journal of Geophysical Research*, *109*, D13204, doi:10.1029/2003JD004324. 9.1

CONSIDINE, D. B., D. J. BERGMANN, and H. LIU (2005), Sensitivity of Global Modeling Initiative chemistry and transport model simulations of radon-222 and lead-210 to input meteorological data, *Atmospheric Chemistry and Physics*, *5*, 3389–3406, doi:10.5194/acp-5-3389-2005. 9.2.2

COVERT, D. S., and J. HEINTZENBERG (1993), Size distributions and chemical properties of aerosol at Ny Ålesund, Svalbard, *Atmospheric Environment*, *27A*, 2989–2997, doi:10.1016/0960-1686(93)90331-R. 5.3.1, 5.3.2

COVERT, D. S., J. L. GRAS, A. WIEDENSOHLER, and F. STRATMANN (1998), Comparison of directly measured CCN with CCN modeled from the number-size distribution in the marine boundary layer during ACE 1 at Cape Grim, Tasmania, *Journal of Geophysical Research*, *103*, 16,597–16,608, doi:10.1029/98JD01093. 9.2.1

CRONE, T. J., and M. TOLSTOY (2010), Magnitude of the 2010 Gulf of Mexico oil leak, *Science*, *330*, 634, doi:10.1126/science.1195840. 7.1

CRUMP, J. G., and J. H. SEINFELD (1981), A new algorithm for inversion of aerosol size distribution data, *Aerosol Science and Technology*, *1*, 15–34, doi:10.1080/02786828208958576. 3.2.2

CRUZ, C. N., and S. N. PANDIS (1997), A study of the ability of pure secondary organic aerosol to act as cloud condensation nuclei, *Atmospheric Environment*, *31*, 2205–2214, doi:10.1016/S1352-2310(97)00054-X. 1.2, 9.1

CUBISON, M., B. ERVENS, G. FEINGOLD, K. S. DOCHERTY, I. M. ULBRICH, L. SHIELDS, K. PRATHER, S. HERING, and J. L. JIMENEZ (2008), The influence of chemical composition and mixing state of Los Angeles urban aerosol on CCN number and cloud properties, *Atmospheric Chemistry and Physics*, *8*, 5649–5667, doi:10.5194/acp-8-5649-2008. 2.1, 3.1, 6.1, 6.3.1, 6.3.2, 6.3.3, 6.3.6, 6.3.6, 8.3.1, 9.1, 9.3.4

D'ALMEIDA, G. A. (1987), On the variability of desert aerosol radiative characteristics, *Journal of Geophysical Research*, *92*, 3017–3026, doi:10.1029/JD092iD03p03017. 9.2.2

DAVIS, E. J. (2006), A history and state-of-the-art of accomodation coefficients, *Atmospheric Research*, *82*, 561–578, doi:10.1016/j.atmosres.2006.02.013. 1.3, 2.3.4, 7.3.2

DE GOUW, J., and J. L. JIMENEZ (2009), Organic aerosols in the earth's atmosphere, *Environmental Science and Technology*, *43*, 7614–7618, doi:10.1021/es9006004. 7.1

DE GOUW, J. A., A. M. MIDDLEBROOK, C. WARNEKE, R. AHMADOV, E. L. ATLAS, R. BAHREINI, D. R. BLAKE, C. A. BROCK, J. BIOUDE, D. W. FAHEY, F. C. FEHSENFELD, J. S. HOLLOWAY, M. L. HENAFF, R. A. LUEB, S. A. MCKEEN, J. F. MEAGHER, D. M. MURPHY, C. PARIS, D. D. PARRISH, A. E. PERRING, I. B. POLLACK, A. R. RAVISHANKARA, A. L. ROBINSON, T. B. RYERSON, J. P. SCHWARZ,

J. R. SPACKMAN, A. SRINIVASAN, and L. A. WATTS (2011), Organic aerosol formation downwind from the Deepwater Horizon oil spill, *Science*, *331*, 1295–1299, doi:10.1126/science.1200320. (document), 7.1, 7.1, 7.3.1

DECARLO, P. F., J. G. SLOWIK, D. R. WORSNOP, P. DAVIDOVITS, and J. L. JIMENEZ (2004), Particle morphology and density characterization by combined mobility and aerodynamic diameter measurements. Part 1: Theory, *Aerosol Science and Technology*, *38*, 1185–1205, doi:10.1080/027868290903907. 3.2.3

DECARLO, P. F., J. R. KIMMEL, A. TRIMBORN, M. J. NORTHWAY, J. T. JAYNE, A. C. AIKEN, M. GONIN, K. FUHRER, T. HORVATH, K. S. DOCHERTY, D. R. WORSNOP, and J. L. JIMENEZ (2006), Field-deployable, high-resolution, time-of-flight aerosol mass spectrometer, *Analytical Chemistry*, *78*, 8281–8289, doi:10.1021/ac061249n. 5.2.2, 6.2.2, 7.2.1

DECESARI, S., M. C. FACCHINI, M. MIRCEA, F. CAVALLI, and S. FUZZI (2003), Solubility properties of surfactants in atmospheric aerosol and cloud/fog water samples, *Journal of Geophysical Research*, *108*, 4685, doi:10.1029/2003JD003566. 5.3.3

DILLON, M. B., M. S. LAMANNA, G. W. SCHADE, A. H. GOLDSTEIN, and R. C. COHEN (2002), Chemical evolution of the Sacramento urban plume: Transport and oxidation, *Journal of Geophysical Research*, *107*, 4045, doi:10.1029/2001JD000969. 6.1

DINAR, E., I. TARANIUK, E. R. GRABER, T. ANTTILA, T. F. MENTEL, and Y. RUDICH (2007), Hygroscopic growth of atmospheric and model humic-like substances, *Journal of Geophysical Research*, *112*, D05211, doi:10.1029/2006JD007442. 4.3.2, 4.1

DRAXLER, R. R., and G. D. ROLPH (2011), HYSPLIT (HYbrid Single-Particle Lagrangian Integrated Trajectory) model access via NOAA ARL READY website (http://ready.arl.noaa.gov/hysplit.php). (document), 8.1

DREWNICK, F., S. S. HINGS, P. DECARLO, J. T. JAYNE, M. GONIN, K. FUHRER, S. WEIMER, J. L. JIMENEZ, K. L. DEMERJIAN, S. BORRMANN, and D. R. WORSNOP (2005), A new time-of-flight aerosol mass spectrometer (TOF-AMS) – Instrument description and first field deployment, *Aerosol Science and Technology*, *39*, 637–658, doi:10.1080/02786820500182040. 5.2.2, 6.2.2, 7.2.1

DUPLISSY, J., P. F. DECARLO, J. DOMMEN, M. R. ALFARRA, A. METZGER, I. BARMPADIMOS, A. S. H. PRÉVÔT, E. WEINGARTNER, T. TRITSCHER, M. GYSEL, A. C. AIKEN, J. L. JIMENEZ, M. R. CANAGARATNA, D. R. WORSNOP, D. R. COLLINS, J. TOMLINSON, and U. BALTENSPERGER (2011), Relating hygroscopicity and composition of organic aerosol particulate matter, *Atmospheric Chemistry and Physics*, *11*, 1155–1165, doi:10.5194/acp-11-1155-2011. 6.3.4, 7.3.1, 8.3.1

DUSEK, U., D. S. COVERT, A. WIEDENSOHLER, C. NEUSÜSS, D. WEISE, and W. CANTRELL (2003), Cloud condensation nuclei spectra derived from size distributions and hygroscopic properties of the aerosol in coastal south-west Portugal during ACE-2, *Tellus*, *55*, 35–53, doi:10.1034/j.1600-0889.2003.00041.x. 9.2.1

DUSEK, U., G. P. FRANK, L. HILDEBRANDT, J. CURTIUS, J. SCHNEIDER, S. WALTER, D. CHAND, F. DREWNICK, S. HINGS, D. JUNG, S. BORRMANN, and M. O. ANDREAE (2006), Size matters more than chemistry for cloud-nucleating ability of aerosol particles, *Science*, *312*, 1375–1378, doi:10.1126/science.1125261. 1.2, 5.3.2, 6.3.2

DUSEK, U., G. P. FRANK, J. CURTIUS, F. DREWNICK, J. SCHNEIDER, A. KÜRTEN, D. ROSE, M. O. ANDREAE, S. BORRMANN, and U. PÖSCHL (2010), Enhanced organic mass fraction and decreased hygroscopicity of cloud condensation nuclei (CCN) during new particle formation events, *Geophysical Research Letters*, *37*, L03804, doi:10.1029/2009GL040930. 3.1, 8.1, 8.3.2

ENGELHART, G. J., A. ASA-AWUKU, A. NENES, and S. N. PANDIS (2008), CCN activity and droplet growth kinetics of fresh and aged monoterpene secondary organic aerosol, *Atmospheric Chemistry and Physics*, *8*, 3937–3949, doi:10.5194/acp-8-3937-2008. 3.1, 3.1, 3.5, 8.4

ENGELHART, G. J., R. H. MOORE, A. NENES, and S. N. PANDIS (2011), Cloud condensation nuclei activity of isoprene secondary organic aerosol, *Journal of Geophysical Research*, *116*, D02207, doi:10.1029/2010JD014706. 8.1, 8.4

ENGVALL, A.-C., R. KREJCI, J. STRÖM, A. MINIKIN, R. TREFFEISEN, A. STOHL, and A. HERBER (2008), In-situ airborne observations of the microphysical properties of the Arctic tropospheric aerosol during late spring and summer, *Tellus B*, *60B*, 392–404, doi:10.1111/j.1600-0889.2008.00348.x. 5.3.2

ERVENS, B., G. FEINGOLD, G. J. FROST, and S. M. KREIDENWEIS (2004), A modeling study of aqueous production of dicarboxylic acids: 1. Chemical pathways and speciated organic mass production, *Journal of Geophysical Research*, *109*, D15205, doi:10.1029/2003JD004387. 5.3.4

ERVENS, B., M. CUBISON, E. ANDREWS, G. FEINGOLD, J. A. OGREN, J. L. JIMENEZ, P. DECARLO, and A. NENES (2007), Prediction of cloud condensation nucleus number concentration using measurements of aerosol size distributions and composition and light scattering enhancement due to humidity, *Journal of Geophysical Research*, *112*, D10S32, doi:10.1029/2006JD007426. 7.5.2, 9.1

ERVENS, B., M. J. CUBISON, E. ANDREWS, G. FEINGOLD, J. A. OGREN, J. L. JIMENEZ, P. K. QUINN, T. S. BATES, J. WANG, Q. ZHANG, H. COE, M. FLYNN, and J. D. ALLAN (2010), CCN predictions using simplified assumptions of organic aerosol composition and mixing state: A synthesis from six different locations, *Atmospheric Chemistry and Physics*, *10*, 4795–4807, doi:10.5194/acp-10-4795-2010. 6.3.6, 6.3.6, 8.1, 8.3.1, 9.1, 9.2.1, 9.1, 9.3.4, 9.3.4

FACCHINI, M. C., M. MIRCEA, S. FUZZI, and R. J. CHARLSON (1999), Cloud albedo enhancement by surface-active organic solutes in growing droplets, *Nature*, *401*, 257–259, doi:10.1038/45758. 1.3, 5.3.3

FEINGOLD, G., and P. Y. CHUANG (2002), Analysis of the influence of film-forming compounds on droplet growth: Implications for cloud microphysical processes and climate, *Journal of the Atmospheric Sciences*, *59*, 2006–2018. 1.3

FISHER, J. A., D. J. JACOB, M. T. PURDY, M. KOPACZ, P. L. SAGER, C. CAROUGE, C. D. HOLMES, R. M. YANTOSCA, R. L. BATCHELOR, K. STRONG, G. S. DISKIN, H. E. FUELBERG, J. S. HOLLOWAY, E. J. HYER, W. W. MCMILLAN, J. WARNER, D. G. STREETS, Q. ZHANG, Y. WANG, and S. WU (2010), Source attribution and interannual variability of arctic pollution in spring constrained by aircraft (ARCTAS, ARCPAC) and satellite (AIRS) observations of carbon monoxide, *Atmospheric Chemistry and Physics*, *10*, 977–996, doi:10.5194/acp-10-977-2010. 5.3.6

FITZGERALD, J. W. (1973), Dependence of the supersaturation spectrum of CCN on aerosol size distribution and composition, *Journal of the Atmospheric Sciences*, *30*, 628–634, doi:10.1175/1520-0469(1973)030<0628:DOTSSO>2.0.CO;2. 1.2

FLAGAN, R. C. (2004), Opposed migration aerosol classifier (OMAC), *Aerosol Science and Technology*, *38*, 890–899, doi:10.1080/027868290505242. 9.1

FOUNTOUKIS, C., and A. NENES (2005), Continued development of a cloud droplet formation parameterization for global climate models, *Journal of Geophysical Research*, *110*, D11212. 9.2.2

FOUNTOUKIS, C., A. NENES, N. MESKHIDZE, R. BAHREINI, W. C. CONANT, H. JONSSON, S. MURPHY, A. SOROOSHIAN, V. VARUTBANGKUL, F. BRECHTEL, R. C. FLAGAN, and J. H. SEINFELD (2007), Aerosol-cloud drop concentration closure for clouds sampled during the International Consortium for Atmospheric Research on Transport and Transformation 2004 campaign, *Journal of Geophysical Research*, *112*, D10S30, doi:10.1029/2006JD007272. 2.3.4, 7.3.2, 9.1, 9.2.3

FRANK, G. P., U. DUSEK, and M. O. ANDREAE (2006), Technical Note: A method for measuring size-resolved CCN in the atmosphere, *Atmospheric Chemistry and Physics Discussions*, *6*, 4879–4895, doi:10.5194/acpd-6-4879-2006. 3.2.3

FUKUTA, N., and V. K. SAXENA (1979), A horizontal thermal gradient cloud condensation nucleus spectrometer, *Journal of Applied Meteorology*, *18*, 1352–1362, doi:10.1175/1520-0450(1979)018<1352:AHTGCC>2.0.CO;2. 2.1

FURUTANI, H., M. DALL'OSTO, G. C. ROBERTS, and K. A. PRATHER (2008), Assessment of the relative importance of atmospheric aging on CCN activity derived from field observations, *Atmospheric Environment*, *42*, 3130–3142, doi:10.1016/j.atmosenv.2007.09.024. 6.1

GARRETT, T. J., and C. ZHAO (2006), Increased arctic cloud longwave emissivity associated with pollution from mid-latitudes, *Nature*, *440*, 787–789, doi:10.1038/nature04636. 5.1

GARRETT, T. J., L. F. RADKE, and P. V. HOBBS (2002), Aerosol effects on cloud emissivity and surface longwave heating in the Arctic, *Journal of the Atmospheric Sciences*, *59*, 769–778, doi:10.1175/1520-0469(2002)059<0769:AEOCEA>2.0.CO;2. 5.1

GASPARINI, R., D. R. COLLINS, E. ANDREWS, P. J. SHERIDAN, J. A. OGREN, and J. G. HUDSON (2006), Coupling aerosol size distributions and size-resolved hygroscopicity to predict humidity-dependent optical properties and cloud condensation nuclei spectra, *Journal of Geophysical Research*, *111*, D05S13, doi:10.1029/2005JD006092. 9.2.1

GENTNER, D. R., R. A. HARLEY, A. M. MILLER, and A. H. GOLDSTEIN (2009), Diurnal and seasonal variability of gasoline-related volatile organic compound emissions in Riverside, California, *Environmental Science and Technology*, *43*, 4247–4252, doi:10.1021/es9006228. 8.3.1

GIEBL, H., A. BERNER, G. REISCHL, H. PUXBAUM, A. KASPER-GIEBL, and R. HITZENBERGER (2002), CCN activation of oxalic and malonic acid test aerosols with the University of Vienna cloud condensation nuclei, *Journal of Aerosol Science*, *33*, 1623–1634, doi:10.1016/S0021-8502(02)00115-5. 1.2, 9.1

GIVATI, A., and D. ROSENFELD (2004), Quantifying precipitation suppression due to air pollution, *Journal of Applied Meteorology*, *43*, 1038–1056, doi:10.1175/1520-0450(2004)043<1038:QPSDTA>2.0.CO;2. 6.1

GOLDSTEIN, A. H., and I. E. GALBALLY (2007), Known and unexplored organic constituents in the Earth's atmosphere, *Environmental Science and Technology*, *41*, 1514–1521, doi:10.1021/es072476p. 8.1

GOOD, N., D. O. TOPPING, J. D. ALLAN, M. FLYNN, E. FUENTES, M. IRWIN, P. I. WILLIAMS, H. COE, and G. MCFIGGANS (2010), Consistency between parameterizations of aerosol hygroscopicity and CCN activity during the RHaMBLe discovery cruise, *Atmospheric Chemistry and Physics*, *10*, 3189–3203, doi:10.5194/acp-10-3189-2010. 9.2.1

GREEN, D. W., and R. H. PERRY (2008), *Perry's Chemical Engineers' Handbook, 8th Edition*, McGraw-Hill. 7.1

GREEN, M. C., R. G. FLOCCHINI, and L. O. MYRUP (1992), The relationship of the extinction coefficient distribution to wind field patterns in southern California, *Atmospheric Environment*, *26*, 827–840, doi:10.1016/0960-1686(92)90243-E. 6.1

GUIBERT, S., J. R. SNIDER, and J.-L. BRENGUIER (2003), Aerosol activation in marine stratocumulus clouds: 1. Measurement validation for a closure study, *Journal of Geophysical Research*, *108*, 8628, doi:10.1029/2002JD002678. 9.2.3

GUNN, R. (1955), The statistical electrification of aerosols by ionic diffusion, *Journal of Colloid Science*, *10*, 107–119, doi:10.1016/0095-8522(55)90081-7. 4

GUNN, R., and R. H. WOESSNER (1956), Measurements of the systematic electrification of aerosols, *Journal of Colloid Science*, *11*, 254–259, doi:10.1016/0095-8522(56)90050-2. 4

GUNTHE, S. S., S. M. KING, D. ROSE, Q. CHEN, P. ROLDIN, D. K. FARMER, J. L. JIMENEZ, M. O. ANDREAE, S. T. MARTIN, and U. PÖSCHL (2009), Cloud condensation nuclei in pristine tropical rainforest air of Amazonia: size-resolved measurements and modeling of atmospheric aerosol composition and CCN activity, *Atmospheric Chemistry and Physics*, *9*, 7551–7575, doi:10.5194/acp-9-7551-2009. 3.1, 8.1, 9.1

HAGEN, D. E., and D. J. ALOFS (1983), Linear inversion method to obtain aerosol size distributions from measurements with a differential mobility analyzer, *Aerosol Science and Technology*, *2*, 465–475, doi:10.1080/02786828308958650. 3.2.2

HALLBERG, A., W. WOBROCK, A. I. FLOSSMANN, K. N. BOWER, K. J. NOONE, A. WIEDENSOHLER, H.-C. HANSSON, M. WENDISCH, A. BERNER, C. KRUISZ, P. LAJ, M. C. FACCHINI, S. FUZZI, and B. G. ARENDS (1997), Microphysics of clouds: Model versus measurements, *Atmospheric Environment*, *31*, 2453–2462, doi:10.1016/S1352-2310(97)00041-1. 9.1

HALLQUIST, M., J. C. WENGER, U. BALTENSPERGER, Y. RUDICH, D. SIMPSON, M. CLAEYS, J. DOMMEN, N. M. DONAHUE, C. GEORGE, A. H. GOLDSTEIN, J. F. HAMILTON, H. HERRMANN, T. HOFFMANN, Y. IINUMA, M. JANG, M. E. JENKIN, J. L. JIMENEZ, A. KIENDLER-SCHARR, W. MAENHAUT, G. MCFIGGANS, T. F. MENTEL, A. MONOD, A. S. H. PRÉVÔT, J. H. SEINFELD, J. D. SURRATT, R. SZMIGIELSKI, and J. WILDT (2009), The formation, properties and impact of secondary organic aerosol: current and emerging issues, *Atmospheric Chemistry and Physics*, *9*, 5155–5236, doi:10.5194/acp-9-5155-2009. 7.1, 8.1

HAYWOOD, J., and O. BOUCHER (2000), Estimates of the direct and indirect radiative forcing due to tropospheric aerosols: A review, *Reviews of Geophysics*, *38*, 513–543, doi:10.1029/1999RG000078. (document), 1.1

HEGG, D. A., R. J. FEREK, and P. V. HOBBS (1995), Cloud condensation nuclei over the Arctic Ocean in early Spring, *Journal of Applied Meteorology*, *34*, 2076–2082, doi:10.1175/1520-0450(1995)034<2076:CCNOTA>2.0.CO;2. 5.1, 5.3.1, 5.3.2

HEGG, D. A., P. V. HOBBS, S. GASSÓ, J. D. NANCE, and A. L. RANGNO (1996), Aerosol measurements in the Arctic relevant to direct and indirect radiative forcing, *Journal of Geophysical Research*, *101*, 23,349–23,363, doi:10.1029/96JD02246. 5.1, 5.3.1, 5.3.2

HEGG, D. A., D. S. COVERT, H. H. JONSSON, and R. WOODS (2009), Differentiating natural and anthropogenic cloud condensation nuclei in the California coastal zone, *Tellus*, *61B*, 669–676, doi:10.1111/j.1600-0889-2009.00435.x. 6.1

HEINTZENBERG, J. (1980), Particle size distribution and optical properties of Arctic haze, *Tellus*, *32*, 251–260, doi:10.1111/j.2153-3490.1980.tb00952.x. 5.3.1

HEINTZENBERG, J., C. LECK, W. BIRMILI, B. WEHNER, M. TJERNSTRÖM, and A. WIEDENSOHLER (2006), Aerosol number–size distributions during clear and fog periods in the summer high Arctic: 1991, 1996, and 2001, *Tellus B*, *58*, 41–50, doi:10.1111/j.1600-0889.2005.00171.x. 5.3.1

HENNIGAN, C. J., M. H. BERGIN, A. G. RUSSELL, A. NENES, and R. J. WEBER (2009), Gas/particle partitioning of water-soluble organic aerosol in Atlanta, *Atmospheric Chemistry and Physics*, *9*, 3613–3628, doi:10.5194/acp-9-3613-2009. 8.1

HERICH, H., L. KAMMERMANN, B. FRIEDMAN, D. S. GROSS, E. WEINGARTNER, U. LOHMANN, P. SPICHTINGER, M. GYSEL, U. BALTENSPERGER, and D. J. CZICZO (2009), Subarctic atmospheric aerosol composition: 2. Hygroscopic growth properties, *Journal of Geophysical Research*, *114*, D13204, doi:10.1029/2008JD011574. 5.3.2

HOPPEL, W. A., J. E. DINGER, and R. E. RUSKIN (1973), Vertical profiles of CCN at various geographical locations, *Journal of the Amospheric Sciences*, *30*, 1410–1420, doi:10.1175/1520-0469(1973)030<1410:VPOCAV>2.0.CO;2. 5.1

HOPPEL, W. A., S. TWOMEY, and T. A. WOJCIECHOWSKI (1979), A segmented thermal diffusion chamber for continuous measurements of CN, *Journal of Aerosol Science*, *10*, 369–373, doi:10.1016/0021-8502(79)90031-4. 2.1

HUDSON, J. G. (1989), An instantaneous CCN spectrometer, *Journal of Atmospheric and Oceanic Technology*, *6*, 1055–1065, doi:10.1175/1520-0426(1989)006<1055:AICS>2.0.CO;2. 2.1

HUDSON, J. G. (1993), Cloud condensation nuclei, *Journal of Applied Meteorology*, *32*, 596–607, doi:10.1175/1520-0450(1993)032<0596:CCN>2.0.CO;2. 9.1

JAYNE, J. T., D. C. LEARD, X. ZHANG, P. DAVIDOVITS, K. A. SMITH, C. A. KOLB, and D. R. WORSNOP (2000), Development of an aerosol mass spectrometer for size and composition analysis of submicron particles, *Aerosol Science and Technology*, *33*, 49–70, doi:10.1080/027868200410840. 9.1

JI, Q., G. E. SHAW, and W. CANTRELL (1998), A new instrument for measuring cloud condensation nuclei: Cloud condensation nucleus "remover", *Journal of Geophysical Research*, *103*, 28,013–28,019, doi:10.1029/98JD01884. 2.1, 5.1

JIMENEZ, J., M. R. CANAGARATNA, N. M. DONAHUE, A. S. H. PREVOT, Q. ZHANG, J. H. KROLL, P. F. DECARLO, J. D. ALLAN, H. COE, N. L. NG, A. C. AIKEN, K. S. DOCHERTY, I. M. ULBRICH, A. P. GRIESHOP, A. L. ROBINSON, J. DUPLISSY, J. D. SMITH, K. R. WILSON, V. A. LANZ, C. HUEGLIN, Y. L. SUN, J. TIAN, A. LAAKSONEN, T. RAATIKAINEN, J. RAUTIAINEN, P. VAATTOVAARA, M. EHN, M. KULMALA, J. M. TOMLINSON, D. R. COLLINS, M. J. CUBISON, E. J. DUNLEA, A. HUFFMAN, T. B. ONASCH, M. R. ALFARRA, P. I. WILLIAMS, K. BOWER, Y. KONDO, J. SCHNEIDER, F. DREWNICK, S. BORRMANN, S. WEIMER, K. DEMERJIAN, D. SALCEDO, L. COTTRELL, R. GRIFFIN, A. TAKAMI, T. MIYOSHI, S. HATAKEYAMA, A. SHIMONO, J. Y. SUN, Y. M. ZHANG, K. DZEPINA, J. R. KIMMEL, D. SUEPER,

J. T. JAYNE, S. C. HERNDON, A. M. TRIMBORN, L. R. WILLIAMS, E. C. WOOD, A. M. MIDDLEBROOK, C. E. KOLB, U. BALTENSPERGER, and D. R. WORSNOP (2009), Evolution of organic aerosols in the atmosphere, *Science*, *326*, 1525–1529, doi:10.1126/science.1180353. 5.1, 5.3.4, 5.3.4, 6.3.4, 7.3.1, 8.3.1

JIMENEZ, J. L., J. T. JAYNE, Q. SHI, C. E. KOLB, D. R. WORSNOP, I. YOURSHAW, J. H. SEINFELD, R. C. FLAGAN, X. ZHANG, K. A. SMITH, J. W. MORRIS, and P. DAVIDOVITS (2003), Ambient aerosol sampling using the Aerodyne Aerosol Mass Spectrometer, *Journal of Geophysical Research*, *108*, 8425, doi:10.1029/2001JD001213. 9.1

JUNGE, C., and E. MCLAREN (1971), Relationship of cloud nuclei spectra to aerosol size distribution and composition, *Journal of the Atmospheric Sciences*, *28*, 382–390, doi:10.1175/1520-0469(1971)028<0382:ROCNST>2.0.CO;2. 1.2

JURÁNYI, Z., M. GYSEL, E. WEINGARTNER, P. F. DECARLO, L. KAMMERMANN, and U. BALTENSPERGER (2010), Measured and modelled cloud condensation nuclei number concentration at the high alpine site Jungfraujoch, *Atmospheric Chemistry and Physics*, *10*, 7891–7906, doi:10.5194/acp-10-7891-2010. 3.1, 9.1

KÄMER, L., U. PÖSCHL, and R. NIESSNER (2000), Microstructural rearrangement of sodium chloride condensation aerosol particles on interaction with water vapor, *Journal of Aerosol Science*, *31*, 673–685, doi:10.1016/S0021-8502(99)00551-0. 2.4.1, 3.2.3, 3.4.1

KAMMERMANN, L., M. GYSEL, E. WEINGARTNER, H. HERICH, D. J. CZICZO, T. HOLST, B. SVENNINGSSON, A. AMETH, and U. BALTENSPERGER (2010), Subarctic atmospheric aerosol composition: 3. Measured and modeled properties of cloud condensation nuclei, *Journal of Geophysical Research*, *115*, D04202, doi:10.1029/2009JD012447. 5.1, 5.3.2, 5.3.3, 9.2.1

KANAKIDOU, M., J. H. SEINFELD, S. N. PANDIS, I. BARNES, F. J. DENTENER, M. C. FACCHINI, R. V. DINGENEN, B. ERVENS, A. NENES, C. J. NIELSEN, E. SWIETLICKI, J. P. PUTAUD, Y. BALKANSKI, S. FUZZI, J. HORTH, G. K. MOORTGAT, R. WINTERHALTER, C. E. L. MYHRE, K. TSIGARIDIS, E. VIGNATI, E. G. STEPHANOU, and J. WILSON (2005), Organic aerosol and global climate modelling: A review, *Atmospheric Chemistry and Physics*, *5*, 1053–1123, doi:10.5194/acp-5-1053-2005. 2.1, 8.1

KARYDIS, V. A., P. KUMAR, D. BARAHONA, I. N. SOKOLIK, and A. NENES (in press), On the effect of dust particles on global CCN and cloud droplet number, *Journal of Geophysical Research*. 9.2.2, 9.2.3

KIM, J. H., S. S. YUM, S. SHIM, S.-C. YOON, J. G. HUDSON, J. PARK, and S.-J. LEE (2011), On aerosol hygroscopicity, cloud condensation nuclei (CCN) spectra and critical supersaturation measured at two remote islands of Korea between 2006 and 2009, *Atmospheric Chemistry and Physics Discussions*, *11*, 19,683–19,727, doi:10.5194/acpd-11-19683-2011. 9.2.1

KING, S. M., T. ROSENOERN, J. E. SHILLING, Q. CHEN, and S. T. MARTIN (2009), Increased cloud activation potential of secondary organic aerosol for atmospheric mass loadings, *Atmospheric Chemistry and Physics*, *9*, 2959–2972, doi:10.5194/acp-9-2959-2009. 3.2.3

KOCH, D., and D. RIND (1998), Beryllium 10/beryllium 7 as a tracer of stratospheric transport, *Journal of Geophysical Research*, *103*, 3907–3917, doi:10.1029/97JD03117. 9.2.3

KÖHLER, H. (1936), The nucleus in and growth of hygroscopic droplets, *Transactions of the Faraday Society*, *32*, 1152–1161, doi:10.1039/TF9363201152. 1.2, 2.1, 4.3.1, 5.2.4, 5.3.3, 6.2.4, 6.3.3, 7.2.1, 7.2.3, 8.2.1, 9.1

KORHONEN, H., K. S. CARSLAW, D. V. SPRACKLEN, D. A. RIDLEY, and J. STRÖM (2008), A global model study of processes controlling aerosol size distributions in the Arctic spring and summer, *Journal of Geophysical Research*, *113*, D08211, doi:10.1029/2007JD009114. 5.3.1

KULMALA, M., and V.-M. KERMINEN (2008), On the formation and growth of atmospheric nanoparticles, *Atmospheric Research*, *90*, 132–150, doi:10.1016/j.atmosres.2008.01.005. 7.3.2

KULMALA, M., H. VEHKAMÄKI, T. PETÄJÄ, M. D. MASO, A. LAURI, V.-M. KERMINEN, W. BIRMILI, and P. H. MCMURRY (2004), Formation and growth rates of ultrafine atmospheric particles: A review of observations, *Journal of Aerosol Science*, *35*, 143–176, doi:10.1016/j.jaerosci.2003.10.003. 8.3.2

KUMAR, P., I. N. SOKOLIK, and A. NENES (2009), Parameterization of cloud droplet formation for global and regional models: Including adsorption activation from insoluble CCN, *Atmospheric Chemistry and Physics*, *9*, 2517–2532, doi:10.5194/acp-9-2517-2009. 1.4, 9.1, 9.2.2, 10.1

KUWATA, M., and Y. KONDO (2009), Measurements of particle masses of inorganic salt particles for calibration of cloud condensation nuclei counters, *Atmospheric Chemistry and Physics*, *9*, 5921–5932, doi:10.5194/acp-9-5921-2009. 3.2.3

KUWATA, M., Y. KONDO, Y. MIYAZAKI, Y. KOMAZAKI, J. H. KIM, S. S. YUM, H. TANIMOTO, and H. MATSUEDA (2008), Cloud condensation nuclei activity at Jeju Island, Korea in spring 2005, *Atmospheric Chemistry and Physics*, *8*, 2933–2948, doi:10.5194/acp-8-2933-2008. 3.1, 9.1

LAAKSONEN, A., P. KORHONEN, M. KULMALA, and R. J. CHARLSON (1998), Modification of the köhler equation to include soluble trace gases and slightly soluble substances, *Journal of the Atmospheric Sciences*, *55*, 853–862, doi:10.1175/1520-0469(1998)055<0853:MOTKHE>2.0CO;2. 1.2

LAAKSONEN, A., M. KULMALA, C. D. O'DOWD, J. JOUTSENSAARI, P. VAATTOVAARA, S. MIKKONEN, K. E. J. LEHTINEN, L. SOGACHEVA, M. D. MASO,

P. AALTO, T. PETÄJÄ, A. SOGACHEV, Y. J. YOON, H. LIHAVAINEN, D. NILSSON, M. C. FACCHINI, F. CAVALLI, S. FUZZI, T. HOFFMANN, F. ARNOLD, M. HANKE, K. SELLEGRI, B. UMANN, W. JUNKERMANN, H. COE, J. D. ALLAN, M. R. ALFARRA, D. R. WORSNOP, M.-L. RIEKKOLA, T. HYÖTYLÄINEN, and Y. VIISANEN (2008), The role of VOC oxidation products in continental new particle formation, *Atmospheric Chemistry and Physics*, *8*, 2657–2665, doi:10.5194/acp-8-2657-2008. 8.3.2

LALA, G. G., and J. E. JIUSTO (1977), An automatic light scattering CCN counter, *Journal of Applied Meteorology*, *16*, 413–418, doi:10.1175/1520-0450(1977)016<0413:AALSCC>2.0.CO;2. 2.1

LANCE, S. (2007), Quantifying compositional impacts of ambient aerosol on cloud droplet formation, Ph.D. thesis, Georgia Institute of Technology. 1.2, 3.1, 8.2.2

LANCE, S., A. NENES, and T. A. RISSMAN (2004), Chemical and dynamical effects on cloud droplet number: Implications for estimates of the aerosol indirect effect, *Journal of Geophysical Research*, *109*, D22208, doi:10.1029/2004JD004596. 9.1, 9.2.2

LANCE, S., J. MEDINA, J. N. SMITH, and A. NENES (2006), Mapping the operation of the DMT continuous-flow CCN counter, *Aerosol Science and Technology*, *40*, 242–254, doi:10.1080/02786820500543290. (document), 2.1, 2.3.2, 2.3.3, 2.3.4, 2.8, 3.1, 3.2.1, 3.2.1, 3.4.1, 5.2.4, 6.2.4, 7.2.1, 7.2.2, 7.5.4, 8.2.1, 9.1

LANCE, S., A. NENES, C. MAZZOLENI, M. K. DUBEY, H. GATES, V. VARUTBANGKUL, T. A. RISSMAN, S. M. MURPHY, A. SOROOSHIAN, R. C. FLAGAN, J. H. SEINFELD, G. FEINGOLD, and H. H. JONSSON (2009), Cloud condensation nuclei activity, closure, and droplet growth kinetics of Houston aerosol during the Gulf of Mexico Atmospheric Composition and Climate Study (GoMACCS), *Journal of Geophysical Research*, *114*, D00F15, doi:10.1029/2008JD011699. 2.1, 3.1, 6.3.1, 6.3.6, 7.3.2, 9.1

LANCE, S., M. D. SHUPE, G. FEINGOLD, C. A. BROCK, J. COZIC, J. S. HOLLOWAY, R. H. MOORE, A. NENES, J. P. SCHWARZ, J. R. SPACKMAN, K. D. FROYD, D. M. MURPHY, J. BRIOUDE, O. R. COOPER, A. STOHL, and J. F. BURKHART (2011), Cloud condensation nuclei as a modulator of ice processes in Arctic mixed-phase clouds, *Atmospheric Chemistry and Physics Discussions*, *11*, 6737–6770, doi:10.5194/acpd-11-6737-2011. 5.1, 5.3.4

LANGMUIR, I. (1917), The constitution and fundamental properties of solids and liquids. II. Liquids, *Journal of the American Chemical Society*, *39*, 1848–1906, doi:10.1021/ja02254a006. 4.2.3

LANGRIDGE, J. M., M. S. RICHARDSON, D. LACK, D. LAW, and D. M. MURPHY (2011), Aircraft instrumentation for comprehensive characterization of aerosol optical properties, Part I: Wavelength-dependent optical extinction and its relative humidity dependence measured using cavity ringdown spectroscopy, *Aerosol Science and Technology*, *45*, 1305–1318, doi:10.1080/02786826.2011.592745. 7.2.1

LATHEM, T., and A. NENES (2011), Water vapor depletion in the DMT continuous flow CCN chamber: Effects on supersaturation and droplet growth, *Aerosol Science and Technology*, *45*, 604–615, doi:10.1080/02786826.2010.551146. 7.2.2, 7.3.2, 7.5.4

LAW, K. S., and A. STOHL (2007), Arctic air pollution: Origins and impacts, *Science*, *315*, 1537–1540, doi:10.1126/science.1137695. 5.1

LEAITCH, R., and W. J. MEGAW (1982), The diffusion tube; a cloud condensation nucleus counter for use below 0.3% supersaturation, *Journal of Aerosol Science*, *13*, 297–319, doi:10.1016/0021-8502(82)90032-5. 2.1

LEE, L. A., K. S. CARSLAW, K. PRINGLE, G. W. MANN, and D. V. SPRACKLEN (2011), Emulation of a complex global aerosol model to quantify sensitivity to uncertain parameters, *Atmospheric Chemistry and Physics Discussions*, *11*, 20,433–20,485, doi:10.5194/acpd-11-20433-2011. 9.1

LEVIN, Z., and W. R. COTTON (Eds.) (2009), *Aerosol Pollution Impact on Precipitation: A Scientific Review*, Springer. 2.1, 3.1

LI, Y. Q., P. DAVIDOVITS, Q. SHI, J. T. JAYNE, C. E. KOLB, and D. R. WORSNOP (2001), Mass and thermal accommodation coefficients of $H_2O$(g) on liquid water as a function of temperature, *Journal of Physical Chemistry A*, *105*, 10,627–10,634, doi:10.1021/jp012758q. 1.3, 2.3.4, 7.3.2, 7.5.4

LIM, H.-J., and B. TURPIN (2002), Origins of primary and secondary organic aerosol in Atlanta: Results of time-resolved measurements during the Atlanta supersite experiment, *Environmental Science and Technology*, *36*, 4489–4496, doi:10.1021/es0206487. 8.1, 8.3.2

LIM, Y. B., Y. TAN, M. J. PERRI, S. P. SEITZINGER, and B. J. TURPIN (2010), Aqueous chemistry and its role in secondary organic aerosol (SOA) formation, *Atmospheric Chemistry and Physics*, *10*, 10,521–10,539, doi:10.5194/acp-10-10521-201. 5.3.4

LIU, X., J. E. PENNER, and M. HERZOG (2005), Global modeling of aerosol dynamics: Model description, evaluation, and interactions between sulfate and nonsulfate aerosols, *Journal of Geophysical Research*, *110*, D18206, doi:10.1029/2004JD005674. 9.2.2

LOHMANN, U., and C. LECK (2005), Importance of submicron surface-active organic aerosols for pristine Arctic clouds, *Tellus B*, *57B*, 261–268, doi:10.1111/j.1600-0889.2005.00144.x. 2.1

LUBIN, D., and A. M. VOGELMANN (2006), A climatologically significant aerosol longwave indirect effect in the Arctic, *Nature*, *439*, 453–456, doi:10.1038/nature04449. 5.1

MAURITSEN, T., J. SEDLAR, M. TJERNSTRÖM, C. LECK, M. MARTIN, M. SHUPE, S. SJOGREN, B. SIERAU, P. O. G. PERSSON, I. M. BROOKS, and E. SWIETLICKI (2011), An Arctic CCN-limited cloud-aerosol regime, *Atmospheric Chemistry and Physics*, *11*, 165–173, doi:10.5194/acp-11-165-2011. 1.1

McFIGGANS, G., P. ARTAXO, U. BALTENSPERGER, H. COE, M. C. FACCHINI, G. FEINGOLD, S. FUZZI, A. LAAKSONEN, U. LOHMANN, T. F. MENTEL, D. M. MURPHY, C. D. O'DOWD, J. R. SNIDER, and E. WEINGARTNER (2006), The effect of physical and chemical aerosol properties on warm cloud droplet activation, *Atmospheric Chemistry and Physics*, *6*, 2593–2649, doi:10.5194/acp-6-2593-2006. 2.1

MEDINA, J., A. NENES, R.-E. P. SOTIRPOULOU, L. D. COTTRELL, L. D. ZIEMBA, P. J. BECKMAN, and R. J. GRIFFIN (2007), Cloud condensation nuclei closure during the International Consortium for Atmospheric Research on Transport and Transformation 2004 campaign: Effects of size-resolved composition, *Journal of Geophysical Research*, *112*, D10S31, doi:10.1029/2006JD007588. 2.1, 3.1, 3.4.2, 5.3.6, 9.1, 9.1

MESKHIDZE, N., A. NENES, W. C. CONANT, and J. H. SEINFELD (2005), Evaluation of a new cloud droplet activation parameterization with in situ data from CRYSTAL-FACE and CSTRIPE, *Journal of Geophysical Research*, *110*, D16202, doi:10.1029/2004JD005703. 9.1, 9.2.3

MOORE, R. H., and A. NENES (2009), Scanning flow CCN analysis – A method for fast measurements of CCN spectra, *Aerosol Science and Technology*, *43*, 1192–1207, doi:10.1080/02786820903289780. 3.1, 6.2.4, 7.2.1, 7.5.4, 8.2.1

MOORE, R. H., E. D. INGALL, A. SOROOSHIAN, and A. NENES (2008), Molar mass, surface tension, and droplet growth kinetics of marine organics from measurements of CCN activity, *Geophysical Research Letters*, *35*, L07,801, doi:10.1029/2008GL033350. 2.1, 3.1, 3.1, 3.5

MOORE, R. H., A. NENES, and J. MEDINA (2010), Scanning mobility CCN analysis – A method for fast measurements of size-resolved CCN distributions and activation kinetics, *Aerosol Science and Technology*, *44*, 861–871, doi:10.1080/02786826.2010.498715. 4.2.4, 5.2.4, 6.2.4, 7.2.1, 8.2.1

MOORE, R. H., R. BAHREINI, C. A. BROCK, K. D. FROYD, J. COZIC, J. S. HOLLOWAY, A. M. MIDDLEBROOK, D. M. MURPHY, and A. NENES (2011), Hygroscopicity and Composition of Alaskan Arctic CCN During April 2008, *Atmospheric Chemistry and Physics Discussions*, *11*, 21,789–21,834, doi:10.5194/acpd-11-21789-2011. 6.2.4, 6.3.2, 6.3.3, 6.3.3, 6.3.5, 6.3.5, 6.3.6, 7.2.3, 9.1, 9.3.4

MOORE, R. H., K. CERULLY, R. BAHREINI, C. A. BROCK, A. M. MIDDLEBROOK, and A. NENES (in preparation), Hygroscopicity and composition of California CCN during summer, 2010, *Journal of Geophysical Research*. 9.1, 9.3.4

MOORE, R. H., T. RAATIKAINEN, J. M. LANGRIDGE, R. BAHREINI, C. A. BROCK, J. S. HOLLOWAY, D. A. LACK, A. M. MIDDLEBROOK, A. E. PERRING, J. P. SCHWARZ, J. R. SPACKMAN, and A. NENES (in review), CCN spectra, hygroscopicity, and droplet activation kinetics of secondary organic aerosol resulting from the 2010 Deepwater Horizon Oil Spill, *Environmental Science and Technology*. 9.1

MOZURKEWICH, M. (1986), Aerosol growth and the condensation coefficient for water: A review, *Aerosol Science and Technology*, *5*, 223–236, doi:10.1080/02786828608959089. 1.3, 7.3.2

MURPHY, D. M., D. J. CZICZO, K. D. FROYD, P. K. HUDSON, B. M. MATTHEW, A. M. MIDDLEBROOK, R. E. PELTIER, A. SULLIVAN, D. S. THOMSON, and R. J. WEBER (2006), Single-particle mass spectrometry of tropospheric aerosol particles, *Journal of Geophysical Research*, *111*, D23S32, doi:10.1029/2006JD007340. 5.2.2, 6.3.1

MURPHY, S. M., H. AGRAWAL, A. SOROOSHIAN, L. T. PADRÓ, H. GATES, S. HERSEY, W. A. WELCH, H. JUNG, J. W. MILLER, D. R. C. III, A. NENES, H. H. JONSSON, R. C. FLAGAN, and J. H. SEINFELD (2009), Comprehensive simultaneous shipboard and airborne characterization of exhaust from a modern container ship at sea, *Environmental Science and Technology*, *43*, 4626–4640, doi:10.1021/es802413j. 9.1

MYRIOKEFALITAKIS, S., K. TSIGARIDIS, N. MIHALOPOULOS, J. SCIARE, A. NENES, A. SEGERS, and M. KANAKIDOU (2011), In-cloud oxalate formation in the global troposphere: a 3-D modeling study, *Atmospheric Chemistry and Physics Discussions*, *11*, 485–530, doi:10.5194/acpd-11-485-2011. 5.3.4

NENES, A., and J. H. SEINFELD (2003), Parameterization of cloud droplet formation in global climate models, *Journal of Geophysical Research*, *108*, 4415, doi:10.1029/2002JD002911. 2.3.4, 2.3.4, 2.3.4, 9.2.2

NENES, A., S. N. PANDIS, and C. PILINIS (1998), ISORROPIA: A new thermodynamic equilibrium model for multiphase multicomponent aerosols, *Aquatic Geochemistry*, *4*, 123–152, doi:10.1023/A:1009604003981. 5.3.1, 6.3.1

NENES, A., S. GHAN, H. ABDUL-RAZZAK, P. Y. CHUANG, and J. H. SEINFELD (2001a), Kinetic limitations on cloud droplet formation and impact on cloud albedo, *Tellus B*, *53*, 133–149, doi:10.1034/j.1600-0889.2001.d01-12.x. 1.3, 2.3.4

NENES, A., P. Y. CHUANG, R. C. FLAGAN, and J. H. SEINFELD (2001b), A theoretical analysis of cloud condensation nucleus (CCN) instruments, *Journal of Geophysical Research*, *106*, 3449–3474, doi:10.1029/2000JD900614. 2.1

NENES, A., R. J. CHARLSON, M. C. FACCHINI, M. KULMALA, A. LAAKSONEN, and J. H. SEINFELD (2002), Can chemical effects on cloud droplet number rival the first indirect effect?, *Geophysical Research Letters*, *29*, 1848, doi:10.1029/2002GL015295. 1.3, 1.3, 7.3.2

NEUMAN, J. A., J. B. NOWAK, C. A. BROCK, M. TRAINER, F. C. FEHSENFELD, J. S. HOLLOWAY, G. HÜBLER, P. K. HUDSON, D. M. MURPHY, J. D. K. NICKS, D. ORSINI, D. D. PARISH, T. B. RYERSON, D. T. SUEPER, A. SULLIVAN, and R. WEBER (2003), Variability in ammonium nitrate formation and nitric acid depletion with altitude and location over California, *Journal of Geophysical Research*, *108*, 4557, doi:10.1029/2003JD003616. 6.1

NG, N. L., M. R. CANAGARATNA, Q. ZHANG, J. L. JIMENEZ, J. TIAN, I. M. ULBRICH, J. H. KROLL, K. S. DOCHERTY, P. S. CHHABRA, R. BAHREINI, S. M. MURPHY, J. H. SEINFELD, L. HILDEBRANDT, N. M. DONAHUE, P. F. DECARLO, V. A. LANZ, A. S. H. PRÉVÔT, E. DINAR, Y. RUDICH, and D. R. WORSNOP (2010), Organic aerosol components observed in Northern Hemispheric datasets from Aersosol Mass Spectrometry, *Atmospheric Chemistry and Physics*, *10*, 4625–4641, doi:10.5194/acp-10-4625-2010. (document), 5.3.4, 5.8, 6.6, 6.3.4

NOAA-NESDIS (2010), Satellite Derived Surface Oil Analysis Products – Deepwater Horizon (www.ssd.noaa.gov/PS/MPS/deepwater.html). (document), 7.1, 7.5

O'DOWD, C. O., M. C. FACCHINI, F. CAVALLI, D. CEBURNIS, M. MIRCEA, S. DECESARI, S. FUZZI, Y. J. YOON, and J.-P. PUTAUD (2004), Biogenically driven organic contribution to marine aerosol, *Nature*, *431*, 676–680, doi:10.1038/nature02959. 4.1

OGAWA, H., and E. TANOUE (2003), Dissolved organic matter in oceanic waters, *Journal of Oceanography*, *59*, 129–147. 4.1, 4.3.2

OLFERT, J. S., P. KULKARNI, and J. WANG (2008), Measuring aerosol size distributions with the fast integrated mobility spectrometer, *Journal of Aerosol Science*, *39*, 940–956, doi:10.1016/j.jaerosci.2008.06.005. 9.1

OPPO, C., S. BELLANDI, N. D. INNOCENTI, A. M. STORTINI, G. LOGLIO, E. SCHIAVUTA, and R. CINI (1999), Surfactant components of marine organic matter as agents for biogeochemical fractionation and pollutant transport via marine aerosols, *Marine Chemistry*, *63*, 235–253, doi:10.1016/S0304-4203(98)00065-6. 4.1

OSBORN, R. J., N. F. TAYLOR, C. W. SPENCER, and D. R. COLLINS (2008), Isolation of ambient particles of known critical supersaturation: The differential activation separator (DAS), *Aerosol Science and Technology*, *42*, 759–772, doi:10.1080/02786820802339512. 2.1

PADRÓ, L. T., and A. NENES (2007), Cloud droplet activation: solubility revisited, *Atmospheric Chemistry and Physics Discussions*, *7*, 2325–2355, doi:10.5194/acpd-7-2325-2007. 1.2

PADRÓ, L. T., A. ASA-AWUKU, R. MORRISON, and A. NENES (2007), Inferring thermodynamic properties from CCN activation experiments: Single-component and binary aerosols, *Atmospheric Chemistry and Physics*, *7*, 5263–5274, doi:10.5194/acp-7-5263-2007. 1.2, 1.4, 2.1, 3.1, 3.1, 3.5, 4.1, 4.2.4, 4.3.1, 4.3.2, 4.3.2, 4.3.2, 4.3.2, 4.3.2, 9.1

PADRÓ, L. T., D. TKACIK, T. LATHEM, C. HENNIGAN, A. P. SULLIVAN, R. J. WEBER, L. G. HUEY, and A. NENES (2010), Investigation of cloud condensation nuclei properties and droplet growth kinetics of the water-soluble aerosol fraction in Mexico City, *Journal of Geophysical Research*, *115*, D09204, doi:10.1029/2009JD013195. 3.1, 3.1, 3.5, 8.4

PADRÓ, L. T., R. H. MOORE, X. ZHANG, N. RASTOGI, R. J. WEBER, and A. NENES (in review), Mixing state and compositional effects on CCN activity and droplet growth kinetics of size-resolved CCN in an urban environment, *Atmospheric Chemistry and Physics Discussions*. 8.3.1, 9.1

PADRÓ MARTINEZ, L. T. (2009), Towards an understanding of the cloud formation potential of carbonaceous aerosol: Laboratory and field studies, Ph.D. thesis, Georgia Institute of Technology. 3.1

PERRING, A. E., J. P. SCHWARZ, J. R. SPACKMAN, R. BAHREINI, J. A. DE GOUW, R. S. GAO, J. S. HOLLOWAY, D. A. LACK, J. M. LANGRIDGE, J. PEISCHL, A. M. MIDDLEBROOK, T. B. RYERSON, C. WARNEKE, L. A. WATTS, and D. W. FAHEY (2011), Characteristics of black carbon aerosol from a surface oil burn during the Deepwater Horizon Oil spill, *Geophysical Research Letters*, *38*, L17809, doi:10.1029/2011GL048356. 7.2, 7.2.1

PETTERS, M. D., and S. M. KREIDENWEIS (2007), A single parameter representation of hygroscopic growth and cloud condensation nucleus activity, *Atmospheric Chemistry and Physics*, *7*, 1961–1971, doi:10.5194/acp-8-6273-2008. 1.2, 3.1, 3.1, 3.2.3, 5.1, 5.3.3, 5.3.3, 6.3.3, 6.3.3, 7.2.3, 7.2.3, 3, 8.1, 8.2.2, 9.2.1

PETTERS, M. D., C. M. CARRICO, S. M. KREIDENWEIS, A. J. PRENNI, P. J. DEMOTT, J. L. C. JR., and H. MOOSMÜLLER (2009), Cloud condensation nucleation activity of biomass burning aerosol, *Journal of Geophysical Research*, *114*, D22205, doi:10.1029/2009JD012353. 3.1, 3.1, 3.2.3

PINCUS, R., and M. B. BAKER (1994), Effect of precipitation on the albedo susceptiblity of clouds in the marine boundary layer, *Nature*, *372*, 250–252, doi:10.1038/372250a0. 1.1

PITZER, K. S., and G. MAYORGA (1973), Thermodynamics of electrolytes. II. Activity and osmotic coefficients for strong electrolytes with one or both ions univalent, *The Journal of Physical Chemisitry*, *77*, 2300–2308, doi:10.1021/j100638a009. 2.4.1, 3.4.1, 5.2.4, 6.2.4

PRINGLE, K. J., H. TOST, A. POZZER, U. PÖSCHL, and J. LELIEVELD (2010), Global distribution of the effective aerosol hygroscopicity parameter for CCN activation, *Atmospheric Chemistry and Physics*, *10*, 5241–5255, doi:10.5194/acp-10-5241-2010. 1.2, 8.1

QUINN, P. K., G. SHAW, E. ANDREWS, E. G. DUTTON, T. RUOHO-AIROLA, and S. L. GONG (2007), Arctic haze: current trends and knowledge gaps, *Tellus B*, *59B*, 99–114, doi:10.1111/j.1600-0889.2006.00238.x. 5.1

QUINN, P. K., T. S. BATES, E. BAUM, N. DOUBLEDAY, A. M. FIORE, M. FLANNER, A. FRIDLIND, T. J. GARRETT, D. KOCH, S. MENON, D. SHINDELL, A. STOHL, and S. G. WARREN (2008a), Short-lived pollutants in the Arctic: their climatic impact and

possible mitigation strategies, *Atmospheric Chemistry and Physics*, *8*, 1723–1735, doi:10.5194/acp-8-1723-2008. 5.1, 6.3.6

QUINN, P. K., T. S. BATES, D. J. COFFMAN, and D. S. COVERT (2008b), Influence of particle size and chemistry on the cloud nucleating properties of aerosols, *Atmospheric Chemistry and Physics*, *8*, 1029–1042, doi:10.5194/acp-8-1029-2008. 9.1

RADKE, L. F., D. A. HEGG, J. H. LYONS, C. A. BROCK, P. V. HOBBS, R. WEISS, and R. RASMUSSEN (1988), *Aerosols and Climate*, chap. Airborne measurements on smokes from biomass burning, pp. 411–422, Deepak Publishing. 9.2.2

RAMANATHAN, V., P. J. CRUTZEN, J. T. KIEHL, and D. ROSENFELD (2001), Aerosols, climate, and the hydrological cycle, *Science*, *294*, 2119–2124, doi:10.1126/science.1064034. 2.1

RAYMOND, T. M., and S. N. PANDIS (2002), Cloud activation of single-component organic aerosol particles, *Journal of Geophysical Research*, *107*, 4787, doi:10.1029/2002JD002159. 1.2, 9.1

RAYMOND, T. M., and S. N. PANDIS (2003), Formation of cloud droplets by multicomponent organic particles, *Journal of Geophysical Research*, *108*, 4469, doi:10.1029/2003JD003503. 1.2, 9.1

REDFIELD, A. C., B. H. KETCHUM, and F. A. RICHARDS (1963), *The Sea 2*, chap. The influence of organisms on the composition of sea water, pp. 26–77, Wiley Interscience. 4.3.2

RIAZI, M. R., and T. A. AL-SAHHAF (1995), Physical properties of *n*-alkanes and *n*-alkylhydrocarbons: Application to petroleum mixtures, *Industrial and Engineering Chemistry Research*, *34*, 4145–4148, doi:10.1021/ie00038a062. 2, 7.1

RIND, D., and J. LERNER (1996), Use of on-line tracers as a diagnostic tool in general circulation model development 1. Horizontal and vertical transport in the troposphere, *Journal of Geophysical Research*, *101*, 12,667–12,683, doi:10.1029/96JD00551. 9.2.3

RINEHART, L. R., E. M. FUJITA, J. C. CHOW, K. MAGLIANO, and B. ZIELINSKA (2006), Spatial distribution of $PM_{2.5}$ associated organic compounds in central California, *Atmospheric Environment*, *40*, 290–303, doi:10.1016/j.atmosenv.2005.09.035. 6.1

RISSLER, J., E. SWIETLICKI, J. ZHOU, G. ROBERTS, M. O. ANDREAE, L. V. GATTI, and P. ARTAXO (2004), Physical properties of the sub-micrometer aerosol over the Amazon rain forest during the wet-to-dry season transition – comparison of modeled and measured CCN concentrations, *Atmospheric Chemistry and Physics*, *4*, 2119–2143, doi:10.5194/acp-4-2119-2004. 5.3.6, 6.3.6

RISSLER, J., A. VESTIN, E. SWIETLICKI, G. FISCH, J. ZHOU, P. ARTAXO, and M. O. ANDREAE (2006), Size distribution and hygroscopic properties of aerosol particles from

dry-season biomass burning in Amazonia, *Atmospheric Chemistry and Physics*, *6*, 471–491, doi:10.5194/acp-6-471-2006. 1.2

RISSMAN, T. A., A. NENES, and J. H. SEINFELD (2004), Chemical amplification (or dampening) of the Twomey effect: Conditions derived from droplet activation theory, *Journal of the Atmospheric Sciences*, *61*, 919–930, doi:10.1175/1520-0469(2004)061<0919:CAODOT>2.0.CO;2. 9.1

RISSMAN, T. A., T. M. VANREKEN, J. WANG, R. GASPARINI, D. R. COLLINS, H. H. JONSSON, F. J. BRECHTEL, R. C. FLAGAN, and J. H. SEINFELD (2006), Characterization of ambient aerosol from measurements of cloud condensation nuclei during 2003 Atmospheric Radiation Measurement Aerosol Intensive Observational Period at the Southern Great Plains site in Oklahoma, *Journal of Geophysical Research*, *111*, D05S11, doi:10.1029/2004JD005695. 9.1

ROBERTS, G., G. MAUGER, O. HADLEY, and V. RAMANATHAN (2006), North American and Asian aerosols over the eastern Pacific Ocean and their role in regulating cloud condensation nuclei, *Journal of Geophysical Research*, *111*, D13205, doi:10.1029/2005JD006661. 6.1, 9.1

ROBERTS, G. C., and A. NENES (2005), A continuous-flow streamwise thermal-gradient CCN chamber for atmospheric measurements, *Aerosol Science and Technology*, *39*, 206–221, doi:10.1080/027868290913988. 2.1, 2.2, 2.3.1, 2.3.2, 2.3.3, 2.3.4, 2.5, 3.1, 3.2.1, 4.2.4, 5.2.4, 6.2.4, 7.2.1, 8.2.1, 9.1

ROBERTS, G. C., D. A. DAY, L. M. RUSSELL, E. J. DUNLEA, J. L. JIMENEZ, J. M. TOMLINSON, D. R. COLLINS, Y. SINOZUKA, and A. D. CLARK (2010), Characeterization of paricle cloud droplet activity and composition in the free troposphere and the boundary layer during INTEX-B, *Atmospheric Chemistry and Physics*, *10*, 6627–6644, doi:10.5194/acp-10-6627-2010. 7.3.1

ROLPH, G. D. (2011), Real-time Environmental Applications and Display sYstem (READY) website (http://ready.arl.noaa.gov). (document), 8.1

ROSE, D., S. S. GUNTHE, E. MIKHAILOV, G. P. FRANK, U. DUSEK, M. O. ANDREAE, and U. PÖSCHL (2008), Calibration and measurement uncertainties of a continuous-flow cloud condensation nuclei counter (DMT-CCNC): CCN activation of ammonium sulfate and sodium chloride aerosol particles in theory and experiment, *Atmospheric Chemistry and Physics*, *8*, 1153–1179, doi:10.5194/acp-8-1153-2008. 2.1, 2.3.2, 2.4.1, 2.4.1, 3.1, 3.2.1, 3.2.1, 3.2.3, 3.4.1, 5.2.4, 6.2.4, 7.2.1, 7.5.4, 8.2.1

ROSE, D., A. NOWAK, P. ACHTERT, A. WIEDENSOHLER, M. HU, M. SHAO, Y. ZHANG, M. O. ANDREAE, and U. PÖSCHL (2010), Cloud condensation nuclei in polluted air and biomass burning smoke near the mega-city Guangzhou, China - Part 1: Size-resolved measurements and implications for the modeling of aerosol particle hygroscopicity and CCN activity, *Atmospheric Chemistry and Physics*, *10*, 3365–3383, doi:10.5194/acp-10-3365-2010. 3.1, 3.1, 5.3.6, 6.3.6

ROSE, D., S. S. GUNTHE, H. SU, R. M. GARLAND, H. YANG, M. BERGHOF, Y. F. CHENG, B. WEHNER, P. ACHTERT, A. NOWAK, A. WIEDENSOHLER, N. TAKEGAWA, Y. KONDO, M. HU, Y. ZHANG, M. O. ANDREAE, and U. PÖSCHL (2011), Cloud condensation nuclei in polluted air and biomass burning smoke near the mega-city Guangzhou, China – Part 2: Size-resolved aerosol chemical composition, diurnal cycles, and externally mixed weakly CCN-active soot particles, *Atmospheric Chemistry and Physics*, *11*, 2817–2836, doi:10.5194/acp-11-2817-2011. 9.1

ROSENFELD, D., W. L. WOODLEY, D. AXISA, E. FREUD, J. G. HUDSON, and A. GIVATI (2008), Aircraft measurements of the impacts of pollution aerosols on clouds and precipitation over the Sierra Nevada, *Journal of Geophysical Research*, *113*, D15203, doi:10.1029/2007JD009544. 6.1

ROTMAN, D. A., J. R. TANNAHILL, D. E. KINNISON, P. S. CONNELL, D. BERGMANN, D. PROCTOR, J. M. RODRIGUEZ, S. J. LIN, R. B. ROOD, M. J. PRATHER, P. J. RASCH, D. B. CONSIDINE, R. RAMAROSON, and S. R. KAWA (2001), Global Modeling Initiative assessment model: Model description, integration, and testing of the transport shell, *Journal of Geophysical Research*, *106*, 1669–1691, doi:10.1029/2000JD900463. 9.2.2

RUBEL, G. O., and J. W. GENTRY (1984), Measurement of the kinetics of solution droplets in the presence of adsorbed monolayers: determination of water accommodation coefficients, *Journal of Physical Chemistry*, *88*, 3142–3148, doi:10.1021/j150658a046. 2.3.4, 7.3.2

RUEHL, C. R., P. Y. CHUANG, and A. NENES (2008), How quickly do cloud droplets form on atmospheric particles?, *Atmospheric Chemistry and Physics*, *8*, 1043–1055, doi:10.5194/acp-8-1043-2008. 2.1, 2.4.2, 3.1, 7.3.2

RUEHL, C. R., P. Y. CHUANG, and A. NENES (2009), Distinct CCN activation kinetics above the marine boundary layer along the California coast, *Geophysical Research Letters*, *36*, L15814, doi:10.1029/2009GL038839. 1.3, 3.1, 7.3.2

RUEHL, C. R., P. Y. CHUANG, and A. NENES (2010), Aerosol hygroscopicity at high (99 to 100%) relative humidities, *Atmospheric Chemistry and Physics*, *10*, 1329–1344, doi:10.5194/acp-10-1329-2010. 10.1

RUSSELL, L. M., R. C. FLAGAN, and J. H. SEINFELD (1995), Asymmetric instrument response resulting from mixing effects in accelerated DMA-CPC measurements, *Aerosol Science and Technology*, *23*, 491–509, doi:10.1080/02786829508965332. 3.2.2, 3.4.1

RYERSON, T. B., K. C. AIKIN, W. M. ANGEVINE, E. L. ATLAS, D. R. BLAKE, C. A. BROCK, F. C. FEHSENFELD, R.-S. GAO, J. A. DE GOUW, D. W. FAHEY, J. S. HOLLOWAY, D. A. LACK, R. A. LUEB, S. MEINARDI, A. M. MIDDLEBROOK, D. M. MURPHY, J. A. NEUMAN, J. B. NOWAK, D. D. PARRISH, J. PEISCHL, A. E. PERRING, I. B. POLLACK, A. R. RAVISHANKARA, J. M. ROBERTS, J. P. SCHWARZ, J. R.

SPACKMAN, H. STARK, C. WARNEKE, and L. A. WATTS (2011), Atmospheric emissions from the Deepwater Horizon spill contrain air-water partitioning, hydrocarbon fate, and leak rate, *Geophysical Research Letters*, *38*, L07803, doi:10.1029/2011GL04672. 7.1

SCHULZ, H. D., and M. ZABEL (Eds.) (2006), *Marine Geochemistry, 2nd Edition*, Springer. 4.3.2, 4.1, 4.3.2

SCHWARZ, J. P., J. R. SPACKMAN, D. W. FAHEY, R. S. GAO, U. LOHMANN, P. STIER, L. A. WATTS, D. S. THOMSON, D. A. LACK, L. PFISTER, M. J. MAHONEY, D. BAUMGARDNER, J. WILSON, and J. M. REEVES (2008), Coatings and their enhancement of black carbon light absorption in the tropical atmosphere, *Journal of Geophysical Research*, *113*, D03203, doi:10.1029/2007JD009042. 7.2.1

SEINFELD, J. H., and S. N. PANDIS (2006), *Atmospheric chemistry and physics: From air pollution to climate change*, 2nd ed., Wiley. 1.2, 1.3, 2.3.4, 2.3.4, 4, 3.4.1

SHANTZ, N. C., W. R. LEAITCH, and P. F. CAFFREY (2003), Effect of organics of low solubility on the growth rate of cloud droplets, *Journal of Geophysical Research*, *108*, 4168, doi:10.1029/2002JD002540. 1.3, 2.1

SHANTZ, N. C., W. R. LEAITCH, L. PHINNEY, M. MOZURKEWICH, and D. TOOM-SAUNTRY (2008), The effect of organic compounds on the growth rate of cloud droplets in marine and forest settings, *Atmospheric Chemistry and Physics*, *8*, 5869–5887, doi:10.5194/acp-8-5869-2008. 3.1

SHANTZ, N. C., R. Y.-W. CHANG, J. G. SLOWIK, A. VLASENKO, J. P. D. ABBATT, and W. R. LEAITCH (2010), Slower CCN growth kinetics of anthropogenic aerosol compared to biogenic aerosol observed at a rural site, *Atmospheric Chemistry and Physics*, *10*, 299–312, doi:10.5194/acp-10-299-2010. 7.3.2

SHAW, G. E. (1983), On the aerosol particle size distribution spectrum in Alaskan air mass systems: Arctic haze and non-haze episodes, *Journal of the Amospheric Sciences*, *40*, 1313–1320, doi:10.1175/1520-0469(1983)040<1313:OTAPSD>2.0.CO;2. 5.3.1

SHAW, G. E. (1984), Microparticle size spectrum of Arctic haze, *Geophysical Research Letters*, *11*, 409–412, doi:10.1029/GL011i005p00409. 5.3.1

SHAW, G. E. (1986), Cloud condensation nuclei associated with Arctic haze, *Atmospheric Environment*, *20*, 1453–1456, doi:10.1016/0004-6981(86)90017-X. 5.1, 5.3.2

SHAW, G. E. (1995), The Arctic haze phenomenon, *Bulletin of the American Meteorological Society*, *76*, 2403–2413, doi:10.1175/1520-0477(1995)076<2403:TAHP>2.0.CO;2. 5.1

SHAW, R. A., and D. LAMB (1999), Experimental determination of the thermal accomodation and condensation coefficients of water, *Journal of Chemical Physics*, *111*, 10,659–106,663, doi:10.1063/1.480419. 1.3, 7.3.2, 7.5.4

SHINOZUKA, Y., A. D. CLARKE, P. F. DECARLO, J. L. JIMENEZ, E. J. DUNLEA, G. C. ROBERTS, J. M. TOMLINSON, D. R. COLLINS, S. G. HOWELL, V. N. KAPUSTIN, C. S. MCNAUGHTON, and J. ZHOU (2009), Aerosol optical properties relevant to regional remote sensing of CCN activity and links to their organic mass fraction: Airborne observations over central Mexico and the US west coast during MILAGRO/INTEX-B, *Atmospheric Chemistry and Physics*, *9*, 6727–6742, doi:10.5194/acp-9-6727-2009. 3.1

SHULMAN, M. L., M. C. JACOBSON, R. J. CARLSON, R. E. SYNOVEC, and T. E. YOUNG (1996), Dissolution behavior and surface tension effects of organic compounds in nucleating cloud droplets, *Geophysical Research Letters*, *23*, 277–280, doi:10.1029/95GL03810. 1.2, 1.3

SHUPE, D., MATTHEW, and J. M. INTERIERI (2004), Cloud radiative forcing of the Arctic surface: The influence of cloud properties, surface albedo, and solar zenith angle, *Journal of Climate*, *17*, 616–628, doi:10.1175/1520-0442(2004)017<0616:CRFOTA>2.0.CO;2. 5.1

SINNARWALLA, A. M., and D. J. ALOFS (1973), A cloud nucleus counter with long available growth time, *Journal of Applied Meteorology*, *12*, 831–835, doi:10.1175/1520-0450(1973)012<0831:ACNCWL>2.0.CO;2. 2.1

SMITH, J. N., M. J. DUNN, T. M. VANREKEN, K. IIDA, M. R. STOLZENBURG, P. H. MCMURRY, and L. G. HUEY (2008), Chemical composition of atmospheric nanoparticles formed from nucleation in Tecamac, Mexico: Evidence for an important role for organic species in nanoparticle growth, *Geophysical Research Letters*, *35*, L04808, doi:10.1029/2007GL032523. 7.3.2

SNIDER, J. R., and J.-L. BRENGUIER (2000), Cloud condensation nuclei and cloud droplet measurements during ACE-2, *Tellus*, *52*, 828–842, doi:10.1034/j.1600-0889.2000.00044.x. 9.1

SNIDER, J. R., S. GUIBERT, J.-L. BRENGUIER, and J.-P. PUTAUD (2003), Aerosol activation in marine stratocumulus clouds: 2. Köhler and parcel theory closure studies, *Journal of Geophysical Research*, *108*, 8629, doi:10.1029/2002JD002692. 9.1

SOLOMON, S., D. QIN, M. MANNING, Z. CHEN, M. MARQUIS, K. B. AVERYT, M. TIGNOR, and H. L. MILLER (Eds.) (2007), *Climate Change 2007: The Physical Science Basis*, Intergovernmental Panel on Climate Change Fourth Assessment Report, Cambridge University Press. (document), 1, 1.1, 1.2, 2.1, 3.1, 9.1

SORJAMAA, R., and A. LAAKSONEN (2007), The effect of $H_2O$ adsorption on cloud drop activation of insoluble particles: A theoretical framework, *Atmospheric Chemistry and Physics*, *7*, 6175–6180, doi:10.5194/acp-7-6175-2007. 1.2

SOROOSHIAN, A., S. M. MURPHY, S. HERSEY, H. GATES, L. T. PADRO, A. NENES, F. J. BRECHTEL, H. JONSSON, R. C. FLAGAN, and J. H. SEINFELD (2008), Comprehensive airborne characterization of aerosol from a major bovine source, *Atmospheric*

*Chemistry and Physics*, *8*, 5489–5520, doi:10.5194/acp-8-5489-2008. 2.1, 3.1, 6.1, 6.3.1

SOTIROPOULOU, R.-E. P., J. MEDINA, and A. NENES (2006), CCN predictions: Is theory sufficient for assessments of the indirect effect?, *Geophysical Research Letters*, *33*, L05816, doi:10.1029/2005GL025148. 9.1

SOTIROPOULOU, R.-E. P., A. NENES, P. J. ADAMS, and J. H. SEINFELD (2007), Cloud condensation nuclei prediction error from application of köhler theory: Importance for the aerosol indirect effect, *Journal of Geophysical Research*, *112*, D12202, doi:10.1029/2006JD007834. 9.1, 9.3.2, 9.3.4

STOCKS, B. J., M. A. FOSBERG, T. J. LYNHAM, L. MEARNS, B. M. WOTTON, Q. YANG, J.-Z. JIN, K. LAWRENCE, G. R. HARTLEY, J. A. MASON, and D. W. MCKENNEY (1998), Climate change and forest fire potential in Russian and Canadian Boreal forests, *Climatic Change*, *38*, 1–13, doi:10.1023/A:1005306001055. 5.4

STOHL, A., E. ANDREWS, J. F. BURKHART, C. FORSTER, A. HERBER, S. W. HOCH, D. KOWAL, C. LUNDER, T. MEFFORD, J. A. OGREN, S. SHARMA, N. SPICHTINGER, K. STEBEL, R. STONE, J. STRÖM, K. TØRSETH, C. WEHRLI, and K. E. YTTRI (2006), Pan-Arctic enhancements of light absorbing aerosol concentrations due to North American boreal forest fires during summer 2004, *Journal of Geophysical Research*, *111*, D22214, doi:10.1029/2006JD007216. 5.1

STOHL, A., T. BERG, J. F. BURKHART, A. M. FJÆRAA, C. FORSTER, A. HERBER, Ø. HOV, C. LUNDER, W. W. MCMILLAN, S. OLTMANS, M. SHIOBARA, D. SIMPSON, S. SOLBERG, K. STEBEL, J. STRÖM, K. TØRSETH, R. TREFFEISEN, K. VIRKKUNEN, and K. E. YTTRI (2007), Arctic smoke – record high air pollution levels in the European Arctic due to agricultural files in Eastern Europe in spring 2006, *Atmospheric Chemistry and Physics*, *7*, 511–534, doi:10.5194/acp-7-511-2007. 5.1

STRÖM, J., J. UMEGÅRD, K. TØRSETH, P. TUNVED, H.-C. HANSSON, K. HOLMÉN, V. WISMANN, A. HERBER, and G. KÖNIG-LANGLO (2003), One year of particle size distribution and aerosol chemical composition measurements at the Zeppelin Station, Svalbard, March 2000 – March 2001, *Physics and Chemistry of the Earth*, *28*, 1181–1190, doi:10.1016/j.pce.2003.08.058. 5.3.1

STROUD, C. A., A. NENES, J. L. JIMENEZ, P. F. DECARLO, J. A. HUFFMAN, R. BRUINTJES, E. NEMITZ, A. E. DELIA, D. W. TOOHEY, A. B. GUENTHER, and S. NANDI (2007), Cloud activating properties of aerosol observed during CELTIC, *Journal of the Atmospheric Sciences*, *64*, 441–459, doi:10.1175/JAS3843.1. 9.1

SULLIVAN, A. P., and R. J. WEBER (2006), Chemical characterization of the ambient organic aerosol soluble in water: 1. Isolation of hydrophobic and hydrophilic fractions with a XAD-8 resin, *Journal of Geophysical Research*, *111*, D05314, doi:10.1029/2005/JD006485. 8.1

TARANIUK, I., E. R. GRABER, A. KOSTINSKI, and Y. RUDICH (2007), Surfactant properties of atmospheric and model humic-like substances (HULIS), *Geophysical Research Letters*, *34*, L16807, doi:10.1029/2007GL029576. 4.2.3, 4.3.2

THOMSON, D. S., M. E. SCHEIN, and D. M. MURPHY (2000), Particle analysis by laser mass spectrometry WB-57F instrument overview, *Aerosol Science and Technology*, *33*, 153–169, doi:10.1080/027868200410903. 5.2.2

TOON, O. B., J. B. POLLACK, and B. N. KHARE (1976), The optical constants of several atmospheric aerosol species: Ammonium sulfate, ammonium oxide, and sodium chloride, *Journal of Geophysical Research*, *81*, 5733–5748, doi:10.1029/JC081i033p05733. 7.1

TRENBERTH, K. E., J. T. FASULLO, and J. KIEHL (2009), Earth's global energy budget, *Bulletin of the American Meteorological Society*, *90*, 311–323, doi:10.1175/2008BAMS2634.1. 1.1

TSI, INCORPORATED (2003), *3936 Scanning Mobility Particle Sizer*. 4, 4

TWOMEY, S. (1963), Measurements of natural cloud nuclei, *Journal de Recherches Atmospheriques*, *1*, 101–105. 2.1

TWOMEY, S. (1974), Pollution and the planetary albedo, *Atmospheric Environment*, *8*, 1251–1256, doi:10.1016/0004-6981(74)90004-3. 1.1

TWOMEY, S. (1977a), The influence of pollution on the shortwave albedo of clouds, *Journal of the Atmospheric Sciences*, *34*, 1149–1152, doi:10.1175/1520-0469(1977)034<1149:TIOPOT>2.0.CO;2. 1.1, 2.1, 5.1, 6.1, 6.3.2, 9.1

TWOMEY, S. (1977b), *Atmospheric Aerosols*, Developments in Atmospheric Science, Elsevier Scientific. 5.3.2

TWOMEY, S. (1991), Aerosols, clouds and radiation, *Atmospheric Environment*, *25*, 2435–2442, doi:10.1016/0960-1686(91)90159-5. 9.3.3

VANREKEN, T. M., T. A. RISSMAN, G. C. ROBERTS, V. VARUTBANGKUL, H. H. JONSSON, R. C. FLAGAN, and J. H. SEINFELD (2003), Toward aerosol/cloud condensation nuclei (CCN) closure during CRYSTAL-FACE, *Journal of Geophysical Research*, *108*, 4633, doi:10.1029/2003JD003582. 5.3.6, 6.3.6, 9.1

VANREKEN, T. M., A. NENES, R. C. FLAGAN, and J. H. SEINFELD (2004), Concept for a new cloud condensation nucleus (CCN) spectrometer, *Aerosol Science and Technology*, *38*, 639–654, doi:10.1080/02786820490479842. 2.1

VESTIN, A., J. RISSLER, E. SWIETLICKI, G. P. FRANK, and M. O. ANDREAE (2007), Cloud-nucleating properties of the Amazonian biomass burning aerosol: Cloud condensation nuclei measurements and modeling, *Journal of Geophysical Research*, *112*, D14201, doi:10.1029/2006JD008104. 3.1, 9.2.1

VETTER, T. A., E. M. PERDUE, E. INGALL, J.-F. KOPRIVNJAK, and P. H. PFROMM (2007), Combining reverse osmosis and electrodialysis for more complete recovery of dissolved organic matter from seawater, *Separation and Purification Technology*, *56*, 383–387, doi:10.1016/j.seppur.2007.04.012. 4.1, 4.2.1

WANG, J., Y.-N. LEE, P. H. DAUM, J. JAYNE, and M. L. ALEXANDER (2008), Effects of aerosol organics on cloud condensation nucleus (CCN) concentration and first indirect aerosol effect, *Atmospheric Chemistry and Physics*, *8*, 6325–6339, doi:10.5194/acp-8-6325-2008. 2.1, 3.1, 6.3.5, 9.1

WANG, J., M. J. CUBISON, A. C. AIKEN, J. L. JIMENEZ, and D. R. COLLINS (2010a), The importance of aerosol mixing state and size-resolved composition on CCN concentration and the variation of the importance with atmospheric aging of aerosols, *Atmospheric Chemistry and Physics*, *10*, 7267–7283, doi:10.5194/acp-10-7267-2010. 5.3.6, 6.3.6, 6.3.6, 8.3.1, 9.1

WANG, L., A. F. KHALIZOV, J. ZHENG, W. XU, Y. MA, V. LA, and R. ZHANG (2010b), Atmospheric nanoparticles formed from heterogeneous reactions of organics, *Nature Geoscience*, *3*, 238–242, doi:10.1038/ngeo778. 7.3.2

WANG, S. C., and R. C. FLAGAN (1989), Scanning electrical mobility spectrometer, *Journal of Aerosol Science*, *20*, 1485–1488, doi:10.1016/0021-8502(89)90868-9. 3.1, 3.2.2, 4, 9.1

WARNEKE, C., R. BAHREINI, J. BRIOUDE, C. A. BROCK, J. A. DE GOUW, D. W. FAHEY, K. D. FROYD, J. S. HOLLOWAY, A. MIDDLEBROOK, L. MILLER, S. MONTZKA, D. M. MURPHY, J. PEISCHL, T. B. RYERSON, J. P. SCHWARZ, J. R. SPACKMAN, and P. VERES (2009), Biomass burning in Siberia and Kazakhstan as an important source for haze over the Alaskan Arctic in April 2008, *Geophysical Research Letters*, *36*, L02,813, doi:10.1029/2008GL036194. 5.3.6

WARNEKE, C., K. D. FROYD, J. BRIOUDE, R. BAHREINI, C. A. BROCK, J. COZIC, J. A. DE GOUW, D. W. FAHEY, R. FERRARE, J. S. HOLLOWAY, A. M. MIDDLEBROOK, L. MILLER, S. MONTZKA, J. P. SCHWARZ, H. SODEMANN, and J. R. SPACKMAN (2010), An important contribution to springtime Arctic aerosol from biomass burning in Russia, *Geophysical Research Letters*, *37*, L01,801, doi:10.1029/2009GL041816. 5.1, 5.4

WEBER, R. J., D. ORSINI, Y. DAUN, Y.-N. LEE, P. J. KLOTZ, and F. BRECHTEL (2001), A particle-into-liquid collector for rapid measurement of aerosol bulk chemical composition, *Aerosol Science and Technology*, *35*, 718–727, doi:10.1080/02786820152546761. 9.1

WEBER, R. J., A. P. SULLIVAN, R. E. PELTIER, A. RUSSELL, B. YAN, M. ZHENG, J. DE GOUW, C. WARNEKE, C. BROCK, J. S. HOLLOWAY, E. L. ATLAS, and E. EDGERTON (2007), A study of secondary organic aerosol formation in the anthropogenic-influenced southeastern United States, *Journal of Geophysical Research*, *112*, D13302, doi:10.1029/2007JD008408. 8.1

WEX, H., T. HENNIG, I. SALMA, R. OCSKAY, A. KISELEV, S. HENNING, A. MASSLING, A. WIEDENSOHLER, and F. STRATMANN (2007), Hygroscopici growth and measured and modeled critical supersaturations of an atmospheric HULIS sample, *Geophysical Research Letters*, *34*, L02818, doi:10.1029/2006GL028260. 3.1

WIEDENSOHLER, A. (1988), Technical note: An approximation of the bipolar charge distribution for particles in the submicron size range, *Journal of Aerosol Science*, *19*, 387–389, doi:10.1016/0021-8502(88)90278-9. 4, 4

YUM, S. S., and J. G. HUDSON (2001), Vertical distributions of cloud condensation nuclei spectra over the springtime Arctic Ocean, *Journal of Geophysical Research*, *106*, 15,045–15,052, doi:10.1029/2000JD900357. 5.1, 5.3.2

YUM, S. S., G. ROBERTS, J. H. KIM, K. SONG, and D. KIM (2007), Submicron aerosol size distributions and cloud condensation nuclei concentrations measured at Gosan, Korea, during the Atmospheric Brown Clouds–East Asian Regional Experiment 2005, *Journal of Geophysical Research*, *112*, D22S32, doi:10.1029/2006JD008212. 9.1

ZHANG, D., K. F. MOORE, R. R. FRIEDL, and M.-T. LEU (2008), Design and characterization of a horizontal thermal gradient cloud condensation nucleus spectrometer, *Journal of Aerosol Science*, *39*, 30–39, doi:10.1016/j.jaerosci.2007.10.004. 2.1

ZHANG, Q., and C. ANASTASIO (2001), Chemistry of fog waters in california's Central Valley – Part 3: Concentrations and speciation of organic and inorganic nitrogen, *Atmospheric Environment*, *35*, 5629–5643, doi:10.1016/S1352-2310(01)00337-5. 6.1

ZHANG, Q., M. R. ALFARRA, D. R. WORSNOP, J. D. ALLAN, H. COE, M. R. CANAGARATNA, and J. L. JIMENEZ (2005a), Deconvolution and quantification of hydrocarbon-like and oxygenated organic aerosols based on aerosol mass spectrometry, *Environmental Science and Technology*, *39*, 4938–4952, doi:10.1021/es048568l. 5.3.4, 7.3.1

ZHANG, Q., D. R. WORSNOP, M. R. CANAGARATNA, and J. L. JIMENEZ (2005b), Hydrocarbon-like and oxygenated organic aerosols in Pittsburgh: Insights into sources and processes of organic aerosols, *Atmospheric Chemistry and Physics*, *5*, 3289–3311, doi:10.5194/acp-5-3289-2005. 6.3.1, 6.3.4

ZHANG, Q., J. L. JIMENEZ, M. R. CANAGARATNA, J. D. ALLAN, H. COE, I. ULBRICH, M. R. ALFARRA, A. TAKAMI, A. M. MIDDLEBROOK, Y. L. SUN, K. DZEPINA, E. DUNLEA, K. DOCHERTY, P. F. DECARLO, D. SALCEDO, T. ONASCH, J. T. JAYNE, T. MIYOSHI, A. SHIMONO, S. HATAKEYAMA, N. TAKEGAWA, Y. KONDO, J. SCHNEIDER, F. DREWNICK, S. BORRMANN, S. WEIMER, K. DEMERJIAN, P. WILLIAMS, K. BOWER, R. BAHREINI, L. COTTRELL, R. J. GRIFFIN, J. RAUTIAINEN, J. Y. SUN, Y. M. ZHANG, and D. R. WORSNOP (2007), Ubiquity and dominance of oxygenated species in organic aerosols in anthropogenically-influenced Northern Hemisphere midlatitudes, *Geophysical Research Letters*, *34*, L13801, doi:10.1029/2007GL029979. 7.1

# VITA

Richard Moore was born in Harrisburg, Pennsylvania, USA, in 1982 to Herbert and Marianne Moore. He attended Middletown Area High School, Middletown, PA, before earning B.S. and M.S. degrees in chemical engineering from Bucknell University in Lewisburg, PA. His masters thesis was supervised by Professor Timothy M. Raymond. In 2006, Richard entered the Ph.D. program of the School of Chemical & Biomolecular Engineering at the Georgia Institute of Technology, Atlanta, Georgia, under the direction of Professor Athanasios Nenes. He is the author or co-author of eleven peer-reviewed journal publications with six additional publications currently in preparation or in review. As a graduate student at Georgia Tech, Richard was supported by graduate research fellowships from the Department of Energy Global Change Education Program and the National Aeronautics and Space Administration Earth and Space Science Program, a Georgia Institute of Technology President's Fellowship, and a Sam Nunn School of International Affairs Fellowship. He is also the recipient of five awards for outstanding student conference presentations and posters, as well as an award for exemplary academic achievement in the School of Chemical & Biomolecular Engineering at Georgia Tech. He will graduate in December of 2011 with a Ph.D. in chemical engineering, a certificate in public policy, and having completed the "Tech to Teaching" program. In 2012, Richard will begin a postdoctoral fellowship at the NASA Langley Research Center under the direction of Dr. Bruce Anderson. He currently lives in Atlanta with his wife, Emily.